Multi-component acoustic characterization of porous media

PROEFSCHRIFT

ter verkrijging van de graad van doctor
aan de Technische Universiteit Delft,
op gezag van de Rector Magnificus prof.ir. K.C.A.M. Luyben,
voorzitter van het College voor Promoties,
in het openbaar te verdedigen op maandag 7 maart 2011 om 15.00 uur

door Karel Nicolaas VAN DALEN

civiel ingenieur
geboren te Papendrecht.

Dit proefschrift is goedgekeurd door de promotoren:
Prof.dr.ir. C.P.A. Wapenaar
Prof.dr.ir. D.M.J. Smeulders

Copromotor:
Dr.ir. G.G. Drijkoningen

Samenstelling promotiecommissie:

Rector Magnificus,	Technische Universiteit Delft, voorzitter
Prof.dr.ir. C.P.A. Wapenaar,	Technische Universiteit Delft, promotor
Prof.dr.ir. D.M.J. Smeulders,	Technische Universiteit Eindhoven, promotor
Dr.ir. G.G. Drijkoningen,	Technische Universiteit Delft, copromotor
Prof.dr. A.V. Metrikine,	Technische Universiteit Delft
Prof.dr.ir. G. Ooms,	Technische Universiteit Delft
Prof.dr.ir. N.B. Roozen,	Technische Universiteit Eindhoven
Dr. C. Glorieux,	Katholieke Universiteit Leuven

This work is financially supported by "The Netherlands Research Centre for Integrated Solid Earth Science" (ISES) and is part of the "NedSeis" research program.

ISBN 978-90-9025970-3

© 2011 by K.N. van Dalen. Some rights reserved. Chapters 4 and 5 are reproduced by permission of the Acoustical Society of America (van Dalen *et al.*, 2010b, 2011). Chapter 6 has been submitted for publication to the Journal of the Acoustical Society of America. Chapter 8 is reproduced by permission of the American Geophysical Union (van Dalen *et al.*, 2010a). No part of this publication may be reproduced or distributed in any form or by any means, or stored in a database or retrieval system, without the prior written permission of the publishers.

Published by: Uitgeverij BOX Press, Oisterwijk, The Netherlands
Printed by: Proefschriftmaken.nl
Cover: Photograph by Jürg Hunziker and Karel van Dalen

Dedicated to my wife Jannine and all others who have supported me

Contents

1 Introduction **1**
1.1 Background and motivation 1
1.2 Research objective and outline 4

2 Governing equations for wave propagation in a fluid-saturated porous medium **7**
2.1 Introduction 7
2.2 Definitions 8
2.3 Continuum description of a porous medium 8
2.4 Stress-strain relations 11
2.4.1 Effect of fluid pressure (unjacketed test) 11
2.4.2 Effect of intergranular stresses (jacketed test) 12
2.4.3 Combination of effects 13
2.4.4 Relation of Biot's elastic constants to physical quantities . . . 14
2.5 Equations of motion 16
2.5.1 Incorporation of frequency-dependent permeability or tortuosity 18
2.5.2 Alternative formulation of the equations of motion 22
2.6 Conclusions 23

3 Green's tensors for wave propagation in a fluid-saturated porous medium **25**
3.1 Introduction 25
3.2 Green's tensors for infinite space 26
3.2.1 Inverse transform of scalar Green's functions 29
3.2.2 Low-frequency approximation 31
3.2.3 High-frequency approximation 36
3.3 Impedances of the wavemodes 37
3.4 Numerical examples 39
3.5 Discussion 44
3.6 Conclusions 45

4 On wavemodes at the interface of a fluid and a fluid-saturated poroelastic solid **47**
4.1 Introduction 47

4.2 Model . . . 49
4.3 Green's functions . . . 52
4.4 Numerical implementation . . . 55
4.5 Numerical results and discussion . . . 56
4.5.1 Residue contribution vs full response . . . 56
4.5.2 Presence of pR-pole and pSt-pole on Riemann sheets . . . 62
4.5.3 Physical significance of additional poles . . . 64
4.6 Conclusions . . . 65
4.7 Appendix A: Transform-domain response . . . 67
4.8 Appendix B: Inverse Fourier integral . . . 69

5 Pseudo interface waves observed at the fluid/porous-medium interface. A comparison of two methods 71
5.1 Introduction . . . 71
5.2 Model . . . 73
5.3 Green's functions . . . 75
5.3.1 Plane-wave domain response . . . 75
5.3.2 Method I: Vertical branch cuts . . . 76
5.3.3 Method II: Hyperbolic branch cuts . . . 78
5.3.4 Inverse Fourier transform . . . 78
5.4 Physical interpretation of separate contributions . . . 79
5.4.1 Approximate pole contributions . . . 80
5.4.2 Approximate branch-cut contributions . . . 80
5.4.3 Physical interpretation of contributions . . . 83
5.5 Numerical results and discussion . . . 84
5.5.1 Separate wavemodes . . . 86
5.5.2 Interfering wavemodes . . . 88
5.5.3 Migration of poles . . . 89
5.6 Discussion . . . 90
5.7 Conclusions . . . 92

6 Impedance and ellipticity of fluid/elastic-solid interface waves: medium characterization and simultaneous displacement - pressure measurements 93
6.1 Introduction . . . 94
6.2 Impedance and ellipticity . . . 95
6.3 Medium characterization . . . 101
6.4 Experiment-specific modeling . . . 102
6.4.1 Acoustic response . . . 103
6.4.2 Effect of optical refractive-index changes integrated along laser beam . . . 104
6.5 Experimental results and impedance extraction . . . 105
6.6 Experimental observations versus model predictions . . . 108
6.7 Discussion . . . 111
6.8 Conclusions . . . 112
6.9 Appendix A: Cagniard-de Hoop solution . . . 113

7 Impedance and ellipticity of fluid/porous-medium interface waves: medium characterization and simultaneous displacement - pressure measurements **115**
7.1 Introduction 115
7.2 Impedance and ellipticity 116
7.3 Porous-medium characterization 121
7.4 Experiment-specific modeling 125
7.5 Experimental results 126
7.6 Experimental observations versus model predictions 128
7.7 Conclusions 130

8 In-situ permeability from integrated poroelastic reflection coefficients **133**
8.1 Introduction 133
8.2 Mesoscopic-flow mechanism 134
8.3 Permeability from integrated reflection coefficients 135
8.4 Discussion 138
8.5 Conclusions 140

9 Conclusions **141**

Bibliography **145**

Summary **155**

Samenvatting **157**

Acknowledgments **160**

Curriculum Vitae **162**

Chapter 1

Introduction

The central theme in this thesis is the characterization of porous media by combining information of full acoustic waveforms as observed in different components (e.g., particle motion and fluid pressure). We focus on the mathematical description of interface wavemodes, their experimental detection and the estimation of medium parameters using either interface or reflected body wavemodes. In this chapter we first give some background information to motivate the work presented in this thesis. Then, we define the specific research goal, and elaborate how the different chapters are linked to this goal and how they contribute to the main line of story.

1.1 Background and motivation

A well-known theory for wave propagation in fluid-saturated porous materials has been developed by Biot (1956a,b). It models the constituents of the porous medium as two immiscible interacting phases, i.e., the solid (porous frame) and the saturating fluid. The most striking feature of this theory is that it predicts the existence of a second compressional wave in addition to the conventional compressional and shear waves that are known in non-porous elastic solids (Achenbach, 1973). This is the result of taking into account the inertia of the fluid phase, which gives the medium an additional degree of freedom next to the motion of the solid. The second compressional wave is usually called the slow compressional (P_2) wave as its velocity is smaller than that of the conventional compressional wave, which, therefore, is addressed as the fast compressional (P_1) wave. The P_1- and shear (S) waves induce a motion of the fluid which is practically in-phase with the motion of the solid. The P_2-mode, however, induces an out-of-phase motion of the fluid and solid, which leads to its strong attenuation by the viscous damping mechanism associated with the relative fluid-solid motion; the P_1- and S-waves have relatively small attenuation. At low frequencies, the P_2-mode shows diffusive behavior and at high frequencies it is propagatory. One of the strong features of Biot's theory is that it can be derived from combining well-defined physical laws and mechanisms without having to resort to empirical relationships, i.e., conservation of momentum, conservation of mass,

theory of elasticity for the elastic behavior of the solid and the fluid, and Darcy's law for the relative fluid-solid motion. Hence, the model parameters have a clear physical meaning and can be determined in the laboratory.

Biot's theory is applied in several fields and on different scales. Among others, there are applications in ultrasonic testing of materials and structures (e.g., Sayers & Dahlin, 1993), wave propagation through cancellous bones (e.g., Cowin, 1999) and medical inverse problems (e.g., Sebaa *et al.*, 2008), noise control and absorption in building and environmental acoustics (e.g., Allard, 1993), borehole logging in geotechnical engineering and reservoir engineering (e.g., Burns, 1990), and reflection seismics in geophysics and seismology (e.g., Carcione, 2007). Generally speaking, for the following three aspects research in the field of wave propagation in porous media has been and is still challenging:

1. the physics of wave propagation,
2. computational physics (simulation of forward wave propagation),
3. material characterization (inverse problems).

Concerning the physics of wave propagation, the existence of the P_2-mode has been experimentally confirmed by Plona (1980). The existence of an additional interface wave at the interface of a fluid and a fluid-saturated porous medium as predicted by Feng & Johnson (1983a,b), i.e., the "true" interface wave, has been experimentally validated by Mayes *et al.* (1986). This wave can exist next to the pseudo-Rayleigh and pseudo-Stoneley waves that are the counterparts of the conventional pseudo-Rayleigh and Stoneley waves at the fluid/elastic-solid interface. A true interface wave propagates only along the interface and decays exponentially with distance normal to the interface. A "pseudo" interface wave, however, is not trapped at the interface as it continuously leaks energy into slower body wavemodes that are radiating away from the interface. Berryman (1980) has found that the predicted body-wave velocities are in very good agreement with the experimentally observed values for all three body wavemodes. For the frequency-dependent attenuation of the P_2-mode Johnson *et al.* (1994) have found excellent agreement between theory and experiment. In addition, for the reflection coefficients as predicted by Biot's theory they have observed reasonably good agreement between the predicted and measured frequency-dependent coefficients at ultrasonic frequencies, for all three body wavemodes. Regarding the P_1- and S-waves, it is well-known that Biot's wavelength-scale attenuation mechanism significantly underestimates their field-observed levels of attenuation in the seismic frequency band (e.g., Pride *et al.*, 2004). Up to this moment, considerable effort is made particularly to model the intrinsic attenuation of the P_1-wave (Müller *et al.*, 2010). Recent studies have shown that the major cause of the enlarged attenuation in porous media can be a wave-induced local fluid flow due to the presence of mesoscopic (sub-wavelength scale) heterogeneities causing fluid-pressure gradients (Pride *et al.*, 2004), i.e., pockets of weakly cemented grains or gas pockets larger than the grain size. It implies that the P_1-wave is attenuated by local conversions into the P_2-mode at the heterogeneities. The proposed models to incorporate this effect illustrate another strong feature of

Biot's theory: it provides a general framework for wave propagation in porous media, which can be modified or extended with additional mechanisms whenever the physical situation requires this. For example, Biot's equations can be coupled with Maxwell's equations for electromagnetics to describe the electrokinetic phenomenon (Pride, 1994), and non-linear wave propagation can be analyzed by modifications or extensions of Biot's equations (e.g., Straughan, 2008). Next to the field of wave attenuation, in the latter two fields still many advances can be made.

In the area of poroelasticity, computational physics has become an essential research and interpretation tool. Particularly in reservoir geophysics, ultrasonic and seismic modeling in porous media is used to study the properties of rocks and to simulate the seismic responses of geologic formations. An overview of the most common direct numerical methods used to solve the (Biot's or extended) partial differential equations is given by Carcione *et al.* (2010a). They discuss the finite-difference, pseudo-spectral and finite-element methods. One of the difficulties is the coexistence of waves and diffusion modes. Next to the direct methods, integral equation and ray tracing methods can be distinguished. In addition, there are the semi-analytical methods that make use of Fourier and Laplace transforms to find analytical solutions in the transformed domains, and apply numerical integration to find the transient responses. Among them are the matrix propagator method (Jocker *et al.*, 2004) and the transmission and reflection matrices method (Lu & Hanyga, 2005) for layered structures, where the latter avoids the stability problems of the former. In the semi-analytical methods questions arise regarding the physical interpretation of individual contributions in the inverse Fourier transform over the wavenumber. Using the contour integration method, Allard *et al.* (2004) have found that loop integrals around branch cuts can contribute to the waveform of a pseudo interface wave, while an interface wave is often considered to originate from a pole residue contribution only (Achenbach, 1973; Feng & Johnson, 1983a).

While there are many publications on the forward problem in poroelasticity, the inverse problem is rarely addressed in the literature, even though information of the porosity, permeability and fluid saturation distributions is very important for geotechnical and reservoir engineers. Some authors employ elastic wave theory combined with rock-physics modeling for the estimation of parameters (e.g., Bachrach, 2006). However, the use of the full poroelastic theory is preferred to directly relate wave characteristics to the poroelastic parameters and to use information that cannot be described by viscoelasticity or elasticity with the Gassmann (1951) formula (De Barros *et al.*, 2010). Chotiros (2002) inverts for poroelastic parameters using the extended Biot theory as formulated by Stoll, using the P_1- and S-wave speeds and attenuations and the reflection loss of the P_1-wave for the inversion. To our knowledge, De Barros *et al.* (2010) are the first to present a full-waveform inversion scheme of the seismic reflection response of a plane-layered fluid-saturated porous medium, thus making more extensive use of the information present in the reflected wave field. However, still only the information present in a single component observation is exploited, i.e., the vertical particle motion. The authors have found that the best results are obtained for the parameters to which the reflection response is most sensitive, namely porosity, consolidation parameter, solid density and shear

modulus. Fluid density, fluid bulk modulus and grain bulk modulus are more difficult to estimate reliably, and permeability, as the most important parameter in the oil industry (Pride *et al.*, 2003), appears to be the most poorly estimated parameter for fully-saturated media. However, close to an interface the permeability can be estimated using the pseudo-Stoneley wave by employing either its attenuation or its full waveform present in a single-component observation, as shown by Tang & Cheng (2004).

1.2 Research objective and outline

From the above outline of research achievements and challenges it is clear that up to now limited use is made of full-waveform information in the area of porous-medium characterization, and that multi-component information is not employed. Hence, in this thesis we aim to investigate the feasibility of exploiting full-waveform information as present in multi-component observations for the estimation of poroelastic parameters, particularly for that of the permeability. Multi-component observations are expected to be sensitive to the poroelastic parameters as they combine the waveforms in both the fluid and solid phases.

In the beginning of the thesis there are two introductory chapters (2 and 3). In Chapter 2 we give the theoretical framework for the wave propagation in a fluid-saturated porous medium. We show the derivation of the governing equations, and discuss the physical mechanisms and involved acoustic parameters. Subsequently, in Chapter 3 we derive the associated infinite-space Green's tensors in order to illustrate the frequency-dependent coupling between the waveforms of a particular body wavemode in solid particle motion and fluid pressure. This coupling is described by the "coupling impedance", which interrelates the waveforms in the different components and can, therefore, be addressed as a "multi-component full-waveform attribute".

For the medium characterization, we focus on using the interface waves at the interface between a fluid and a fluid-saturated porous medium for two reasons. In the first place, for seismic frequencies poroelastic effects are known to be more pronounced at interfaces than inside a medium (Gurevich, 1996) and, as a result, the interface waves can be particularly sensitive to the permeability (Rosenbaum, 1974; Winkler *et al.*, 1989). Secondly, the experimental validation of the use of multi-component full waveforms is relatively simple for interface waves in the ultrasonic regime for which a non-contact detection method using laser ultrasonics is available (Allard *et al.*, 2002, 2003, 2004).

As the above-mentioned true interface wave has rather limited range of existence, we will only consider the pseudo interface waves. In order to use their waveforms for characterization purposes, we first need to determine if and how the pseudo interface wave can be attributed to an individual contribution of the inverse Fourier integral over wavenumber (or slowness). In Chapter 4 we introduce this problem and confirm the observation of Allard *et al.* (2004) that the waveform is not necessarily captured by a pole residue contribution only. In Chapter 5 we proceed with the analysis and determine under which conditions the waveform of a pseudo interface wave is

entirely captured by a pole residue.

Next, we investigate how the multi-component full-waveform information of the interface waves can be exploited and what parameters can be estimated. To introduce our approach, in Chapter 6 we start with the interface waves in the fluid/elastic-solid configuration. Using the findings in Chapter 5, we can readily define the interface-wave impedance and ellipticity, which are both attributes that interrelate the full waveforms observed in different components. We investigate the sensitivities of these attributes to the medium parameters and, based on that, a way is presented to uniquely estimate Young's modulus and Poisson's ratio. The main principle is that we optimally use the sensitivities of the multi-component full-waveform attributes by exploiting them simultaneously for the estimation of the parameters. Further, in a laboratory validation experiment we examine the feasibility of the extraction of the interface-wave impedances from a simultaneous particle displacement and fluid pressure measurement using laser ultrasonics and a needle hydrophone; the feasibility of extracting the ellipticity using laser ultrasonics has already been reported by Blum *et al.* (2010).

In Chapter 7, we investigate the use of multi-component full-waveform information employing the fluid/porous-medium interface waves. By applying the same principle we analyze the feasibility of the estimation of the Young's modulus and Poisson's ratio (similar as in Chapter 6), being purely elastic parameters, and of the permeability and porosity, which are poroelastic parameters governing the attenuation mechanism related to the relative fluid-solid motion. We incorporate the porosity next to the permeability because often many combinations of permeability and porosity can explain the observed value of a wave attribute, and our approach of combining wave attributes provides a way to cope with this non-uniqueness problem. Next to the combination of the interface-wave impedance and ellipticity, we analyze the combination of impedance and attenuation because the latter can be particularly sensitive to the permeability (Rosenbaum, 1974; Winkler *et al.*, 1989). Further, like in Chapter 6, we include a laboratory validation experiment to investigate the feasibility of the extraction of the interface-wave impedances.

Finally, a synthetic application of multi-component full-waveform information for the estimation of permeability and porosity using a reflected seismic wavefield is illustrated in Chapter 8. We include a mesoscopic-flow mechanism to get realistic seismic attenuation. As a result, the P_1-wave is sensitive to permeability at seismic frequencies. For the parameter estimation, we apply a similar principle as for the interface waves. However, now we combine the frequency- and angle-dependent (layer/layer-interface) reflection coefficients of different wavemodes rather than different attributes of a single wavemode. Multi-component information is required to extract the reflection coefficients from the observed reflection response; we assume this step done and address the parameter estimation only. The use of the reflection coefficients implies that full-waveform information is exploited as a reflection coefficient describes the reflection response from a layer interface.

In Chapter 9 we summarize the main conclusions from all chapters.

Chapter 2

Governing equations for wave propagation in a fluid-saturated porous medium

2.1 Introduction

In this thesis we study the wave propagation in fluid-saturated porous media. We investigate how various wavemodes can be described mathematically and detected experimentally (especially the interface wavemodes), and how the various waves can be used to characterize acoustic parameters of a porous medium. Therefore, in this chapter we give the theoretical framework for the description of the wave propagation in a fluid-saturated porous medium. Originally, this theory was developed by Biot (1956a). Here, we show the derivation of the governing equations and discuss the physical mechanisms and involved acoustic parameters.

First, we give the definitions of integral transforms and some notation conventions that we use in this chapter and throughout the thesis (Section 2.2). Then, we show that a fluid-saturated porous medium can be considered as a continuum and discuss the underlying assumptions (Section 2.3). In Section 2.4 we derive stress-strain relations associated with Biot's theory from straightforward constitutive and continuity equations following Kelder (1998) and Wisse (1999). This shows that the involved elastic constants are clearly related to physical quantities. Subsequently, we combine the stress-strain relations with the momentum equations to finally obtain the equations of motions (Section 2.5). We present the equations of motion in two different formulations that are known in the literature.

2.2 Definitions

First, we define the integral transforms that is used in this thesis. For frequency-domain analysis we use the Fourier transform over time t defined as

$$\hat{\mathbf{u}}(\mathbf{x},\omega) = \int_{-\infty}^{\infty} \mathbf{u}(\mathbf{x},t)\exp(-\mathrm{i}\omega t)\,dt, \tag{2.1}$$

where ω denotes angular frequency, i is the imaginary unit and $\mathbf{u}$ is a displacement vector, but the Fourier transform can be applied to any other relevant field quantity. The vector $\mathbf{x} = (x_1, x_2, x_3)^T$ contains the spatial coordinates, where x_1 and x_2 are horizontal coordinates and x_3 is the vertical coordinate being positive in downward direction; the superscript T denotes the transpose. Because the time-domain signal $\mathbf{u}$ is real-valued it holds that $\hat{\mathbf{u}}(-\omega) = \hat{\mathbf{u}}^*(\omega)$, where the asterisk denotes complex conjugation. Hence it is sufficient to consider $\omega \geq 0$ only.

The Fourier transform over all spatial coordinates is defined as

$$\breve{\hat{\mathbf{u}}}(\mathbf{k},\omega) = \int_{-\infty}^{\infty}\int_{-\infty}^{\infty}\int_{-\infty}^{\infty} \hat{\mathbf{u}}(\mathbf{x},\omega)\exp(\mathrm{i}\mathbf{k}\cdot\mathbf{x})\,dx_1dx_2dx_3, \tag{2.2}$$

where $\mathbf{k} = (k_1, k_2, k_3)^T$ is the wavenumber vector. Throughout the thesis we often use slowness $\mathbf{p}$ which is related to the wavenumber according to $\mathbf{k} = \omega\mathbf{p}$ (Aki & Richards, 1980). The hat ($\hat{\mathbf{u}}$) refers to the $(\mathbf{x},\omega)$-domain and the combined bar/breve ($\breve{\hat{\mathbf{u}}}$) to the $(\mathbf{k},\omega)$-domain. We use a single breve ($\breve{\mathbf{u}}$) to indicate the $(\mathbf{p},\omega)$-domain.

Alternatively, when dealing with media that have discontinuities in x_3-direction (interfaces between layers), we apply the Fourier transform over horizontal coordinates only according to

$$\tilde{\hat{\mathbf{u}}}(\mathbf{k}_r, x_3, \omega) = \int_{-\infty}^{\infty}\int_{-\infty}^{\infty} \hat{\mathbf{u}}(\mathbf{x},\omega)\exp\left(\mathrm{i}\mathbf{k}_r\cdot\mathbf{r}\right)\,dx_1dx_2, \tag{2.3}$$

where $\mathbf{k}_r = (k_1, k_2)^T$ is the horizontal wavenumber vector and $\mathbf{r} = (x_1, x_2)^T$ is the horizontal space vector. In the case we work with the slowness rather than the wavenumber we apply $\mathbf{k}_r = \omega\mathbf{p}_r$ (see above). The combined bar/tilde ($\tilde{\hat{\mathbf{u}}}$) refers to the $(\mathbf{k}_r, x_3, \omega)$-domain, and a single tilde ($\tilde{\mathbf{u}}$) refers to the $(\mathbf{p}_r, x_3, \omega)$-domain.

When using index notation we invoke the Einstein's summation convention for repeated indices. However, the summation convention does not apply to Greek symbols (e.g., α, β) because we use these to indicate different wavemodes. Further, the Kronecker delta is denoted δ_{ij} and is defined as

$$\delta_{ij} = \begin{cases} 1, & i = j, \\ 0, & i \neq j. \end{cases} \tag{2.4}$$

2.3 Continuum description of a porous medium

As a basis for the derivation of the stress-strain relations associated with the theory for wave propagation in a fluid-saturated porous medium, in this section we give the underlying assumptions and we define stresses and strains.

The Biot theory describes porous materials as a medium consisting of two interpenetrating phases: the solid phase (porous frame) and the fluid phase (Biot, 1956a). The original theory has been developed using a semi-phenomenological macroscopic approach, based on a set of physically realistic assumptions. This approach means that the microscopic dimensions of the individual constituents of the saturated porous medium are not considered, i.e., the medium is considered as a continuum. The following assumptions were made:

1. The fluid-saturated porous material is constituted in such a way that the fluid phase is fully interconnected. Any sealed void space is considered as a part of the solid.

2. A so-called representative elementary volume element is defined, which is small compared to the relevant wavelength but large compared to the individual grains and pores of the system. Each volume element is described by its averaged displacement of the solid parts $\mathbf{u}(\mathbf{x}, t)$ and of the fluid parts $\mathbf{U}(\mathbf{x}, t)$.

3. The deformation of the elementary volume element is assumed to be linearly elastic and reversible. This implies that displacements for both fluid and solid phases are small. The governing equations can be represented in their linearized form.

4. The solid is considered to have compressibility and shear rigidity, while the fluid only has compressibility as it is assumed to be a Newtonian fluid: the fluid does not sustain any shear force for static displacements.

5. The solid and fluid are assumed homogeneous and isotropic, and all possible dissipation mechanisms related to the solid itself are not taken into account. Only dissipation due to viscous relative fluid-solid motion is incorporated.

6. Thermoelastic and chemical reaction effects are assumed to be absent and the system behaves adiabatically.

Following these assumptions, we can now define porosity, stresses and strains unambiguously. Considering a fluid-filled elastic porous matrix with a statistical distribution of interconnected pores, the porosity is usually defined by

$$\phi = \frac{V_f}{V_b}, \tag{2.5}$$

where V_f is the volume of the pores contained in a sample of bulk volume V_b, and the term "porosity" refers to the effective porosity (see assumption 1 above).

Within the restrictions of the linearized theory the (macroscopic) deformation of solid and fluid are described by the small-strain tensors, e_{ij} and ε_{ij}, respectively, according to

$$e_{ij} = \tfrac{1}{2}(\partial_i u_j + \partial_j u_i), \tag{2.6}$$

$$\varepsilon_{ij} = \tfrac{1}{2}(\partial_i U_j + \partial_j U_i). \tag{2.7}$$

where $\partial_j = \partial/\partial x_j$. It is evident that $e_{ij} = e_{ji}$ and $\varepsilon_{ij} = \varepsilon_{ji}$.

If we consider a cube of unit size of the bulk material (solid and fluid), the total stress tensor can be defined as

$$\tau_{b,ij} = \begin{pmatrix} \tau_{11} + \tau & \tau_{12} & \tau_{13} \\ \tau_{21} & \tau_{22} + \tau & \tau_{23} \\ \tau_{31} & \tau_{32} & \tau_{33} + \tau \end{pmatrix}, \tag{2.8}$$

where τ represents the total normal tension force per unit **bulk** area A_b applied to the fluid part of the faces of the cube. The total stress tensor is symmetric, i.e., $\tau_{b,ij} = \tau_{b,ji}$, which can be shown using the balance of angular momentum (Achenbach, 1973). Denoting the pressure of the fluid in the pores by p_f we can write

$$\tau = -\phi p_f, \tag{2.9}$$

where p_f is defined positive in compression. The remaining components τ_{ij} of the total stress tensor are the forces per unit **bulk** area applied to that portion of the cube faces occupied by the solid. They are a result of both the fluid pressure p_f and the additional intergranular stresses σ_{ij},

$$\tau_{ij} = -\sigma_{ij} - (1 - \phi) p_f \delta_{ij}, \tag{2.10}$$

where the Kronecker delta reflects the assumption that the pore fluid cannot sustain any shear forces. The intergranular stresses are also defined positive in compression, and are called "additional" because they add up to the stresses in the solid induced by the fluid pressure.

For later use, we also define the forces per unit **solid** area A_s applied to that portion of the cube faces occupied by the solid

$$\tau_{ij} A_b / A_s = -\sigma_{ij}/(1 - \phi) - p_f \delta_{ij}. \tag{2.11}$$

Obviously, the total normal tension force per unit **fluid** area A_f applied to the fluid part of the faces of the cube can be written as

$$\tau A_b / A_f = -p_f, \tag{2.12}$$

where $A_f/A_b = V_f/V_b$ and Eq. (2.5) have been used.

Using now Eqs. (2.9) and (2.10) the total stress tensor (Eq. (2.8)) in the bulk material can be written as

$$\tau_{b,ij} = \begin{pmatrix} -\sigma_{11} - p_f & -\sigma_{12} & -\sigma_{13} \\ -\sigma_{21} & -\sigma_{22} - p_f & -\sigma_{23} \\ -\sigma_{31} & -\sigma_{32} & -\sigma_{33} - p_f \end{pmatrix}, \tag{2.13}$$

where $\sigma_{ij} = \sigma_{ji}$ (see Eq. (2.8)). This expression for the total stress tensor is also given by Verruijt (1982), where it must be noted that he has denoted the total stress tensor as σ_{ij} and the intergranular stress as $\bar{\sigma}_{ij}$.

2.4 Stress-strain relations

We now derive the stress-strain relations for a fluid-saturated porous medium and relate the elastic coefficients of the model to physical quantities.

Following the assumptions and definitions as mentioned in the previous section, and by a generalization of the procedure followed in the classical theory of elasticity (Love, 1944), the elastic potential energy density E_p for a fluid-saturated porous medium can be written as (Biot, 1955)

$$E_p = \tfrac{1}{2}(\tau_{11}e_{11} + \tau_{22}e_{22} + \tau_{33}e_{33} + 2\tau_{12}e_{12} + 2\tau_{13}e_{13} + 2\tau_{23}e_{23} + \tau\varepsilon), \qquad (2.14)$$

where $\varepsilon = \varepsilon_{kk}$. In Eq. (2.14) the symmetry property of the stresses and strains has been used, $\tau_{ij} = \tau_{ji}$ and $e_{ij} = e_{ji}$, respectively. Following the generalized Hooke's law, here the number of independent elastic coefficients is twenty eight, which is known as general anisotropic poroelasticity. When the material is isotropic, i.e., when there are no preferred directions in the material which also means that the principal stress and strain directions coincide, this is reduced to four distinct elastic coefficients. Introducing the elastic constants A, Q, R and G, the stress-strain relations for an isotropic porous medium can be written as (Biot, 1956a)

$$\tau_{ij} = 2Ge_{ij} + Ae_{kk}\delta_{ij} + Q\varepsilon\delta_{ij}, \qquad (2.15)$$

$$\tau = Qe_{kk} + R\varepsilon. \qquad (2.16)$$

The elastic constants A, Q, R are generalized elastic coefficients that can be related to physical quantities such as porosity ϕ, the fluid bulk modulus K_f, the bulk modulus of the grains K_s, the bulk of the drained matrix K_b, and the (drained) composite shear modulus G.

The elastic coefficients were related to physical quantities by Gassmann (1951), Biot & Willis (1957), Geertsema & Smit (1961), Stoll (1974), Brown & Korringa (1975) and Berryman (1981), using so-called static "Gedanken" experiments on jacketed and unjacketed porous samples. Here, we discuss these tests following Kelder (1998), who derived the stress-strain relations from straightforward continuity and constitutive relations. In the gedanken experiments the volume effects caused by the stresses in the porous medium are investigated. As these stresses can be expressed in terms of fluid pressure and intergranular stresses (see Eqs. (2.9) and (2.10)), we discuss two experiments in which the influences of the two stresses are studied separately. By superposition of the results, and in combination with continuity equations, we arrive at stress-strain relations in the form equivalent to Eqs. (2.15) and (2.16).

2.4.1 Effect of fluid pressure (unjacketed test)

The first experiment is the so-called unjacketed test in which the influence of the fluid pressure is studied. When a porous sample is fully submerged in a watertank (pressure change dp_e) and the sample is assumed to be fully water-saturated, it is immediately clear that the fluid pressure must be continuous over the interface

(Deresiewicz & Skalak, 1963),

$$dp_f = dp_e. \tag{2.17}$$

For the intergranular stresses at the interface we can write

$$d\sigma_{11} = d\sigma_{22} = d\sigma_{33} = 0. \tag{2.18}$$

As there are no changes in the intergranular stresses, the unjacketed test is used to study the volume effects caused by the pore pressure changes. Defining the bulk modulus K_a, the bulk volume change dV_b is measured in this test,

$$dV_b = -\frac{V_b}{K_a} dp_f. \tag{2.19}$$

In the case of homogeneous media, either isotropic or not, the application of an incremental pressure dp_e means applying this increment both to the outer and inner pore surface, which leads to a linear mapping and does not change the porosity ϕ ($d\phi = 0$). Therefore we may write for the volume change of the matrix grains

$$dV_s = (1-\phi) dV_b = -\frac{1}{K_a} V_s dp_f. \tag{2.20}$$

This means that for homogeneous media K_a can also be interpreted as the bulk modulus of the individual grains, which we denote by K_s. Hence, in Eqs. (2.19) and (2.20) K_a can be replaced by K_s.

2.4.2 Effect of intergranular stresses (jacketed test)

The second experiment is the so-called jacketed test in which the influence of intergranular stresses is studied. In this case, a porous sample is jacketed and fully submerged in a watertank (pressure change dp_e) and the inside of the jacket is made to communicate with the atmosphere through a tube to ensure constant internal fluid pressure. Now we can write (Deresiewicz & Skalak, 1963)

$$dp_e = d\sigma_{11} = d\sigma_{22} = d\sigma_{33}, \tag{2.21}$$

see also Eq. (2.13) and $dp_f = 0$. As there are no pore pressure changes, the jacketed test is used to study the volume effects caused by intergranular stresses. Defining the matrix bulk modulus K_b, the bulk volume change dV_b,

$$dV_b = -\frac{V_b}{K_b} d\sigma. \tag{2.22}$$

is measured in this test, where σ is the isotropic component of the intergranular stress ($\sigma = \frac{1}{3}\sigma_{kk}$). In the literature, it is often assumed that a dry specimen exhibits the same properties as a fully saturated one and therefore the conventional jacketed test is usually performed on a dry specimen. Assuming that the response of the solid particles to a unit increase of the average stress induced by the intergranular

forces equals the response to a unit increase of the uniform stress induced in these particles by the fluid pressure, we can write for the volume change of the particles (see Eqs. (2.11) and (2.20))

$$dV_s = -\frac{1}{(1-\phi)}\frac{1}{K_s}V_s d\sigma. \tag{2.23}$$

The associated change in porosity $d\phi$ can be found using the relation $dV_s = d[(1-\phi)V_b)]$ (cf. Eq. (2.20))

$$d\phi = -\left(\frac{1-\phi}{K_b} - \frac{1}{K_s}\right) d\sigma. \tag{2.24}$$

It can be argued that a small increase of the intergranular stress must result in a decrease of the porosity, so $\partial\phi/\partial\sigma < 0$. From Eq. (2.24), we then find that $(1-\phi)K_s > K_b$, which was also previously stated by Verruijt (1982).

2.4.3 Combination of effects

Now, the bulk volume change dV_b can be described as a function of both the pore pressure change and the change of the intergranular stresses, and thus as a summation of the effects discussed in both experiments (see Eqs. (2.19) and (2.22))

$$\frac{dV_b}{V_b} = -\frac{1}{K_b}d\sigma - \frac{1}{K_s}dp_f. \tag{2.25}$$

Introducing $de = de_{kk} = dV_b/V_b$, integrating Eq. (2.25) and ignoring the integration constants, which is allowed because we only consider varying (dynamic) quantities, we obtain

$$-\sigma = K_b e + \frac{K_b}{K_s}p_f. \tag{2.26}$$

Next, we want to include the effect of shear strain. When we measure the shear modulus of a dry sample, i.e., $p_f = 0$, the shear modulus G of the matrix can be incorporated following Hooke's law for an isotropic solid. As only the intergranular stress σ_{ij} can produce shear strain, it can be seen from Eq. (2.26) that the stress-strain relation for the bulk can be written as

$$-\sigma_{ij} = \left(K_b - \frac{2}{3}G\right) e\delta_{ij} + 2Ge_{ij} + \frac{K_b}{K_s}p_f\delta_{ij}. \tag{2.27}$$

This relation does not yet have the final form of Eqs. (2.10) and (2.15). Therefore, we proceed with the derivation below. In the literature, the effective stress σ'_{ij} is often introduced in such a way that the deformation of the matrix is fully determined by that stress (Verruijt, 1982)

$$-\sigma'_{ij} = -\sigma_{ij} - \frac{K_b}{K_s}p_f\delta_{ij} = \left(K_b - \frac{2}{3}G\right) e\delta_{ij} + 2Ge_{ij}. \tag{2.28}$$

2.4.4 Relation of Biot's elastic constants to physical quantities

We continue with the derivation of stress-strain relations for a fluid-saturated porous medium by combining the constitutive equations with continuity equations. The constitutive equation for the solid is found by combination of Eqs. (2.20) and (2.23), and using $dV_s/V_s = -d\rho_s/\rho_s$. For the fluid, the bulk modulus K_f is introduced. The constitutive equations read

$$\frac{1}{\rho_s}\partial_t\rho_s = \frac{1}{K_s}\partial_t p_f + \frac{1}{(1-\phi)}\frac{1}{K_s}\partial_t\sigma, \tag{2.29}$$

$$\frac{1}{\rho_f}\partial_t\rho_f = \frac{1}{K_f}\partial_t p_f. \tag{2.30}$$

The linearized continuity equations read (Smeulders, 1992)

$$(1-\phi)\partial_t\rho_s - \rho_s\partial_t\phi + (1-\phi)\rho_s\nabla\cdot\mathbf{v} = 0, \tag{2.31}$$

$$\phi\partial_t\rho_f + \rho_f\partial_t\phi + \phi\rho_f\nabla\cdot\mathbf{V} = \phi\partial_t\theta_m, \tag{2.32}$$

where $\mathbf{v} = \partial_t\mathbf{u}$ and $\mathbf{V} = \partial_t\mathbf{U}$ are the averaged velocities of the solid and fluid, respectively. For later use we include a source term in the equation for the fluid; θ_m denotes the volume density of (fluid) mass injection having dimensions [kgm^{-3}] (Wapenaar & Berkhout, 1989). We do not include a similar source term for the solid because it is found in the literature only for the fluid (Bonnet, 1987). As the physical meaning of this (fluid) source may not be immediately clear we further discuss its nature in Chapter 3.

As we are dealing with a linearized theory, in Eqs. (2.31) and (2.32) and all subsequent equations the products of quantities (e.g., $\phi\partial_t\rho_f$) are understood as follows: the quantity preceding the derivative (ϕ) denotes the unperturbed (background) value, and the quantity to which the derivative is applied ($\partial_t\rho_f$) denotes the wave-induced variation of that quantity.

By combining the solid relations, Eqs. (2.29) and (2.31), and the fluid equations, Eqs. (2.30) and (2.32), respectively, we eliminate the factors $\partial\rho_s$ and $\partial\rho_f$ and obtain

$$\frac{1-\phi}{K_s}\partial_t p_f + \frac{1}{K_s}\partial_t\sigma - \partial_t\phi + (1-\phi)\nabla\cdot\mathbf{v} = 0, \tag{2.33}$$

$$\frac{\phi}{K_f}\partial_t p_f + \partial_t\phi + \phi\nabla\cdot\mathbf{V} = \frac{\phi}{\rho_f}\partial_t\theta_m. \tag{2.34}$$

Elimination of the porosity term ($\partial\phi$) by adding the equations yields

$$\left(\frac{1-\phi}{K_s} + \frac{\phi}{K_f}\right)\partial_t p_f + \frac{1}{K_s}\partial_t\sigma + (1-\phi)\nabla\cdot\mathbf{v} + \phi\nabla\cdot\mathbf{V} = \frac{\phi}{\rho_f}\partial_t\theta_m, \tag{2.35}$$

which is usually called the "storage equation"; it forms a basic relationship in consolidation problems (Verruijt, 1982).

Now we eliminate either σ or p_f from the combination of Eqs. (2.26) and (2.35). Using the identity $\partial_t e = \nabla \cdot \mathbf{v}$ this yields

$$\phi' \partial_t \sigma + \phi K_b \nabla \cdot \mathbf{v} - \phi K_f \frac{K_b}{K_s} \nabla \cdot \mathbf{V} = \phi K_f \partial_t \theta_m, \tag{2.36}$$

$$\phi' \partial_t p_f + K_f \left(1 - \phi - \frac{K_b}{K_s}\right) \nabla \cdot \mathbf{v} + \phi K_f \nabla \cdot \mathbf{V} = -\phi K_f \frac{K_b}{K_s} \partial_t \theta_m, \tag{2.37}$$

where we have introduced

$$\phi' = \phi + \frac{K_f}{K_s} \left(1 - \phi - \frac{K_b}{K_s}\right). \tag{2.38}$$

Then, by combining Eqs. (2.27) and (2.37), and Eqs. (2.26) and (2.36), respectively, we obtain the following set of stress-strain relations for a fluid-saturated porous medium in a form similar to Eqs. (2.10) and (2.15), and (2.9) and (2.16) (except for the volume injection source), respectively,

$$-\sigma_{ij} - (1-\phi) p_f \delta_{ij} = G(\partial_i u_j + \partial_j u_i) + A \partial_k u_k \delta_{ij} + Q(\partial_k U_k - \theta)\delta_{ij}, \tag{2.39}$$

$$-\phi p_f = Q \partial_k u_k + R(\partial_k U_k - \theta). \tag{2.40}$$

Here, we note that ϕ is the unperturbed value of the porosity; cf. Eqs. (2.31) and (2.32). Further, we have used $\rho_f^{-1} \partial_t \theta_m = \partial_t (\rho_f^{-1} \theta_m) = \partial_t \theta$, which is possible because ρ_f denotes the unperturbed fluid density; θ denotes the volume density of volume injection (Wapenaar & Berkhout, 1989), which is a dimensionless quantity. Indefinite integration over time has been applied to obtain Eqs. (2.39) and (2.40), where the integration constants are ignored because we only consider varying (dynamic) quantities. In the above derivation of Eqs. (2.39) and (2.40) the generalized elastic constants A, Q and R (cf. Eqs. (2.15) and (2.16)) are found to be related to the physical quantities ϕ, K_b, K_f, K_s and G according to

$$A = K_b - \frac{2}{3} G + \frac{K_f (1 - \phi - \frac{K_b}{K_s})^2}{\phi'}, \tag{2.41}$$

$$Q = \frac{\phi K_f (1 - \phi - \frac{K_b}{K_s})}{\phi'}, \tag{2.42}$$

$$R = \frac{\phi^2 K_f}{\phi'}. \tag{2.43}$$

In the limit case in which the porous matrix and the fluid are much more compressible than the grains themselves (i.e., $K_b/K_s, K_f/K_s \to 0$), the expressions reduce to

$$A = K_b - \frac{2}{3} G + \frac{K_f (1-\phi)^2}{\phi}, \tag{2.44}$$

$$Q = K_f (1 - \phi), \tag{2.45}$$

$$R = \phi K_f. \tag{2.46}$$

From Eqs. (2.41)-(2.43) it can be derived that

$$K_b = A - \frac{Q^2}{R} + \frac{2}{3}G, \tag{2.47}$$

which shows a similarity with the elastic case, where the well-known Lamé constants λ and G are related to the bulk modulus according to (Achenbach, 1973)

$$K_b = \lambda + \frac{2}{3}G. \tag{2.48}$$

Obviously, the Lamé constant λ of a porous material, under condition of constant fluid pressure (see Section 2.4.2), is found as

$$\lambda = A - Q^2/R. \tag{2.49}$$

2.5 Equations of motion

Next, we derive the equations of motion by combination of the stress-strain relations with momentum equations. We derive two different formulations of the equations of motion and we show that a viscous mechanism can be incorporated, describing the frequency-dependent interaction between fluid and solid.

The momentum equations for a porous medium have been derived by Biot (1956a) using Lagrange's equations. Starting from the linearized Navier-Stokes equations and the linearized equations of elasticity, Burridge & Keller (1981) arrived at the same result using a two-space method of homogenization for the case that the viscosity of the saturating fluid is relatively small. In this section we summarize the derivation by Biot.

For both the solid and the fluid phase, Lagrange's equation including dissipation can be formulated as (Achenbach, 1973; Graff, 1975; Davis, 1988; Allard, 1993; Pierce, 2007)

$$\partial_t \left(\frac{\partial E_k}{\partial v_i} \right) + \frac{\partial E_d}{\partial v_i} = T_{s,i} + F_{s,i}, \tag{2.50}$$

$$\partial_t \left(\frac{\partial E_k}{\partial V_i} \right) + \frac{\partial E_d}{\partial V_i} = T_{f,i} + F_{f,i}, \tag{2.51}$$

where E_k is the kinetic energy density of the porous medium, E_d denotes the dissipation function, $T_{s,i}$ is the elastic force (due to stresses) acting on the solid per unit volume, $T_{f,i}$ is the elastic force acting on the fluid per unit volume, and $F_{s,i}$ and $F_{f,i}$ are the external volume forces acting on the solid and fluid phase, respectively. The expression for the kinetic energy density reads (Biot, 1956a)

$$E_k = \tfrac{1}{2}(\rho_{11} v_i v_i + \rho_{22} V_i V_i + 2\rho_{12} v_i V_i). \tag{2.52}$$

The density terms ρ_{11}, ρ_{22} and ρ_{12} are related to the density of the solid ρ_s and that

of the fluid ρ_f according to

$$\rho_{11} = (1-\phi)\rho_s - \rho_{12}, \tag{2.53}$$
$$\rho_{22} = \phi\rho_f - \rho_{12}, \tag{2.54}$$
$$\rho_{12} = -(\alpha_\infty - 1)\phi\rho_f. \tag{2.55}$$

The latter density term represents a mass coupling parameter between the solid and the fluid, which exists due to the (infinite-frequency) tortuosity α_∞ of the porous network: $\alpha_\infty \geq 0$, and hence $\rho_{12} \leq 0$. We discuss α_∞ more extensively in Section 2.5.1.

Dissipation depends only on the relative motion of the fluid and the solid phases. Like Eq. (2.52), the dissipation function can be expressed in terms of six velocity components. For the isotropic case it reads (Biot, 1956a)

$$E_d = \tfrac{1}{2} b_0 (v_i - V_i)(v_i - V_i), \tag{2.56}$$

where the coefficient b_0 is related to the Darcy flow permeability k_0 and the dynamic viscosity η of the saturating fluid as

$$b_0 = \frac{\eta\phi^2}{k_0}. \tag{2.57}$$

The nature of the dissipation mechanism is discussed in more detail in Section 2.5.1.

The forces $T_{s,i}$ and $T_{f,i}$ are related to spatial derivatives of the stresses. Using Eqs. (2.39) and (2.40) the expressions read

$$\begin{aligned} T_{s,i} &= \partial_j \sigma_{ij} - (1-\phi)\partial_i p_f \\ &= G\partial_i\partial_j u_j + G\partial_j^2 u_i + A\partial_i\partial_j u_j + Q(\partial_i\partial_j U_j - \partial_i\theta), \end{aligned} \tag{2.58}$$
$$\begin{aligned} T_{f,i} &= -\phi\partial_i p_f \\ &= Q\partial_i\partial_j u_j + R(\partial_i\partial_j U_j - \partial_i\theta). \end{aligned} \tag{2.59}$$

Now, by combining Eqs. (2.50), (2.52), (2.56) and (2.58), and by combining Eqs. (2.51), (2.52), (2.56) and (2.59), we obtain the following equations of motion

$$\begin{aligned} \rho_{11}\partial_t^2\mathbf{u} + \rho_{12}\partial_t^2\mathbf{U} + b_0\partial_t(\mathbf{u}-\mathbf{U}) &= P\nabla\nabla\cdot\mathbf{u} - G\nabla\times\nabla\times\mathbf{u} \\ &\quad + Q\nabla\nabla\cdot\mathbf{U} + \mathbf{f}, \end{aligned} \tag{2.60}$$
$$\rho_{12}\partial_t^2\mathbf{u} + \rho_{22}\partial_t^2\mathbf{U} - b_0\partial_t(\mathbf{u}-\mathbf{U}) = Q\nabla\nabla\cdot\mathbf{u} + R\nabla\nabla\cdot\mathbf{U} + \mathbf{F}, \tag{2.61}$$

where $P = A + 2G$ and we have used the vector identity $\nabla^2\mathbf{u} = \nabla\nabla\cdot\mathbf{u} - \nabla\times\nabla\times\mathbf{u}$ to separate dilatation and rotation terms. The source terms are defined as

$$\mathbf{f} = \mathbf{F}_s - Q\nabla\theta, \tag{2.62}$$
$$\mathbf{F} = \mathbf{F}_f - R\nabla\theta. \tag{2.63}$$

Eqs. (2.60) and (2.61) are the equations of motion for wave propagation in a fluid-saturated porous medium, as originally derived by (Biot, 1956a) (without source terms). The incorporated dissipation mechanism being frequency-independent, however, simplifies reality too much. Therefore, in the next section we modify the associated terms in Eqs. (2.60) and (2.61).

2.5.1 Incorporation of frequency-dependent permeability or tortuosity

In this section we discuss the behavior of the dissipation mechanism which describes the frequency-dependent interaction between the solid and the fluid. Starting from the low- and high frequency limits, the behavior in the intermediate frequency band is obtained for the rigid frame limit ($\mathbf{u} = \mathbf{0}$). We clarify the relation between frequency-dependent permeability and tortuosity, illustrate their behavior using a numerical example, and finally we show how the frequency-dependent dissipation mechanism can be included in the general equations of motion Eqs. (2.60) and (2.61).

In the rigid-frame limit, after application of the Fourier transform over time (Eq. (2.1)), the equation of motion for the fluid reduces to

$$-\nabla\hat{p}_f = \left(-\omega^2\alpha_\infty\rho_f + \mathrm{i}\omega\frac{\eta\phi}{k_0}\right)\hat{\mathbf{U}}, \tag{2.64}$$

which is obtained from Eq. (2.61) by expressing $\nabla\nabla\cdot\mathbf{U}$ in terms of p_f using Eq. (2.40).

In the low-frequency limit the acceleration term tends to zero and the viscous forces are dominant. Hence, Eq. (2.64) reduces to

$$\lim_{\omega\to 0}(-\nabla\hat{p}_f) = \mathrm{i}\omega\frac{\eta\phi}{k_0}\hat{\mathbf{U}}, \tag{2.65}$$

which is the well-known Darcy's law for flow through porous media. In the high-frequency limit the acceleration term dominates the viscous forces, and we obtain

$$\lim_{\omega\to\infty}(-\nabla\hat{p}_f) = -\omega^2\alpha_\infty\rho_f\hat{\mathbf{U}}. \tag{2.66}$$

In this equation the tortuosity α_∞ appears as a modification of the acceleration term of the fluid. To understand this, it is important to realize that we are dealing with a macroscopic (continuum) theory. The macroscopic length scale is related to the wavelength L at which measurable, continuous and differentiable quantities can be identified. The microstructure of a random porous medium is generally characterized by a length scale proportional to the pore size (Smeulders *et al.*, 1992). The direction of the acceleration on the microscale may very well differ from the macroscopic acceleration direction. For instance, when the macroscopic flow is one-dimensional, the microscopic flow is at least two-dimensional. Smeulders *et al.* (1992) relate the microscopic flow field to the macroscopic flow field using an averaging technique of homogenization. In the high-frequency limit they obtain

$$\alpha_\infty = \frac{\langle|\mathbf{v}_p|^2\rangle}{|\mathbf{v}_0|^2}, \tag{2.67}$$

where $\langle\rangle$ denotes the averaging operator, $\mathbf{v}_p$ is the microscopic potential flow solution and $\mathbf{v}_0$ is the macroscopic velocity of the fluid. In this way, one can imagine that the local variations of the flow contribute to the inertia term on the macroscopic

level. In a cylindrical duct the averaged microscopic velocity equals the macroscopic velocity and, consequently, $\alpha_\infty = 1$.

Considering now Eq. (2.64), we observe that the momentum equation of the fluid is constituted by superposition of the low- and high-frequency limits described above. This simple superposition is, however, too simplified a description of the frequency-dependent dissipation process. A more realistic description has been proposed by Biot (1956b) and by Johnson *et al.* (1987). Here, we follow the latter model where either the concept of dynamic permeability $\hat{k}(\omega)$ is introduced, or the concept of dynamic tortuosity $\hat{\alpha}(\omega)$, by reformulations of Eq. (2.64) according to

$$-\nabla \hat{p}_f = \mathrm{i}\omega \frac{\eta\phi}{\hat{k}(\omega)} \hat{\mathbf{U}}, \tag{2.68}$$

$$-\nabla \hat{p}_f = -\omega^2 \hat{\alpha}(\omega) \rho_f \hat{\mathbf{U}}. \tag{2.69}$$

Obviously, Eqs. (2.68) and (2.69) are alternative descriptions of the same physical reality and therefore, $\hat{k}(\omega)$ and $\hat{\alpha}(\omega)$ are related as

$$\hat{\alpha}(\omega) = -\frac{\mathrm{i}\eta\phi}{\omega\rho_f \hat{k}(\omega)}. \tag{2.70}$$

In the low-frequency limit, the dynamic permeability approaches the stationary value (see Eq. (2.65))

$$\lim_{\omega\to 0} \hat{k}(\omega) = k_0, \tag{2.71}$$

and, consequently, using Eq. (2.70) for the dynamic tortuosity it follows that

$$\lim_{\omega\to 0} \hat{\alpha}(\omega) = -\frac{\mathrm{i}\eta\phi}{\omega\rho_f k_0}. \tag{2.72}$$

In this limit the fluid follows a Stokes flow pattern on the pore scale (i.e., the flow is described by the linearized Navier-Stokes equation with intertia terms neglected). In the high-frequency limit the fluid obeys a potential flow pattern (i.e., the flow described by the linearized Navier-Stokes equation with viscosity terms neglected) on the pore scale, except for a very thin boundary layer $\delta = \sqrt{2\eta/(\omega\rho_f)}$ at the pore walls; hence, tortuosity and permeability are given as

$$\lim_{\omega\to\infty} \hat{\alpha}(\omega) = \alpha_\infty, \tag{2.73}$$

$$\lim_{\omega\to\infty} \hat{k}(\omega) = -\frac{\mathrm{i}\eta\phi}{\omega\rho_f \alpha_\infty}, \tag{2.74}$$

where we have again used Eq. (2.70). For the intermediate frequency range Johnson *et al.* (1987) postulated a branching function connecting the two limiting situations based on the ratio of the viscous skin depth δ and the characteristic length scale of

Table 2.1: Material parameters as used for water-saturated Sand of Mol (Degrande *et al.*, 1998). We assume that $M = 1$ (see Eq. (2.77)).

Solid (frame) density ρ_s [kgm^{-3}]	2650
Fluid density ρ_f [kgm^{-3}]	1000
Tortuosity α_∞	1.789
Porosity ϕ	0.388
Permeability k_0 [μm^2]	10.214
Dynamic fluid viscosity η [Pa·s]	0.001
Shear modulus G [GPa]	111.86
Frame bulk modulus K_b [MPa]	298.3
Grain bulk modulus K_s [GPa]	36.5
Fluid bulk modulus K_f [GPa]	2.22

the pores Λ according to

$$\hat{k}(\omega) = k_0 \left[\left(1 + \mathrm{i} \frac{M}{2} \frac{\omega}{\omega_c} \right)^{\frac{1}{2}} + \mathrm{i} \frac{\omega}{\omega_c} \right]^{-1}, \tag{2.75}$$

$$\hat{\alpha}(\omega) = \alpha_\infty \left[1 - \mathrm{i} \frac{\omega_c}{\omega} \left(1 + \mathrm{i} \frac{M}{2} \frac{\omega}{\omega_c} \right)^{\frac{1}{2}} \right], \tag{2.76}$$

where $\mathrm{Re}(\hat{k}) \geq 0$ and $\mathrm{Re}(\hat{\alpha}) \geq 0$ for $\omega \geq 0$, and

$$\omega_c = \frac{\eta \phi}{k_0 \rho_f \alpha_\infty}, \quad M = \frac{8 \alpha_\infty k_0}{\phi \Lambda^2}. \tag{2.77}$$

The rollover frequency ω_c denotes the frequency where the inertia effects and the viscous effects are of the same order of magnitude. The pore-shape factor M is often close to 1 (Johnson *et al.*, 1987; Smeulders *et al.*, 1992).

Before incorporating the dissipation mechanism in the equations of motion, we visualize the frequency-dependent behavior of $\hat{k}(\omega)$ and $\hat{\alpha}(\omega)$. For material properties related to Sand of Mol (Degrande *et al.*, 1998) (the parameter values are given in Table 2.1), which is representative of a water-saturated shallow subsurface situation of loosely packed sand, we show the behavior in Figure 2.1. We observe that the magnitude of the dynamic permeability $|\hat{k}|$ reduces to the Darcy permeability k_0 in the low-frequency limit, which agrees with Eq. (2.65). In the low-frequency limit, $|\hat{\alpha}|$ tends to infinity as ω^{-1} (see Eq. (2.72)), which can be understood from Eq. (2.69). In the high-frequency limit, the magnitude of the dynamic tortuosity $|\hat{\alpha}|$ goes to α_∞, which agrees with Eq. (2.66). The value of $|\hat{k}|$ tends to zero (see Eq. (2.74)), which is because the pressure variation is too fast for the fluid to react (cf. Eq. (2.68)). For the intermediate frequency range, the behavior is described by the branching functions of Johnson *et al.* (1987) (Eqs. (2.75) and (2.76)), showing a point of inflection at approximately the rollover frequency $f_c = \omega_c/(2\pi) = 3387$ Hz. The phases $\angle\hat{k}$ and $\angle\hat{\alpha}$ (Figure 2.1) are also consistent with the low- and high-frequency limits (see Eqs. (2.71)-(2.74)).

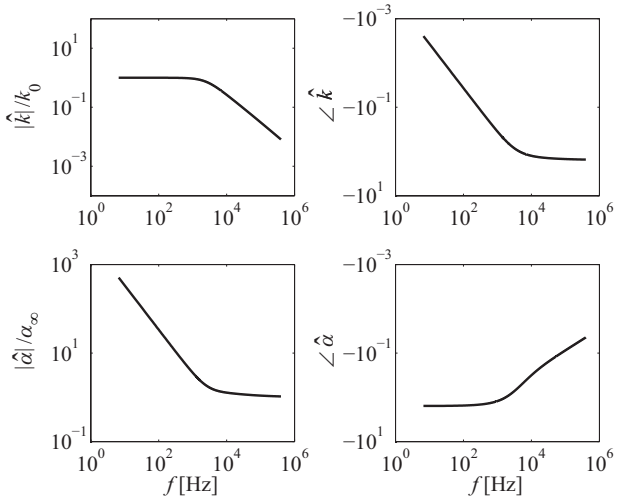

Figure 2.1: Frequency-dependent permeability and tortuosity according to the viscous attenuation mechanism of Johnson *et al.* (1987) (Eqs. (2.75) and (2.76)). Both magnitudes and phases are shown.

The expression for dynamic permeability (Eq. (2.75)) can be substituted in Eq. (2.68), and that of the dynamic tortuosity (Eq. (2.76)) in Eq. (2.69). One of these should be used to incorporate the frequency-dependent dissipation mechanism in the equations of motion for deformable (non-rigid) porous media (Eqs. (2.60) and (2.61)). In this thesis we choose to work with dynamic permeability. By rewriting of the expression Eq. (2.68) to a form comparable with Eq. (2.64), we find that the effect can be incorporated by simply replacing b_0 by $\hat{b}(\omega)$ according to

$$\hat{b}(\omega) = b_0 \left(1 + \mathrm{i}\omega\tau_c\right)^{\frac{1}{2}}, \tag{2.78}$$

where $\tau_c = M/(2\omega_c)$ and $\mathrm{Re}(\hat{b}) \geq 0$ for $\omega \geq 0$. Then, the $(\mathbf{x}, \omega)$-domain representation of the equations of motion (Eqs. (2.60) and (2.61)) can be written as

$$-\omega^2\hat{\rho}_{11}\hat{\mathbf{u}} - \omega^2\hat{\rho}_{12}\hat{\mathbf{U}} = P\nabla\nabla\cdot\hat{\mathbf{u}} - G\nabla\times\nabla\times\hat{\mathbf{u}} + Q\nabla\nabla\cdot\hat{\mathbf{U}} + \hat{\mathbf{f}}, \tag{2.79}$$

$$-\omega^2\hat{\rho}_{12}\hat{\mathbf{u}} - \omega^2\hat{\rho}_{22}\hat{\mathbf{U}} = Q\nabla\nabla\cdot\hat{\mathbf{u}} + R\nabla\nabla\cdot\hat{\mathbf{U}} + \hat{\mathbf{F}}, \tag{2.80}$$

where $\hat{b}(\omega)$ shows up in the frequency-dependent density terms that read

$$\hat{\rho}_{11} = \rho_{11} - \mathrm{i}\hat{b}/\omega, \tag{2.81}$$

$$\hat{\rho}_{22} = \rho_{22} - \mathrm{i}\hat{b}/\omega, \tag{2.82}$$

$$\hat{\rho}_{12} = \rho_{12} + \mathrm{i}\hat{b}/\omega. \tag{2.83}$$

The $(\mathbf{x}, t)$-domain equivalents of these terms are time-dependent convolution operators. Their expressions can be found using a standard inverse Laplace transform

(Prudnikov *et al.*, 1992) and read

$$\rho_{11}(t) = \rho_{11}\delta(t) + b_0\varrho(t), \tag{2.84}$$
$$\rho_{22}(t) = \rho_{22}\delta(t) + b_0\varrho(t), \tag{2.85}$$
$$\rho_{12}(t) = \rho_{12}\delta(t) - b_0\varrho(t), \tag{2.86}$$

where $\delta(...)$ denotes the Dirac delta function (Abramowitz & Stegun, 1972) and

$$\varrho(t) = \left(\frac{\exp(-t/\tau_c)}{\sqrt{\pi t/\tau_c}} + \operatorname{erf}\left(\sqrt{t/\tau_c}\right) \right) H(t). \tag{2.87}$$

Here, $H(t)$ denotes the Heaviside step function, i.e., $H(t) = \{0, \frac{1}{2}, 1\}$ for $\{t < 0, t = 0, t > 0\}$, and erf(...) denotes the error function (Abramowitz & Stegun, 1972).

Now we have arrived at the general form of the equations of motion that incorporate the frequency-dependent dissipation mechanism, and which we will often use in this thesis. We refer to it as the $(\mathbf{u}, \mathbf{U})$-formulation because the equations of motion are expressed in the field quantities $\mathbf{u}$ and $\mathbf{U}$. For completeness, a less well-known but more compact representation of Biot's equations of motion is given in the next section.

2.5.2 Alternative formulation of the equations of motion

An alternative to the $(\mathbf{u}, \mathbf{U})$-formulation of the equations of motion is the so-called $(\mathbf{u}, p_f)$–formulation in which the equations of motion are expressed in terms of $\hat{\mathbf{u}}$ and $\hat{p}_f$ (Bonnet, 1987; Wiebe & Antes, 1991; van Dalen *et al.*, 2008; Schanz, 2009). The equations are obtained by rewriting of Eqs. (2.79) and (2.80), and using Eqs. (2.58) and (2.59) to eliminate $\mathbf{U}$. The result is

$$\omega^2\hat{\rho}_{eq}\hat{\mathbf{u}} + (\lambda + 2G)\nabla\nabla\cdot\hat{\mathbf{u}} - G\nabla\times\nabla\times\hat{\mathbf{u}} = \frac{\phi H_S}{R}\nabla\hat{p}_f - (\hat{\mathbf{f}} + \beta_S\hat{\mathbf{F}}), \tag{2.88}$$
$$\omega^2\hat{\rho}_{22}\hat{p}_f + R\nabla^2\hat{p}_f = -\omega^2\hat{\rho}_{22}\frac{H_S}{\phi}\nabla\cdot\hat{\mathbf{u}} + \frac{R}{\phi}\nabla\cdot\hat{\mathbf{F}}. \tag{2.89}$$

The Lamé parameter λ has already been defined in Eq. (2.49). Further, the following definitions hold

$$\hat{\rho}_{eq} = d_0/\hat{\rho}_{22}, \tag{2.90}$$
$$d_0 = \hat{\rho}_{11}\hat{\rho}_{22} - \hat{\rho}_{12}^2, \tag{2.91}$$
$$H_S = Q + R\beta_S, \tag{2.92}$$
$$\beta_S = -\hat{\rho}_{12}/\hat{\rho}_{22}, \tag{2.93}$$

where $\hat{\rho}_{eq}$ reduces to $\rho_{11} + \rho_{22} + 2\rho_{12} = \rho$ (bulk density) for $\omega \to 0$; the physical meaning of β_S is given later (below Eq. (3.23)).

The similarity of the equations of motion Eqs. (2.88) and (2.89) with those of an elastic solid and an acoustic medium, respectively, is obvious (Achenbach, 1973;

de Hoop, 1995). The difference lies in the definition of the specific density and elastic constants, and in the coupling terms of the equations that can be interpreted as source terms.

Bonnet (1987) showed that only four out of the seven field variables ($\mathbf{u}$,$\mathbf{U}$,p_f) are independent. Therefore, the $(\mathbf{u}, p_f)$-formulation provides a set of independent equations governing wave propagation in a fluid-saturated porous medium. The $(\mathbf{u}, \mathbf{U})$-formulation, which is the original form of Biot's equations (Biot, 1956a), is used more often but only four of the six equations are independent.

In wave propagation problems either the $(\mathbf{u}, \mathbf{U})$-formulation or the $(\mathbf{u}, p_f)$–for–mulation can be used. In Chapter 3 we derive Green's tensors for both sets of equations to illustrate the basic properties of the wave propagation process in a porous medium.

2.6 Conclusions

In this chapter we derived the equations of motion for wave propagation in a fluid-saturated porous medium. First, we illustrated that the stress-strain relations associated with Biot's theory can be obtained from constitutive and continuity equations, by considering the porous medium as a two-phase continuum. This shows that the involved elastic constants are clearly related to physical quantities, i.e., the bulk moduli of the grains, the porous solid and the fluid, to the shear modulus and to the porosity. By combination of the stress-strain relations with Lagrange's momentum equations for the solid and fluid, the equations of motion were found. We presented the equations of motion in two different formulations that are known in the literature, i.e., the $(\mathbf{u}, \mathbf{U})$-formulation (solid and fluid particle displacements) and the $(\mathbf{u}, p_f)$-formulation (solid particle displacement and fluid pressure). The latter formulation shows that an arbitrary wave field in a fluid-saturated porous medium has only four independent field quantities.

Chapter 3

Green's tensors for wave propagation in a fluid-saturated porous medium

3.1 Introduction

The wave propagation process in a fluid-saturated porous medium is described by the infinite-space Green's tensors which are the fundamental solutions (impulse responses) of the equations of motion. The goal of this chapter is to derive these Green's tensors in order to illustrate the frequency-dependent attributes (e.g., velocity) and waveforms of the existing wavemodes.

The Green's tensors have already been derived by several authors using either Helmholtz decomposition or the so-called Kupradze's method (Burridge & Vargas, 1979; Norris, 1985; Bonnet, 1987; Manolis & Beskos, 1989; Philippacopoulos, 1998; Sahay, 2001), and considering different sources. In the paper by Burridge & Vargas (1979) only a force applied to the total medium (fluid and solid) is included, i.e., a vector containing three sources (components). Other authors considered only a force applied to the solid of the porous medium (Norris, 1985; Philippacopoulos, 1998), which implies also three sources, while Manolis & Beskos (1989) included forces applied to both the solid and fluid, i.e., six sources. Sahay (2001) also included six sources but with a different physical meaning, i.e., one force associated with the in-phase fluid-solid motion (applied to the center of mass of the porous medium), and one with the relative motion of the fluid and solid. Bonnet (1987) introduced four sources corresponding with the four independent field variables $\mathbf{u}$ and p_f ($(\mathbf{u}, p_f)$-formulation; see Chapter 2), i.e., a force applied to the solid and a supplementary scalar source related to the fluid. The physical meaning of the scalar source was, however, not given because Bonnet simply used the analogy with thermoelasticity to include separate sources.

In this chapter we derive the Green's tensors for a fluid-saturated porous medium in a way similar to that used by de Hoop (1995) for an elastic solid, by straightfor-

ward application of the Fourier transform. In doing so, we find the Green's tensors in the $(\mathbf{p},\omega)$-domain and obtain the $(\mathbf{x},\omega)$-domain expressions using the inverse transform. We show the Green's tensors for both the $(\mathbf{u},\mathbf{U})$- and the $(\mathbf{u},p_f)$-formulations of the equations of motion incorporating a force applied to the solid and a force applied to the fluid, and a scalar source. Our scalar source shows two physical realizations of Bonnet's scalar source, i.e., the divergence of the force applied to the fluid or the Laplacian (∇^2) and the fluid volume injection source (see Chapter 2: divergence of Eq. (2.63)). Further, we derive the impedances of the wavemodes that exist in a porous medium, i.e., the fast and slow compressional waves and the shear wave. We address particularly the "coupling impedances" of the compressional waves. The coupling impedance is defined as the spectral ratio of the pressure in the fluid, induced by a particular wavemode, and the associated radial component of the particle velocity in the solid. It thus interrelates the waveforms present in all independent field variables in one quantity and can be addressed as a "multi-component full-waveform attribute". Finally, we use low-and high-frequency approximations and numerical examples to illustrate the frequency-dependence of the attributes of the possible wavemodes, of the corresponding transient waveforms as excited by point sources, and of the differences between the waveforms in velocity and fluid pressure as described by the coupling impedances.

The derivation of the Green's tensors for the $(\mathbf{u},\mathbf{U})$- and $(\mathbf{u},p_f)$-formulations, and how they are related, is shown in Section 3.2. In Sections 3.2.2 and 3.2.3, respectively, we present low- and high-frequency approximations of the solutions of the $(\mathbf{u},\mathbf{U})$-formulation, which reveal some fundamental properties of the wave propagation process. Subsequently, the derivation of the impedances is given in Section 3.3. The numerical examples are shown in Section 3.4 and a discussion is given in Section 3.5.

3.2 Green's tensors for infinite space

In this section we derive the Green's tensors for a fluid-saturated porous medium for both the $(\mathbf{u},\mathbf{U})$- and the $(\mathbf{u},p_f)$-formulations of the equations of motion. In addition, we give low- and high-frequency approximations of the tensors related to the $(\mathbf{u},\mathbf{U})$-formulation.

For arbitrary loading $(\breve{\mathbf{f}},\breve{\mathbf{F}})$, the response $(\breve{\mathbf{u}},\breve{\mathbf{U}})$ in the $(\mathbf{p},\omega)$-domain is obtained using the spatial Fourier transform with respect to all (spatial) coordinates (Eq. (2.2)). Applying this transform to the equations of motion of the $(\mathbf{u},\mathbf{U})$-formulation (Eqs. (2.79) and (2.80)), we obtain

$$(-\hat{\rho}_{11}+Gp_jp_j)\,\breve{u}_i-\hat{\rho}_{12}\breve{U}_i+(P-G)\,p_ip_j\breve{u}_j+Qp_ip_j\breve{U}_j=\omega^{-2}\breve{f}_i, \tag{3.1}$$

$$-\hat{\rho}_{12}\breve{u}_i-\hat{\rho}_{22}\breve{U}_i+Qp_ip_j\breve{u}_j+Rp_ip_j\breve{U}_j=\omega^{-2}\breve{F}_i. \tag{3.2}$$

We multiply (dot product) the equations by p_i and obtain the following identities

$$p_i \breve{u}_i = \frac{p_j}{\omega^2 d_2 \Delta_P} \left(+(-\hat{\rho}_{22} + Rp^2)\breve{f}_j - (-\hat{\rho}_{12} + Qp^2)\breve{F}_j \right), \tag{3.3}$$

$$p_i \breve{U}_i = \frac{p_j}{\omega^2 d_2 \Delta_P} \left(-(-\hat{\rho}_{12} + Qp^2)\breve{f}_j + (-\hat{\rho}_{11} + Pp^2)\breve{F}_j \right), \tag{3.4}$$

where $p^2 = p_m p_m$ and

$$\Delta_P = p^4 + \frac{d_1}{d_2} p^2 + \frac{d_0}{d_2}. \tag{3.5}$$

Here, the factors d_0, d_1 and d_2 are defined as

$$d_0 = \hat{\rho}_{11}\hat{\rho}_{22} - \hat{\rho}_{12}^2, \tag{3.6}$$

$$d_1 = -(R\hat{\rho}_{11} + P\hat{\rho}_{22} - 2Q\hat{\rho}_{12}), \tag{3.7}$$

$$d_2 = PR - Q^2. \tag{3.8}$$

Substituting Eqs. (3.3) and (3.4) into the left-hand side (third and fourth terms) of Eqs. (3.1) and (3.2), the solution to the set of algebraic Eqs. (3.1) and (3.2) can be written as

$$\begin{bmatrix} \breve{u}_i \\ \breve{U}_i \end{bmatrix} = \begin{bmatrix} \breve{g}_{ij} & \breve{q}_{ij} \\ \breve{q}_{ij} & \breve{G}_{ij} \end{bmatrix} \begin{bmatrix} \breve{f}_j \\ \breve{F}_j \end{bmatrix}. \tag{3.9}$$

Here, the right-hand side contains products of $(\mathbf{p}, \omega)$-domain functions. The matrix contains the Green's tensors that read

$$\breve{g}_{ij} = -\frac{1}{G}\frac{(-\delta_{ij}p^2 + p_i p_j)}{\omega^2 p^2}\frac{1}{\Delta_S} + \frac{(-\hat{\rho}_{22} + Rp^2)}{d_2}\frac{p_i p_j}{\omega^2 p^2}\frac{1}{\Delta_P}, \tag{3.10}$$

$$\breve{q}_{ij} = \frac{1}{G}\frac{\hat{\rho}_{12}}{\hat{\rho}_{22}}\frac{(-\delta_{ij}p^2 + p_i p_j)}{\omega^2 p^2}\frac{1}{\Delta_S} - \frac{(-\hat{\rho}_{12} + Qp^2)}{d_2}\frac{p_i p_j}{\omega^2 p^2}\frac{1}{\Delta_P}, \tag{3.11}$$

$$\breve{G}_{ij} = \frac{1}{G}\frac{(-\hat{\rho}_{11} + Gp^2)}{\hat{\rho}_{22}}\frac{(-\delta_{ij}p^2 + p_i p_j)}{\omega^2 p^2}\frac{1}{\Delta_S} + \frac{(-\hat{\rho}_{11} + Pp^2)}{d_2}\frac{p_i p_j}{\omega^2 p^2}\frac{1}{\Delta_P}. \tag{3.12}$$

The quantities Δ_P and Δ_S represent the "denominators" of the compressional and shear waves, respectively, and can be written as

$$\Delta_P = \Delta_{P1}\Delta_{P2} = (p^2 - s_{P1}^2)(p^2 - s_{P2}^2), \tag{3.13}$$

$$\Delta_S = p^2 - \frac{d_0}{G\hat{\rho}_{22}} = p^2 - s_S^2. \tag{3.14}$$

The body-wave slownesses of the fast and slow compressional wave are denoted s_{P1} and s_{P2}, respectively, and s_S is that of the shear wave. They are defined as

$$s_{P1,P2}^2 = \frac{1}{2d_2}\left(-d_1 \mp (d_1^2 - 4d_0 d_2)^{\frac{1}{2}} \right), \tag{3.15}$$

$$s_S^2 = \frac{d_0}{G\hat{\rho}_{22}}. \tag{3.16}$$

Here we choose $\mathrm{Im}(s_\alpha) \leq 0$ for $\omega \geq 0$, where $\alpha = \{P1, P2, S\}$. When set to zero, Eqs. (3.13) and (3.14) represent the dispersion equations for P- and S-waves, respectively, with solutions $p = \pm s_{P1,P2}$ and $p = \pm s_S$. Now, we split the compressional wave term into two separate parts

$$\frac{1}{\Delta_P} = \frac{1}{\Delta_{P1} - \Delta_{P2}} \left(\frac{1}{\Delta_{P2}} - \frac{1}{\Delta_{P1}} \right) = \frac{1}{s_{P2}^2 - s_{P1}^2} \left(\frac{1}{\Delta_{P2}} - \frac{1}{\Delta_{P1}} \right). \tag{3.17}$$

We define the $(\mathbf{p}, \omega)$-domain scalar Green's functions as

$$\breve{\mathcal{G}}_\alpha = \frac{1}{\omega^2 \Delta_\alpha}, \tag{3.18}$$

which are $(\mathbf{p}, \omega)$-domain solutions of the corresponding Helmholtz equations with point-source excitation (see Section 3.2.1). In the $(\mathbf{x}, \omega)$-domain these functions can be written as

$$\hat{\mathcal{G}}_\alpha = \frac{\exp\left(-\mathrm{i}\omega s_\alpha |\mathbf{x}|\right)}{4\pi |\mathbf{x}|}, \tag{3.19}$$

which is shown in Section 3.2.1. Then, by using the identity $\mathrm{i}\omega p_i \leftrightarrow -\partial_i$ (and thus $\omega^2 p_i p_j \leftrightarrow -\partial_i \partial_j$; see Eq. (2.2)), applying $\nabla^2 \hat{\mathcal{G}}_\alpha = -\omega^2 s_\alpha^2 \hat{\mathcal{G}}_\alpha$ (for $\mathbf{x} \neq \mathbf{0}$), where we recall that the summation convention does not apply for Greek subscripts (Section 2.2), and rearranging of terms we find the $(\mathbf{x}, \omega)$-domain representations of the Green's tensors (Eqs. (3.10)-(3.12)),

$$\begin{bmatrix} \hat{g}_{ij} \\ \hat{q}_{ij} \\ \hat{G}_{ij} \end{bmatrix} = \omega^{-2} \begin{bmatrix} G^{-1}(\omega^2 \delta_{ij} + s_S^{-2} \partial_i \partial_j) & -a_{P1} \partial_i \partial_j & a_{P2} \partial_i \partial_j \\ G^{-1} \beta_S (\omega^2 \delta_{ij} + s_S^{-2} \partial_i \partial_j) & -a_{P1} \beta_{P1} \partial_i \partial_j & a_{P2} \beta_{P2} \partial_i \partial_j \\ G^{-1} \beta_S^2 (\omega^2 \delta_{ij} + s_S^{-2} \partial_i \partial_j) & -a_{P1} \beta_{P1}^2 \partial_i \partial_j & a_{P2} \beta_{P2}^2 \partial_i \partial_j \end{bmatrix} \times \begin{bmatrix} \hat{\mathcal{G}}_S & \hat{\mathcal{G}}_{P1} & \hat{\mathcal{G}}_{P2} \end{bmatrix}^T. \tag{3.20}$$

Here, the complex-valued factors $a_{P1,P2}$ read

$$a_{P1,P2} = \frac{1}{d_2 s_{P1,P2}^2} \frac{\hat{\rho}_{22} - R s_{P1,P2}^2}{s_{P2}^2 - s_{P1}^2}, \tag{3.21}$$

and the complex-valued β_α are (the expression of β_S is repeated - see Eq. (2.93))

$$\beta_{P1,P2} = -\frac{\hat{\rho}_{11} - P s_{P1,P2}^2}{\hat{\rho}_{12} - Q s_{P1,P2}^2} = -\frac{\hat{\rho}_{12} - Q s_{P1,P2}^2}{\hat{\rho}_{22} - R s_{P1,P2}^2}, \tag{3.22}$$

$$\beta_S = -\frac{\hat{\rho}_{12}}{\hat{\rho}_{22}}. \tag{3.23}$$

Remarkably, in Eq. (3.20) the terms related to individual wavemodes differ only in the presence of the factors β_α and β_α^2. Hence, these factors can be interpreted as the fluid-solid "amplitude ratios" (Allard, 1993).

From Eq. (3.9) it is obvious that the physical responses in the $(\mathbf{x},\omega)$-domain are found according to

$$\begin{bmatrix} \hat{u}_i \\ \hat{U}_i \end{bmatrix} = \begin{bmatrix} \hat{g}_{ij} & \hat{q}_{ij} \\ \hat{q}_{ij} & \hat{G}_{ij} \end{bmatrix} * \begin{bmatrix} \hat{f}_j \\ \hat{F}_j \end{bmatrix}, \tag{3.24}$$

where the asterisk denotes convolution over all spatial coordinates. We note that the Green's tensors (Eq. (3.20)) are symmetric, i.e., $\hat{g}_{ij} = \hat{g}_{ji}$, $\hat{q}_{ij} = \hat{q}_{ji}$, and $\hat{G}_{ij} = \hat{G}_{ji}$. The Green's matrix in Eq. (3.24) is symmetric too, which can be expected from the structure of the equations of motion in the $(\mathbf{u},\mathbf{U})$-formulation (Eqs. (2.79) and (2.80)).

The Green's tensors for the $(\mathbf{u},p_f)$-formulation (Eqs. (2.88) and (2.89)) can be derived in a similar way. The result is

$$\begin{bmatrix} \hat{u}_i \\ -\phi\hat{p}_f \end{bmatrix} = \begin{bmatrix} \hat{g}_{ij} & \hat{q}_{ij} \\ \hat{h}_j & \hat{k}_j \end{bmatrix} * \begin{bmatrix} \hat{f}_j \\ \hat{F}_j \end{bmatrix}, \tag{3.25}$$

where

$$\begin{bmatrix} \hat{h}_j \\ \hat{k}_j \end{bmatrix} = \begin{bmatrix} a_{P1}s_{P1}^2 H_{P1}\partial_j & -a_{P2}s_{P2}^2 H_{P2}\partial_j \\ a_{P1}s_{P1}^2 H_{P1}\beta_{P1}\partial_j & -a_{P2}s_{P2}^2 H_{P2}\beta_{P2}\partial_j \end{bmatrix} \begin{bmatrix} \hat{\mathcal{G}}_{P1} \\ \hat{\mathcal{G}}_{P2} \end{bmatrix}. \tag{3.26}$$

Here, the stiffness terms $H_{P1,P2}$ are defined as

$$H_{P1,P2} = Q + R\beta_{P1,P2}. \tag{3.27}$$

Obviously, the first line in Eq. (3.25) is the same as in the $(\mathbf{u},\mathbf{U})$-formulation (see Eq. (3.24)). The second line (tensors $\hat{h}_j$ and $\hat{k}_j$) can be obtained from the $(\mathbf{u},\mathbf{U})$-formulation using the stress-strain relation of the fluid phase (Eq. (2.16)), and applying the convolution property $\partial_i(\hat{g}_{ij} * \hat{f}_j) = \partial_i\hat{g}_{ij} * \hat{f}_j$ (Bracewell, 1986).

The spatial derivatives in Eqs. (3.20) and (3.26) can be expressed in terms of the scalar Green's functions. When $|\mathbf{x}| \neq 0$ it holds

$$\partial_j\hat{\mathcal{G}}_\alpha(\mathbf{x},\omega) = \left(-\frac{n_j}{|\mathbf{x}|} - \mathrm{i}\omega s_\alpha n_j\right)\hat{\mathcal{G}}_\alpha(\mathbf{x},\omega), \tag{3.28}$$

$$\partial_i\partial_j\hat{\mathcal{G}}_\alpha(\mathbf{x},\omega) = \left(\frac{1}{|\mathbf{x}|^2}(3n_in_j - \delta_{ij}) + \frac{\mathrm{i}\omega s_\alpha}{|\mathbf{x}|}(3n_in_j - \delta_{ij}) - \omega^2 s_\alpha^2 n_in_j\right) \times \hat{\mathcal{G}}_\alpha(\mathbf{x},\omega), \tag{3.29}$$

where $n_i = x_i/|\mathbf{x}|$ denotes the normalized direction vector.

Now, we have derived the Green's tensors for both the $(\mathbf{u},\mathbf{U})$- and the $(\mathbf{u},p_f)$-formulations of the equations of motion. What remains is the inverse Fourier transform of the scalar Green's function $\hat{\mathcal{G}}_\alpha$ (see Eq. (3.18)); we show this below.

3.2.1 Inverse transform of scalar Green's functions

We now show how the $(\mathbf{x},\omega)$-domain representation of the scalar Green's functions $\hat{\mathcal{G}}_\alpha$ as introduced in the previous section (Eq. (3.18)), can be obtained using the

contour integration method (Fuchs *et al.*, 1964). The functions are solutions of the corresponding Helmholtz equation with point-source excitation

$$(\nabla^2 + \omega^2 s_\alpha^2)\hat{\mathcal{G}}_\alpha = -\delta(\mathbf{x}). \tag{3.30}$$

We start from Eq. (3.18) and apply the inverse spatial Fourier transform (Eq. (2.2))

$$\hat{\mathcal{G}}_\alpha(\mathbf{x},\omega) = \frac{\omega}{(2\pi)^3}\int_{-\infty}^{\infty}\int_{-\infty}^{\infty}\int_{-\infty}^{\infty}\frac{1}{\Delta_\alpha}\exp(-\mathrm{i}\omega\mathbf{p}\cdot\mathbf{x})\,dp_1dp_2dp_3, \tag{3.31}$$

where $\omega \geq 0$. Introducing spherical coordinates according to de Hoop (1995) (Eqs. (13.3-4)-(13.3-6)), this integral expression can be written as

$$\hat{\mathcal{G}}_\alpha(\mathbf{x},\omega) = \frac{\omega}{(2\pi)^3}\int_0^{\infty}\int_0^{\pi}\int_0^{2\pi}\frac{p^2}{\Delta_\alpha}\sin(\vartheta)\exp\left(-\mathrm{i}\omega p|\mathbf{x}|\cos(\vartheta)\right)\,d\varphi d\vartheta dp, \tag{3.32}$$

where $p = |\mathbf{p}|$. The integration over φ implies just multiplication by 2π. The integration over ϑ can be carried out using the elementary integral (Gradshteyn & Ryzhik, 1980)

$$\int_0^{\pi}\sin(z)\exp\left(-\mathrm{i}a\cos(z)\right)\,dz = \frac{2\sin(a)}{a}. \tag{3.33}$$

Then, we can write Eq. (3.32) as

$$\begin{aligned}\hat{\mathcal{G}}_\alpha(\mathbf{x},\omega) &= \frac{1}{2\pi^2|\mathbf{x}|}\int_0^{\infty}\frac{p}{\Delta_\alpha}\sin(\omega p|\mathbf{x}|)\,dp \\ &= -\frac{1}{4\mathrm{i}\pi^2|\mathbf{x}|}\int_{-\infty}^{\infty}\frac{p}{\Delta_\alpha}\exp(-\mathrm{i}\omega p|\mathbf{x}|)\,dp.\end{aligned} \tag{3.34}$$

We use the latter integral as a starting point for the contour integration in the complex p-plane (Fuchs *et al.*, 1964). The integral can be evaluated by considering p as a complex variable and closing the original integration path in the complex p-plane. Closing the integration contour by a semicircle located in the lower half-plane (see Figure 3.1) ensures the vanishing of the response for $|\mathbf{x}| \to \infty$. Application of Cauchy's theorem then gives

$$\begin{aligned}\hat{\mathcal{G}}_\alpha(\mathbf{x},\omega) &= -2\pi\mathrm{i}\cdot\mathrm{Res}_{p\to s_\alpha}\left(-\frac{1}{4\mathrm{i}\pi^2|\mathbf{x}|}\frac{p}{(p-s_\alpha)(p+s_\alpha)}\exp(-\mathrm{i}\omega p|\mathbf{x}|)\right) \\ &= \frac{\exp(-\mathrm{i}\omega s_\alpha|\mathbf{x}|)}{4\pi|\mathbf{x}|},\end{aligned} \tag{3.35}$$

because $p = s_\alpha$ is the only pole of the integrand inside the integration contour (recall that $\mathrm{Im}(s_\alpha) \leq 0$; see Section 3.2) as the poles are lying symmetrically with respect to the origin, and the contribution along the semicircle vanishes on account of Jordan's lemma (Achenbach, 1973; de Hoop, 1995). The functions $\hat{\mathcal{G}}_{P1}$ and $\hat{\mathcal{G}}_S$ are equivalent

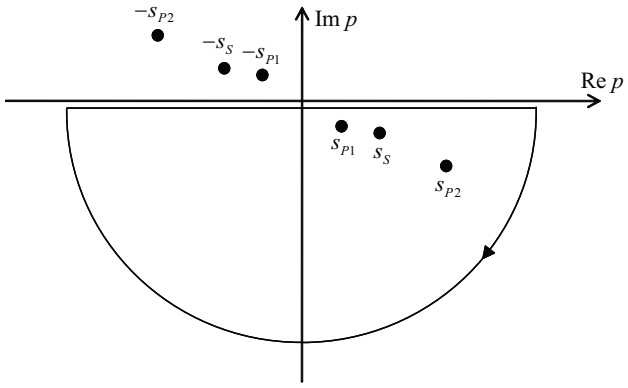

Figure 3.1: Complex p-plane with closed integration contour (Cauchy's theorem) and poles for the evaluation of the scalar Green's function $\hat{\mathcal{G}}_\alpha$, $\alpha = \{P_1, P_2, S\}$. The direction of integration is indicated.

to the corresponding Green's functions known in elasticity (de Hoop, 1995). For a porous medium, however, the wave slownesses are generally complex-valued as there is attenuation due to viscous relative fluid-solid motion. Therefore, in general, the time-domain representation $\mathcal{G}_\alpha$ cannot be evaluated in closed form. In the case of zero viscosity, the closed form solution reads

$$\mathcal{G}_\alpha(\mathbf{x}, t) = \frac{\delta(t - s_\alpha|\mathbf{x}|)}{4\pi|\mathbf{x}|}, \tag{3.36}$$

which can be shown using the integral representation of the Dirac delta function $2\pi\delta(a) = \int_{-\infty}^{\infty} \exp(\mp i a\omega t)\, d\omega$. In case of non-zero viscosity, $\mathcal{G}_\alpha$ is not an infinitely short pulse but a broader one due to attenuation and dispersion effects (see Section 3.4).

3.2.2 Low-frequency approximation

In the low- and high-frequency regimes the wave propagation process through a porous medium behaves quite differently. In this and the following sections we show the low- and high-frequency approximations of the previously derived Green's tensors to elucidate the differences in physical behavior of the separate body wavemodes depending on frequency. We start with the low-frequency approximations and restrict ourselves to the $(\mathbf{u}, \mathbf{U})$-solution Eq. (3.20).

For frequencies much smaller than the rollover frequency, i.e., $\omega \ll \omega_c$ (see Eq.

Table 3.1: Low-frequency approximation ($\omega \ll \omega_c$) of all terms in the matrix of the $(\mathbf{u}, \mathbf{U})$-solution Eq. (3.20). We have omitted the factors $(1 + \mathcal{O}(\omega/\omega_c))$ in the P_2-mode terms because they are of minor importance.

	S-terms $(\cdot\delta_{ij})$	S-terms $(\cdot\partial_i\partial_j)$
$\hat{g}_{ij}$	$\dfrac{1}{G}$	$\dfrac{1}{\omega^2\rho}\left(1+\mathrm{i}\dfrac{\omega}{\omega_c}\dfrac{\rho_{22}+\rho_{12}}{\alpha_\infty\rho}\right)$
$\hat{q}_{ij}$	$\dfrac{1}{G}\left(1-\mathrm{i}\dfrac{\omega}{\omega_c}\dfrac{1}{\alpha_\infty}\right)$	$\dfrac{1}{\omega^2\rho}\left(1-\mathrm{i}\dfrac{\omega}{\omega_c}\dfrac{\rho_{11}+\rho_{12}}{\alpha_\infty\rho}\right)$
$\hat{G}_{ij}$	$\dfrac{1}{G}\left(1-\mathrm{i}\dfrac{\omega}{\omega_c}\dfrac{2}{\alpha_\infty}\right)$	$\dfrac{1}{\omega^2\rho}\left(1-\mathrm{i}\dfrac{\omega}{\omega_c}\dfrac{2(\rho_{11}+\rho_{12})+\rho_{22}+\rho_{12}}{\alpha_\infty\rho}\right)$

P_1-terms $(\cdot\partial_i\partial_j)$	P_2-terms $(\cdot\partial_i\partial_j)$
$-\dfrac{1}{\omega^2\rho}\left(1+\mathrm{i}\dfrac{\omega}{\omega_c}\dfrac{H^2(\rho_{22}+\rho_{12})^2-\rho^2(R+Q)^2}{\rho_{22}\rho H^2}\right)$	$+\dfrac{1}{\mathrm{i}\omega\omega_c}\dfrac{(R+Q)^2}{\rho_{22}H^2}$
$-\dfrac{1}{\omega^2\rho}\left(1-\mathrm{i}\dfrac{\omega}{\omega_c}\dfrac{H^2(\rho_{11}+\rho_{12})(\rho_{22}+\rho_{12})-\rho^2(P+Q)(R+Q)}{\rho_{22}\rho H^2}\right)$	$-\dfrac{1}{\mathrm{i}\omega\omega_c}\dfrac{(P+Q)(R+Q)}{\rho_{22}H^2}$
$-\dfrac{1}{\omega^2\rho}\left(1+\mathrm{i}\dfrac{\omega}{\omega_c}\dfrac{H^2(\rho_{11}+\rho_{12})^2-\rho^2(P+Q)^2}{\rho_{22}\rho H^2}\right)$	$+\dfrac{1}{\mathrm{i}\omega\omega_c}\dfrac{(P+Q)^2}{\rho_{22}H^2}$

Table 3.2: High-frequency approximation ($\omega \gg \omega_c$) of all terms in the matrix of the $(\mathbf{u}, \mathbf{U})$-solution Eq. (3.20). We have omitted the factors $(1 + \mathcal{O}(\omega_c/\omega)^{\frac{1}{2}})$ in all terms because they are of minor importance.

	S-terms $(\cdot\delta_{ij})$	S-terms $(\cdot\partial_i\partial_j)$	P_1-terms $(\cdot\partial_i\partial_j)$	P_2-terms $(\cdot\partial_i\partial_j)$
$\hat{g}_{ij}$	$+\dfrac{1}{G}$	$+\dfrac{\rho_{22}}{\omega^2\bar{d}_0}$	$-\dfrac{1}{\omega^2 d_2 s_{P1,\infty}^2}\dfrac{\rho_{22}-Rs_{P1,\infty}^2}{s_{P2,\infty}^2-s_{P1,\infty}^2}$	$+\dfrac{1}{\omega^2 d_2 s_{P2,\infty}^2}\dfrac{\rho_{22}-Rs_{P2,\infty}^2}{s_{P2,\infty}^2-s_{P1,\infty}^2}$
$\hat{q}_{ij}$	$-\dfrac{1}{G}\dfrac{\rho_{12}}{\rho_{22}}$	$-\dfrac{\rho_{12}}{\omega^2\bar{d}_0}$	$+\dfrac{1}{\omega^2 d_2 s_{P1,\infty}^2}\dfrac{\rho_{12}-Qs_{P1,\infty}^2}{s_{P2,\infty}^2-s_{P1,\infty}^2}$	$-\dfrac{1}{\omega^2 d_2 s_{P2,\infty}^2}\dfrac{\rho_{12}-Qs_{P2,\infty}^2}{s_{P2,\infty}^2-s_{P1,\infty}^2}$
$\hat{G}_{ij}$	$+\dfrac{1}{G}\dfrac{\rho_{12}^2}{\rho_{22}^2}$	$+\dfrac{1}{\omega^2\bar{d}_0}\dfrac{\rho_{12}^2}{\rho_{22}}$	$-\dfrac{1}{\omega^2 d_2 s_{P1,\infty}^2}\dfrac{\rho_{11}-Ps_{P1,\infty}^2}{s_{P2,\infty}^2-s_{P1,\infty}^2}$	$+\dfrac{1}{\omega^2 d_2 s_{P2,\infty}^2}\dfrac{\rho_{11}-Ps_{P2,\infty}^2}{s_{P2,\infty}^2-s_{P1,\infty}^2}$

(2.77)), we find for the body-wave slownesses (Eqs. (3.15) and (3.16))

$$s_{P1} \cong s_{P1,0}\left(1 - \mathrm{i}\frac{\omega}{\omega_c}\frac{D^2}{2\rho_{22}\rho H^2}\right), \tag{3.37}$$

$$s_{P2} \cong \exp\left(-\mathrm{i}\frac{\pi}{4}\right)\left(\frac{\rho_{22}H}{d_2}\right)^{\frac{1}{2}}\left(\frac{\omega_c}{\omega}\right)^{\frac{1}{2}}\left(1 + \mathcal{O}\left(\frac{\omega}{\omega_c}\right)\right), \tag{3.38}$$

$$s_S \cong s_{S,0}\left(1 - \mathrm{i}\frac{\omega}{\omega_c}\frac{\phi\rho_f}{2\alpha_\infty\rho}\right), \tag{3.39}$$

where we have designated the second term of s_{P2} as $\mathcal{O}(\omega/\omega_c)$ because it is of minor importance here. Further, we have used the following auxiliary terms - following Pierce (2007)

$$\begin{aligned} s_{P1,0} &= (\rho/H)^{\frac{1}{2}}, \\ s_{S,0} &= (\rho/G)^{\frac{1}{2}}, \\ H &= P + R + 2Q, \\ D &= (\rho_{11} + \rho_{12})(R + Q) - (\rho_{22} + \rho_{12})(P + Q), \\ \rho &= \rho_{11} + \rho_{22} + 2\rho_{12}, \end{aligned} \tag{3.40}$$

where ρ is the bulk material density, and $s_{P1,0}$ and $s_{S,0}$ are the real-valued slownesses in the low-frequency limit $\omega \to 0$. The physical meaning of H, which is the well-known "Gassmann modulus", and of D is explained later. The low-frequency approximations of the slownesses (Eqs. (3.37)-(3.39)) were also found by Norris (1985). The low-frequency approximations of the terms in the Green's tensors (Eq. (3.20)) are given in Table (3.1). From the involved terms we observe that there is no relative fluid-solid motion induced by the P_1- and S-waves for $\omega \to 0$ (i.e., $\hat{g}_{ij;P1,S} = \hat{q}_{ij;P1,S} = \hat{G}_{ij;P1,S}$), and that there is relative fluid-solid motion associated with the P_2-mode ($\hat{g}_{ij,P2} \neq \hat{q}_{ij,P2} \neq \hat{G}_{ij,P2}$). This also follows from the amplitude ratios (Eqs. (3.22) and (3.23)), for which the low-frequency approximations read ($\omega \ll \omega_c$):

$$\beta_{P1} \cong 1 + \mathrm{i}\frac{\omega}{\omega_c}\frac{D}{\rho_{22}H}, \tag{3.41}$$

$$\beta_{P2} \cong -\frac{P+Q}{R+Q}\left(1 + \mathcal{O}\left(\frac{\omega}{\omega_c}\right)\right), \tag{3.42}$$

$$\beta_S \cong 1 - \mathrm{i}\frac{\omega}{\omega_c}\frac{1}{\alpha_\infty}. \tag{3.43}$$

These expressions were also found by Pierce (2007). As a consequence of the vanishing relative motion for $\omega \to 0$, the P_1- and S-waves propagate unattenuated through the porous medium which behaves as an ordinary elastic solid (Eqs. (3.37) and (3.39)). The behavior of the P_2-mode is entirely different. The slowness lies at $-\pi/4$ rad in the complex ω-plane showing that it is a diffusive mode (Eqs. (3.38)), which is strongly attenuated. The involved motions of solid and fluid are out-of-phase, as expressed by Eq. (3.42).

We note that the low-frequency terms of $\hat{q}_{ij}$ in Table 3.1 can also be found by multiplication of the low-frequency terms of $\hat{g}_{ij}$ and the corresponding low-frequency fluid-solid amplitude ratios (Eqs. (3.41)-(3.43)), and neglecting the $\mathcal{O}(\omega/\omega_c)^2$-term. Obviously, this general property (cf. Eq. (3.20)) remains valid in the low-frequency regime.

The unattenuated and diffusive behaviors in the low-frequency limit, respectively, can also be directly obtained from the governing equations Eqs. (2.88) and (2.89) (or from Eqs. (2.79) and (2.80)). First, inserting $\hat{\mathbf{u}} = \hat{\mathbf{U}}$ in the stress-strain relation of the fluid (Eq. (2.40)) and taking $\theta = 0$ (source term) for simplicity, we have

$$-\phi\hat{p}_f = (Q+R)\nabla\cdot\hat{\mathbf{u}}. \tag{3.44}$$

Then, substituting this equality into Eq. (2.88), we find the ordinary elastic wave equation governing the P_1- and S-wave propagation (omitting $\hat{\mathbf{F}}$ because it is of minor importance now)

$$\omega^2\rho\hat{\mathbf{u}} + H\nabla\nabla\cdot\hat{\mathbf{u}} - G\nabla\times\nabla\times\hat{\mathbf{u}} = -\hat{\mathbf{f}}, \tag{3.45}$$

where the density is ρ and the constrained modulus (plane-wave modulus) for a fluid-saturated medium is denoted H (Eq. (3.40)), which is the "Gassmann modulus" as derived by Gassmann (1951) for the low-frequency limit. Its value is greater than that of the constrained modulus $\lambda + 2G$ (cf. Eq. (2.49)) for dry/drained materials (or equivalent elastic solids) because H also includes the stiffness of the undrained fluid (the fluid does not move relative to the solid, as explained above). The Green's tensor of Eq. (3.45) is (de Hoop, 1995)

$$\hat{g}_{ij} = \frac{1}{\omega^2 G}\left(\omega^2\delta_{ij} + \frac{1}{s_{S,0}^2}\partial_i\partial_j\right)\hat{\mathcal{G}}_S - \frac{1}{\omega^2\rho}\partial_i\partial_j\hat{\mathcal{G}}_{P1}, \quad \omega\to 0, \tag{3.46}$$

which corresponds to the P_1- and S-wave terms in Table 3.1 for $\omega\to 0$. The involved wave slownesses in the solution Eq. (3.46) are exactly $s_{P1,0}$ and $s_{S,0}$, respectively (see Eq. (3.40)), which indicates the unattenuated character of the P_1- and S-waves.

To obtain the diffusive behavior of the P_2-mode directly from the governing equations, we insert $\hat{\mathbf{u}} = \beta_{P2,0}\hat{\mathbf{U}}$, where $\beta_{P2,0} = -(P+Q)/(R+Q)$ (see Eq. (3.42)), into the stress-strain relation of the fluid Eq. (2.40), and we again take $\theta = 0$ (source term). Then, we have

$$-\phi\hat{p}_f = -\frac{d_2}{R+Q}\nabla\cdot\hat{\mathbf{u}}, \tag{3.47}$$

where d_2 has already been specified in Eq. (3.8). Now, substituting this equality into Eq. (2.80), we find that the P_2-mode behavior is described by the following equation,

$$-\mathrm{i}\omega\kappa_{P2}\hat{\mathbf{u}} + \nabla\nabla\cdot\hat{\mathbf{u}} = -\frac{R+Q}{d_2}\nabla\cdot\hat{\mathbf{F}}, \tag{3.48}$$

which reduces to a diffusion equation when $\nabla\nabla\cdot\hat{\mathbf{u}} = \nabla^2\hat{\mathbf{u}}$ (which can be applied since the compressional mode is irrotational: $\nabla\times\hat{\mathbf{u}} = \mathbf{0}$); $\kappa_{P2} = b_0 H/d_2$ denotes

the slow-wave diffusivity (Pierce, 2007). The corresponding Green's tensor of Eq. (3.48) reads

$$\hat{q}_{ij} = -\frac{1}{\mathrm{i}\omega\omega_c}\frac{R+Q}{\rho_{22}H}\left(\delta(\mathbf{x})\delta_{ij} + \partial_i\partial_j\hat{\mathcal{G}}_{P2}\right), \quad \omega \to 0. \tag{3.49}$$

The expression of $\hat{\mathcal{G}}_{P2}$ is still as in Eq. (3.19), but the involved slowness is exactly the low-frequency limit slowness in Eq. (3.38) (first term), which indicates the diffusive nature of the P_2-mode. The solution Eq. (3.49) shows similarity with the P_2-mode term of the low-frequency limit approximation of $\hat{q}_{ij}$ (see Table 3.1), but it differs by a factor $(P+Q)/H$ and there is an additional non-propagating or non-diffusing term $\delta(\mathbf{x}) = \delta(x_1)\delta(x_2)\delta(x_3)$.

The equalities Eqs. (3.44) and (3.47), which are based on the result that $\hat{\mathbf{u}} = \hat{\mathbf{U}}$ for the P_1- and S-waves and $\hat{\mathbf{u}} = \beta_{P2,0}\hat{\mathbf{U}}$ for the P_2-mode (see Table 3.1), show that $\hat{p}_f$ is (solely) dependent on $\hat{\mathbf{u}}$ in the low-frequency limit. Therefore, the number of independent field variables reduces from four to three (see Section 2.5.2). The equations of motion (Eqs. (2.88) and (2.89)) become dependent and can be solved separately (decoupled equations), giving the same information. For (slightly) higher frequencies, however, there is relative fluid-solid motion which is different for all wavemodes (cf. Eqs. (3.41)-(3.43)). Then, Eqs. (2.88) and (2.89) are independent and need to be solved simultaneously, giving the Green's tensors in Eq. (3.25).

The relative fluid-solid motion is expressed by the amplitude ratios not being equal to 1; see Eqs. (3.41)-(3.43). The parameter D (see Eqs. (3.40)) and (3.41)) characterizes the mismatch between the material properties of the fluid and the solid for the P_1-wave, allowing for relative motion (Pierce, 2007). This, in turn, gives rise to attenuation, which is expressed by the complex-valued wave slownesses. If one is only interested in the motion of the solid due to the P_1- and S-waves, one could describe the behavior of the system for $\omega \ll \omega_c$ by an equivalent viscoelastic wave equation (Norris, 1985)

$$\omega^2\rho\hat{\mathbf{u}} + \hat{H}\nabla\nabla\cdot\hat{\mathbf{u}} - \hat{G}\nabla\times\nabla\times\hat{\mathbf{u}} = -\hat{\mathbf{f}}, \tag{3.50}$$

with real-valued density ρ and complex-valued frequency-dependent Gassmann and shear moduli according to

$$\hat{H} = H\left(1 + \mathrm{i}\frac{\omega}{\omega_c}\frac{D^2}{\rho_{22}\rho H^2}\right), \tag{3.51}$$

$$\hat{G} = G\left(1 + \mathrm{i}\frac{\omega}{\omega_c}\frac{\phi\rho_f}{\alpha_\infty\rho}\right). \tag{3.52}$$

The Green's tensor of Eq. (3.50) is (de Hoop, 1995)

$$\hat{g}_{ij} = \frac{1}{\omega^2\hat{G}}\left(\omega^2\delta_{ij} + \frac{1}{s_S^2}\partial_i\partial_j\right)\hat{\mathcal{G}}_S - \frac{1}{\omega^2\rho}\partial_i\partial_j\hat{\mathcal{G}}_{P1}, \quad \omega \ll \omega_c, \tag{3.53}$$

which corresponds to the P_1- and S-wave terms in Table 3.1, except for the first term $(1/G)$ of $\hat{g}_{ij}$. The involved complex-valued wave slownesses $s_{P1} = (\rho/\hat{H})^{\frac{1}{2}}$ and

$s_S = (\rho/\hat{G})^{\frac{1}{2}}$ in Eq. (3.53) can be written in terms of those in Eqs. (3.37) and (3.39), respectively, by applying a simple Taylor expansion, and correspond to the ones given by Pierce (2007) for $\omega \ll \omega_c$.

3.2.3 High-frequency approximation

Next, we show the high-frequency approximations ($\omega \gg \omega_c$) of the $(\mathbf{u}, \mathbf{U})$-solution Eq. (3.20) in Table 3.2. For the corresponding wave slownesses we find

$$s_{P1} \cong s_{P1,\infty}\left(1-(1-\mathrm{i})\left(\frac{\omega_c}{\omega}\right)^{\frac{1}{2}}\frac{M^{\frac{1}{2}}\rho_{22}H}{4d_2(s^2_{P2,\infty}-s^2_{P1,\infty})}\left(1-\frac{s^2_{P1,0}}{s^2_{P1,\infty}}\right)\right), \quad (3.54)$$

$$s_{P2} \cong s_{P2,\infty}\left(1+(1-\mathrm{i})\left(\frac{\omega_c}{\omega}\right)^{\frac{1}{2}}\frac{M^{\frac{1}{2}}\rho_{22}H}{4d_2(s^2_{P2,\infty}-s^2_{P1,\infty})}\left(1-\frac{s^2_{P1,0}}{s^2_{P2,\infty}}\right)\right), \quad (3.55)$$

$$s_S \cong s_{S,\infty}\left(1-(1-\mathrm{i})\left(\frac{\omega_c}{\omega}\right)^{\frac{1}{2}}\frac{M^{\frac{1}{2}}}{4}\left(1-\frac{s^2_{S,0}}{s^2_{S,\infty}}\right)\right). \quad (3.56)$$

Here, the high-frequency limit ($\omega \to \infty$) slownesses $s_{P1,P2;\infty}$ and $s_{S,\infty}$ are defined as

$$s_{P1,P2;\infty} = \left(\frac{1}{2d_2}\left(\bar{d}_1 \mp (\bar{d}_1^2 - 4\bar{d}_0 d_2)^{\frac{1}{2}}\right)\right)^{\frac{1}{2}},$$
$$s_{S,\infty} = \left(\frac{\bar{d}_0}{G\rho_{22}}\right)^{\frac{1}{2}}, \quad (3.57)$$

being real-valued and in which the auxilary quantities are defined as

$$\bar{d}_0 = \rho_{11}\rho_{22} - \rho_{12}^2 > 0,$$
$$\bar{d}_1 = \rho_{11}R + \rho_{22}P - 2\rho_{12}Q > 0. \quad (3.58)$$

From Table 3.2 we observe that there is relative fluid-solid motion associated with all body wavemodes in the high-frequency limit ($\hat{g}_{ij,\alpha} \neq \hat{q}_{ij,\alpha} \neq \hat{G}_{ij,\alpha}$), which is, generally, different for the three wavemodes $\alpha = \{P_1, P_2, S\}$. This is confirmed by the expressions for the amplitude ratios that are given as

$$\beta_{P1,\infty} \cong -\frac{\rho_{11} - Ps^2_{P1,\infty}}{\rho_{12} - Qs^2_{P1,\infty}} = -\frac{\rho_{12} - Qs^2_{P1,\infty}}{\rho_{22} - Rs^2_{P1,\infty}}, \quad (3.59)$$

$$\beta_{P2,\infty} \cong -\frac{\rho_{11} - Ps^2_{P2,\infty}}{\rho_{12} - Qs^2_{P2,\infty}} = -\frac{\rho_{12} - Qs^2_{P2,\infty}}{\rho_{22} - Rs^2_{P2,\infty}}, \quad (3.60)$$

$$\beta_{S,\infty} \cong -\frac{\rho_{12}}{\rho_{22}}. \quad (3.61)$$

Although there is relative fluid-solid motion in the high-frequency limit, its attenuative effect is negligible. The body-wave slownesses are real-valued (Eq. (3.57)),

which shows that all wavemodes are indeed propagatory (also the P_2-mode). For lower frequencies (still $\omega \gg \omega_c$), there is non-zero attenuation as expressed by the complex-valued body-wave slownesses (Eqs. (3.54)-(3.56)).

In both cases $\omega \gg \omega_c$ and $\omega \to \infty$ the quantities $\hat{p}_f$ and $\hat{\mathbf{u}}$ are independent, which implies that the system of coupled equations (Eqs. (2.88) and (2.89)) should be solved simultaneously.

3.3 Impedances of the wavemodes

Now, we derive the impedances I^s_α and I^f_α associated with the wavemodes that exist in a porous medium. For each of the wavemodes, the impedance is defined as the spectral ratio of the far-field stress or pressure, and a corresponding component of the particle velocity, in either the solid or the fluid phase according to (see de Hoop (1995): Eqs. (13.7-31)-(13.7-34))

$$-\hat{\tau}_{ij,\alpha} n_i = \mathrm{i}\omega \hat{u}_{j,\alpha} I^s_\alpha, \tag{3.62}$$

$$\hat{p}_\alpha = \mathrm{i}\omega \hat{U}_{i,\alpha} n_i I^f_\alpha. \tag{3.63}$$

Here, $\hat{\tau}_{ij,\alpha}$ denotes the total stress tensor in the solid induced by the particular wavemode α (Eq. (2.15)), and its multiplication with the direction vector n_i (cf. Eq. (3.28)) implies taking the traction vector $\hat{t}_{j,\alpha}$. The multiplication of the fluid particle displacement $\hat{U}_{i,\alpha}$ with n_i in Eq. (3.63) implies that we take the radial component of the particle displacement (which is the resulting particle displacement in the far field). From the definitions it is clear that the impedance expresses the resistance of the particular phase to the motion induced by the wavemode in that phase.

Making use of the derived Green's tensors (Eq. (3.26)), applying the derivatives according to Eqs. (3.28) and (3.29) and taking the far-field terms only (in both cases: the last term in the brackets), we obtain

$$I^s_{P1,P2} = s_{P1,P2}(P + Q\beta_{P1,P2}), \tag{3.64}$$

$$I^f_{P1,P2} = s_{P1,P2} \frac{H_{P1,P2}}{\phi \beta_{P1,P2}}, \tag{3.65}$$

$$I^s_S = s_S G. \tag{3.66}$$

The shear-wave impedance in the fluid I^f_S it not defined as both the left- and right-hand sides of Eq. (3.63) vanish (for $\alpha = S$): the S-wave does not contribute to the fluid pressure as its motion equivoluminal (Achenbach, 1973; de Hoop, 1995), and the corresponding particle motion $\hat{U}_{i,S}$ is perpendicular to the direction of propagation n_i. Allard (1993) derived identical expressions for the compressional-wave impedances in each of the phases.

In addition, we derive the impedances of the wavemodes that express the coupling between the solid and the fluid phase. For each of the compressional wavemodes, we define this "coupling impedance" as the spectral ratio of the associated fluid pressure

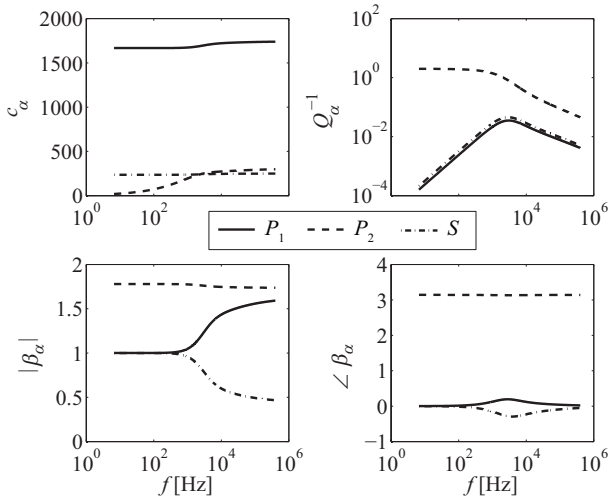

Figure 3.2: Frequency-dependent properties for the existing body wavemodes ($\alpha = \{P_1, P_2, S\}$): phase velocities c_α, inverse quality factors Q_α^{-1} (from Eqs. (3.15) and (3.16)), and magnitudes and phases of the amplitude ratios β_α (Eqs. (3.22) and (3.23)).

and the radial component of the particle velocity according to (shear-wave coupling impedance is not defined)

$$\hat{p}_{P1,P2} = \mathrm{i}\omega \hat{u}_{i;P1,P2} n_i I_{P1,P2}. \tag{3.67}$$

It represents the resistance of the fluid phase to the motion induced by the particular wavemode in the solid phase. Again using Eqs. (3.26), (3.28) and (3.29), we find

$$I_{P1,P2} = s_{P1,P2} \frac{H_{P1,P2}}{\phi}. \tag{3.68}$$

The derived quantities Eqs. (3.64)-(3.66) and (3.68) can be addressed as the far-field impedances or as the impedances associated with plane waves. The impedances are independent of the properties of the source and only incorporate the properties of the medium. The dimensions correspond with the well-known plane-wave impedance $s_f K_f = (\rho_f K_f)^{\frac{1}{2}}$ of an acoustic wave in an unbounded fluid (Allard, 1993; de Hoop, 1995); here the slowness of the acoustic wave is denoted as $s_f = (\rho_f / K_f)^{\frac{1}{2}}$.

The definition of the coupling impedance shows that it combines the information present in all independent field variables in one frequency-dependent complex-valued quantity for each of the compressional wavemodes (see Section 3.2). Like the other impedances, they can be addressed as "multi-component full-waveform attributes" as they interrelate the waveforms (responses) observed in different components. In Section 3.4 we discuss the behavior of the coupling impedances in more detail and illustrate their relation with the time-domain waveforms in $\mathbf{v}$ and p_f. To facilitate this, here we give the low- and high-frequency limit approximations of the coupling

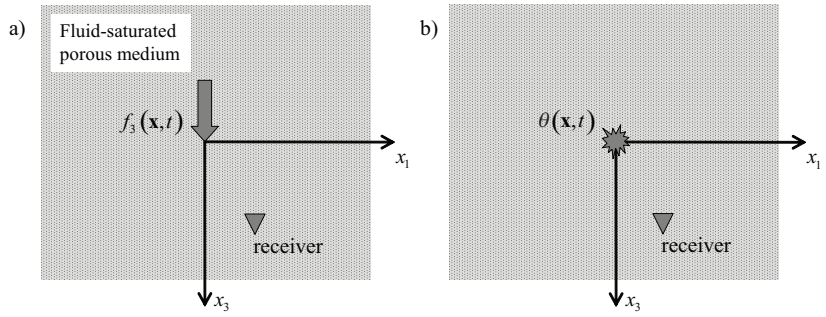

Figure 3.3: Configurations with point force $f_3(\mathbf{x},t)$ (a) and volume injection source $\theta(\mathbf{x},t)$ (b) to excite various wavemodes in a fluid-saturated porous medium. In all computed responses $x_3/x_1 = 2$ and $x_2 = 0$. Other parameter values are listed in Table 3.3.

impedances. For $\omega \to 0$, the expressions read

$$I_{P1,0} = s_{P1,0}\frac{R+Q}{\phi}, \tag{3.69}$$

$$I_{P2,0} = \exp\left(\mathrm{i}\frac{3}{4}\pi\right)\frac{(\rho_{22}Hd_2)^{\frac{1}{2}}}{\phi(R+Q)}\left(\frac{\omega_c}{\omega}\right)^{\frac{1}{2}}. \tag{3.70}$$

The fast-wave impedance $I_{P1,0}$ is real-valued and positive, which expresses that the fluid pressure is in-phase with the (radial) particle velocity. The slow-wave impedance $I_{P2,0}$ is frequency-dependent and complex-valued due to the diffusive nature of the P_2-mode and the associated out-of-phase motion. In the high-frequency limit $\omega \to \infty$ the expressions of the impedances read

$$I_{P1,P2;\infty} = s_{P1,P2;\infty}\frac{Q+R\beta_{P1,P2;\infty}}{\phi}, \tag{3.71}$$

which are both real-valued.

3.4 Numerical examples

To highlight the characteristic features of the wave propagation process, in this section we illustrate the frequency-dependence of the attributes (e.g., velocity) of the existing body wavemodes, and of their waveforms that are excited by point sources. We look at the waveforms in different components of the transient responses, i.e., particle velocity and fluid pressure, to verify the nature of the coupling between these components as predicted by the coupling impedances.

As in Chapter 2, we take material properties of Sand of Mol (Degrande *et al.*, 1998), being representative of a water-saturated shallow subsurface situation of loosely packed sand. The parameter values are specified in Table 2.1. Given these values, the generalized elastic constants (Eqs. (2.41)-(2.43)) are determined and

Table 3.3: Three different configurations to illustrate the wave propagation process in a fluid-saturated porous medium. In all cases, $x_3/x_1 = 2$ and $x_2 = 0$. S_{max}-values are either in [N] or in [m^3/m^3], depending on the source type. See Figures 3.3a and 3.3b for schematic drawings of the configurations.

	f_0 [Hz]	t_s [s]	x_3 [m]	Source	S_{max}
1	500	$1.5 \cdot 10^{-2}$	414	f_3	$1 \cdot 10^4$
2	3500	$1.5 \cdot 10^{-2}$	15.08	f_3	10
3	$500 \cdot 10^3$	$1 \cdot 10^{-5}$	0.108	f_3; θ	$2.5 \cdot 10^{-7}$; $3 \cdot 10^{-20}$

using those we have calculated the phase velocities $c_\alpha = 1/\mathrm{Re}(s_\alpha)$ (Eqs. (3.15) and (3.16)),[i] the inverse quality factors $Q_\alpha^{-1} = 2 \cdot |\mathrm{Im}(s_\alpha)/\mathrm{Re}(s_\alpha)|$ and the amplitude ratios β_α (Eqs. (3.22) and (3.23)) of the three different body wavemodes, i.e., $\alpha = \{P_1, P_2, S\}$. The results are shown in Figure 3.2 as a function of frequency f. We observe that the P_1- and S-waves have only slight dispersion. Their low- and high-frequency limits agree with the expressions in Eqs. (3.40) and (3.57), respectively. The P_2-wave velocity shows strong variation from the low-frequency diffusive behavior to the high-frequency propagational behavior; see Eqs. (3.38) and (3.55). We observe that c_{P2} can be larger than c_S, depending on frequency and the material properties.

The inverse quality factors, which represent the intrinsic attenuation per cycle of the wavemodes (Aki & Richards, 1980), show that the P_2-mode is much stronger attenuated than the P_1- and S-waves. In the low-frequency limit Q_{P1}^{-1} and Q_S^{-1} tend to zero, while Q_{P2}^{-1} tends to a constant value, which confirms Eqs. (3.37)-(3.39) for $\omega \to 0$. In the high-frequency limit all Q_α^{-1} tend to zero due to the viscous mechanism becoming less important, confirming Eqs. (3.54)-(3.56).

The amplitude ratios β_α show that the fluid and solid phase move in-phase (same amplitude and phase) for the P_1- and S-waves in the low-frequency limit, which confirms Eqs. (3.41) and (3.43). The amplitude ratio of the P_2-wave (β_{P2}) shows a complete out-of-phase motion of fluid and solid (confirming Eq. (3.42)), which, obviously, explains the strong attenuation of this mode. At higher frequencies also the P_1- and S-waves have a relative fluid-solid motion, but the behavior is essentially still in-phase. The P_2-wave has an out-of-phase motion for the entire frequency band.

In fact, we can consider the P_2-mode as a generalization to the full frequency range of a stationary flow through rigid porous frame (Darcy's law, Eq. (2.65); low-frequency limit), or of the compressional wave propagating through a lossless fluid inside a rigid porous frame (Eq. (2.66); high-frequency limit). The generalization also implies that the motion of the porous frame is not blocked but considered as a separate degree of freedom. This, in turn, guarantees the existence of two additional

[i] The harmonic body waves that exist in an isotropic fluid-saturated porous (dispersive) medium are so-called homogeneous plane waves for which the phase velocity is equal to the energy propagation velocity (Carcione, 2007). Therefore, in this thesis we address the phase velocity simply as "wave velocity" or "(propagation) velocity". In the case of a propagating pulse, being a superposition of many plane waves, various definitions of the propagation velocity are possible, e.g., the "centrovelocity" being the velocity of the centroid of the pulse in time or space (Carcione *et al.*, 2010b). In this thesis, we only consider phase velocities.

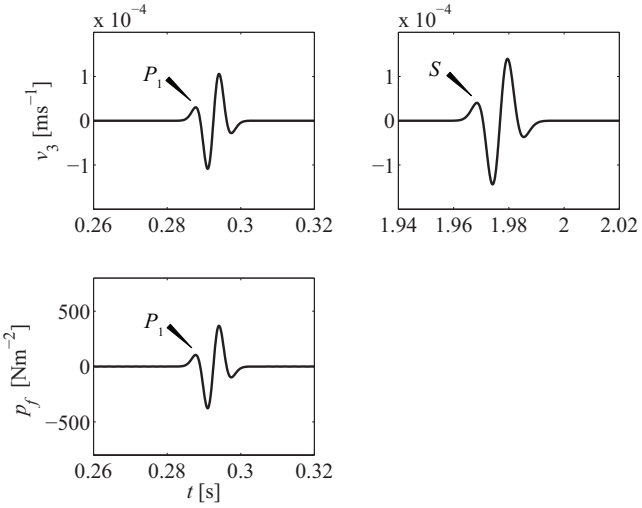

Figure 3.4: Response in v_3 and p_f for $\omega_0 \ll \omega_c$ (configuration 1, Table 3.3). The S-wave contribution is absent in p_f, and the P_2-wave contribution is vanishingly small in v_3 and p_f; therefore, the corresponding time windows are not shown.

wavemodes: the P_1- and S-waves.

Next, we illustrate the wave propagation in the $(\mathbf{x}, t)$-domain using the responses excited by a point source in an infinite porous space. We either use a point force excitation in the x_3-direction applied to the solid (f_3), or a volume injection in the fluid (θ), according to

$$\{f_3(\mathbf{x},t), \theta(\mathbf{x},t)\} = S(t)\delta(x_1)\delta(x_2)\delta(x_3), \tag{3.72}$$

$$S(t) = S_{max}\left(\tfrac{1}{2}\omega_0^2\bar{t}^2 - 1\right)\exp\left(-\tfrac{1}{4}\omega_0^2\bar{t}^2\right), \tag{3.73}$$

where $S(t)$ denotes the Ricker signature (Ricker, 1953), and where $\bar{t} = t - t_s$ $(t > 0)$; $t_s > 0$ denotes the time shift, $\omega_0 = 2\pi f_0$ and f_0 is the center frequency. S_{max} represents the magnitude of the point force [N] or the magnitude of the (volume density of) volume injection [$\mathrm{m}^3/\mathrm{m}^3$]. We have calculated the Green's tensors (Eqs. (3.20) and (3.26)) for these excitations assuming three different center frequencies to illustrate the frequency dependence of the waveforms: $\omega_0 \ll \omega_c$, $\omega_0 \cong \omega_c$ and $\omega_0 \gg \omega_c$. In all cases the distances have been chosen such that $\omega_0 s_{P1}(\omega_0)|\mathbf{x}| = 220$, $x_3/x_1 = 2$ and $x_2 = 0$; see Table 3.3 for the specific values of S_{max}, ω_0, t_s and $\mathbf{x}$. We only show the time-domain responses in the vertical component of particle velocity v_3 and the fluid pressure p_f. They are obtained using a standard fast-Fourier transform algorithm applied to the $(\mathbf{x}, \omega)$-domain responses (Eqs. (3.24) and (3.25)). The responses due to the point force are shown in Figures 3.4-3.6. For the volume injection, we only show the response for configuration 3 (Figure 3.7) because this is sufficient to illustrate the differences from the point force excitation, i.e., the excited wavemodes and their mutual strength.

For $\omega_0 \ll \omega_c$ and $\omega_0 \cong \omega_c$ (Figures 3.4 and 3.5, respectively) only the P_1- and

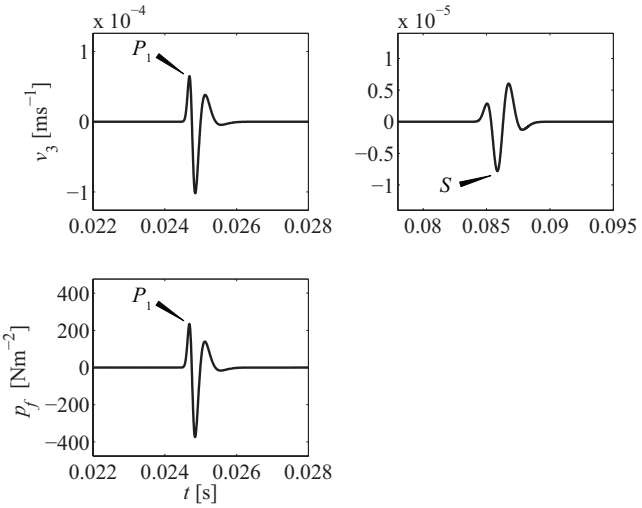

Figure 3.5: Response in v_3 and p_f for $\omega_0 \cong \omega_c$ (configuration 2, Table 3.3). The S-wave contribution is absent in p_f, and the P_2-wave contribution is vanishingly small in v_3 and p_f; therefore, the corresponding time windows are not shown.

S-waves can be detected. The P_2-mode is too much attenuated to be observed. For $\omega_0 \gg \omega_c$ the P_2-mode is a propagating wave, but still its amplitude is orders of magnitude smaller than that of the P_1- and S-waves (Figure 3.5). When we excite the fluid instead of the solid by means of the fluid volume injection source, the difference in strength is approximately the same (Figure 3.7), and hence, it cannot be attributed to the type of excitation; the difference in strength is, however, not always so big. The strength of the P_2-mode highly depends on the material parameters of the specific material. Remarkably, the P_1- and S-waveforms are different for the various excitation frequencies. This illustrates the frequency-dependent nature of the response as a result of the dispersion, which is an important difference compared with the response in an elastic solid (de Hoop, 1995); there, the waveforms are very similar for the different excitation frequencies.

For the S-wave, it can be verified that it does not contribute to the fluid pressure in all responses (cf. Figures 3.4-3.7). This is due to the absence of an S-wave contribution in the Green's tensors for the fluid pressure (Eqs. (3.25) and (3.26)), which is reasonable since only the solid and fluid dilatations contribute to the fluid pressure; see the stress-strain relation Eq. (2.40). The shear-wave exhibits a rotational motion which is equivoluminal. We note, however, that the S-wave does induce a motion of the fluid (cf. Eqs. (3.20) and (3.24)) which is, generally, not equal to that of the solid (as expressed by β_S being not equal to one).

In all configurations the waveform of the P_1-wave in p_f looks very much the same as that in v_3 (see Figures 3.4-3.7). For the P_2-wave, the phase in the two components is opposite, but the waveforms are also quite similar. To verify the nature of the coupling between the particle velocity of the solid and the pressure of the fluid, we consider the coupling impedances I_{P1} and I_{P2} (Eq. (3.68)). These

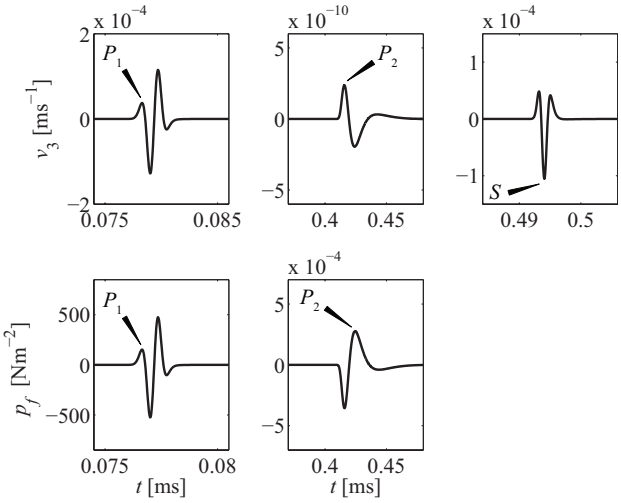

Figure 3.6: Response in v_3 and p_f for $\omega_0 \gg \omega_c$ (configuration 3, Table 3.3) for point force f_3. All wavemodes (P_1,P_2,S) can be observed. The S-wave contribution is absent in p_f and therefore, the corresponding time window is not shown.

quantities also include v_1 and v_2, but their far-field waveforms of the P_1-waves are only scaled versions of that in v_3 (factor n_1/n_3 and n_2/n_3, respectively; see Eq. (3.29)). They do not contain additional information about the medium but only about the direction of propagation. For configuration 2, we show the magnitudes and phases of I_{P1} and I_{P2}, respectively, and the magnitude and phase of I_{P1} as retrieved from the separate P_1-wave in the full responses in Figure 3.8. For the P_1-wave, we observe that there is variation over frequency especially for frequencies around ω_c, indicating that the coupling between p_f and $\mathbf{v}$ is frequency-dependent. However, the variations are small, which explains that this frequency-dependence is difficult to be observed in the time domain. At $\omega_0 \ll \omega_c$ and $\omega_0 \gg \omega_c$ the coupling is practically frequency-independent, and the phase $\angle I_{P1}$ is close to zero, which confirms the in-phase character of the waveforms in p_f and $\mathbf{v}$ (cf. Eqs. (3.69) and (3.71)). Concerning the retrieved $|I_{P1}|$ and $\angle I_{P1}$, we observe that especially the latter deviates from the exact value at low frequencies because the far-field assumption does not hold there, which has been used to derive the exact result (Eq. (3.68)). The P_2-wave coupling between p_f and $\mathbf{v}$ exhibits stronger frequency dependence: for different frequencies the magnitude of the pressure compared to the magnitude of the particle velocity can be quite different, which is related to the stronger dispersion of the P_2-mode due to the more significant interaction between fluid and solid. The phase $\angle I_{P2}$ goes to $3\pi/4$ in the low-frequency limit, which confirms Eq. (3.70), and to π in the high-frequency limit (Eq. (3.71)), confirming the out-of-phase character of the waveforms in p_f and $\mathbf{v}$ (Figures 3.6 and 3.7). The P_2-waveforms in p_f and $\mathbf{v}$ can be quite different depending on frequency due to the variations in $\angle I_{P2}$.

By definition, the coupling impedance of a compressional wavemode interrelates

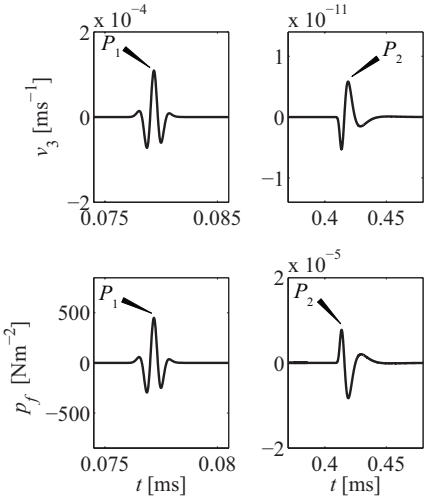

Figure 3.7: Response in v_3 and p_f for $\omega_0 \gg \omega_c$ (configuration 3, Table 3.3) for volume injection source θ. Only the P_1- and P_2-waves are excited by this source. Therefore, the time windows corresponding to the S-wave are not shown.

the waveforms in all independent field variables in one frequency-dependent complex-valued quantity; see Eq. (3.68). Consequently, the coupling impedance contains all the information about the medium that is carried by the corresponding wavemode, which makes it useful to be employed for determining local in-situ medium properties. This can be advantageous in decomposition algorithms of seismic data, where one needs to know the medium properties at the level of the receivers (e.g., Wapenaar & Berkhout, 1989). The quantities can also be used to verify the nature of the coupling between the medium and a geophone or a hydrophone (e.g., Drijkoningen *et al.*, 2006).

3.5 Discussion

Finally, we address the scalar source as present in Eqs. (2.63) and (2.89). When $\nabla \cdot \hat{\mathbf{F}} \propto \nabla^2 \hat{\theta}$ (volume injection) it does not excite shear waves, which can be shown using the derived Green's functions, i.e., the S-wave part in $\hat{u}_i = \hat{q}_j * \hat{F}_j$ vanishes (Eqs. (3.20) and (3.25)). This is also illustrated in Figure 3.7, where the S-wave is absent in v_3, confirming the statement of Bonnet (1987) that the scalar source cannot excite shear waves as it is spherically symmetric (see Section 3.1). However, when $\nabla \cdot \hat{\mathbf{F}} = \nabla \cdot \hat{\mathbf{F}}_f$, generally, the scalar source is not spherically symmetric: the S-wave part does not vanish. This seems to contradict Bonnet's statement, but we should realize that the components of the force source are generally independent of each other, giving more than four independent source terms (even though combined in the scalar source). This invalidates the underlying assumption of Bonnet's scalar source, and thus resolves the apparent contradiction.

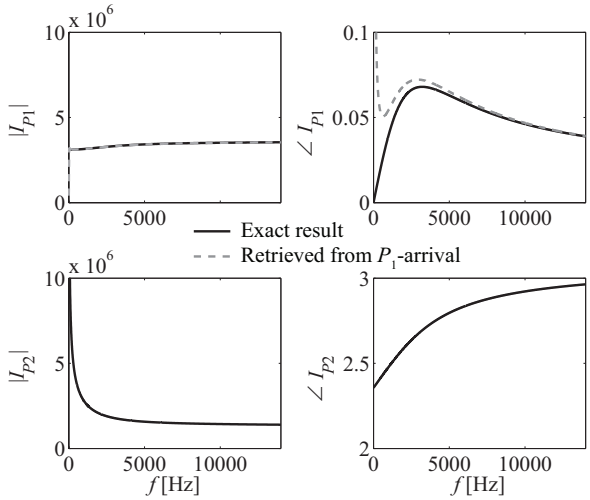

Figure 3.8: Frequency-dependent coupling impedances I_{P1} and I_{P2}. Magnitudes and phases are given. For I_{P1}, both the exact result and that retrieved from the P_1-arrival in Figure 3.5 are shown.

In the previous section we have illustrated the Green's tensors incorporating only the macroscopic (wavelength scale) loss mechanism as introduced by Johnson *et al.* (1987) (see also Section 2.5.1). However, also other (additional) attenuation mechanisms can be included, depending on the the specific medium of interest. For instance, sub-wavelength scale (mesoscopic) heterogeneities can be present in the soil, e.g., gas pockets larger than the grain size or pockets of weakly cemented grains, and can be accounted for using mesoscopic flow mechanisms (Smeulders & van Dongen, 1997; Pride & Berryman, 2003; Pride *et al.*, 2004; Müller & Gurevich, 2005; Vogelaar, 2009). When the structure of the governing macroscopic equations stays the same (e.g., when an attenuation mechanism is incorporated using frequency-dependent elastic moduli), the form of the Green's tensors also stays exactly the same and hence, the presented Green's tensors can be applied in more complicated situations. In the case of the mesoscopic flow mechanisms, the frequency-dependence of I_{P1} and I_{P2} (and also of β_α) shown in this section can be quite different, especially for the lower (seismic) frequencies, which also will induce differences in waveforms between p_f and $\mathbf{v}$.

3.6 Conclusions

In this chapter we derived the Green's tensors for wave propagation in a fluid-saturated porous medium. The Green's tensors are known in the literature, but we obtained them differently by straightforward application of the Fourier transform to the governing equations of motion. We showed the Green's tensors for both the $(\mathbf{u}, \mathbf{U})$- and the $(\mathbf{u}, p_f)$-formulations of the equations of motion incorporating a force applied to the solid and a force applied to the fluid, and a scalar source related to

the fluid. Further, for each of the fast (P_1) and slow (P_2) compressional wavemodes, we derived the far-field coupling impedance, which is defined as the spectral ratio of the associated fluid pressure and the radial component of the particle velocity. The coupling impedance interrelates the waveforms of the specific wavemode in all independent field variables and hence, it can be referred to as a "multi-component full-waveform attribute".

Using limit-case expressions and numerical examples we illustrated the frequency-dependence of the existing wavemodes, confirming the findings in the literature: the P_1- and S-waves are propagatory over the entire frequency regime, and the associated fluid and solid motions are in-phase, giving only slight relative fluid-solid motion; the P_2-mode is diffusive in the low-frequency regime and propagatory in the high-frequency regime, and the motions of fluid and solid are out-of-phase, which implies a considerable relative fluid-solid motion giving rise to strong attenuation. In addition, we showed that the waveforms (point-source responses) differ for different excitation frequencies, which illustrates the frequency-dependent character of the responses as a result of the dispersion. Further, we illustrated the frequency-dependent coupling between the fluid pressure and the particle velocity as expressed by the coupling impedances, which can be significant particularly for the P_2-mode. Finally, we showed that the scalar source in the fluid does not excite shear waves (Bonnet, 1987) in the case that it is a volume injection. However, in the case that the scalar source consists of the divergence of the fluid force, it does excite shear waves.

Chapter 4

On wavemodes at the interface of a fluid and a fluid-saturated poroelastic solid[i]

Abstract

Pseudo interface waves can exist at the interface of a fluid and a fluid-saturated poroelastic solid. These waves are typically related to the pseudo-Rayleigh pole and the pseudo-Stoneley pole in the complex slowness plane. It is found that each of these two poles can contribute (as a residue) to a full transient wave motion when the corresponding Fourier integral is computed on the principal Riemann sheet. This contradicts the generally accepted explanation that a pseudo interface wave originates from a pole on a non-principal Riemann sheet. It is also shown that part of the physical properties of a pseudo interface wave can be captured by loop integrals along the branch cuts in the complex slowness plane. Moreover, it is observed that the pseudo-Stoneley pole is not always present on the principal Riemann sheet depending also on frequency rather than on the contrast in material parameters only. Finally, it is shown that two additional zeroes of the poroelastic Stoneley dispersion equation, which are comparable with the $\bar{P}$-poles known in non-porous elastic solids, do have physical significance due to their residue contributions to a full point-force response.

4.1 Introduction

Interface waves such as Rayleigh and Stoneley waves are often used to investigate materials. One can think of applications in ultrasonic testing of structures, borehole logging in geotechnical and reservoir engineering, and surface seismics in geophysics;

[i]This chapter has been published as a journal paper in *J. Acoust. Soc. Am.* **127** (4), 2240–2251 (van Dalen *et al.*, 2010b). Note that minor changes have been introduced to make the text consistent with the other chapters of this thesis.

see e.g., Ewing *et al.* (1957); Viktorov (1967); Aki & Richards (1980); Burns (1990). In the case of porous materials, interface waves carry information on elastic properties but also on properties like porosity, permeability and fluid mobility (Burns, 1990). Rosenbaum (1974) found that, compared to all other surface and body wavemodes, the Stoneley-type wave that travels along the open-pore interface of a fluid and a porous medium, carries the best measure of permeability.

Several theoretical studies were performed on interface waves that propagate along the boundary of a porous medium. These studies were carried out in the context of Biot's theory for wave propagation in fluid-saturated poroelastic solids. Deresiewicz (1962) showed the existence of a Rayleigh-type wave that propagates along the free surface of a poroelastic half-space and analyzed the frequency-dependent phase velocity and attenuation.

For a fluid/poroelastic-medium configuration (Rosenbaum, 1974) predicted the existence of the pseudo-Rayleigh (pR) and the pseudo-Stoneley (pSt) wave. The latter was explicitly named as such by Feng & Johnson (1983a,b) since a pseudo interface wave has part of its energy leaking into slower bulk modes as it propagates along the interface. Feng & Johnson (1983a) also showed the existence of another interface wavemode, the non-leaky true interface wave. It was found that the existence of this wave depends on whether or not the pores are open for pore fluid to flow across the interface. Feng & Johnson (1983b) derived Green's functions (impulse responses) for high-frequency Biot theory that confirmed the existence of the three different waves.

Experimental evidence was found for all three types of interface wavemodes; see e.g., Mayes *et al.* (1986); Adler & Nagy (1994); Allard *et al.* (2004).

Feng & Johnson (1983a) argued that other zeroes of the poroelastic Stoneley dispersion equation have no physical significance as pseudo interface modes. The corresponding propagation velocities would be larger than that of the shear wave, which is not realistic in their opinion.

In order to obtain the characteristics of the interface wavemodes, Feng & Johnson (1983a) used the zeroes of the non-viscid poroelastic Stoneley dispersion equation in the complex plane to obtain the propagation velocities and attenuations. Gubaidullin *et al.* (2004) went a step further and analyzed the frequency dependence of the interface wavemodes by incorporating the viscous loss mechanism of Johnson *et al.* (1987). They also used the zeroes of the dispersion equation to derive the characteristics of the interface waves. The same approach was adopted by Edelman & Wilmanski (2002), Albers (2006) and Markov (2009). In most of the papers specific restrictions for the involved square roots (i.e., their Riemann sheets) are given.

The generally accepted explanation for a pseudo interface wave is that it originates from a zero that forms a pole singularity on another Riemann sheet than the so-called "principal" sheet. It affects the behavior of the integrand on the principal Riemann sheet by causing a local maximum in the integrand (van der Hijden, 1984). In case the pole lies close to the real axis, it might have a contribution to the Green's function.

In a series of publications, Allard *et al.* (2002, 2003, 2004) studied the propagation of interface waves along the boundaries of poroelastic and non-porous elastic

media. In the case of an air/air-saturated poroelastic-solid configuration, they found that taking the residue of the pseudo-Rayleigh pole is sufficient to describe the entire pseudo-Rayleigh waveform (Allard *et al.*, 2003). For the water/water-saturated poroelastic-solid configuration, they found that the pseudo-Stoneley pole residue describes the entire waveform of the pseudo-Stoneley wave (Allard *et al.*, 2004). However, for the water/elastic-solid configuration they found that the pseudo-Rayleigh waveform is strongly affected by the loop integrals along the branch cuts.

In summary, taking just the location of the zeroes of the dispersion equation rather than computing the full transient response is a very fast way to predict the kinematic properties of pseudo interface waves, but the question arises whether these predictions are always complete.[ii]

Therefore, in this chapter we analyze the three-dimensional transient wave propagation due to a point force applied at the interface of a fluid and a fluid-saturated poroelastic solid. The aims are

1. To investigate whether a zero of the poroelastic Stoneley dispersion equation indeed yields the pertinent physical properties of the corresponding pseudo interface wavemode. This is done by quantitative comparison between the residues of specific poles and the full transient response;

2. To verify whether a pseudo interface wave indeed necessarily originates from a pole on a non-principal Riemann sheet;

3. To verify the physical significance of additional zeroes of the poroelastic Stoneley dispersion equation that are not related to pseudo interface waves (Feng & Johnson, 1983a).

The chapter is organized as follows. In Section 4.2 we present the model to analyze the fluid/poroelastic-medium configuration. Subsequently, in Section 4.3 the derivation of the Green's functions is summarized. The implementation of the numerical integration is discussed in Section 4.4. We discuss the results in Section 4.5. The conclusions are given in Section 4.6.

4.2 Model

To study the transient wave propagation in a fluid/poroelastic-medium configuration, we consider a configuration that consists of a fluid half-space on top of a fluid-saturated poroelastic half-space. A vertical point force $F(t)$ is applied at the interface (see Figure 4.1a; Figure 4.1b is referred to later). Both half-spaces are considered to be homogeneous and isotropic. The configuration is similar to the one applied by Gubaidullin *et al.* (2004), but extended to three dimensions.

The behavior in the lower half-space ($x_3 > 0$) is governed by the well-known Biot equations of motion for a fluid-saturated poroelastic solid that were extensively discussed in The Journal of the Acoustical Society of America; see e.g., Biot (1956a,b).

[ii] Here, the question is whether the predictions are complete in the far field (see also Chapter 5). In the near field various waves interfere; there, a pole never gives a complete description.

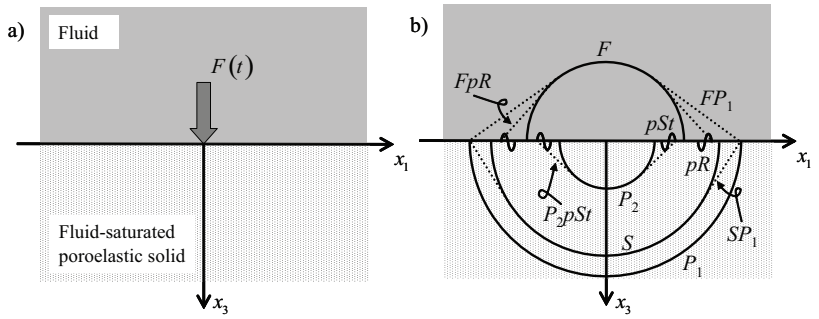

Figure 4.1: a) Point force $F(t)$ applied at the interface of a fluid-saturated poroelastic half-space and a fluid half-space. Both half-spaces are homogeneous and isotropic. b) Schematic snapshot of the full response with separate arrivals: fast compressional (P_1) wave, slow compressional (P_2) wave, shear (S) wave, fluid (F) wave, pseudo-Rayleigh (pR) wave and pseudo-Stoneley (pSt) wave. The double-mode symbols (e.g., SP_1) indicate lateral waves. The first symbol denotes the wavemode of the specific arrival; the second denotes the one from which it is radiated. Here, the F-wave velocity is assumed higher than the P_2-wave velocity. For clarity, we have omitted the following arrivals: FS, P_2P_1, P_2S, P_2pR and P_2F.

Following Biot's theory, we assume that for long wavelength disturbances with respect to the characteristic pore scale, average local displacements can be defined for the solid (frame) $\mathbf{u}(\mathbf{x},t) = (u_1, u_2, u_3)^T$ and the fluid $\mathbf{U}(\mathbf{x},t) = (U_1, U_2, U_3)^T$. Considering a cube of unit size of bulk material (porosity ϕ), the forces per unit bulk area applied to that part of the cube faces occupied by the solid are denoted by τ_{ij}. They are constituted by both fluid pressure p_f and intergranular stresses σ_{ij} according to

$$\tau_{ij} = -\sigma_{ij} - (1-\phi)p_f\delta_{ij}, \tag{4.1}$$

where δ_{ij} is the Kronecker delta. The total normal tension force per unit bulk area applied to the fluid faces of the unit cube, denoted by τ, is constituted by p_f only

$$\tau = -\phi p_f. \tag{4.2}$$

Here, σ_{ij} and p_f are defined positive in compression and, consequently, τ_{ij} and τ are positive in tension; see also Gubaidullin *et al.* (2004). In the case of isotropic materials, the stress-strain relations for the solid and the fluid can be written as

$$\tau_{ij} = G(\partial_i u_j + \partial_j u_i) + A\partial_k u_k \delta_{ij} + Q\partial_k U_k \delta_{ij}, \tag{4.3}$$

$$\tau = Q\partial_k u_k + R\partial_k U_k, \tag{4.4}$$

where Einstein's summation convention for repeated indices is applied, and $\partial_j = \partial/\partial x_j$. A, Q, and R are generalized elastic constants that can be related via so-called "Gedanken" experiments to porosity, grain bulk modulus K_s, fluid bulk modulus K_f, bulk modulus of porous drained frame K_b, and shear modulus G of both drained frame and total composite (Biot & Willis, 1957; Allard, 1993). The physical background of Eqs. (4.3) and (4.4) is discussed in more detail in Biot (1956a).

The equations of motion are found from combination of momentum conservation and the stress-strain relations, Eqs. (4.3) and (4.4), and can be written (in the case there are sources present for $x_3 > 0$) as (Biot, 1956a,b)

$$\rho_{11}\partial_t^2\mathbf{u} + \rho_{12}\partial_t^2\mathbf{U} + b(t) * \partial_t(\mathbf{u} - \mathbf{U}) = P\nabla\nabla\cdot\mathbf{u} - G\nabla\times\nabla\times\mathbf{u} + Q\nabla\nabla\cdot\mathbf{U}, \tag{4.5}$$

$$\rho_{12}\partial_t^2\mathbf{u} + \rho_{22}\partial_t^2\mathbf{U} - b(t) * \partial_t(\mathbf{u} - \mathbf{U}) = Q\nabla\nabla\cdot\mathbf{u} + R\nabla\nabla\cdot\mathbf{U}, \tag{4.6}$$

where the asterisk denotes convolution, $P = A + 2G$, and the effective densities are defined as

$$\begin{aligned}\rho_{11} &= (1-\phi)\rho_s - \rho_{12},\\ \rho_{22} &= \phi\rho_f - \rho_{12},\\ \rho_{12} &= -(\alpha_\infty - 1)\phi\rho_f,\end{aligned} \tag{4.7}$$

where the tortuosity $\alpha_\infty \geq 1$, and hence $\rho_{12} \leq 0$. Solid and fluid densities are denoted as ρ_s and ρ_f, respectively. The linear time-convolution operator b was formulated in the frequency domain as the viscous correction factor by Johnson *et al.* (1987), according to (cf. Eq. (4.15))

$$\hat{b}(\omega) = b_0(1 + \tfrac{1}{2}\mathrm{i}M\omega/\omega_c)^{\frac{1}{2}}, \tag{4.8}$$

where the viscous damping factor $b_0 = \phi^2\eta/k_0$ and $\mathrm{Re}(\hat{b}(\omega)) \geq 0$ for $\omega \geq 0$. Here, the dynamic fluid viscosity is denoted by η and k_0 represents the zero-frequency Darcy permeability. The shape factor M is usually taken equal to 1 (Smeulders *et al.*, 1992). The rollover frequency, which represents the transition from low-frequency viscosity-dominated to high-frequency inertia-dominated behavior, is defined as $\omega_c = \eta\phi/(\alpha_\infty\rho_f k_0)$.

The behavior of the upper (fluid) half-space ($x_3 < 0$) is governed by the acoustic wave equation

$$\rho_F\partial_t^2 p_F = K_F\nabla^2 p_F, \tag{4.9}$$

where K_F and ρ_F denote the bulk modulus and density of the fluid, respectively, and p_F denotes the fluid pressure.

We assume that the behavior at the interface is governed by conventional open-pore conditions, i.e., by continuity of volume flux and fluid pressure, and vanishing intergranular vertical and shear stresses. The force is applied to the solid. The open-pore boundary is a realistic choice to model the fluid/poroelastic-medium interface (Burns, 1990), and a limiting case of the situation where a finite surface flow impedance is considered; see e.g., Deresiewicz & Skalak (1963); Gurevich & Schoenberg (1999); Gubaidullin *et al.* (2004). It implies that the true interface wave is absent in the response (Feng & Johnson, 1983a,b). Hence, in the limit of $x_3 \to 0$ the following

conditions should be satisfied

$$(1-\phi)u_3 + \phi U_3 - U_{F,3} = 0, \tag{4.10}$$
$$p_f - p_F = 0, \tag{4.11}$$
$$\sigma_{13} = 0, \tag{4.12}$$
$$\sigma_{23} = 0, \tag{4.13}$$
$$\sigma_{33} = F(t)\delta(x_1)\delta(x_2), \tag{4.14}$$

where $\delta(...)$ denotes the Dirac delta function, and $U_{F,3}$ denotes the vertical particle displacement in the upper half-space. The fact that the intergranular stress σ_{33} is zero does not imply that the total solid stress τ_{33} vanishes; see Eq. (4.1).

The medium is considered to be at rest at $t \leq 0$. At infinite distance from the source the motions are bounded.

4.3 Green's functions

In this section we summarize the derivation of the Green's functions (impulse responses) as described by the solution to the set of governing equations Eqs. (4.5), (4.6) and (4.9)-(4.14). The main part of the derivation is given in Appendices A and B and we refer to them where necessary.

In order to analyze the response in the plane-wave domain, the Fourier transform is applied over time t according to

$$\hat{\mathbf{u}}(\mathbf{x},\omega) = \int_{-\infty}^{\infty} \mathbf{u}(\mathbf{x},t)\exp(-\mathrm{i}\omega t)\,dt, \tag{4.15}$$

where ω denotes the angular frequency and i the imaginary unit. Because $\mathbf{u}(\mathbf{x},t)$ is real-valued it is sufficient to consider $\omega \geq 0$ only. Following Aki & Richards (1980), the Fourier transform over horizontal spatial coordinates can be defined as,

$$\tilde{\mathbf{u}}(\mathbf{p}_r, x_3, \omega) = \int_{-\infty}^{\infty}\int_{-\infty}^{\infty} \hat{\mathbf{u}}(\mathbf{x},\omega)\exp(\mathrm{i}\omega\mathbf{p}_r\cdot\mathbf{r})\,dx_1dx_2, \tag{4.16}$$

where $\mathbf{p}_r = (p_1, p_2)^T$ is the horizontal slowness vector and $\mathbf{r} = (x_1, x_2)^T$ is the horizontal space vector. The transforms are applied similarly to the other field quantities. The hat refers to the $(\mathbf{x},\omega)$-domain and the tilde to the $(\mathbf{p}_r, x_3, \omega)$-domain.

The response in the $(\mathbf{p}_r, x_3, \omega)$-domain is described by the physical quantities $\tilde{u}_i$ and $\tilde{p}_f$ in the lower half-space, collected in the vector $\tilde{\mathbf{w}} = (\tilde{u}_1, \tilde{u}_2, \tilde{u}_3, -\phi\tilde{p}_f)^T$, and by $\tilde{p}_F$ in the upper half-space; see Eqs. (4.29), (4.32) and (4.34). The expressions for the response are obtained using Helmholtz decomposition of the equations of motion and substitution of the general solutions into the boundary conditions. This gives a set of equations that is solved analytically (see Appendix A).

The response can be written in terms of Green's functions according to

$$\tilde{\mathbf{w}} = \tilde{\mathbf{g}}^{+}\hat{F} = \frac{\tilde{\mathbf{n}}^{+}}{\Delta_{St}}\hat{F}, \tag{4.17}$$

$$\tilde{p}_F = \tilde{g}^{-}\hat{F} = \frac{\tilde{n}^{-}}{\Delta_{St}}\hat{F}, \tag{4.18}$$

where $\tilde{\mathbf{g}}^{+}$ and $\tilde{g}^{-}$ are the Green's functions in the lower and upper media, respectively, $\tilde{\mathbf{n}}^{+}$ and $\tilde{n}^{-}$ are the corresponding numerators, and $\hat{F}$ is the Fourier transform of the force signature. From Eqs. (4.29), (4.32) and (4.34) it follows that $\tilde{\mathbf{g}}^{+}$ consists of a superposition of all possible body modes: the fast (P_1) and slow (P_2) compressional waves, and the vertically-polarized shear (SV) wave. The horizontally-polarized shear (SH) mode is not excited by the vertical force. The Green's function $\tilde{g}^{-}$ only contains the fluid (F) compressional mode. Both Green's functions have the "Stoneley-wave denominator" $\Delta_{St} = \Delta_{St}(p_r, \omega)$ that is associated with interface waves along the fluid/poroelastic-medium interface, which is very similar to the "Scholte-wave denominator" for a fluid/elastic-solid interface (de Hoop & van der Hijden, 1983). Here, $p_r = (p_1^2 + p_2^2)^{\frac{1}{2}}$ denotes the magnitude of the horizontal slowness.

The body-wave slownesses s_α, $\alpha = \{P_1, P_2, F, S\}$, are defined in Appendix A (Table 4.3). The corresponding vertical slownesses are defined as $q_\alpha = (s_\alpha^2 - p_r^2)^{\frac{1}{2}}$, where $\mathrm{Im}(q_\alpha) \leq 0$ for real p_r due to Sommerfeld's radiation condition.

To find the Green's functions in the $(\mathbf{x}, \omega)$-domain, the inverse Fourier transform is applied according to

$$\hat{\mathbf{g}}^{+} = \frac{\omega^2}{(2\pi)^2}\int_{-\infty}^{\infty}\int_{-\infty}^{\infty}\frac{\tilde{\mathbf{n}}^{+}(\mathbf{p}_r, x_3, \omega)}{\Delta_{St}}\exp(-\mathrm{i}\omega\mathbf{p}_r\cdot\mathbf{r})\,dp_1 dp_2, \tag{4.19}$$

where $\omega \geq 0$ and where we include the argument of $\tilde{\mathbf{n}}^{+}$ in view of the involved derivative operator (see below). We only show the derivation of $\hat{\mathbf{g}}^{+}$, but the expression for $\hat{g}^{-}$ is obtained by simply replacing $\tilde{\mathbf{n}}^{+}$ by $\tilde{n}^{-}$. When cylindrical coordinates are introduced, Eq. (4.19) can be written as

$$\hat{\mathbf{g}}^{+} = \frac{\omega^2}{4\pi}\int_{-\infty}^{\infty}\frac{\tilde{\mathbf{n}}^{+}(p_r, \partial_h, x_3, \omega)}{\Delta_{St}}H_0^{(2)}(\omega p_r r)p_r\,dp_r, \tag{4.20}$$

where $r = (x_1^2 + x_2^2)^{\frac{1}{2}}$ and in which the horizontal derivatives ∂_h, $h = \{1, 2\}$, are applied to the Hankel function $H_0^{(2)}(...)$; see Eqs. (4.39) and (4.40) (Appendix B).

Now we change the real-axis integral into a contour integral in the complex p_r-plane. The idea is that by integration in the complex plane, contributions from loop integrals and from pole residues can be distinguished. We choose branch cuts along the hyperbolic lines $\mathrm{Im}(q_\alpha) = 0$ (Ewing *et al.*, 1957). In this way $\mathrm{Im}(q_\alpha) \leq 0\ \forall\ p_r$, which ensures the decay of the exponential terms $\exp(\mp\mathrm{i}\omega q_\alpha x_3)$ for large $|p_r|$ (see Eqs. (4.29) and (4.32)). The branch cuts depart from the branch points associated with the body-wave slownesses s_α, as shown in Figure 4.2. The q_F-branch cut reduces to the imaginary axis and part of the real axis since the slowness of the fluid wave (s_F) is real.

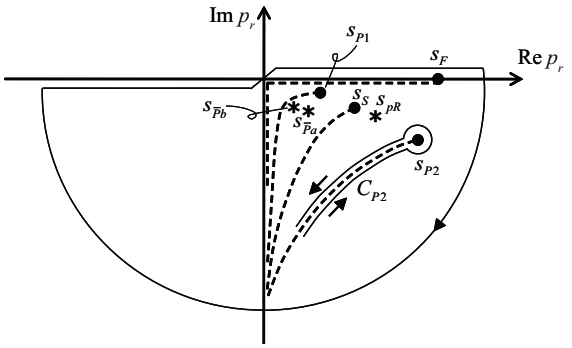

Figure 4.2: Complex p_r-plane with $(--)$ branch cuts, $(\bullet)$ branch points s_α, $\alpha = \{P_1, P_2, F, S\}$, and $(*)$ poles s_{pR} (pseudo-Rayleigh), $s_{\bar{P}a}$ and $s_{\bar{P}b}$ (additional), for the calculation of the Green's functions for Bentheimer/air configuration 2 (see Table 4.1). The branch points are formed by the body-wave slownesses specified in Appendix A (Table 4.3). The hyperbolic branch cuts are described by $\mathrm{Im}(q_\alpha) = 0$. Poles are zeroes of the poroelastic Stoneley denominator; see Eq. (4.21). Only part of the closed integration contour $(-)$ is displayed: real axis, arc in lower half-plane and loop C_{P2} along the q_{P2}-branch cut. The direction of integration is indicated.

The current branch cuts are referred to as the "fundamental" branch cuts (Attenborough *et al.*, 1980). The corresponding Riemann sheet is referred to as the "principal" Riemann sheet (van der Hijden, 1984), or the "physical" Riemann sheet (Aki & Richards, 1980).

In Figure 4.2 the closed contour is also displayed. It is formed by the entire real axis, the loops along the branch cuts and around the branch points, and an arc of infinite radius in the lower half-plane. For $\mathrm{Re}(p_r) \leq 0$ the horizontal part of the contour lies just below the axis due to the presence of a branch cut of the Hankel function at the negative real axis (Abramowitz & Stegun, 1972).

Applying Cauchy's Residue Theorem (Fuchs *et al.*, 1964), we obtain

$$\hat{\mathbf{g}}^+ = \int_{-\infty}^{\infty} \tilde{\mathbf{f}}^+ \, dp_r = -2\pi\mathrm{i} \sum_\beta \mathrm{Res}_{p_r = s_\beta} \tilde{\mathbf{f}}^+ - \sum_\alpha \int_{C_\alpha} \tilde{\mathbf{f}}^+ \, dp_r, \tag{4.21}$$

$$\tilde{\mathbf{f}}^+ = \frac{\omega^2}{4\pi} \frac{\tilde{\mathbf{n}}^+(p_r, \partial_h, x_3, \omega)}{\Delta_{St}} H_0^{(2)}(\omega p_r r) p_r,$$

where every s_β denotes a first-order pole of the integrand inside the integration contour and every C_α denotes a loop along the specific branch cut. In Eq. (4.21), the contribution of the arc vanishes because of Jordan's lemma (Achenbach, 1973). The contributions around the branch points are also zero.

The poles s_β result from zeroes of the poroelastic Stoneley dispersion equation ($\Delta_{St} = 0$) on the principal Riemann sheet. The number of poles N present inside contour C is determined by applying the Principle of the Argument to the Stoneley equation (Fuchs *et al.*, 1964)

$$N = \frac{1}{2\pi\mathrm{i}} \oint_C \frac{\partial_{p_r} \Delta_{St}}{\Delta_{St}} \, dp_r. \tag{4.22}$$

Table 4.1: Various configurations for which the transient response is calculated. The type of sandstone is Bentheimer. For fused glass beads, the bulk modulus of the drained matrix is chosen as $K_b = 10$ GPa and the permeability as $k_0 = 10^{-11}$ m^2. The upper half-space is filled with either water ($K_F = K_f$, $\rho_F = \rho_f$), or air ($K_F = 1.42 \cdot 10^2$ kPa, $\rho_F = 1.25$ kgm^{-3}) or a light fluid ($K_F = K_f/10$, $\rho_F = \rho_f/8$). For every configuration the pole(s) present on the principal Riemann sheet are indicated: pseudo-Stoneley (pSt), pseudo-Rayleigh (pR) and two additional ($\bar{P}_a$, $\bar{P}_b$) poles.

	Porous solid	Saturating fluid	Upper half-space	Pole(s)
1	Sandstone	water	water	pSt
2	Sandstone	water	air	$\bar{P}_a$, $\bar{P}_b$,[iii] pR
3	Sandstone	water	light fluid	pR, pSt[iii]
4	Fused glass beads	water	water	pSt[iii]

The residue of the integrand at a first-order pole is given as

$$\mathrm{Res}_{p_r=s_\beta}\tilde{\mathbf{f}}^+ = \left[\frac{\omega^2}{4\pi}\frac{\tilde{\mathbf{n}}^+(p_r,\partial_h,x_3,\omega)}{\partial_{p_r}\Delta_{St}}H_0^{(2)}(\omega p_r r)p_r\right]_{p_r=s_\beta}. \tag{4.23}$$

4.4 Numerical implementation

To perform the integration along the hyperbolic branch cuts we choose $p_{r,im} = \mathrm{Im}(p_r)$ as the variable of integration according to

$$\int_{C_\alpha}\tilde{\mathbf{f}}^+\frac{\partial p_r}{\partial p_{r,im}}\,dp_{r,im}, \tag{4.24}$$

where

$$p_r = \frac{\mathrm{Re}(s_\alpha)\mathrm{Im}(s_\alpha)}{p_{r,im}} + \mathrm{i}p_{r,im}, \qquad \frac{\partial p_r}{\partial p_{r,im}} = -\frac{\mathrm{Re}(s_\alpha)\mathrm{Im}(s_\alpha)}{p_{r,im}^2} + \mathrm{i}. \tag{4.25}$$

For the q_F-branch cut, the integration path is the imaginary axis and part of the real axis, which follows from Eq. (4.25) for vanishing imaginary part of the slowness $\mathrm{Im}(s_F) \uparrow 0$ (Figure 4.2). Along the cut of q_α, at the left side $\mathrm{Re}(q_\alpha) > 0$ and at the right side $\mathrm{Re}(q_\alpha) < 0$. At the specific cut $\mathrm{Im}(q_\alpha) = 0$ and everywhere else $\mathrm{Im}(q_\alpha) < 0$.

The numerical integration is performed using an adaptive 8-point Legendre-Gauss algorithm (Abramowitz & Stegun, 1972; Davis & Rabinowitz, 1975), which can handle integrable singularities such as branch points.

For the numerical implementation of the Principle of the Argument, we apply Eq. (4.22) separately for the areas between the various parts of the integration contour (branch cuts, real axis, arc; cf. Figure 4.2) to find out where the poles can be expected. Subsequently, the pole locations are found numerically by minimizing

[iii] Its residue is not shown.

the left-hand side of equation $|\Delta_{St}|= 0$. Since it contains local minima and branch-cut discontinuities, it is important to choose a proper starting value. This requires some manual iteration. The accuracy, as expressed by $|\Delta_{St}(p_r = s_\beta)|/|\Delta_{St}(p_r = 0)|$, is typically $\mathcal{O}(10^{-10})$. Here, s_β denotes the numerical value of the pole location.

4.5 Numerical results and discussion

In this section, we investigate the transient responses for four different fluid/poro–elastic-medium configurations (see Table 4.1). In the first three configurations water-saturated Bentheimer sandstone (see Table 4.2) is used as porous medium. The upper half-space is subsequently filled with water, air or a light fluid. In the fourth configuration, which is the one of Feng & Johnson (1983a,b) the porous medium is formed by water-saturated fused glass beads while the upper half-space is filled with water.

For every configuration, we will show the vertical component of particle velocity v_3 and the fluid pressure p_f for an observation point at the interface $x_3 = 0$ at offset $r = x_1 = 0.1$ m. Fluid pressure is related to dilatation only (see Eq. (4.4)) and hence, v_3 and p_f contain different information. Also, the comparison between the full response and a pole residue can be different in v_3 and p_f, as will be shown.

The point force has Ricker signature (Ricker, 1953).

$$F(t) = F_{max}\left(\tfrac{1}{2}\omega_0^2\bar{t}^2 - 1\right)\exp\left(-\tfrac{1}{4}\omega_0^2\bar{t}^2\right), \tag{4.26}$$

where $\bar{t} = t - t_s$ $(t > 0)$, $\omega_0 = 2\pi f_0$ and centre frequency $f_0 = 500$ kHz (see Figure 4.3). The magnitude[iv] $F_{max} = 2.5 \cdot 10^{-7}$ N and time shift $t_s = 5$ μs. We have performed the integration for the frequency range $0 < f \leq 2$ MHz. The full responses have been obtained by multiplication of the spectra of the Green's functions and the source (see Eqs. (4.17) and (4.18)), and using a standard fast Fourier-transform algorithm.

4.5.1 Residue contribution vs full response

First, we address the relation between a pole and a pseudo interface wave, as raised in point (1) in the Introduction (Section 4.1). For configurations 1-3 the full transient responses and separate pole residues (see Eq. (4.21)) are displayed in Figures 4.3-4.5. We have identified the different arrivals in the full responses using the propagation velocities as obtained from the modal slownesses.[v] Head waves have been identified

[iv] Corrected for a typo in the value of F_{max} given in van Dalen *et al.* (2010b).

[v] Here, we have taken a representative frequency to calculate the pertaining velocities. Regarding a body wavemode, the phase velocity (being the inverse of the real part of the slowness) is a proper measure for the propagation velocity because the phase velocity and energy velocity coincide; see Section 3.4. To our knowledge, the problem of energy propagation associated with a pseudo interface wavemode has not yet been considered in the literature. Hence, in this thesis we also take the phase velocity as the propagation velocity of a pseudo interface wavemode, where the former is calculated from the associated pole location. For completeness we note that, in fact, here the poles as found using vertical branch cuts should be taken (method I: cf. Sections 5.3 and 5.4.3), which can have slightly different locations compared to the poles found using the current branch cuts (Section 5.5.1).

Table 4.2: Material parameters as used for water-saturated Bentheimer sandstone (Wisse, 1999). The bulk modulus of the matrix K_b is found according to $K_b = K_p - \frac{4}{3}G$.

Solid (frame) density ρ_s [kgm^{-3}]	2630
Fluid density ρ_f [kgm^{-3}]	1000
Tortuosity α_∞	2.4
Porosity ϕ	0.23
Permeability k_0 [μm^2]	3.7
Dynamic fluid viscosity η [Pa·s]	0.001
Shear modulus G [GPa]	6.8
Constrained modulus K_p [GPa]	14
Grain bulk modulus K_s [GPa]	36.5
Fluid bulk modulus K_f [GPa]	2.22

geometrically using the pertaining modal velocities, and are indicated with double-mode symbols (e.g., SP_1: the shear (S) wave radiated by the fast (P_1) compressional wave). For the sake of clarity, a schematic snapshot of the full response with the different arrivals is shown in Figure 4.1b.

We first note that the P_1-wave is present quite strongly in v_3 although this component is perpendicular to the direction of propagation of this longitudinal wave (Figures 4.4 and 4.5). This is due to the contraction in vertical direction that can easily take place at the air/sandstone or light-fluid/sandstone interface. Remarkably, there is an arrival present in p_f at the S-wave arrival time (Figures 4.4 and 4.5). This is not an S-wavefront but radiated slow compressional (P_2) and fluid (F) head waves; cf. Figure 4.1b.

Now, we focus on the comparison of interface waves in the full responses and corresponding pole residues. The pole(s) that are present on the principal Riemann sheet that contribute a residue are given in Table 4.1, for each configuration separately. We have found the pseudo-Stoneley (pSt), the pseudo-Rayleigh (pR) and two additional ($\bar{P}_a$, $\bar{P}_b$) poles. The latter ones are discussed in Section 4.5.3.

For configuration 1 (water as upper fluid), only the pSt-pole is found on the principal Riemann sheet. From Figure 4.3 we observe that its residue yields the entire pSt-waveform. For configuration 2 (air as upper fluid), the pR-pole is found on the principal Riemann sheet. From Figure 4.4 it is observed that its residue coincides with the pR-waveform in the full response of v_3 (actually, the difference is non-zero but too small to be observed). However, it does not coincide with that in the full response of p_f. Its contribution is opposite, which means that the loop integrals along the branch cuts also contribute to the pseudo interface waveform. This has also been found by Allard *et al.* (2004). It implies that part of the pertinent physical properties of the pseudo interface wave is captured by the loop integrals. This is more pronounced for configuration 3 (light upper fluid), as shown in Figure 4.5, in which both the pR-pole and the pSt-pole are found on the principal Riemann sheet. In both components (v_3 and p_f) the pR-pole residue does not coincide with the pR-waveform in the full response. The pSt-pole residue is not displayed separately because the pSt-wave strongly interferes with the F-wave.

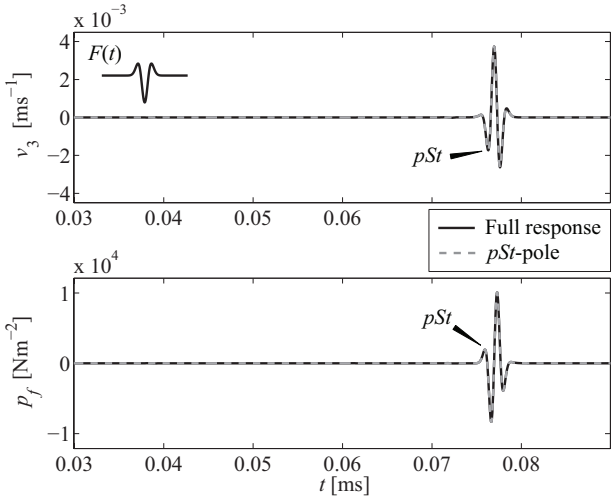

Figure 4.3: Full response and pSt-pole residue at $x_2 = x_3 = 0$ and offset $x_1 = 0.10$ m for Bentheimer/water configuration 1. The pSt-pole residue coincides with the pSt-waveform in the full response. Other wavemodes are too weak to be observed in this figure. The source signature $F(t)$ is also displayed.

To investigate how the residues and the interface waveforms in the full responses compare for an observation point that lies off the interface, we have calculated the

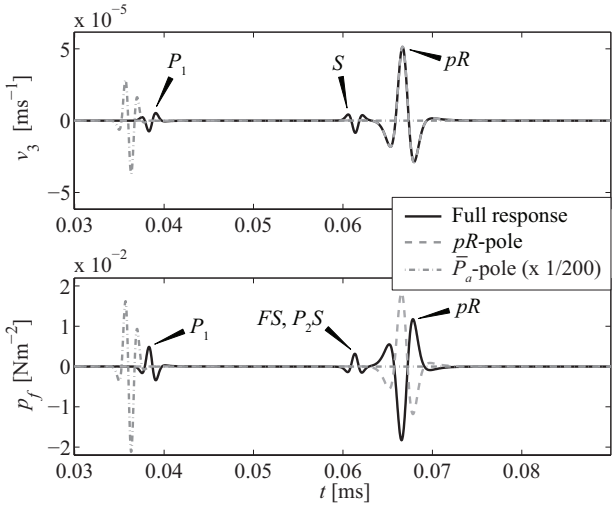

Figure 4.4: Full response and residues of pR-pole and $\bar{P}_a$-pole at $x_2 = x_3 = 0$ and offset $x_1 = 0.10$ m for Bentheimer/air configuration 2. The $\bar{P}_a$-pole residue has been scaled down by a factor 200 to make it entirely visible. The pR-pole residue coincides with the pR-waveform in the full response of v_3.

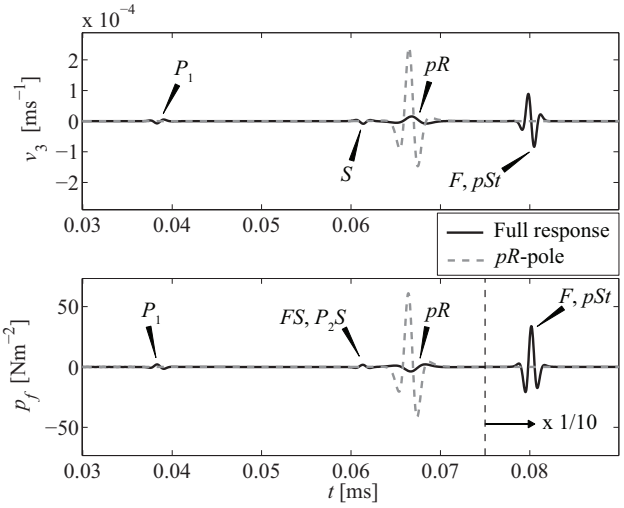

Figure 4.5: Full response and pR-pole residue at $x_2 = x_3 = 0$ and offset $x_1 = 0.10$ m for Bentheimer/light-fluid configuration 3. From the dashed vertical line onwards, the response p_f has been scaled down by a factor 10 to make it entirely visible.

responses for configurations 1-3 at $x_3 = 0.01$ m and offset $r = x_1 = 0.1$ m. The corresponding results are displayed in Figures 4.6-4.8. Compared to the previous responses at $x_3 = 0$, various head waves can now be distinguished as separate arri-

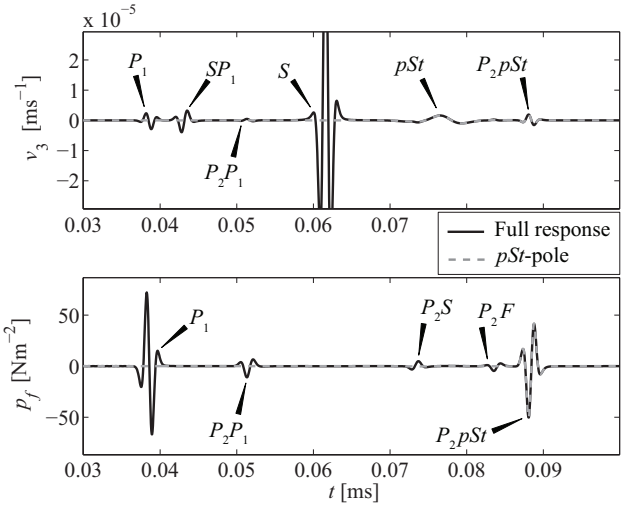

Figure 4.6: Full response and pSt-pole residue at $x_2 = 0$, $x_3 = 0.01$ m, and offset $x_1 = 0.10$ m for Bentheimer/water configuration 1. The pSt-pole residue coincides with the pSt- and P_2pSt-waveforms in the full response.

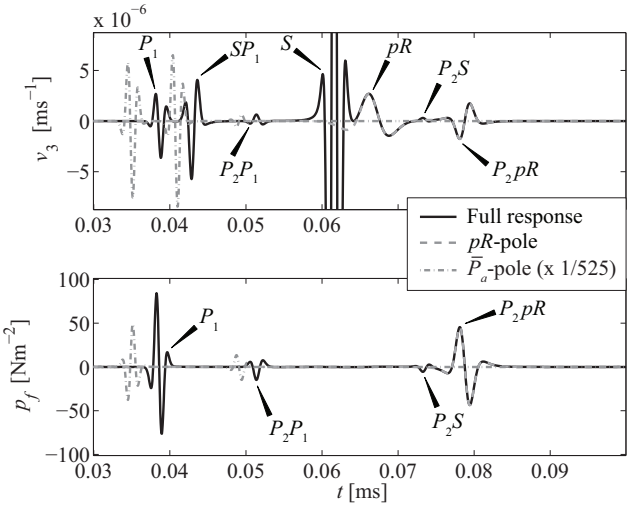

Figure 4.7: Full response and residues of pR-pole and $\bar{P}_a$-pole at $x_2 = 0$, $x_3 = 0.01$ m, and offset $x_1 = 0.10$ m for Bentheimer/air configuration 2. The pR-pole residue coincides with the pR- and the P_2pR-waveforms in the full response. The $\bar{P}_a$-pole residue has been scaled down by a factor 525 to make it entirely visible.

vals, generated by the body wavefronts that propagate along the interface; cf. Figure 4.1b. From Figures 4.6-4.8 we also observe that the residues now yield two waveforms in the full responses. The first one (pR or pSt) is the waveform of the specific

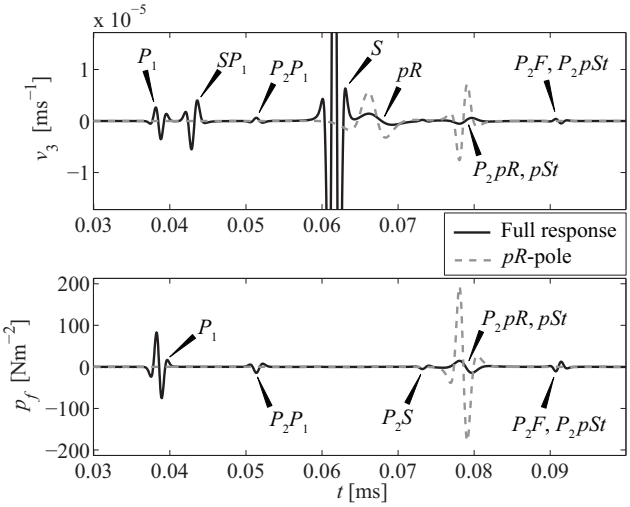

Figure 4.8: Full response and pR-pole residue at $x_2 = 0$, $x_3 = 0.01$ m, and offset $x_1 = 0.10$ m for Bentheimer/light-fluid configuration 3.

interface wave itself while the second (P_2pR or P_2pSt) corresponds to the P_2-mode that is radiated by the propagating pseudo interface wave. For configurations 1 (water as upper fluid, Figure 4.6) and 2 (air as upper fluid, Figure 4.7), it is observed that both waveforms are now captured entirely by the residue of the corresponding pole. For configuration 3 (light upper fluid, Figure 4.8) this is not the case, as for $x_3 = 0$.

In addition to the observations on responses with entire waveforms, we give attention to the characteristics of a pseudo interface wave. With regard to the propagation velocity, we observe that it is predicted properly by the residue of the corresponding pole for all presented numerical results. Concerning the attenuation, it has been proposed by van der Hijden (1984) to quantify the true attenuation of a pseudo interface wave on the basis of the full transient response. This has been done by Rosenbaum (1974), but he has only shown the decay of the total waveform, which would result in one value for the attenuation. This is quite restrictive and therefore we use the following method to retrieve the frequency-dependent attenuation from a windowed pseudo interface waveform in the full response. Here, attenuation is defined by $\mathrm{Im}(s_\beta^{tr})$, where s_β^{tr} represents the true wave slowness and $\beta = \{pR, pSt\}$. As a starting point, we consider the pseudo interface wave in the far field where it does not interfere with other wavemodes, and we assume that it is described by

$$\hat{v}_{\beta,3}(r) \propto r^{-\frac{1}{2}} \exp(-\mathrm{i}\omega s_\beta^{tr} r), \tag{4.27}$$

which is found from the asymptotic behavior of the Hankel function (Abramowitz & Stegun, 1972). The imaginary part of the wave slowness can be retrieved by comparing the amplitude spectra of the windowed waveform $|\hat{v}_{\beta,3}(r)|$ at two different observation points $r = r_a$ and $r = r_b$, according to

$$\mathrm{Im}\left(s_\beta^{tr}(f)\right) = \frac{1}{2\pi f(r_b - r_a)} \ln\left(\frac{r_b^{\frac{1}{2}}|\hat{v}_{\beta,3}(r_b)|}{r_a^{\frac{1}{2}}|\hat{v}_{\beta,3}(r_a)|}\right). \tag{4.28}$$

For configurations 1 (water as upper fluid) and 3 (light upper fluid), the attenuations are displayed in Figures 4.9 and 4.10, respectively, together with the corresponding predictions obtained from the poles $p_r = s_\beta$. The limited frequency range is due to the limited bandwidth of the retrieved spectra. For configuration 1 (water as upper fluid) we observe that the attenuation is described very well by the pSt-pole, except for the low frequencies where the far-field approximation of the Hankel function in Eq. (4.27) is not valid. For configuration 3 (light upper fluid), however, the true attenuation of the pR-wave is much greater than the value obtained from the pR-pole residue. Obviously, the loop integrals along the branch cuts can not only affect the waveform but also the spatial decay of a pseudo interface wave.

Sometimes, a residue of a pole is (implicitly) considered to represent the corresponding interface-wave part of the spectrum of the Green's function (see e.g., Feng & Johnson (1983a); Edelman & Wilmanski (2002); Gubaidullin *et al.* (2004); Albers (2006); Markov (2009)) while the loop integrals are considered to constitute the part related to body waves and head waves (if present). This can be true but we emphasize that the choice of branch cuts is not unique. Therefore, the integration can

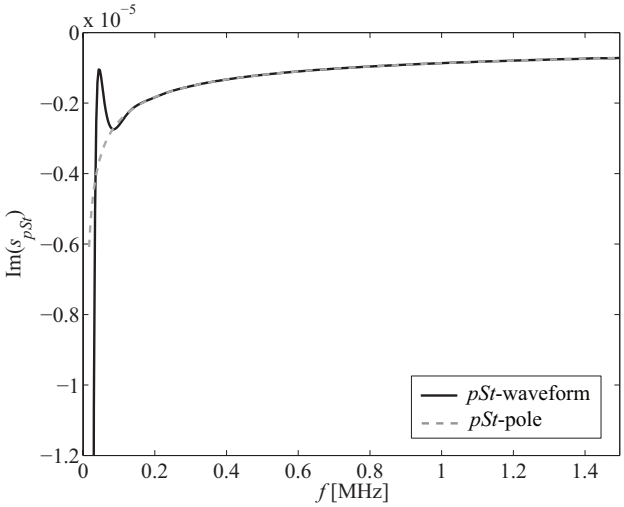

Figure 4.9: True attenuation, defined as $\mathrm{Im}(s^{tr}_{pSt})$, retrieved from windowed pSt-waveforms for Bentheimer/water configuration 1, at $x_2 = x_3 = 0$ and from offsets $x_1 = 0.24 - 0.26$ m. The attenuation $\mathrm{Im}(s_{pSt})$ obtained from the corresponding pole residue is also displayed.

be performed on another physically allowed Riemann sheet, i.e., a Riemann sheet that also meets the requirement of $\mathrm{Im}(q_\alpha) \leq 0$ for real p_r (Viktorov, 1967; Aki & Richards, 1980), which is the original path of integration (see Eq. (4.20)). This has been done by Tsang (1978) and Allard *et al.* (2004), and has been clarified by Harris & Achenbach (2002). Then, the construction of the $(\mathbf{x}, \omega)$-domain Green's function is different as other poles have to be taken into account and different loop integrals are to be evaluated. Therefore, it might very well be that (part of) the pertinent physical properties of a true or pseudo interface wave are captured by the integrals along the closed contour, rather than by the residue of a specific pole (alone).

From the current observations, we conclude that a residue of a pole on the principal Riemann sheet does not necessarily yield all the pertinent physical properties of the corresponding pseudo interface wave.

4.5.2 Presence of pR-pole and pSt-pole on Riemann sheets

Now we address the issue concerning the origin of a pseudo interface wave, as raised in point (2) of the Introduction (Section 4.1). In the computations in the previous subsection, we have already found that a pole related to a pseudo interface wave can be located on the principal Riemann sheet and, obviously, contribute a residue to the full response (see Table 4.1). This contradicts the conventional explanation that a pseudo interface wave originates from a pole on a different Riemann sheet, and is accounted for only by the loop integrals along branch cuts by causing a local maximum in the integrand. Allard *et al.* (2004) have already found this contradiction, but they have not referred to this as such because their concern was to determine

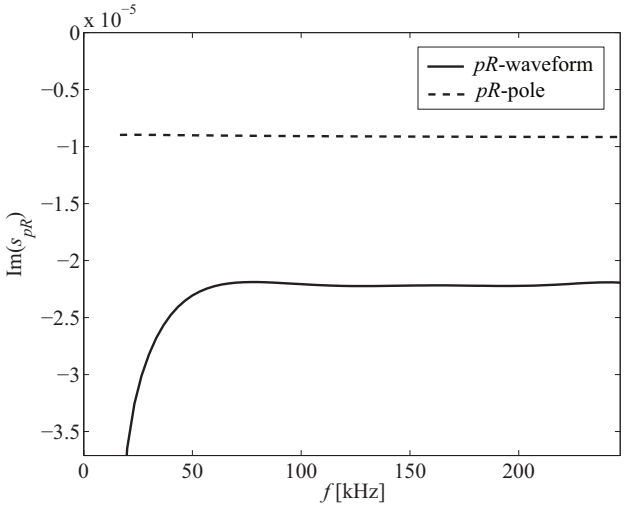

Figure 4.10: True attenuation, defined as $\mathrm{Im}(s_{pR}^{tr})$, retrieved from windowed pR-waveforms for Bentheimer/light-fluid configuration 3, at $x_2 = x_3 = 0$ and from offsets $x_1 = 0.24 - 0.26$ m. The attenuation $\mathrm{Im}(s_{pR})$ obtained from the corresponding pole is also displayed.

whether or not a pole is related to a separate arrival in the full response.

Surprisingly, in case of fused glass beads saturated with water and covered with water (configuration 4, Figure 4.11) the pSt-pole is present on the principal Riemann sheet only for a limited frequency range. In Figure 4.12 the position of the pole in the complex plane is given, as expressed by $\mathrm{Im}(s_{pSt})$. Also the position of the q_{P2}-branch cut is displayed, as expressed by its imaginary part at $\mathrm{Re}(p_r) = \mathrm{Re}(s_{pSt})$. As frequency increases, the pSt-pole moves towards the branch cut and as soon as it reaches the cut, it vanishes from the sheet. The pole is not present on the principal sheet for 310 kHz $\leq f \leq$ 2 MHz. Therefore, the residue of the pSt-pole is not shown in Figure 4.11. For the material properties used by Gubaidullin *et al.* (2004), exactly the same situation occurs, although the transition takes place at a different frequency. Obviously, the presence of a pole on a certain Riemann sheet is not only a matter of the contrast in material parameters of the half-spaces (Scholte, 1947), but can also depend on frequency in case of viscous poroelastic media.

The behavior of the pSt-pole illustrates both the non-conventional and the conventional explanation about the origin of a pseudo interface wave. The pole does contribute a residue over a certain frequency range and not outside that specific range. For the pR-wave present in the full response of configuration 4 (Figure 4.11) only the conventional explanation holds as the pR-pole is not found on the principal Riemann sheet and the entire waveform is captured by the loop integrals.

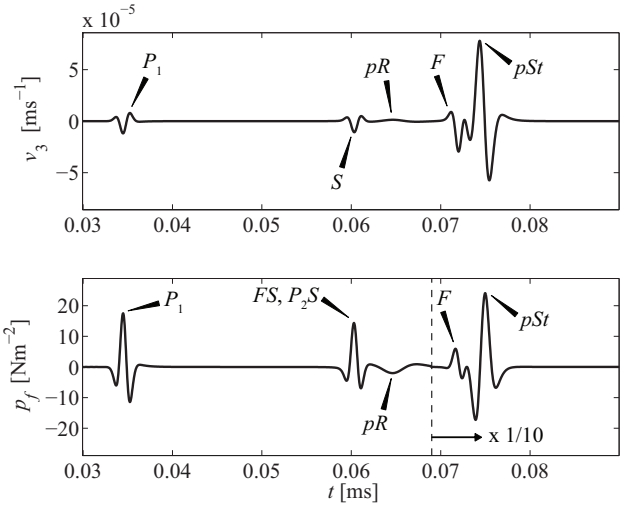

Figure 4.11: Full response at $x_2 = x_3 = 0$ and offset $x_1 = 0.10$ m for fused glass beads/water configuration 4. From the dashed vertical line onwards, the response p_f has been scaled down by a factor 10 to make it entirely visible.

4.5.3 Physical significance of additional poles

Finally, we give attention to the physical significance of two additional zeroes of the poroelastic Stoneley dispersion equation ($\Delta_{St} = 0$) as raised in point (3) of the Introduction (Section 4.1). In configuration 2 (air as upper fluid), these zeroes show up as poles on the principal Riemann sheet at $p_r = s_{\bar{P}a}$ and $p_r = s_{\bar{P}b}$. They are located to the left of the fast compressional-wave slowness ($\mathrm{Re}(s_{\bar{P}a,\bar{P}b}) < \mathrm{Re}(s_{P1})$) close to the q_{P1}-branch cut (see Figure 4.2; $p_r = s_{\bar{P}a}$ signifies the pole that lies the closest to $p_r = s_{P1}$). The additional ($\bar{P}_a$, $\bar{P}_b$) poles are comparable with the so-called "$\bar{P}$-poles" that occur in non-porous elastic solids with an interface, as described by Gilbert & Laster (1962) and Aki & Richards (1980). The scaled real and imaginary parts of the poles are displayed in Figure 4.13. The $\bar{P}_b$-pole is only present on the principal Riemann sheet for limited frequency range 818.75 kHz $\leq f \leq$ 2 MHz.

Allard *et al.* (2002) have also found one of the poles and have referred to it as an improper surface mode. Feng & Johnson (1983a) have stated that poles located to the left of shear-wave branch point ($\mathrm{Re}(p_r) < \mathrm{Re}(s_S)$) have lost all physical significance as pseudo interface modes. In the latter paper, the authors consider pseudo interface modes in the conventional way. In their configuration, the additional poles might indeed lie on a different Riemann sheet, but we find that they can also show up on the principal Riemann sheet. From Figure 4.4 we observe that the $\bar{P}_a$-pole has a substantial residue contribution to the full response, although it does not correspond to an interface wavemode ($\bar{P}_b$-pole similarly). Any pole that contributes to the full response should be considered as physically significant.

Gilbert & Laster (1962) and Aki & Richards (1980) have related the $\bar{P}$-poles in elastic solids to a separate arrival. However, van der Hijden (1984) has stated that

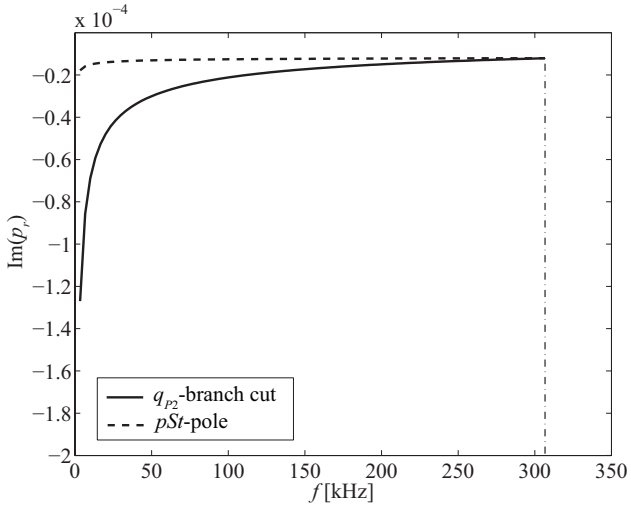

Figure 4.12: The pSt-pole location in the complex p_r-plane, expressed by $\mathrm{Im}(p_r) = \mathrm{Im}(s_{pSt})$, with respect to the q_{P2}-branch cut location at $\mathrm{Re}(p_r) = \mathrm{Re}(s_{pSt})$, expressed by $\mathrm{Im}(p_r) = \mathrm{Re}(s_{P2})\mathrm{Im}(s_{P2})/\mathrm{Re}(s_{pSt})$, for configuration 4. The $(-\cdot)$ line indicates the intersection point of both lines.

the concept of a separate pulse should be dismissed because it is just a peculiar tail to the compressional head-wave arrival. Harris & Achenbach (2002) have confirmed this by stating that the poles yield features of the lateral waves. The observations in the current computations for poroelastic media also confirm this. From Figure 4.7 we observe that the $\bar{P}_a$-pole contributes to the head waves generated by the P_1-wavefront. It also contributes to the P_1-wavefront itself because it yields a strong pulse that arrives even earlier (Figures 4.4 and 4.7), which is obviously explained by the pole lying to the left of the compressional-wave slowness. The same is true for the $\bar{P}_b$-pole. The early-arriving parts are not present in the full responses and hence, the P_1-waveform is constituted by both the residues of the $\bar{P}$-poles and the loop integrals along the branch cuts. The fact that a pole contributes to the P_1-waveform illustrates that it lies in the vicinity of the saddle point of the body wave, as used in asymptotic ray theory (van der Waerden, 1952; Tsang, 1978).

There is one remarkable difference between the $\bar{P}$-poles in elastic and the ones in poroelastic media. In the former, the poles never show up on the principal Riemann sheet (Aki & Richards, 1980) while this is possible for the latter. A similarity lies in the fact that in elastic solids (with rather small values of Poisson's ratio) the poles lie also to the left of the compressional-wave slowness (Tsang, 1978).

4.6 Conclusions

In this chapter we analyzed the three-dimensional transient response of a fluid/poro–elastic-medium configuration that is subjected to a vertical point force at the inter-

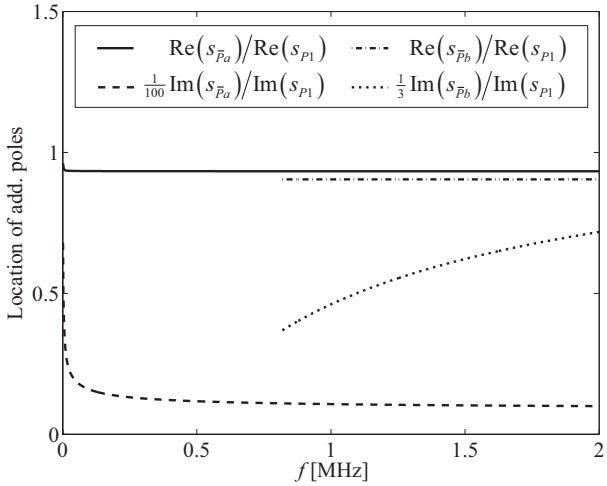

Figure 4.13: The location of the additional poles $p_r = s_{\bar{P}a}$ and $p_r = s_{\bar{P}b}$ in the complex p_r-plane with respect to the P_1-wave slowness s_{P1}. The $\bar{P}_b$-pole is only present on the principal Riemann sheet for limited frequency range 818.75 kHz $\leq f \leq$ 2 MHz.

face. For different materials, we quantitatively compared the full transient response with the residue contributions of pole singularities present on the so-called "principal" or "physical" Riemann sheet of integration. The poles are formed by zeroes of the poroelastic Stoneley dispersion equation, i.e., the pseudo-Rayleigh (pR) pole and the pseudo-Stoneley (pSt) pole.

We found that the residues of these poles do not necessarily contain all pertinent physical properties of the corresponding pseudo interface waves. Part of them can be captured by the loop integrals along the branch cuts. Therefore, it can be erroneous to use only the location of a zero of the Stoneley dispersion equation on the principal Riemann sheet, to predict the entire waveform, the propagation velocity and attenuation of the corresponding pseudo interface wave.

According to the generally accepted explanation about the origin of a pseudo interface wave, it originates from a pole that lies on a non-principal Riemann sheet. The influence of the pole is only indirect in the sense that it causes a local maximum in the integrand of the Green's function when its location is close to the real axis. We found, however, that this conventional explanation is not necessarily confirmed in the context of Biot's theory for poroelasticity. The poles can show up on the principal Riemann sheet. For the pSt-pole, we even showed that its presence on the principal Riemann sheet is not only determined by the contrast in the material properties, but also by frequency.

Finally, we found that two additional zeroes of the poroelastic Stoneley dispersion equation do have physical significance due to their residue contributions to the fast compressional wavefront, and to the head waves that are radiated by this wavefront. In the literature the additional poles are, however, referred to as non-physical because they are not related to pseudo interface waves. The poles are comparable with the

Table 4.3: Symbols used in Appendix A. The various indices are defined as: $\alpha = \{P_1, P_2, F, S\}$; $\chi = \{P_1, P_2, S\}$; $\kappa = \{P_1, P_2\}$.

$\hat{\rho}_{11}$	=	$\rho_{11} - \mathrm{i}\hat{b}/\omega$
$\hat{\rho}_{22}$	=	$\rho_{22} - \mathrm{i}\hat{b}/\omega$
$\hat{\rho}_{12}$	=	$\rho_{12} + \mathrm{i}\hat{b}/\omega$
d_0	=	$\hat{\rho}_{11}\hat{\rho}_{22} - \hat{\rho}_{12}^2$
d_1	=	$-(R\hat{\rho}_{11} + P\hat{\rho}_{22} - 2Q\hat{\rho}_{12})$
d_2	=	$PR - Q^2$
s_κ^2	=	$(-d_1 \mp (d_1^2 - 4d_0d_2)^{\frac{1}{2}})/(2d_2)$, $\mathrm{Im}(s_k) \leq 0$ for $\omega \geq 0$
s_S^2	=	$d_0/(G\hat{\rho}_{22})$, $\mathrm{Im}(s_S) \leq 0$ for $\omega \geq 0$
s_F^2	=	ρ_F/K_F
p_r	=	$(p_1^2 + p_2^2)^{\frac{1}{2}} \geq 0$
q_α	=	$(s_\alpha^2 - p_r^2)^{\frac{1}{2}}$, $\mathrm{Im}(q_\alpha) \leq 0$ for real p_r
β_κ	=	$-(\hat{\rho}_{11} - Ps_\kappa^2)/(\hat{\rho}_{12} - Qs_\kappa^2)$
β_S	=	$-\hat{\rho}_{12}/\hat{\rho}_{22}$
A'	=	$A - (1-\phi)Q/\phi$
Q'	=	$Q - (1-\phi)R/\phi$
H_κ	=	$Q + R\beta_\kappa$
K_κ	=	$A' + Q'\beta_\kappa + 2G$
ϕ_χ	=	$1 - \phi + \phi\beta_\chi$
Δ_1	=	$s_{P2}^2 H_{P2} - s_{P1}^2 H_{P1}$
Δ_2	=	$q_{P1}s_{P2}^2 H_{P2} - q_{P2}s_{P1}^2 H_{P1}$
Δ_3	=	$-4p_r^4\phi\hat{\rho}_{22}^{-1}(q_{P1}s_{P1}^2 H_{P1} - q_{P2}s_{P2}^2 H_{P2}) + 4p_r^2 q_S q_{P1} q_{P2}\phi\hat{\rho}_{22}^{-1}\Delta_1$
		$+2p_r^2 s_S^2(q_{P1}(\phi_{P1} + \phi d_2^{-1}H_{P1}K_{P2}) - q_{P2}(\phi_{P2} + \phi d_2^{-1}H_{P2}K_{P1}))$
		$-s_S^2 G^{-1}(q_{P1}\phi_{P1}s_{P2}^2 K_{P2} - q_{P2}\phi_{P2}s_{P1}^2 K_{P1})$

"$\bar{P}$-poles" known in non-porous elastic solids; see Gilbert & Laster (1962) and Aki & Richards (1980). Depending on the specific material parameters and frequency, they can be present on the principal Riemann sheet or on another one.

4.7 Appendix A: Transform-domain response

In this Appendix we derive the $(\mathbf{p}_r, x_3, \omega)$-domain solution to Eqs. (4.5), (4.6) and (4.9)-(4.14). Many of the involved symbols are explained in Table 4.3.

The general solution to the acoustic wave equation (Eq. (4.9)) in the $(\mathbf{p}_r, x_3, \omega)$-domain can be readily found by applying the Fourier transform (Eqs. (4.15) and (4.16)) and solving the obtained ordinary differential equation. The result is

$$\tilde{p}_F = \mathrm{i}\omega\rho_F\tilde{A}_F \exp(+\mathrm{i}\omega q_F x_3), \qquad x_3 < 0, \tag{4.29}$$

where $\tilde{A}_F$ is the complex plane-wave amplitude of the fluid (F) wave and $q_F = (s_F^2 - p_r^2)^{\frac{1}{2}}$ is the vertical slowness. It contains the wave slowness s_F and the magnitude of the horizontal slowness p_r that are defined in Table 4.3.

The general solution to the Biot equations (Eqs. (4.5) and (4.6)) can be derived by applying Helmholtz decomposition in the $(\mathbf{x},\omega)$-domain to these equations, according to (Allard, 1993; Gubaidullin *et al.*, 2004)

$$\hat{\mathbf{u}} = \nabla\hat{\varphi}_{P1} + \nabla\hat{\varphi}_{P2} + \nabla\times\hat{\boldsymbol{\psi}}, \tag{4.30}$$

$$\hat{\mathbf{U}} = \beta_{P1}\nabla\hat{\varphi}_{P1} + \beta_{P2}\nabla\hat{\varphi}_{P2} + \beta_S\nabla\times\hat{\boldsymbol{\psi}}, \tag{4.31}$$

where $\hat{\varphi}_{P1}$ and $\hat{\varphi}_{P2}$ denote the scalar potentials for the fast (P_1) and slow (P_2) compressional waves, respectively, and $\hat{\boldsymbol{\psi}}$ the shear-wave (S) vector potential. β_{P1}, β_{P2} and β_S are the well-known fluid-solid amplitude ratios (Allard, 1993) for the separate body wavemodes (Table 4.3).

Applying the Helmholtz decomposition, the governing equations are decoupled and once the spatial Fourier transform (Eq. (4.16)) is applied, the decoupled equations turn into ordinary differential equations for $\tilde{\varphi}_{P1}$ and $\tilde{\varphi}_{P2}$, and $\tilde{\boldsymbol{\psi}}$ that can be solved separately. The general solution for the displacements is obtained by adding the separate contributions according to Eqs. (4.30) and (4.31). When the shear-wave term is split into a vertically-polarized (SV) and a horizontally-polarized (SH) part, and the fluid pressure is calculated using Eqs. (4.2) and (4.4), the result for the wave vector $\tilde{\mathbf{w}} = (\tilde{u}_1, \tilde{u}_2, \tilde{u}_3, -\phi\tilde{p}_f)^T$ can be written as

$$\tilde{\mathbf{w}} = \begin{bmatrix} p_1 & p_1 & q_S\frac{p_1}{p_r} & s_S^2\frac{p_2}{p_r^2} \\ p_2 & p_2 & q_S\frac{p_2}{p_r} & -s_S^2\frac{p_1}{p_r^2} \\ q_{P1} & q_{P2} & -p_r & 0 \\ -\mathrm{i}\omega s_{P1}^2 H_{P1} & -\mathrm{i}\omega s_{P2}^2 H_{P2} & 0 & 0 \end{bmatrix} \begin{bmatrix} \tilde{A}_{P1}\mathrm{e}^{-\mathrm{i}\omega q_{P1}x_3} \\ \tilde{A}_{P2}\mathrm{e}^{-\mathrm{i}\omega q_{P2}x_3} \\ \tilde{A}_{SV}\mathrm{e}^{-\mathrm{i}\omega q_S x_3} \\ \tilde{A}_{SH}\mathrm{e}^{-\mathrm{i}\omega q_S x_3} \end{bmatrix}, \tag{4.32}$$

for $x_3 > 0$. Next to the solid displacements $\tilde{\mathbf{u}}$, the wave vector $\tilde{\mathbf{w}}$ contains the fluid pressure $\tilde{p}_f$ rather then the fluid displacements $\tilde{\mathbf{U}}$ because the four components of $\tilde{\mathbf{w}}$ describe the wave field totally: there are only four independent variables; see Bonnet (1987). In Eq. (4.32), $\tilde{A}_{P1}$, $\tilde{A}_{P2}$, $\tilde{A}_{SV}$ and $\tilde{A}_{SH}$ denote the complex plane-wave amplitudes of the corresponding body wavemodes. In Table 4.3 the vertical slownesses q_{P1}, q_{P2} and q_S are defined (together with q_F), as well as the fluid compressibility terms H_{P1} and H_{P2}.

The body-wave slownesses have $\mathrm{Im}(s_\alpha) \leq 0$ for $\omega \geq 0$ and Sommerfeld's radiation condition requires that $\mathrm{Im}(q_\alpha) \leq 0$ for real p_r for all body modes, $\alpha = \{P_1, P_2, F, S\}$.

The complex plane-wave amplitudes are determined by the boundary conditions at the interface $x_3 = 0$. Applying the transforms (Eqs. (4.15) and (4.16)) to the boundary conditions (Eqs. (4.10)-(4.14)) and substituting the wave fields (Eqs. (4.29) and (4.32)) the following set of equations is obtained

$$\begin{bmatrix} 2Gp_r^2 - s_{P1}^2K_{P1} & 2Gp_r^2 - s_{P2}^2K_{P2} & 0 & 2Gp_rq_S & 0 \\ s_{P1}^2H_{P1} & s_{P2}^2H_{P2} & -\phi\rho_F & 0 & 0 \\ q_{P1}\phi_{P1} & q_{P2}\phi_{P2} & q_F & -p_r\phi_S & 0 \\ 2p_rq_{P1} & 2p_rq_{P2} & 0 & s_S^2 - 2p_r^2 & +\frac{p_2}{p_1p_r}q_Ss_S^2 \\ 2p_rq_{P1} & 2p_rq_{P2} & 0 & s_S^2 - 2p_r^2 & -\frac{p_1}{p_2p_r}q_Ss_S^2 \end{bmatrix}$$
$$\times \begin{bmatrix} \tilde{A}_{P1} & \tilde{A}_{P2} & \tilde{A}_F & \tilde{A}_{SV} & \tilde{A}_{SH} \end{bmatrix}^T = \begin{bmatrix} \frac{\hat{F}}{\mathrm{i}\omega} & 0 & 0 & 0 & 0 \end{bmatrix}^T, \tag{4.33}$$

which is similar to that in Gubaidullin *et al.* (2004), but extended to three dimensions. The constrained moduli K_{P1} and K_{P2} are defined in Table 4.3. The solution is calculated analytically using MAPLE©

$$\begin{aligned}
\tilde{A}_{P1} &= \frac{-\hat{F}\left(\phi\rho_F q_{P2}(s_S^2\phi_{P2} - 2p_r^2\phi\hat{\rho}_{22}^{-1}s_{P2}^2 H_{P2}) + q_F(s_S^2 - 2p_r^2)s_{P2}^2 H_{P2}\right)}{\mathrm{i}\omega G\Delta_1\Delta_{St}},\\
\tilde{A}_{P2} &= \frac{\hat{F}\left(\phi\rho_F q_{P1}(s_S^2\phi_{P1} - 2p_r^2\phi\hat{\rho}_{22}^{-1}s_{P1}^2 H_{P1}) + q_F(s_S^2 - 2p_r^2)s_{P1}^2 H_{P1}\right)}{\mathrm{i}\omega G\Delta_1\Delta_{St}},\\
\tilde{A}_F &= \frac{\hat{F}\left((q_{P1}\phi_{P1}s_{P2}^2 H_{P2} - q_{P2}\phi_{P2}s_{P1}^2 H_{P1})(s_S^2 - 2p_r^2) + 2p_r^2\Delta_2\phi_S\right)}{\mathrm{i}\omega G\Delta_1\Delta_{St}},\\
\tilde{A}_{SV} &= \frac{2p_r\hat{F}\left(\phi^2\rho_F\hat{\rho}_{22}^{-1}q_{P1}q_{P2}\Delta_1 + q_F\Delta_2\right)}{\mathrm{i}\omega G\Delta_1\Delta_{St}},
\end{aligned} \tag{4.34}$$

and $\tilde{A}_{SH} = 0$. Here, the "poroelastic Stoneley-wave denominator" (see Section 4.3) is defined as

$$\Delta_{St} = q_F\Delta_R + \phi\rho_F\Delta_3/\Delta_1, \tag{4.35}$$

which is associated with interface waves along the fluid/poroelastic-medium interface. It is very similar to the "Scholte-wave denominator" for a fluid/elastic-solid interface (de Hoop & van der Hijden, 1983), and equivalent to the one as given by Denneman *et al.* (2002). It contains the "poroelastic Rayleigh-wave denominator" that is associated with interface waves along a vacuum/poroelastic-medium interface

$$\Delta_R = (s_S^2 - 2p_r^2)^2 + 4p_r^2 q_S\Delta_2/\Delta_1, \tag{4.36}$$

which is very similar to the one for a vacuum/elastic-solid interface (Achenbach, 1973; Aki & Richards, 1980).

Now the plane-wave amplitudes are known, the $(\mathbf{p}_r, x_3, \omega)$-domain solution to Eqs. (4.5), (4.6) and (4.9)-(4.14) is determined and given by Eqs. (4.29) and (4.32).

4.8 Appendix B: Inverse Fourier integral

In this Appendix we show how Eq. (4.19) can be written in terms of a single integral according to Eq. (4.20), following Aki & Richards (1980). Transforming Eq. (4.19) to cylindrical coordinates according to $p_1 = p_r\cos\varphi$, $p_2 = p_r\sin\varphi$, and $x_1 = r\cos\vartheta$, $x_2 = r\sin\vartheta$, where $r = (x_1^2 + x_2^2)^{\frac{1}{2}}$, it can be written as

$$\hat{\mathbf{g}}^+ = \frac{\omega^2}{(2\pi)^2}\int_0^\infty\int_0^{2\pi}\frac{\tilde{\mathbf{n}}^+(p_r,\varphi,x_3,\omega)}{\Delta_{St}}\exp\left(-\mathrm{i}\omega p_r r\cos(\varphi-\vartheta)\right)p_r\,d\varphi dp_r. \tag{4.37}$$

The φ-dependence of $\tilde{\mathbf{n}}^+$ can be replaced by (horizontal) partial-derivative operators ∂_h, $h = \{1,2\}$, since the factors p_h that appear in $\tilde{\mathbf{n}}^+$ (cf. Eqs. (4.17) and (4.32)) correspond to horizontal derivatives ($-\mathrm{i}\omega p_h \leftrightarrow \partial_h$) in the $(\mathbf{x},\omega)$-domain. Therefore,

$\tilde{\mathbf{n}}^+(p_r, \varphi, x_3, \omega)$ is defined such that it contains the appropriate derivative operators, according to

$$\begin{aligned}\hat{\mathbf{g}}^+ &= \frac{\omega^2}{(2\pi)^2}\int_0^\infty \frac{\tilde{\mathbf{n}}^+(p_r, \partial_h, x_3, \omega)}{\Delta_{St}} \int_0^{2\pi} \exp\left(-\mathrm{i}\omega p_r r\cos(\varphi-\vartheta)\right)\, d\varphi p_r dp_r \\ &= \frac{\omega^2}{2\pi}\int_0^\infty \frac{\tilde{\mathbf{n}}^+(p_r, \partial_h, x_3, \omega)}{\Delta_{St}} J_0(\omega p_r r) p_r\, dp_r, \end{aligned} \tag{4.38}$$

where we have used the integral representation of the zeroth-order Bessel function $J_0(...)$; see Gradshteyn & Ryzhik (1980). The Bessel function is replaced by the sum of two zeroth-order Hankel functions of the first and second kind (Gradshteyn & Ryzhik, 1980), i.e., $J_0(z) = \frac{1}{2}(H_0^{(1)}(z) + H_0^{(2)}(z))$. Using the equality $H_0^{(1)}(z) = -H_0^{(2)}(-z)$ and the evenness of the $(\mathbf{p}_r, x_3, \omega)$-domain Green's functions in p_r, Eq. (4.38) can be written as

$$\hat{\mathbf{g}}^+ = \frac{\omega^2}{4\pi}\int_{-\infty}^\infty \frac{\tilde{\mathbf{n}}^+(p_r, \partial_h, x_3, \omega)}{\Delta_{St}} H_0^{(2)}(\omega p_r r) p_r\, dp_r, \tag{4.39}$$

where the horizontal derivatives are applied to the Hankel function before the integration is performed, according to

$$\partial_h H_0^{(2)}(\omega p_r r) = -\omega p_r \frac{x_h}{r} H_1^{(2)}(\omega p_r r). \tag{4.40}$$

Chapter 5

Pseudo interface waves observed at the fluid/porous-medium interface. A comparison of two methods[i]

Abstract

At the fluid/porous-medium interface the pseudo-Rayleigh (pR) and pseudo-Stoneley (pSt) waves exist. The relation with the corresponding poles in the slowness plane is not unambiguous, depending on the choice of branch cuts. For a point-force excitation, the far-field Green's functions are computed using vertical branch cuts (method I) implying that the pR- and pSt-poles obey the radiation condition. Then, a separate pseudo interface wave is entirely captured by the corresponding pole residue because the loop integral along a branch cut contributes to a body wave only. When hyperbolic branch cuts are used (method II) the poles lie on the "principal" Riemann sheet. Then, also the loop integrals necessarily contribute to the pR-wave because the pR-pole is different from that in method I. They do not contribute to the pSt-wave when the pSt-pole lies on the principal Riemann sheet because the pole is identical to that in method I. When the pSt-pole has migrated to another Riemann sheet, however, the pSt-wave is fully captured by the loop integrals. In conclusion, the phase velocity and attenuation of a separate pseudo interface wave can be computed from the pole location in method I, but should be extracted from the full response in method II.

5.1 Introduction

Interface waves that travel along the boundary of a porous medium carry information of the acoustic properties of that medium. They can be utilized to characterize

[i]This chapter has been accepted for publication as a journal paper in *J. Acoust. Soc. Am.* **129** (van Dalen *et al.*, 2011). Note that minor changes have been introduced to make the text consistent with the other chapters of this thesis.

several parameters belonging either to the solid frame or to the saturating fluid. Applications exist in ultrasonic testing of structures, borehole logging in geotechnical and reservoir engineering, and surface seismics in geophysics.

Several theoretical studies were performed on interface waves propagating along the boundary of a porous medium. Most of them were carried out in the context of Biot's theory for wave propagation in fluid-saturated poroelastic solids and discuss the fluid/porous-medium configuration (Rosenbaum, 1974; Feng & Johnson, 1983a,b; Edelman & Wilmanski, 2002; Allard *et al.*, 2003, 2004; Gubaidullin *et al.*, 2004; Albers, 2006; van Dalen *et al.*, 2010b). In general, three types of interface wavemodes can exist at such an interface: the pseudo-Rayleigh (pR) wave, the pseudo-Stoneley (pSt) wave and the true interface wave. The former are called "pseudo" because part of their energy is leaking into slower body wavemodes as they propagate along the interface due to their supersonic character. Some conditions for the existence of the pseudo interface waves have been given by Feng & Johnson (1983a). The "true" interface wave is called as such since it is slower than all body wavemodes and therefore non-leaky, and it is comparable to the Stoneley wave at the fluid/elastic-solid interface. It is only present for the closed-pore boundary, where fluid is not free to flow across the interface, or in case of a relatively soft porous frame (Feng & Johnson, 1983a).

For material characterization using the pseudo interface waves it is important to have predictions of the propagation characteristics of the individual wavemodes, i.e., the velocity and attenuation. Feng & Johnson (1983a) computed phase velocities and attenuations of the pseudo interface waves from the location of the zeroes (pR- and pSt-poles) of the poroelastic Stoneley dispersion equation in the complex plane. Physical constraints for the involved square roots were derived using the radiation condition, defining the Riemann sheets where the zeroes lie on. A similar approach was adopted by Edelman & Wilmanski (2002) and Gubaidullin *et al.* (2004).

In other papers the full transient response excited by a source is considered (Allard *et al.*, 2004; van Dalen *et al.*, 2010b), i.e., the acoustic wave motion including all excited wavemodes. The pseudo interface waves are then part of the full response as computed by evaluation of the inverse Fourier integral over horizontal slowness (or wavenumber) using contour integration on the "principal" Riemann sheet. In that case, the residue of a pole contributes to the waveform of a pseudo interface wave, but in a recent paper it has been observed that the waveform can also be affected by the loop integrals along the hyperbolic branch cuts (van Dalen *et al.*, 2010b). Consequently, the wave is not necessarily captured by the residue of the corresponding pole only. Now the question arises why and under which conditions the velocity and attenuation of a pseudo interface wave can be computed directly from the pole location.

To answer this question, in this chapter we compute the transient point-force response observed at the fluid/porous-medium interface using two different methods to compose the Green's functions (impulse responses). Method I is representative of Feng & Johnson (1983a), Edelman & Wilmanski (2002) and Gubaidullin *et al.* (2004), and method II of Allard *et al.* (2004) and van Dalen *et al.* (2010b). In method I we use vertical branch cuts for the involved square roots, which implies

that the contributing poles are formed exactly by the zeroes found using the square-root restrictions of Feng & Johnson (1983a). We show that, in the case of separated waves in the far field, the loop integral along a branch cut only contributes to a single body wave. Consequently, the far-field waveform of a separate pseudo interface wave is captured by the residue contribution of the corresponding pole only. In method II we use the hyperbolic branch cuts and we elucidate that the use of these branch cuts is responsible for the contributions of the loop integrals to the pseudo interface waves: there can be various singularities close to the integration path of a branch cut. Unique physical interpretation is only possible for the pSt-pole in a specific situation. Further, we explain the differences and similarities of the poles encountered in the two methods, and explain the physical reason of the migration of pSt-pole from one to another Riemann sheet, as originally observed in method II (van Dalen *et al.*, 2010b). Numerical examples are shown to illustrate our findings.

We utilize the model describing the three-dimensional transient response due to a point force applied normal to the interface of a fluid/porous-medium configuration (see Figure 5.1) (van Dalen *et al.*, 2010b), but we restrict ourselves to an observation point on the interface. In Section 5.2 we summarize the governing equations. We elaborate the two different methods in Section 5.3. In Section 5.4 we investigate the contributions of poles and branch cuts in more detail. Numerical results are discussed in Section 5.5 and conclusions are given in Section 5.7.

5.2 Model

We consider the configuration of a fluid half-space on top of a fluid-saturated poroelastic half-space, with a point force $F(t)$ applied normal to the interface (see Figure 5.1; the schematic response is referred to later) (van Dalen *et al.*, 2010b). Both half-spaces are considered to be homogeneous and isotropic, and the interface is an open-pore boundary. In this section we summarize the governing equations.

The behavior in the lower half-space ($x_3 > 0$) is governed by the well-known Biot equations of motion for a fluid-saturated poroelastic solid that were extensively discussed in this Journal; see e.g., Biot (1956a,b). We assume that for long-wavelength disturbances with respect to the characteristic pore scale, average local displacements can be defined for the solid (frame) $\mathbf{u}(\mathbf{x},t) = (u_1,u_2,u_3)^T$ and the fluid $\mathbf{U}(\mathbf{x},t) = (U_1,U_2,U_3)^T$. The equations of motion are found from usual combination of mass and momentum conservation, and constitutive relations giving (Biot, 1956a,b)

$$\rho_{11}\partial_t^2\mathbf{u} + \rho_{12}\partial_t^2\mathbf{U} + b(t) * \partial_t(\mathbf{u}-\mathbf{U}) = P\nabla\nabla\cdot\mathbf{u} - G\nabla\times\nabla\times\mathbf{u} + Q\nabla\nabla\cdot\mathbf{U}, \tag{5.1}$$

$$\rho_{12}\partial_t^2\mathbf{u} + \rho_{22}\partial_t^2\mathbf{U} - b(t) * \partial_t(\mathbf{u}-\mathbf{U}) = Q\nabla\nabla\cdot\mathbf{u} + R\nabla\nabla\cdot\mathbf{U}, \tag{5.2}$$

where $\partial_t = \partial/\partial t$, the asterisk denotes convolution, and P, Q and R are generalized elastic constants that are related to porosity ϕ, grain bulk modulus K_s, fluid bulk modulus K_f, bulk modulus of porous drained frame K_b, and shear modulus G of

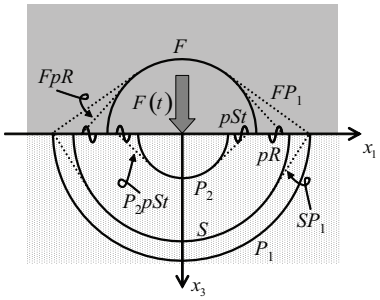

Figure 5.1: Point force $F(t)$ applied normal to interface of fluid-saturated porous half-space and fluid half-space, and schematic response (snapshot): fast compressional (P_1) wave, slow compressional (P_2) wave, shear (S) wave, fluid (F) wave, pseudo-Rayleigh (pR) wave and pseudo-Stoneley (pSt) wave. Double-mode symbols (e.g., SP_1) indicate lateral waves: first symbol denotes wavemode of specific arrival, the second that from which it is radiated. Here, F-wave velocity is assumed higher than P_2-wave velocity and smaller than S-wave velocity. For clarity, we omitted arrivals FS, P_2P_1, P_2S, P_2pR and P_2F.

both drained frame and total composite (Biot & Willis, 1957). The effective densities are defined as

$$\begin{aligned} \rho_{11} &= (1-\phi)\rho_s - \rho_{12}, \\ \rho_{22} &= \phi\rho_f - \rho_{12}, \\ \rho_{12} &= -(\alpha_\infty - 1)\phi\rho_f, \end{aligned} \tag{5.3}$$

where the tortuosity $\alpha_\infty \geq 1$, and hence $\rho_{12} \leq 0$. Solid and fluid densities are denoted as ρ_s and ρ_f, respectively. The linear time-convolution operator $b(t)$ was formulated in the frequency domain as the viscous correction factor by Johnson *et al.* (1987) according to (cf. Eq. (5.11))

$$\hat{b}(\omega) = b_0(1 + \tfrac{1}{2}\mathrm{i}M\omega/\omega_c)^{\frac{1}{2}}, \tag{5.4}$$

where the viscous damping factor $b_0 = \phi^2\eta/k_0$ and $\mathrm{Re}(\hat{b}(\omega)) \geq 0$ for $\omega \geq 0$. Here, η denotes the dynamic fluid viscosity and k_0 the zero-frequency Darcy permeability. The shape factor M is usually taken equal to 1 (Smeulders *et al.*, 1992). The rollover frequency, which represents the transition from low-frequency viscosity-dominated to high-frequency inertia-dominated behavior, is defined as $\omega_c = \eta\phi/(\alpha_\infty\rho_f k_0)$.

The behavior of the upper (fluid) half-space ($x_3 < 0$) is governed by the acoustic wave equation

$$\rho_F\partial_t^2 p_F = K_F\nabla^2 p_F, \tag{5.5}$$

where K_F and ρ_F denote the bulk modulus and density of the fluid, respectively, and p_F denotes the fluid pressure.

The behavior at the interface is governed by conventional open-pore conditions (Deresiewicz & Skalak, 1963), i.e., by continuity of volume flux and fluid pressure, and vanishing intergranular vertical stress σ_{33} and shear stresses σ_{13} and σ_{23}

(Biot, 1956a). The open-pore boundary can be a realistic choice to model the fluid/poroelastic-medium interface (Burns, 1990), but it is a limiting case of the general situation where a finite surface flow impedance is considered (Deresiewicz & Skalak, 1963). When the point force $F(t)$ is applied to the solid, in the limit of $x_3 \to 0$ the following conditions should be satisfied

$$(1-\phi)u_3 + \phi U_3 - U_{F,3} = 0, \tag{5.6}$$
$$p_f - p_F = 0, \tag{5.7}$$
$$\sigma_{13} = 0, \tag{5.8}$$
$$\sigma_{23} = 0, \tag{5.9}$$
$$\sigma_{33} = F(t)\delta(x_1)\delta(x_2), \tag{5.10}$$

where $\delta(...)$ denotes the Dirac delta function, and $U_{F,3}$ denotes the vertical particle displacement in the upper half-space.

The medium is considered to be at rest at $t \leq 0$. At infinite distance from the source the motions are bounded.

5.3 Green's functions

In this section we first summarize the plane-wave domain solution to the set of governing equations (Eqs. (5.1), (5.2) and (5.5)-(5.10)), as derived earlier (van Dalen *et al.*, 2010b). Then we show how the space-frequency $(\mathbf{x}, \omega)$-domain Green's functions are composed using the two different methods (see Section 5.1).

5.3.1 Plane-wave domain response

In order to consider the plane-wave domain response, we apply the Fourier transform over time t according to

$$\hat{\mathbf{u}}(\mathbf{x}, \omega) = \int_{-\infty}^{\infty} \mathbf{u}(\mathbf{x}, t) \exp(-\mathrm{i}\omega t)\, dt, \tag{5.11}$$

where ω denotes the angular frequency and i the imaginary unit. Because $\mathbf{u}(\mathbf{x}, t)$ is real-valued it is sufficient to consider $\omega \geq 0$ only. Following Aki & Richards (1980) the Fourier transform over horizontal spatial coordinates can be defined as

$$\tilde{\mathbf{u}}(\mathbf{p}_r, x_3, \omega) = \int_{-\infty}^{\infty}\int_{-\infty}^{\infty} \hat{\mathbf{u}}(\mathbf{x}, \omega) \exp(\mathrm{i}\omega \mathbf{p}_r \cdot \mathbf{r})\, dx_1 dx_2, \tag{5.12}$$

where $\mathbf{p}_r = (p_1, p_2)^T$ is the horizontal slowness vector and $\mathbf{r} = (x_1, x_2)^T$ is the horizontal space vector. The transforms are applied similarly to the other field quantities. The hat refers to the $(\mathbf{x}, \omega)$-domain and the tilde to the $(\mathbf{p}_r, x_3, \omega)$-domain.

The response in the plane-wave domain $(\mathbf{p}_r, x_3, \omega)$ is described by the physical quantities $\tilde{u}_i$ and $\tilde{p}_f$ in the lower half-space, grouped in the vector $\tilde{\mathbf{w}} =$

$(\tilde{u}_1, \tilde{u}_2, \tilde{u}_3, -\phi\tilde{p}_f)^T$, and by $\tilde{p}_F$ in the upper half-space. The expressions for the response can be obtained using standard Helmholtz decomposition of the equations of motion, and the boundary conditions. The resulting set of equations can be solved analytically. Finally, the $(\mathbf{p}_r, \omega, x_3)$-domain solution can be written in terms of Green's functions as

$$\tilde{\mathbf{w}} = \tilde{\mathbf{g}}^+ \hat{F} = \frac{\tilde{\mathbf{n}}^+}{\Delta_{St}} \hat{F}, \tag{5.13}$$

$$\tilde{p}_F = \tilde{g}^- \hat{F} = \frac{\tilde{n}^-}{\Delta_{St}} \hat{F}. \tag{5.14}$$

Here, $\tilde{\mathbf{g}}^+$ and $\tilde{g}^-$ are the Green's functions for $x_3 > 0$ and $x_3 < 0$, respectively, with numerators $\tilde{\mathbf{n}}^+$ and $\tilde{n}^-$, and $\Delta_{St}(p_r, \omega)$ is the "poroelastic Stoneley-wave denominator". $\hat{F}$ is the Fourier transform of the force signature. The Green's functions are linear combinations of the body modes: $\tilde{\mathbf{g}}^+$ contains the fast compressional (P_1) wave, the slow compressional (P_2) wave, and the vertically-polarized shear (S) wave; $\tilde{g}^-$ only contains the fluid (F) wave (see Figure 5.1). The corresponding propagation terms are $\exp(\mp \mathrm{i}\omega q_\alpha x_3)$, where $\alpha = \{P_1, P_2, F, S\}$; in the argument, the + relates to the upper medium and the − to the lower. The vertical slownesses are defined as $q_\alpha = (s_\alpha^2 - p_r^2)^{\frac{1}{2}}$, with $\mathrm{Im}(q_\alpha) \leq 0$ for real p_r. Here, s_α are the body-wave slownesses having $\mathrm{Im}(s_\alpha) \leq 0$ for $\omega \geq 0$, and p_r denotes the magnitude of the horizontal slowness.

The $(\mathbf{x}, \omega)$-domain Green's functions are found by evaluation of the inverse Fourier transform over horizontal slowness (cf. Eq. (5.12)). When cylindrical coordinates are introduced, it follows that (van Dalen *et al.*, 2010b)

$$\hat{g}_3^+ = \frac{\omega^2}{4\pi} \int_{-\infty}^{\infty} \frac{\tilde{n}_3^+}{\Delta_{St}} H_0^{(2)}(\omega p_r r) p_r \, dp_r, \tag{5.15}$$

where $r = (x_1^2 + x_2^2)^{\frac{1}{2}}$ and $H_0^{(2)}(...)$ is the Hankel function of zeroth order and second kind. We only specify the expression for $\hat{g}_3^+$; the other Green's functions are obtained by simply replacing $\tilde{n}_3^+$ in Eq. (5.15) by the other numerators. For brevity, from this point we omit the superscript, i.e., $\hat{g}_3^+ = \hat{g}_3$.

Now, we change the real-axis integral into a contour integral in the complex p_r-plane (Fuchs *et al.*, 1964). The idea is that by integration in the complex plane, contributions from branch cuts and poles can be distinguished. Two different sets of branch cuts are employed to make the square roots single-valued in the entire p_r-plane.

5.3.2 Method I: Vertical branch cuts

In the first method (see also Feng & Johnson (1983a); Edelman & Wilmanski (2002); Gubaidullin *et al.* (2004)) we compose the Green's functions using branch cuts for the square roots q_α along vertical half-lines departing from the corresponding branch points being the body-wave slownesses s_α, as shown in Figure 5.2. In this figure also the closed integration contour is displayed, which is formed by the entire real axis,

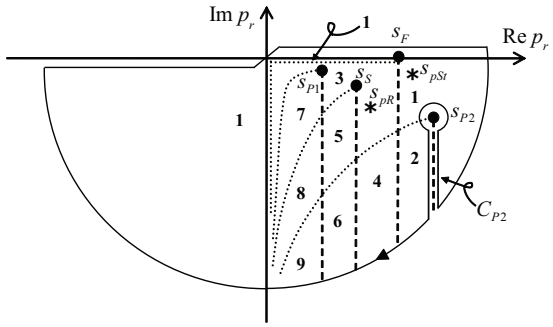

Figure 5.2: Complex p_r-plane for method I with $(--)$ vertical branch cuts of square roots q_α departing from corresponding $(\bullet)$ branch points s_α, $\alpha = \{P_1, P_2, F, S\}$. Poles $(*)$ s_{pR} (pseudo-Rayleigh) and s_{pSt} (pseudo-Stoneley) are zeroes of poroelastic Stoneley denominator; see Eq. (5.18). Only part of closed integration contour $(-)$ is displayed: real axis, arc in lower half-plane and loop C_{P2} along q_{P2}-branch cut. Direction of integration is indicated. Every $(\cdots)$ line indicates transition between two Riemann sheets as indicated by numbers (Figure 5.3 and Table 5.1). Here, F-wave velocity is assumed higher than P_2-wave velocity and smaller than S-wave velocity.

the loops along the branch cuts and around the branch points, and an arc of infinite radius in the lower half-plane. For $\mathrm{Re}(p_r) \leq 0$ the horizontal part of the contour lies just below the axis due to the presence of a branch cut of the Hankel function at the negative real axis (Abramowitz & Stegun, 1972).

The meaning of the dotted hyperbolas in Figure 5.2 is illustrated in Figure 5.3, where the behavior of q_{P1} in the complex plane is sketched. There is a (abrupt) sign change over the vertical branch cut and throughout the rest of the p_r-plane the magnitude changes smoothly. Along the dotted hyperbolas either the imaginary part is zero (for $\mathrm{Re}(p_r) < \mathrm{Re}(s_{P1})$) or the real part (for $\mathrm{Re}(p_r) > \mathrm{Re}(s_{P1})$) (Harris, 2001). The other roots behave similarly. Hence, the dotted lines in Figure 5.2 indicate where $\mathrm{Im}(q_\alpha) = 0$. Crossing such a line means that one moves from one to another Riemann sheet.

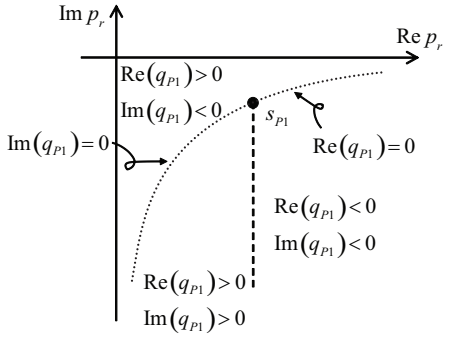

Figure 5.3: Complex p_r-plane in method I with $(--)$ q_{P1}-branch cut departing from branch point s_{P1}. Hyperbolic lines $(\cdots)$ indicate where either $\mathrm{Re}(q_{P1}) = 0$ or $\mathrm{Im}(q_{P1}) = 0$. In various areas signs of real and imaginary parts of q_{P1} are indicated.

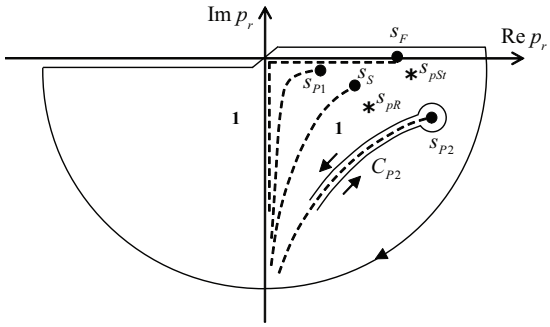

Figure 5.4: Complex p_r-plane for method II with $(--)$ hyperbolic branch cuts of square roots q_α departing from corresponding $(\bullet)$ branch points s_α, $\alpha = \{P_1, P_2, F, S\}$. Poles $(*)$ s_{pR} (pseudo-Rayleigh) and s_{pSt} (pseudo-Stoneley) are zeroes of poroelastic Stoneley denominator; see Eq. (5.18). Only part of closed integration contour $(-)$ is displayed (cf. Figure 5.2). Direction of integration is indicated. Integration is done entirely on the principal Riemann sheet (indicated by 1; Table 5.1). Here, F-wave velocity is assumed higher than P_2-wave velocity and smaller than S-wave velocity.

Consequently, inside the closed contour (Figure 5.2) nine different Riemann sheets can be distinguished. Throughout the entire complex plane the signs of the square roots q_α are calculated given the requirement that $\mathrm{Im}(q_\alpha) \leq 0$ on the real p_r-axis, which is the original path of integration (see Eq. (5.15)) (Aki & Richards, 1980). We indicate every Riemann sheet according to the sign of $\mathrm{Im}(q_\alpha)$, e.g., $\mathrm{sgn}(\mathrm{Im}(q_{P1}, q_{P2}, q_F, q_S)) = (- - --)$ is the sheet where all roots have imaginary parts smaller than or equal to zero, which is the "principal" Riemann sheet (Aki & Richards, 1980; van der Hijden, 1984). In Figure 5.2 this sheet is indicated by 1. In Table 5.1 an overview is given of all Riemann sheets inside the contour.

5.3.3 Method II: Hyperbolic branch cuts

In the second method (see also Allard *et al.* (2004); van Dalen *et al.* (2010b)) we compose the Green's functions using branch cuts exactly along the hyperbolic lines $\mathrm{Im}(q_\alpha) = 0$; see Figure 5.4. This implies that $\mathrm{Im}(q_\alpha) < 0$ over the rest of p_r-plane (Harris, 2001), and ensures the decay of the exponential terms $\exp(\mp \mathrm{i}\omega q_\alpha x_3)$ for large $|p_r|$ (present in Eqs. (5.13) and (5.14)). The q_F-branch cut coincides with the imaginary axis and part of the real axis since the slowness of the fluid (s_F) is real-valued. The current branch cuts imply that the integration is performed entirely on the principal Riemann sheet.

In Figure 5.4 also the closed contour is displayed, similar as in Figure 5.2.

5.3.4 Inverse Fourier transform

We now compose the $(\mathbf{x}, \omega)$-domain Green's function $\hat{g}_3$ as a summation of the contributions of the branch cuts and the residues of the poles that lie inside the

Table 5.1: Various Riemann sheets present inside closed contours in Figures 5.2 and 5.4. Every Riemann sheet is characterized by signs of imaginary parts of involved square roots.

	$\mathrm{Im}(q_{P1})$	$\mathrm{Im}(q_{P2})$	$\mathrm{Im}(q_F)$	$\mathrm{Im}(q_S)$
1	−	−	−	−
2	−	+	−	−
3	−	−	+	−
4	−	+	+	−
5	−	−	+	+
6	−	+	+	+
7	+	−	+	−
8	+	−	+	+
9	+	+	+	+

contour. In both methods Cauchy's residue theorem (Fuchs *et al.*, 1964) leads to

$$\hat{g}_3 = \sum_\alpha \hat{g}_{3,\alpha} + \sum_\beta \hat{g}_{3,\beta}, \tag{5.16}$$

where $\hat{g}_{3,\alpha}$ denotes the contribution of the loop integral along the q_α-branch cut,

$$\hat{g}_{3,\alpha} = -\frac{\omega^2}{4\pi} \int_{C_\alpha} \frac{\tilde{n}_3}{\Delta_{St}} H_0^{(2)}(\omega p_r r) p_r \, dp_r, \tag{5.17}$$

and $\alpha = \{P_1, P_2, F, S\}$. Here, C_α represents the integration loop. In Eq. (5.16), $\hat{g}_{3,\beta}$ denotes the residue contribution of a first-order pole s_β of the integrand inside the integration contour, which is typically the pseudo-Rayleigh (pR) pole or the pseudo-Stoneley (pSt) pole (see Figures 5.2 and 5.4) (van Dalen *et al.*, 2010b),

$$\hat{g}_{3,\beta} = -2\pi \mathrm{i} \left[\frac{\omega^2}{4\pi} \frac{\tilde{n}_3}{\partial_{p_r} \Delta_{St}} H_0^{(2)}(\omega p_r r) p_r \right]_{p_r = s_\beta}. \tag{5.18}$$

Obviously, both methods give the same Green's function $\hat{g}_3$, but due to the different branch cuts the integrands are defined differently (we consider $\tilde{n}_3/\partial_{p_r}\Delta_{St}$ on different Riemann sheets) and consequently, the contributions of the loop integrals $\hat{g}_{3,\alpha}$ and of the pole residues $\hat{g}_{3,\beta}$ are not the same. We can even encounter different poles on the different Riemann sheets on which the integration is performed.

5.4 Physical interpretation of separate contributions of the far-field interface response

In this section we determine to what wavemode(s) of the interface response the loop integral along a single branch cut and a single pole residue contribute(s), respectively. To facilitate this we only consider the far-field situation and we approximate the loop integral using the saddle-point method. This leads to expressions that have

a straightforward physical interpretation. We only elaborate the separate contributions for method I because for method II it is clear on beforehand that the loop integral along a branch cut can contribute to several waves in the full response, including the pseudo interface waves (van Dalen *et al.*, 2010b). Unique physical interpretation is only possible for the pSt-pole in a specific situation, as we will discuss in Section 5.5.

5.4.1 Approximate pole contributions

First, we consider the residue contributions $\hat{g}^I_{3,\beta}(x_3 = 0)$ as given by Eq. (5.18). Considering the wavefield in the far field ($|\omega p_r r| \gg 1$), we can write (Abramowitz & Stegun, 1972)

$$\hat{g}^I_{3,\beta}(x_3 = 0) \cong \left(\frac{\omega^3}{2\pi r}\right)^{\frac{1}{2}} \left.\frac{\tilde{n}_3}{\partial_{p_r}\Delta_{St}}\right|_{x_3=0,p_r=s_\beta} s_\beta^{\frac{1}{2}} \mathrm{e}^{-\mathrm{i}\omega s_\beta r - \mathrm{i}\frac{\pi}{4}} \tag{5.19}$$

$$= A_\beta(\omega, r)\mathrm{e}^{-\mathrm{i}\omega \mathrm{Re}(s_\beta) r + \mathrm{i}\varphi_\beta(\omega)}, \tag{5.20}$$

where A_β is the amplitude and φ_β the r-independent phase angle of the wavemode that has phase propagation slowness $\mathrm{Re}(s_\beta)$, i.e., the pseudo-Rayleigh (pR) or the pseudo-Stoneley (pSt) wave. All contributing poles s_β have $\mathrm{Im}(s_\beta) < 0$ as they lie inside the integration contour. This ensures the vanishing of the displacements for $r \to \infty$ (Eq. (5.19)).

5.4.2 Approximate branch-cut contributions

Next, we focus on the contributions of the branch cuts $\hat{g}^I_{3,\alpha}(x_3 = 0)$ as given by Eq. (5.17). Introducing $p_r = s_\alpha - \mathrm{i}\xi$, where ξ is a local variable of integration and considering the far field ($|\omega p_r r| \gg 1$), we can write for the contribution of C_α - taking both sides (L: left; R: right) in one integral

$$\hat{g}^I_{3,\alpha}(x_3 = 0) \cong \left(\frac{\omega^3}{8\pi^3 r}\right)^{\frac{1}{2}} \mathrm{e}^{-\mathrm{i}\omega s_\alpha r + \mathrm{i}\frac{3}{4}\pi}$$

$$\times \int_0^\infty \left(\frac{\tilde{n}_{3,L}}{\Delta_{St,L}} - \frac{\tilde{n}_{3,R}}{\Delta_{St,R}}\right)_{x_3=0} p_r^{\frac{1}{2}} \mathrm{e}^{-\omega r \xi}\, d\xi \tag{5.21}$$

$$= A_\alpha(\omega, r)\mathrm{e}^{-\mathrm{i}\omega \mathrm{Re}(s_\alpha) r + \mathrm{i}\varphi_\alpha(\omega, r)}, \tag{5.22}$$

where the signs of all roots q_α can be determined from Figures 5.2 and 5.3, and Table 5.1, and where $\mathrm{Re}(p^{\frac{1}{2}}) \geq 0 \;\forall\; p$ (Aki & Richards, 1980); A_α is some amplitude and φ_α a phase angle. We now show how the integral over ξ contributes to A_α and φ_α using a saddle-point approximation. We only show the approximation of the loop integral C_F, but the others (C_{P1}, C_{P2} and C_S) can be approximated similarly.

From Eq. (5.21) it is observed that the integration path is the path of steepest descent of the far-field integrand at $x_3 = 0$ (Tsang, 1978). The saddle point coincides with the branch point of the particular branch cut, i.e., $p_r = s_\alpha$. This is a limiting

case of the more general situation where $x_3 \neq 0$ and the saddle point lies at $p_r = s_\alpha r/R_0$, where $R_0 = (x_1^2 + x_2^2 + x_3^2)^{\frac{1}{2}}$ (Jeffreys & Jeffreys, 1946; Brekhovskikh, 1960; Aki & Richards, 1980).

We employ Watson's lemma (Achenbach, 1973) to evaluate the integral for $\omega r \to \infty$

$$\int_0^\infty \xi^{+a} f_F(\xi,\omega) \mathrm{e}^{-\omega r \xi}\, d\xi = \sum_{n=0}^{\infty} \partial_\xi^n f_F(\xi,\omega)\Big|_{\xi=0} \frac{\Gamma(a+n+1)}{(\omega r)^{a+n+1}}, \tag{5.23}$$

where $\partial_\xi^n = \partial^n/\partial\xi^n$, $a > -1$, $\Gamma(...)$ is the gamma function, and

$$f_F(\xi,\omega) = \xi^{-a} p_r^{\frac{1}{2}} \left(\frac{\tilde{n}_{3,L}}{\Delta_{St,L}} - \frac{\tilde{n}_{3,R}}{\Delta_{St,R}} \right)_{x_3=0}. \tag{5.24}$$

For the situation that $\mathrm{Re}(s_{P2}) > s_F$ (which is the case in the numerical examples that we will consider), we have along the integration path (see Figures 5.2 and 5.3, and Table 5.1)

$$p_r = s_F - \mathrm{i}\xi, \tag{5.25}$$

$$\mathrm{Im}(q_{P1}, q_S) < 0, \tag{5.26}$$

$$\mathrm{Re}(q_{P2}) > 0, \tag{5.27}$$

$$\mathrm{Im}(q_{F,L}) \geq 0, \qquad \mathrm{Im}(q_{F,R}) \leq 0. \tag{5.28}$$

For $a = \frac{1}{2}$, $\partial_\xi^n f_F(\xi,\omega)$ is finite at $\xi = 0$ (which can be shown using MAPLE©) and hence, using $\Gamma(\frac{3}{2}) = \frac{1}{2}\sqrt{\pi}$, Eq. (5.21) can be approximated as

$$\hat{g}_{3,F}^{I,os}(x_3 = 0) = \frac{1}{4\sqrt{2}\pi r^2} f_F(0,\omega) \mathrm{e}^{-\mathrm{i}\omega s_F r + \mathrm{i}\frac{3}{4}\pi}, \tag{5.29}$$

which is the "ordinary" saddle-point approximation (Tsang, 1978) (indicated by superscript "os") because it only uses the zeroth-order term (see Eq. (5.23)). The error is of $\mathcal{O}(\omega^{-1} r^{-3})$ provided that $f_F(0,\omega)$ is not singular in the vicinity of the saddle point.

A pole lying in the vicinity of the saddle point invalidates the ordinary approximation. For instance, as we will discuss in a numerical example (Section 5.5), the pSt-pole can lie very close to the fluid-wave branch point strongly affecting the behavior of $f_F(\xi,\omega)$. We now show how to include the effect of the proximity of pSt-pole in the approximation of the fluid branch-cut contribution. We use the "modified" saddle-point method where the singular part of the integrand is split off and handled separately (van der Waerden, 1952; Brekhovskikh, 1960; Tsang, 1978).

First, we make a transform of variable, $\xi = \zeta^2/(\omega r)$, so that

$$p_r = s_F - \mathrm{i}\zeta^2/(\omega r), \tag{5.30}$$

and

$$\hat{g}_{3,F}^{I}(x_3 = 0) \cong \left(\frac{\omega}{8\pi^3 r^3}\right)^{\frac{1}{2}} \mathrm{e}^{-\mathrm{i}\omega s_F r + \mathrm{i}\frac{3}{4}\pi} I, \tag{5.31}$$

where

$$I = \int_0^\infty y(p_r,\omega)\mathrm{e}^{-\zeta^2}\,d\zeta, \tag{5.32}$$

$$y(p_r,\omega) = 2\zeta p_r^{\frac{1}{2}}\left(\frac{\tilde{n}_{3,L}}{\Delta_{St,L}} - \frac{\tilde{n}_{3,R}}{\Delta_{St,R}}\right)_{x_3=0}. \tag{5.33}$$

We split off the singular part from $y(p_r,\omega)$ by defining

$$y(p_r,\omega) = w(p_r,\omega) + \frac{y_{pSt}}{p_r - s_{pSt}}, \tag{5.34}$$

where $y_{pSt} = y_{pSt}(\omega)$ according to

$$y_{pSt} = \lim_{p_r\to s_{pSt}}\left((p_r - s_{pSt})y(p_r,\omega)\right), \tag{5.35}$$

$$= -2\zeta_{pSt}s_{pSt}^{\frac{1}{2}}\left.\frac{\tilde{n}_{3,R}}{\partial_{p_r}\Delta_{St,R}}\right|_{x_3=0,p_r=s_{pSt}}. \tag{5.36}$$

At $p_r = s_{pSt}$ the roots take on the same signs as at the right side of the q_F-branch cut; see Eqs. (5.26)-(5.28). The quantity ζ_{pSt} is the value that ζ assumes at the pSt-pole; from Eq. (5.30) we find

$$\zeta_{pSt} = \left(\mathrm{i}\omega r(s_{pSt} - s_F)\right)^{\frac{1}{2}}, \tag{5.37}$$

where $\mathrm{Im}(\zeta_{pSt}) < 0$. It represents a normalized distance between the fluid-wave branch point (saddle point) and the pSt-pole. Its magnitude squared is the so-called "numerical distance". Combining Eqs. (5.32) and (5.34), we have

$$I = I_1 + I_2, \tag{5.38}$$

$$I_1 = \int_0^\infty w(p_r,\omega)\mathrm{e}^{-\zeta^2}\,d\zeta, \tag{5.39}$$

$$I_2 = \int_0^\infty \frac{y_{pSt}}{p_r - s_{pSt}}\mathrm{e}^{-\zeta^2}\,d\zeta. \tag{5.40}$$

Watson's lemma can now again be applied to approximate I_1 since the nearby singularity has been removed. The approximation of the first term of I_1 ($y(p_r,\omega)$) leads to the result of Eq. (5.29). To approximate the second term of I_1 ($-y_{pSt}/(p_r - s_{pSt})$) we need to include two terms of Watson's lemma to get the same order in ωr. The integral I_2 can be expressed in terms of the complementary error function (Gradshteyn & Ryzhik, 1980). The final result of the modified saddle-point approximation (indicated by superscript "ms") is found by combining Eqs. (5.31) and (5.38)-(5.40)

$$\hat{g}_{3,F}^{I,ms}(x_3=0) = \frac{1}{4\sqrt{2}\pi r^2}\mathrm{e}^{-\mathrm{i}\omega s_F r + \mathrm{i}\frac{3}{4}\pi}\left(f_F(0,\omega) + \frac{(\omega r)^{\frac{1}{2}}y_{pSt}}{s_{pSt} - s_F}\left(1 + \frac{1}{2\zeta_{pSt}^2}\right)\right.$$
$$\left. + \sqrt{\pi}\frac{(\omega r)^{\frac{3}{2}}y_{pSt}}{\zeta_{pSt}}\mathrm{erfc}(\mathrm{i}\zeta_{pSt})\mathrm{e}^{-\zeta_{pSt}^2}\right). \tag{5.41}$$

The second and third terms inside the brackets are the correction terms of the modified saddle-point approximation with respect to the ordinary one; they cancel when $|\zeta_{pSt}| \to \infty$, i.e., when the pole is far away from the saddle point.

In general, also poles that do not lie inside the closed contour can influence the integrands of the loop integrals along the branch cuts. For instance, the $\bar{P}$-poles that are located close to $p_r = s_{P1}$ (van Dalen *et al.*, 2010b), can lie on sheet 1 and the $(+--)$-sheet, respectively, below sheet 3 and 7 (see Figure 5.2), and still invalidate the ordinary saddle-point approximation (Tsang, 1978). In practice, it is probably the best to evaluate the full integrals numerically, which ensures that all effects of nearby poles are included properly. However, the current approximations allow us to physically interpret the separate contributions in method I.

5.4.3 Physical interpretation of contributions

Using the results of the previous Sections (5.4.1 and 5.4.2) we are able to physically interpret the separate contributions of the Green's functions. Comparing Eqs. (5.21), (5.22) and (5.29), we observe that in the case that there is no pole in the vicinity of the saddle point, the integral over ξ contributes to the phase angle φ_F such that it is only ω-dependent: $\varphi_F = \varphi_F(\omega)$ (this is also the case if more terms of Watson's lemma are included). It does not modify the phase slowness of the exponential term. Therefore, in the far field, a branch-cut contribution in method I only corresponds to a separate body wave in the interface response. Its geometrical decay of the pole residue behaves as r^{-2}, which is typical for a body/head wave propagating along the interface (Aki & Richards, 1980). Consequently, if the loop integral only contributes to a separate body wavemode, the far-field residue contribution of a pole (pR or pSt; Eqs. (5.19) and (5.20)) must capture the entire waveform of a separate pseudo interface wave in the interface response, i.e., the pR- or the pSt-wave. The geometrical decay behaves as $r^{-\frac{1}{2}}$, which is typical for an interface wave.

For the case that there is a pole close to the saddle point, we observe that the integral over ξ contributes to the phase angle φ_F such that it is also r-dependent: $\varphi_F = \varphi_F(\omega, r)$ (cf. Eqs. (5.21), (5.22) and (5.41)). In Eq. (5.41) the term $\operatorname{erfc}(\mathrm{i}\zeta_{pSt}) \exp(-\zeta_{pSt}^2)$ seemingly describes some dispersion of the F-wave. However, this term is merely a consequence of the interference of the body wave and the interface wave due to the proximity of the pole and the saddle point. In this case, separate interface and body waves cannot be distinguished (see also next section).

In method II the branch cuts follow curved paths in the complex plane. Hence, the integrand of a loop integral can encounter several singularities in the complex plane and thus contribute to the waveforms of the corresponding wavemodes. This is the reason that in method II, a body wave cannot be attributed to a single branch-cut contribution and, as a consequence, the residue contribution of an individual pole does not necessarily contain the entire waveform of the corresponding pseudo interface wave.

Table 5.2: Various configurations for which the transient response is considered. The type of sandstone is Bentheimer (van Dalen *et al.*, 2010b). For fused glass beads (Feng & Johnson, 1983a), bulk modulus of drained matrix is chosen as $K_b = 10$ GPa and permeability as $k_0 = 10\ \mu\text{m}^2$. Saturating fluid (water) has bulk modulus $K_f = 2.22$ GPa and density $\rho_f = 1000\ \text{kgm}^{-3}$. Upper half-space is filled with either light fluid ($K_F = \frac{1}{10}K_f$, $\rho_F = \frac{1}{8}\rho_f$) or water ($K_F = K_f$, $\rho_F = \rho_f$). For every configuration the poles (pseudo-Stoneley (pSt) and pseudo-Rayleigh (pR)) present inside integration contour are indicated for both methods (I,II).

	Porous solid	Saturating fluid	Upper half-space	Poles method I	Poles method II
1	Sandstone	water	light fluid	pR, pSt	pR, pSt
2	Glass beads	water	water	pR, pSt	pSt[ii]
3	Sandstone	water	water	pR,[iii] pSt	pSt

5.5 Numerical results and discussion

In this section, we subsequently discuss various wavemodes that are excited by the point force and verify to what parts (poles and branch cuts) of the Green's functions their waveforms are related, in both the methods I and II. We show the transient interface responses for three different fluid/porous-medium configurations (see Table 5.2) yielding illustrative results for the theoretical elaborations. For clarity, we adhere to the distinction between separate and interfering wavemodes (Sections 5.5.1 and 5.5.2, respectively) as introduced Section 5.4.3. Finally, in Section 5.5.3 we address the migration of poles, which we first encounter in Section 5.5.1.

In the first and third configurations the porous medium is a water-saturated Bentheimer sandstone (van Dalen *et al.*, 2010b). The upper half-space is either a light fluid or water. The second configuration is identical to that of Feng & Johnson (1983a,b). For every configuration, we show the vertical component of particle velocity v_3 for an observation point at the interface $x_3 = 0$ at offset $r = x_1 = 0.10$ m. The point force has Ricker signature (Ricker, 1953),

$$F(t) = F_{max}\left(\tfrac{1}{2}\omega_0^2\bar{t}^2 - 1\right)\exp\left(-\tfrac{1}{4}\omega_0^2\bar{t}^2\right), \tag{5.42}$$

where $\bar{t} = t - t_s$ ($t > 0$), $\omega_0 = 2\pi f_0$ and centre frequency $f_0 = 500$ kHz (see Figure 5.5). The magnitude $F_{max} = 2.5 \cdot 10^{-7}$ N and time shift $t_s = 5\ \mu$s. We have performed the integration over p_r for the frequency range $0 < f \leq 2$ MHz. The particle velocity is obtained from multiplication of the spectra of the Green's function by the source signature (Eq. (5.13)), and by iω. A standard fast Fourier-transform algorithm is applied for the transform to the time domain.

For both methods we have evaluated the loop integrals by numerical integration of the exact integrands (Eq. (5.17); no approximations involved). Similarly, in the evaluation of the pole residues we have used the full expressions (Eq. (5.18)). The poles inside the closed integration contour contributing a residue are given in Table 5.2. We have identified the pseudo-Stoneley (pSt) and the pseudo-Rayleigh (pR) poles using the Principle of the Argument to the Stoneley denominator Δ_{St} (Fuchs

[ii] Not present inside integration contour for $f \geq 310$ kHz.
[iii] Its residue is not shown.

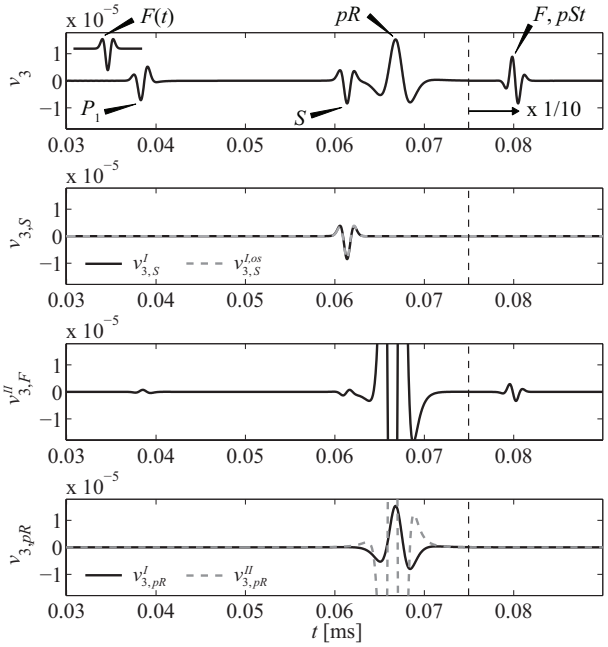

Figure 5.5: Bentheimer/light-fluid (configuration 1): full response (v_3) including source signature $F(t)$ (Eq. (5.42)), q_S-branch cut contribution in method I ($v^I_{3,S}$) and its approximation ($v^{I,os}_{3,S}$), q_F-branch cut contribution ($v^{II}_{3,F}$) and pR-pole residues ($v^I_{3,pR}$, $v^{II}_{3,pR}$), at $x_2 = x_3 = 0$ and $x_1 = 0.10$ m. Residue $v^{II}_{3,pR}$ and pR-wave part of $v^{II}_{3,F}$ are not entirely visible on scale of this figure. Units are [ms^{-1}]. From dashed vertical line onwards, responses have been scaled by $\frac{1}{10}$.

et al., 1964; van Dalen *et al.*, 2010b); this principle gives the number of poles inside a closed integration contour. In method I the pSt-pole lies on sheet 1 or 2, and the pR-pole on sheet 3 or 4 (see Figure 5.2 and Table 5.1). In method I the poles all lie on sheet 1 (see Figure 5.4).

For all three configurations the full responses and separate contributions are displayed in Figures 5.5 and 5.7-5.9. Obviously, the full responses are the same in both methods (and not displayed separately). We have identified the different arrivals in the full responses using the phase velocities as obtained from the modal slownesses. For the sake of clarity, a schematic snapshot of the full response with the different arrivals is shown in Figure 5.1. Here, body waves are indicated by the solid lines and interface waves by short wavelets; lateral waves (either head waves or wavefronts radiated by the pseudo interface waves) are indicated by dotted lines. At the interface, head waves and body waves coincide and therefore, the head waves are not indicated separately in the figures in this section. Superscripts (I and II) refer to the different methods.

5.5.1 Separate wavemodes

We consider the separate (non-interfering) wavemodes present in the full responses. First, we consider the S-wave. It can be observed that, in the response of configuration 1 (Figure 5.5), its waveform is fully captured by the contribution of the q_S-branch cut $v^I_{3,S}$ in method I (Eq. (5.17)). The ordinary saddle-point approximation $v^{I,os}_{3,S}$ (Eq. (5.29)), which is also shown, provides a good approximation of the exact result. In Figure 5.5 we also show the contribution of the q_F-branch cut in method II ($v^{II}_{3,F}$). Obviously, it contributes to many waveforms including to that of the S-wave.

Next, we consider the pR-wave. For configuration 1 (Figure 5.5), in both methods there is a pR-pole present inside the contour. In method I, where it lies on sheet 3 (see Figure 5.2), its residue contribution v^I_{pR} coincides with the entire waveform. However, in method II where the pole lies on sheet 1 (see Figure 5.4), its residue contribution $v^{II}_{3,pR}$ is significantly different in magnitude and waveform. The q_F-branch cut ($v^{II}_{3,F}$) also contributes to the waveform (Figure 5.5). Both contributions are very strong but partially cancel each other; together they constitute the pR-wave. In Figure 5.6 we display the locations of the pR-pole as encountered in the two methods. Remarkably, there is a difference in both the real and imaginary parts. This illustrates that the pR-pole can lie on different Riemann sheets simultaneously at rather different locations (p_r-values); in fact, we have here two different pR-poles. For configuration 2 (Figure 5.7) the pR-waveform is again fully captured by the pR-pole in method I ($v^I_{3,pR}$), but in method II there is no pR-pole at all present inside the contour and hence, the entire waveform is captured by the loop integrals.

So far, the numerical results confirm the findings in Section 5.4.3 that, in method I, a separate pseudo interface wave is entirely captured by the residue contribution of the corresponding pole in the far-field interface response. The reason is that the loop integral along a branch cut only contributes to a separate body wave (provided that are no singularities in the vicinity of the branch point). For method II, our results show that a loop integral can contribute to the pR-wave, and several other wavemodes, as it encounters various singularities along the integration path (see Figure 5.4). We argue that the loop integrals even necessarily contribute to the pR-wave because the encountered pR-pole, and its residue, differ from those in method I where the pole residue contains the entire waveform. In some situations the pR-wave is entirely captured by the loop integrals when there is no pR-pole present inside the integration contour (on principal Riemann sheet).

Finally, we discuss the pSt-wave. For configuration 2 (Figure 5.7) there is a clear difference between the two methods for the pSt-wave: the residue contribution $v^I_{3,pSt}$ contains the entire waveform, but in method II the waveform is constituted by the residue contribution $v^{II}_{3,pSt}$ and the loop integral along the q_{P2}-branch cut ($v^{II}_{3,P2}$). For configuration 3 (Figure 5.8), however, in both methods the residue contribution of the pSt-pole ($v^I_{3,pSt}$ and $v^{II}_{3,pSt}$) contains the entire pSt-waveform in the full response. In the former situation (configuration 2) the q_{P2}-branch cut lies close to the real axis (cf. Figure 5.4 for small $\mathrm{Im}(s_{P2})$), and the pSt-pole lies in between. For increasing frequency the q_{P2}-branch cut comes so close to the real

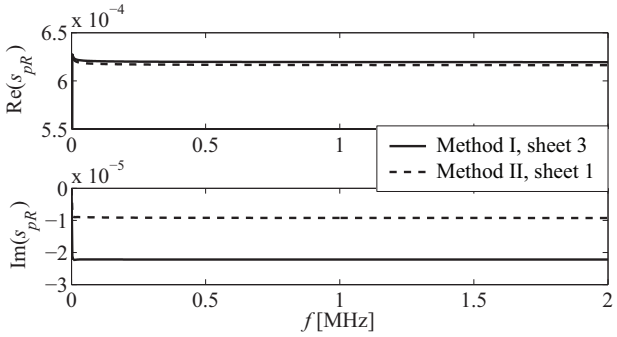

Figure 5.6: Bentheimer/light-fluid (configuration 1): location of pR-pole in methods I and II. Units are [sm^{-1}].

axis that the pSt-pole even crosses the branch cut and vanishes from the principal Riemann sheet (see also Section 5.5.3) (van Dalen *et al.*, 2010b). For $f \geq 310$ kHz the pSt-wave is totally captured by the loop integral. For $f < 310$ kHz it is fully captured by the pole while the loop integral along the q_{P2}-branch cut does not contribute, even though the pole lies close to the integration path. When the integral is evaluated, however, its contribution turns out to be zero. This is necessarily the case because, contrary to the pR-pole (discussed above), the pSt-pole is exactly the same pole in both methods (same Riemann sheet and location). The residue contributions are identical. As the residue contribution in method I contains the entire waveform, this should also be the case for method II and, consequently, the contribution of any loop integral to the pSt-wave has to be equal to zero for $f < 310$ kHz. Now, it is also clear why in the latter situation (configuration 3) the pSt-pole contains the entire pSt-waveform even for method II: it is because the pole lies on sheet 1 over the entire considered frequency range.

In conclusion, the observations in this section illustrate that in method I all information that belongs to a separate pseudo interface wave is captured by the corresponding pole. Hence, the phase velocity and attenuation can be simply computed from the pole location. In method II, generally, these properties should not be computed using pole locations but from isolated (separate) waveforms in the full response. For the pSt-wave, however, in method II one can suffice with the pole location for sufficiently low frequencies so that the pole lies on the principal Riemann sheet.

In the case of a separate "true" interface wave (see Section 5.1), in both methods the corresponding pole will contain the entire waveform because the pole lies to the right of every branch point on sheet 1 (see Figures 5.2 and 5.4) at exactly the same location (same pole) and, consequently, the branch cuts cannot contribute. Therefore, in both methods the pole location provides all information to compute velocity and attenuation.

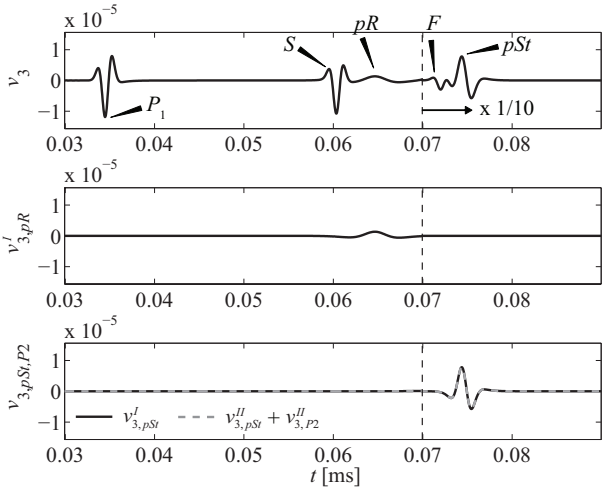

Figure 5.7: Glass beads/water (configuration 2): full response (v_3), pR-pole residue ($v^I_{3,pR}$) and pSt-wave as constituted by either pSt-pole residue ($v^{II}_{3,pSt}$) and q_{P2}-branch cut contribution ($v^{II}_{3,P2}$), or only pSt-pole residue ($v^I_{3,pSt}$), at $x_2 = x_3 = 0$ and $x_1 = 0.10$ m. Units are [ms^{-1}]. From dashed vertical line onwards, responses have been scaled by $\frac{1}{10}$.

5.5.2 Interfering wavemodes

Next, we consider the interfering (simultaneously arriving) F- and pSt-waves in the response for configuration 1 (Figure 5.9). There is strong interference, which is caused by the small difference in propagation velocities. Mathematically, this results in a small numerical distance (Eq. (5.37)) when the loop integral of the q_F-cut is approximated (method I), as announced in Section 5.4.2. In Figure 5.9 we show the exact q_F-branch cut contribution ($v^I_{3,F}$; Eq. (5.17)) and the corresponding ordinary ($v^{I,os}_{3,F}$) and modified ($v^{I,ms}_{3,F}$) saddle-point approximations (Eqs. (5.29) and (5.41), respectively); $v^{I,ms}_{3,F}$ is indistinguishable from $v^I_{3,F}$ and therefore not displayed separately. It can be observed that the error in $v^{I,os}_{3,F}$ is very significant in waveform and amplitude. In Figure 5.10 we compare both saddle-point approximations and the full numerical solution of the branch-cut contribution $\hat{g}^I_{F,3}$ over the considered frequency band. Obviously, the modified approximation is accurate except for low frequencies where the far-field assumption is not valid (there, the fixed propagation distance r is not much larger than the wavelength).

The important notion here is that the interfering F- and pSt-waves (Figure 5.9) cannot be considered as separate arrivals. The combined waveform is one arrival that is constituted by the pSt-pole residue and the q_F-branch cut contribution. The correction terms in Eq. (5.41) that modify the phase slowness of the q_F-contribution (compared to Eq. (5.29)) support this idea. Similarly, the pseudo-Rayleigh pole can lie in the vicinity of the shear-wave branch point (Tsang, 1978), and constitute together a combined shear-Rayleigh wave.

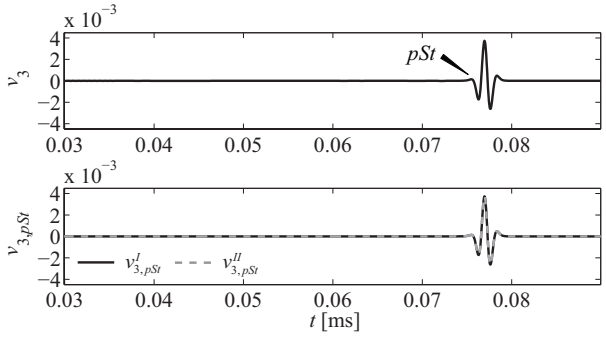

Figure 5.8: Bentheimer/water (configuration 3): full response (v_3) and pSt-pole residues ($v^I_{3,pSt}$, $v^{II}_{3,pSt}$), at $x_2 = x_3 = 0$ and $x_1 = 0.10$ m. In v_3, only the pSt-wave can be observed on the scale of this figure. Units are [ms^{-1}].

In method II the combined F, pSt-wave is also constituted by the q_F-branch cut contribution ($v^{II}_{3,F}$) and the pSt-pole residue ($v^{II}_{3,pSt}$); see Figure 5.9. The pole residue is identical to that in method I ($v^I_{3,pSt}$) because in both methods the pole is the same (see Section 5.5.1). The loop integral along the branch cut, however, also contributes to other waves (see Section 5.5.1).

For comparison, we consider again the pSt-wave in configuration 2 (Figure 5.7) as discussed in Section V.A. The wave does not (strongly) interfere with the F-wave and it can be verified that the associated numerical distance (in method I) is larger. However, we observe that, even when both wavemodes are mathematically related to individual parts of the Green's function (in method I), it can be difficult to separate the waves in time due to the small difference in propagation velocity and dispersion effects. Recording the waves at very large distances, where the pSt-wave has been (fully) separated from the F-wave, probably makes no sense because the pSt-wave will completely be attenuated due to energy radiation and dissipation. Therefore, one needs to use the entire response or at least the interfering wavemodes for material characterization. Generally, the pR-pole and the pSt-pole found using the square-root constraints of method I are related to separate arrivals when their real parts are sufficiently different from those of the adjacent branch points.

5.5.3 Migration of poles

Finally, we discuss the reason of the migration of the pSt-pole from one Riemann sheet to another (Albers, 2006; van Dalen *et al.*, 2010b). Using method II we have found that for configuration 2 the pole vanishes from the principal Riemann sheet at a certain frequency (see Table 5.1). Because the pSt-pole found in method I is identical (see Section 5.5.1), we can use this method to illustrate to which sheet the pole migrates, and explain the physical origin of the phenomenon. We consider the complex p_r-plane (Figure 5.2) with the pSt-pole lying on sheet 1. The crucial point is that the branch point of the slow compressional wave comes closer to the real axis when frequency increases. In the limit of $\omega \to \infty$ it even lies on the real axis because

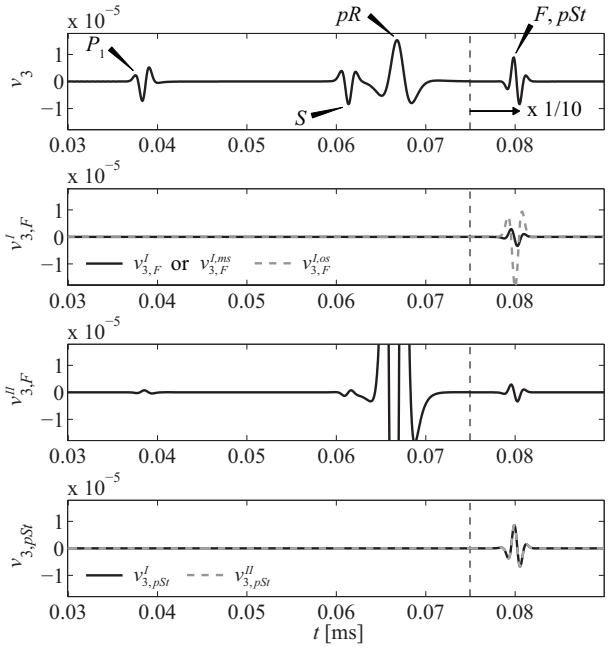

Figure 5.9: Bentheimer/light-fluid (configuration 1): full response (v_3), q_F-branch cut contributions ($v^I_{3,F}$ and $v^{II}_{3,F}$) and its approximations for method I ($v^{I,os}_{3,F}$, $v^{I,ms}_{3,F}$), and pSt-pole residues for both methods ($v^I_{3,pSt}, v^{II}_{3,pSt}$), at $x_2 = x_3 = 0$ and $x_1 = 0.10$ m. In $v^{II}_{3,F}$, pR-wave part is not entirely visible on scale of this figure. Units are [ms^{-1}]. From dashed vertical line onwards, responses have been scaled by $\frac{1}{10}$.

the viscous mechanism is inactivated and the wave propagates without intrinsic attenuation (similar to the s_F-branch point). However, for increasing frequency the pSt-pole does not migrate to the real axis because it continues radiating slow compressional waves (see Figure 5.1). Hence, at some frequency the pSt-pole must migrate from sheet 1 to sheet 2 as the (transition) line along which $\mathrm{Im}(q_{P2}) = 0$ migrates towards the real axis. Similarly, the pR-pole (found in method I) migrates from sheet 3 to sheet 4 when frequency increases.

In fact, the migration of the poles has already been reported by Gubaidullin *et al.* (2004), but they did not refer to it as such. They observed that the imaginary part of the square root q_α of a radiated body wave can have positive or negative sign, depending on frequency. Our analysis now provides the physical reason for this.

5.6 Discussion

In the previous section we have shown the transient responses excited at the open-pore interface between a fluid and a porous medium. We would like to emphasize, however, that the general conclusions about the physical interpretation of poles and branch cuts are equally valid for closed-pore conditions or for the boundary

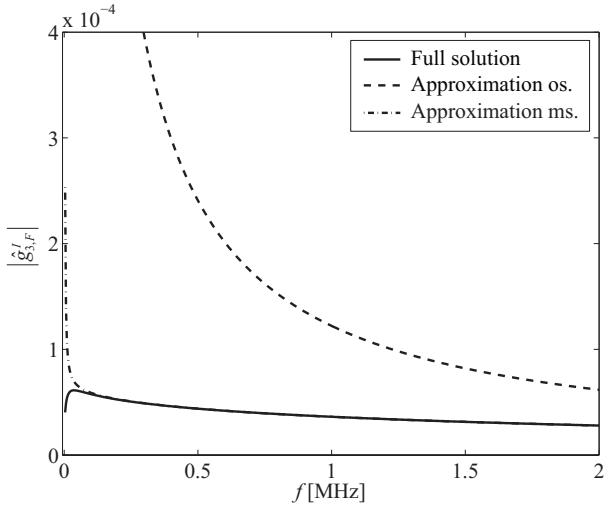

Figure 5.10: Bentheimer/light-fluid (configuration 1): full numerical solution of q_F-branch cut contribution in method I ($\hat{g}^I_{3,F}$), and its ordinary ($\hat{g}^{I,os}_{3,F}$) and modified ($\hat{g}^{I,ms}_{3,F}$) saddle-point approximations, at $x_2 = x_3 = 0$ and $x_1 = 0.10$ m. Units are [m/(Ns)].

conditions with a finite surface flow impedance (Deresiewicz & Skalak, 1963).

Closely related to this, it can easily be seen that for a separate "true" interface wave (see Section 5.1) (Feng & Johnson, 1983a,b), in both the methods (I and II) the corresponding pole will contain the entire waveform. This is because the pole lies to the right of every branch point on sheet 1 (see Figures 5.2 and 5.4) at exactly the same location (same pole), where the branch cuts cannot contribute. Therefore, in both methods the pole location provides all information to compute phase velocity and attenuation of the true interface wave.

In our opinion, the general conclusions (from Section 5.5) are also not restricted to the configuration of two half-spaces. They capture the situation of a layered rather than a homogeneous porous half-space and the situation where the porous medium includes a third phase (e.g., gas) too. A difficulty will be to find all pole locations accurately. Further, as there will be more interface wavemodes (including higher-order wavemodes), various arrivals can interfere, which makes physical interpretation of arrivals difficult.

Furthermore, our analysis, which shows that a pseudo interface wave is uniquely described by a pole (method I), could be used as a starting point for the analysis of energy radiation. Gubaidullin *et al.* (2004) have already addressed this problem, but a more comprehensive analysis is desirable and should include transient responses to show when exactly the waves are radiative and when not.

Finally, we indicate how our work regarding pseudo interface waves at the fluid/porous-medium interface connects to the literature on the pR-wave at the fluid/elastic-solid interface (Roever *et al.*, 1959; Phinney, 1961; van der Hijden, 1984). Measures for the velocity of the entire pR-pulse can be derived based on a zero-

crossing in the (exact) time-domain Green's function or on the pulse maximum (Roever *et al.*, 1959; van der Hijden, 1984). These velocity measures differ from the velocity of harmonic waves that can be derived from the location of the pR-pole (Roever *et al.*, 1959; Phinney, 1961). The latter value represents the phase velocity and is the elastic counterpart of the phase velocity that we have found for the pR-pole (method I). However, in our case this velocity is frequency-dependent and therefore, it is probably impossible to find similar velocity measures for the entire pulse.

5.7 Conclusions

The pseudo-Rayleigh (pR) and pseudo-Stoneley (pSt) waves exist at the interface of a fluid and a fluid-saturated porous medium. These pseudo interface waves are related to the pR-pole and the pSt-pole, respectively, of the poroelastic Stoneley dispersion equation. However, the residue of such a pole does not always capture the entire waveform of the corresponding wave. Therefore, the question arises why and under which conditions the phase velocity and attenuation of a pseudo interface wave can be computed directly from the pole location.

To evaluate the physical interpretation of the poles we computed the point-force response observed at the fluid/porous-medium interface. We compose the Green's functions using two different methods. In method I vertical branch cuts are used for the involved square roots in the complex slowness plane, which implies that the contributing poles are exactly found on Riemann sheets determined by the radiation condition (see Feng & Johnson (1983a); Edelman & Wilmanski (2002); Gubaidullin *et al.* (2004)). In method II hyperbolic branch cuts are used, which implies that the contributing poles are found on the "principal" Riemann sheet (see Allard *et al.* (2004); van Dalen *et al.* (2010b)).

Using saddle-point approximations we showed that, in the case of separated waves in the far field, the loop integral along a branch cut only contributes to a single body wave in method I. Consequently, the far-field waveform of a pseudo interface wave is entirely captured by the residue contribution of the corresponding pole. For method II, we illustrated that the loop integral along a branch cut can contribute to several waves as it encounters various singularities along its integration path. The loop integrals necessarily contribute to the pR-wave because the pR-pole lies on a different Riemann sheet and at a different location compared to the pole in method I, where it contains the entire waveform. The loop integrals do not contribute to the pSt-wave as long as the pSt-pole lies on the principal Riemann sheet because this pole is identical to that in method I, where it captures the entire waveform. However, at a relatively high frequency the pole migrates to another Riemann sheet due to the slow compressional wave becoming less attenuated; then, the pSt-wave is fully captured by the loop integrals in method II.

As a consequence, the phase velocity and attenuation of a separate pseudo interface wave can be simply computed from the location of the corresponding pole in method I. In method II, generally, these properties should be extracted from isolated waveforms in the full response as the pole does not necessarily provide all information to compute velocity and attenuation.

Chapter 6

Impedance and ellipticity of fluid/elastic-solid interface waves: medium characterization and simultaneous displacement - pressure measurements[i]

Abstract

The interface-wave impedance and ellipticity are wave attributes that interrelate the full waveforms as observed in different components. For each of the fluid/elastic-solid interface waves, i.e., the pseudo-Rayleigh (pR) and Stoneley (St) waves, the impedance and ellipticity are found to have different functional dependencies on the Young's modulus and Poisson's ratio. By combining the attributes in a cost function, unique and stable estimates of these parameters can be obtained, particularly using the St-wave. In a validation experiment, the impedance of the laser-excited pR-wave is successfully extracted from a simultaneous measurement of the normal particle displacement and the fluid pressure at a water/aluminum interface. The displacement is measured using a laser Doppler vibrometer (LDV) and the pressure with a needle hydrophone. Any LDV-measurement is perturbed by refractive-index changes along the LDV-beam once acoustic waves interfere with the beam. Using a model that accounts for these perturbations, we predict an impedance decrease of 26% with respect to the plane-wave impedance of the pR-wave for the water/aluminum configuration. Although this deviates from the experimentally extracted impedance, there is excellent agreement between the observed and predicted pR-waveforms in both the particle displacement and fluid pressure.

[i]This chapter has been submitted for publication as a journal paper to *J. Acoust. Soc. Am.* Note that minor changes have been introduced to make the text consistent with the other chapters of this thesis.

6.1 Introduction

Interface waves that travel along the boundary of a medium carry information of the acoustic parameters. The waves can be utilized to determine these parameters in-situ. Applications exist in many different fields and scales, e.g., in non-destructive testing of materials and structures, borehole logging in geotechnical and reservoir engineering, surface seismics in geophysics, and seismology.

For medium characterization, often simply the propagation velocity and the attenuation of an interface wave are employed (Glorieux *et al.*, 2001; Rix, 2005). In that case, a single-component measurement is sufficient, e.g., the detection of the normal particle velocity induced by the waves. The full waveforms of an interface wave as present in different components exhibit, however, particular properties that are also worth exploiting in medium characterization. Typically, the well-known Rayleigh wave at the vacuum/elastic-solid interface induces a retrograde elliptical motion of the material particles at the interface (Viktorov, 1967). The ratio of the principal axes of the corresponding ellipse is a function of Poisson's ratio only (Malischewsky & Scherbaum, 2004). In order to extract the ellipticity, which is defined as the spectral ratio of the tangential and normal particle displacements at the interface (Munirova & Yanovskaya, 2001; Malischewsky & Scherbaum, 2004; Ferreira & Woodhouse, 2007), one needs to record at least two components of the particle displacement. For the "pseudo" Rayleigh (pR) wave and the Stoneley (St) wave that exist at the fluid/elastic-solid interface (Viktorov, 1967; de Hoop & van der Hijden, 1983; van der Hijden, 1984; Glorieux *et al.*, 2001), in addition to the ellipticity the impedance can be distinguished, which can be defined as the spectral ratio of the fluid pressure and the normal component of the particle velocity at the interface (de Hoop, 1995). Obviously, for the extraction of the interface-wave impedance also a two-component measurement is required.

Nishizawa *et al.* (1998) have measured two components of an ultrasonic wave field at an interface using laser Doppler vibrometers. Two mutually orthogonal beams at 45° incidence, and a normally incident beam were applied to detect the tangential and normal components, respectively. In general, ultrasonic laser interferometers and vibrometers give reliable absolute values of particle displacement or velocity, and have particular advantages, i.e., physical coupling to the sample is not required, they have a broadband response and a sub-millimeter focal-point size (Scruby & Drain, 1990). Recently, the elliptical particle motion of the Rayleigh wave has successfully been measured using an adaptive laser interferometer by Blum *et al.* (2010) by applying only one laser beam and taking advantage of the surface roughness of the sample that causes the light to scatter away from the incidence direction. Further, in several publications it is shown that laser ultrasonics can be used to detect the pR- and St-waves at fluid/elastic-solid interfaces (Desmet *et al.*, 1996, 1997; Glorieux *et al.*, 2001).

Laser ultrasonics can also be applied to assess the acoustic pressure at the fluid/elastic-solid interface by using a Doppler beam skimming over the surface, normal to the direction of propagation of the wave field (Mattei & Adler, 2000; Han *et al.*, 2006). Then, using the photoelastic effect, the recorded signal can be conver-

ted into acoustic pressure (Solodov *et al.*, 2009). However, the involved width of the acoustic wavefront is quite difficult to estimate, which makes the absolute values of the pressure rather uncertain.

The goal of this chapter is to show the feasibility of characterizing an elastic solid by simultaneously using the impedance and ellipticity of each of the ultrasonic pR- and St-waves at the fluid/elastic-solid interface.

To this end, we first define the impedance and ellipticity theoretically and show that they have different functional dependencies on the Young's modulus and Poisson's ratio, for each of the pR- and St-waves. By combining the impedance and ellipticity in a cost function, we take advantage of this difference and show that unique estimates of Young's modulus and Poisson's ratio can be obtained simultaneously. This illustrates the feasibility of medium characterization using the interface-wave impedance and ellipticity.

Motivated by this result, we show the feasibility of the extraction of interface-wave impedance from a simultaneous normal particle displacement and fluid pressure measurement at ultrasonic frequencies. We restrict ourselves to the extraction of impedance because the extraction of ellipticity has already been performed successfully. We present an experimental set-up using a laser Doppler vibrometer (LDV) for the particle displacement measurement and a needle hydrophone to record the absolute values of the fluid pressure. For a water/aluminum configuration, we show how the impedance of the pR-wave can be successfully extracted from the measurement.

Finally, we compare the experimentally observed waveforms with the modeled predictions obtained using the Cagniard-de Hoop method (de Hoop & van der Hijden, 1983). In the model we include the interference of the acoustic waves in the fluid and the LDV-beam that crosses the fluid. The laser light is perturbed by the pressure-induced refractive-index changes. The integrated effect of the perturbations along the beam gives an additional contribution in the displacement measurement, which can be quite substantial (Allard *et al.*, 2004). We quantify the effect on the predicted waveforms and on the extracted pR-wave impedance, and discuss the effect of the involved measurement inaccuracies in the impedances and ellipticities on the estimated values of Young's modulus and Poisson's ratio.

In Section 6.2 we define the impedance and ellipticity, and illustrate their behaviors. We show how the Young's modulus and Poisson's ratio can be estimated in Section 6.3. Then, in Section 6.4 we give expressions for the acoustic response and derive an expression for the additional contribution to the LDV-measurement. We show the experimental results and the extracted impedance in Section 6.5, and compare them with modeled predictions in Section 6.6. The effect of inaccuracies is discussed in Section 6.7 and conclusions are given in Section 6.8.

6.2 Impedance and ellipticity

In this section we define expressions for the impedance and ellipticity associated with the pR- and St-waves at the fluid/elastic-solid interface. We use the plane-wave domain solutions of the governing equations that correspond to interface waves and

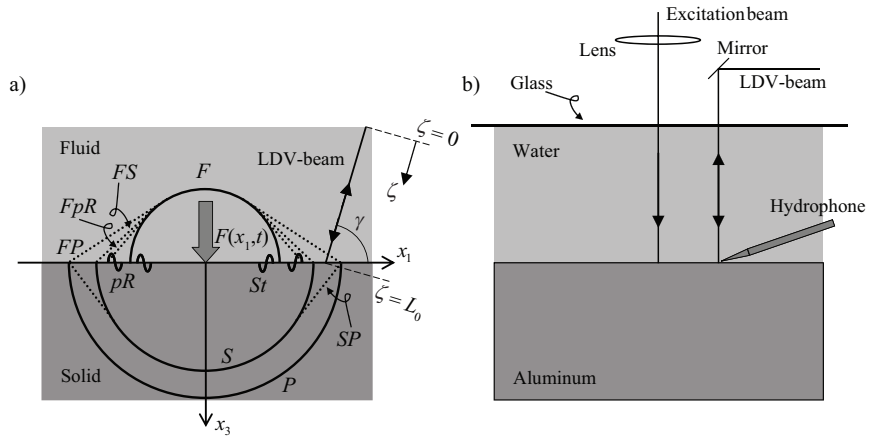

Figure 6.1: a) Fluid/elastic-solid configuration, model for the acoustic response excited by a laser (modeled as normal force $F(x_1, t)$) and schematic response: compressional (P) wave, shear (S) wave, fluid (F) wave, pseudo-Rayleigh (pR) wave and Stoneley (St) wave. Double-mode symbols (e.g., SP) indicate lateral waves (dotted lines): the first symbol denotes the wavemode of the specific arrival; the second denotes the one from which it is radiated. The position of the Doppler beam with general orientation (angle γ) is determined by the local ζ-axis. b) Schematic overview of the experimental set-up used for the simultaneous detection of interface waves at water/aluminum interface.

illustrate the dependencies of the impedance and ellipticity on the Young's modulus and Poisson's ratio for each of the wavemodes.

Let us define the physical model and the corresponding solution. We consider a fluid half-space on top of an elastic solid (see Figure 6.1a; the response and the LDV-beam are discussed later). Both media are homogeneous and isotropic. The behavior of the elastic solid ($x_3 > 0$) is governed by the elastic wave equation (Achenbach, 1973)

$$\rho \partial_t^2 \mathbf{u} = (\lambda + 2\mu) \nabla \nabla \cdot \mathbf{u} - \mu \nabla \times \nabla \times \mathbf{u}, \tag{6.1}$$

where $\partial_t = \partial / \partial t$, λ and μ are the Lamé constants, ρ denotes the material density, and $\mathbf{u}(\mathbf{x}, t) = (u_1, u_3)^T$ is the particle displacement vector. We assume a two-dimensional wave motion because this is sufficient to define the impedances and ellipticities of the interface waves, and because the experimentally-observed wave motion approximates two-dimensional wave propagation (see Section 6.4). The behavior of the fluid ($x_3 < 0$) is governed by the acoustic wave equation (Wapenaar & Berkhout, 1989)

$$\rho_F \partial_t^2 p_F = K_F \nabla^2 p_F, \tag{6.2}$$

where K_F and ρ_F denote the bulk modulus and density of the fluid, respectively, and p_F denotes the fluid pressure.

The boundary conditions at the fluid/elastic-solid interface comprise the continuity of the normal component of particle displacement, continuity of the normal

component of the traction, and the vanishing of the tangential component of the traction in the solid. Incorporating a force acting normally on the boundary $F(x_1,t)$ [Nm^2] to excite waves (Figure 6.1a), in the limit of $x_3 \to 0$ the following conditions should be satisfied

$$u_3 - U_{F,3} = 0, \tag{6.3}$$

$$\tau_{33} + p_F = -F(x_1,t), \tag{6.4}$$

$$\tau_{13} = 0. \tag{6.5}$$

Here, $U_{F,3}$ is the vertical component of the fluid particle displacement $\mathbf{U}_F(\mathbf{x},t)$ and τ_{ij} is the stress tensor in the solid.

We apply the Fourier transform over time t and horizontal coordinate x_1 according to

$$\tilde{\bar{\mathbf{u}}}(k,x_3,\omega) = \int_{-\infty}^{\infty}\int_{-\infty}^{\infty} \mathbf{u}(\mathbf{x},t)\exp\left(-\mathrm{i}(\omega t - kx_1)\right)\,dtdx_1, \tag{6.6}$$

where ω denotes the angular frequency, k is the horizontal angular wavenumber and i is the imaginary unit. It is assumed that $\mathbf{u}(\mathbf{x},t)$ is real-valued and hence, it is sufficient to consider $\omega \geq 0$. The transforms are also applied to the other field quantities. In this section we use $k = \omega p$, where p is the horizontal slowness, because this enables us to show that the characteristic determinant (see further) and the impedance and ellipticity derived from that, are independent of frequency. The combined bar/tilde refers to the (k,x_3,ω)-domain, and a single tilde refers to the (p,x_3,ω)-domain.

In the (p,x_3,ω)-domain, the wave fields in the lower and upper media are described by physically relevant solutions of the acoustic and elastic wave equations (Eqs. (6.1) and (6.2)), respectively, according to (Achenbach, 1973; de Hoop & van der Hijden, 1983)

$$\tilde{u}_1 = \frac{p}{\mathrm{i}\omega}\tilde{A}_P\tilde{F}\exp(-\mathrm{i}\omega q_P x_3) + \frac{q_S}{\mathrm{i}\omega}\tilde{A}_S\tilde{F}\exp(-\mathrm{i}\omega q_S x_3), \tag{6.7}$$

$$\tilde{u}_3 = \frac{q_P}{\mathrm{i}\omega}\tilde{A}_P\tilde{F}\exp(-\mathrm{i}\omega q_P x_3) - \frac{p}{\mathrm{i}\omega}\tilde{A}_S\tilde{F}\exp(-\mathrm{i}\omega q_S x_3), \tag{6.8}$$

for $x_3 > 0$, and

$$\tilde{p}_F = \tilde{A}_F\tilde{F}\exp(+\mathrm{i}\omega q_F x_3), \tag{6.9}$$

for $x_3 < 0$. Here $q_\alpha = (s_\alpha^2 - p^2)^{\frac{1}{2}}$, with $\alpha = \{P,F,S\}$, are the vertical slownesses having $\mathrm{Im}(q_\alpha) \leq 0$ for real p, and s_α are the corresponding body-wave slownesses being the reciprocal of the wave velocities ($c_\alpha = 1/s_\alpha$). The complex-valued amplitude factors $\tilde{A}_\alpha$ are determined by the boundary conditions. Using the momentum equation of the fluid and the stress-strain relation of the elastic solid (Achenbach, 1973; Wapenaar & Berkhout, 1989), the following set of equations for the $\tilde{A}_\alpha$ is obtained

$$\begin{bmatrix} q_P & q_F/\rho_F & -p \\ \mu(s_S^2 - 2p^2) & -1 & -2\mu p q_S \\ 2pq_P & 0 & s_S^2 - 2p^2 \end{bmatrix} \begin{bmatrix} \tilde{A}_P \\ \tilde{A}_F \\ \tilde{A}_S \end{bmatrix} = \begin{bmatrix} 0 \\ 1 \\ 0 \end{bmatrix}. \tag{6.10}$$

The solution can be easily found and reads

$$\tilde{A}_P = +\frac{s_S^2}{\rho}\frac{s_S^2 - 2p^2}{\Delta_{St}}, \tag{6.11}$$

$$\tilde{A}_F = -\frac{\rho_F}{\rho}\frac{q_P}{q_F}\frac{s_S^4}{\Delta_{St}}, \tag{6.12}$$

$$\tilde{A}_S = -\frac{s_S^2}{\rho}\frac{2pq_P}{\Delta_{St}}, \tag{6.13}$$

where Δ_{St} is the characteristic determinant of the matrix in Eq. (6.10),

$$\Delta_{St} = \Delta_R + s_S^4\frac{q_P}{q_F}\frac{\rho_F}{\rho}, \tag{6.14}$$

which is the "Stoneley-wave denominator" of the fluid/elastic-solid interface (de Hoop & van der Hijden, 1983) (or "Scholte-wave denominator"). It contains the "Rayleigh-wave denominator",

$$\Delta_R = (s_S^2 - 2p^2)^2 + 4p^2 q_S q_P, \tag{6.15}$$

which is associated with the stress-free vacuum/solid interface (Achenbach, 1973).

The signs of the roots q_P, q_F and q_S are very important to obtain the proper solutions (zeroes) for the interface wave slownesses in Eq. (6.14). The St-wave is a "true" interface wave that only propagates along the interface and decays with distance from the interface. The zero of the Stoneley denominator (Eq. (6.14)) related to the St-wave ($p = s_{St}$), which forms the St-pole in the response (Eqs. (6.7)-(6.9)), is found on the real p-axis at $s_{St} > s_F$ and lies on the Riemann sheet where $\mathrm{Im}(q_\alpha) \leq 0$ (principal Riemann sheet) (de Hoop & van der Hijden, 1983). The pseudo-Rayleigh (pR) wave is a "pseudo" interface wave that radiates a fluid wavefront as it propagates along the interface (see Figure 6.1a: FpR-front), and decays with distance from the interface into the solid. The zero of Eq. (6.14) related to the pR-wave ($p = s_{pR}$) is complex-valued with $\mathrm{Im}(s_{pR}) < 0$ and lies on the Riemann sheet where $\mathrm{Im}(q_F) > 0$ and $\mathrm{Im}(q_{P,S}) \leq 0$ (Viktorov, 1967; Feng & Johnson, 1983a; van Dalen *et al.*, 2011). The velocity and attenuation of the interface waves are fully characterized by these slownesses, i.e., by their real and imaginary parts, and, at the interface, their far-field waveforms are fully captured by the residue contributions of the corresponding poles once the response (Eqs. (6.7)-(6.9)) is transformed to the $(\mathbf{x}, t)$-domain (van Dalen *et al.*, 2011).

Consequently, we can define the impedance and ellipticity in (p, x_3, ω)-domain by the spectral ratio of two components for $x_3 = 0$, evaluated at the specific slownesses s_β, where $\beta = \{pR, St\}$. Evaluation of the full waveforms, which often implies the evaluation of integrals numerically, is not required. Still, the particular information present in the multi-component waveforms of an interface wave is captured by these wave attributes and can be easily exploited (see Section 6.3). We define the impedance I_β as the spectral ratio of the fluid pressure and the vertical particle velocity at the interface, which expresses the resistance to the particle motion induced by the

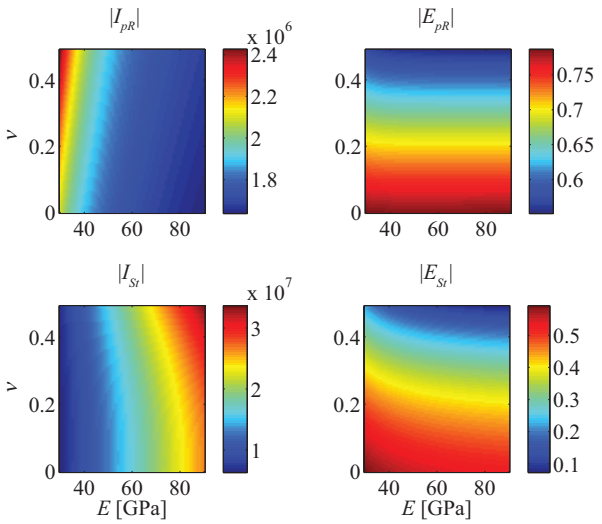

Figure 6.2: Magnitudes of impedances I_β [kgm^{-2}s^{-1}] and ellipticities E_β [-] of the pseudo-Rayleigh and Stoneley waves ($\beta = \{pR, St\}$) at the fluid/elastic-solid interface as a function of Young's modulus E and Poisson's ratio ν.

particular wave (Pierce, 2007), and the ellipticity E_β as the spectral ratio of the horizontal and the vertical particle displacements (so-called H/V-ratio) (Malischewsky & Scherbaum, 2004). The result can be written as

$$I_\beta = \left.\frac{\tilde{p}_F}{\mathrm{i}\omega\tilde{u}_3}\right|_{p=s_\beta, x_3=0} = \left.-\frac{\rho_F}{q_F}\right|_{p=s_\beta}, \tag{6.16}$$

$$E_\beta = \left.\frac{\tilde{u}_1}{\tilde{u}_3}\right|_{p=s_\beta, x_3=0} = \left.\frac{p}{q_P}\frac{s_S^2 - 2p^2 - 2q_P q_S}{s_S^2}\right|_{p=s_\beta}. \tag{6.17}$$

We note that both the impedance and ellipticity are independent of frequency as the model is non-dispersive in nature.

We have now defined the impedances and ellipticities in the (p, x_3, ω)-domain (Eqs. (6.16) and 6.17)). Their expressions are independent of the properties of the force as it is divided out. Therefore, the quantities are solely attributes of the waves. In the $(\mathbf{x}, \omega)$-domain the expressions also correctly describe the ratios of the components as the source is still divided out. Hence, they can be referred to as the plane-wave or far-field impedances and ellipticities, respectively (de Hoop, 1995).

In the limiting case of a free surface (vacuum/elastic solid), only the Rayleigh wave can exist, which is a true interface wave. The corresponding zero of Eq. (6.15) lies on the Riemann sheet where $\mathrm{Im}(q_{P,S}) \leq 0$. The ellipticity E_R follows from Eq. (6.17) for $\Delta_R(p = s_R) = 0$ and reads (Stein & Wysession, 2003; Malischewsky & Scherbaum, 2004; Borcherdt, 2009)

$$E_R = \left.-\frac{2pq_S}{s_S^2 - 2p^2}\right|_{p=s_R, x_3=0} = -2\mathrm{i}\frac{(1 - s_S^2/s_R^2)^{\frac{1}{2}}}{2 - s_S^2/s_R^2}, \tag{6.18}$$

Table 6.1: Values of material parameters of aluminum (Young's modulus E, Poisson's ratio ν, density ρ) and water (bulk modulus K_F, density ρ_F). Further, the values of propagation velocities for body wavemodes $c_\alpha = 1/s_\alpha$, $\alpha = \{P, F, S\}$, interface wavemodes $c_\beta = 1/\mathrm{Re}(s_\beta)$, $\beta = \{pR, St\}$, and impedances I_β and ellipticities E_β of the interface wavemodes (Eqs. (6.16) and (6.17)) are included.

E [GPa]	70
ν	0.33
ρ [kgm^{-3}]	2700
K_F [GPa]	2.22
ρ_F [kgm^{-3}]	1000
c_P [ms^{-1}]	6198
c_S [ms^{-1}]	3122
c_{pR} [ms^{-1}]	2923
c_F [ms^{-1}]	1490
c_{St} [ms^{-1}]	1487
I_{pR} [kgm^{-2}s^{-1}]	$-1.731 \cdot 10^6 + 1.817 \cdot 10^4$i
E_{pR}	$+7.188 \cdot 10^{-2} - 0.6364$i
I_{St} [kgm^{-2}s^{-1}]	$-2.174 \cdot 10^7$i
E_{St}	-0.2994i

where s_R is the slowness of the Rayleigh wave with $s_R > s_S$. The Rayleigh-wave ellipticity is a function of Poisson's ratio only (Malischewsky & Scherbaum, 2004). From Eq. (6.18) it can be observed that $\tilde{u}_1$ and $\tilde{u}_3$ have exactly $\frac{\pi}{2}$ phase difference, i.e., $\angle(E_R) = -\frac{\pi}{2}$, which indicates retrograde elliptical particle motion at the interface associated with the Rayleigh wave. The corresponding ellipse has principal axes that are oriented vertically and horizontally, respectively (Borcherdt, 2009).

In Figure 6.2 we depict the magnitudes of the impedances and ellipticities of the pR- and St-waves (fluid/elastic solid) as a function of Young's modulus E and Poisson's ratio ν. The values of the non-varying material parameters are taken according to a water/aluminum configuration (see Table 6.1). The magnitudes of I_{pR} and I_{St} are mainly dependent on E (variation mainly in E-direction). The magnitudes of E_{pR} and E_{St} are, however, mainly dependent on ν, similar to the ellipticity of the "true" Rayleigh wave. The phases of I_{pR} and E_{pR} vary only slightly over the (E, ν)-domain (and are therefore not displayed): $\angle(I_{pR}) \cong \pi$, which implies that the pressure and the vertical particle velocity induced by the pR-wave are out of phase; $\angle(E_{pR}) \cong -\frac{\pi}{2}$, implying that the particle motion is retrograde elliptical as for the true Rayleigh wave, but the principal axes of the ellipse are slightly rotated as the phase difference between $\tilde{u}_1$ and $\tilde{u}_3$ is not exactly $\frac{\pi}{2}$ due to s_{pR} being complex-valued (Borcherdt, 2009). The phases of the attributes of the St-wave are constant, i.e., $\angle(I_{St}) = -\frac{\pi}{2}$ and $\angle(E_{St}) = -\frac{\pi}{2}$. The latter equality shows that the St-wave also induces a retrograde elliptical particle motion.

In this section, we have only shown the behaviors of the impedances and ellipticities in the (E, ν)-domain. The attributes are less sensitive to the material density ρ of the solid and hence these dependencies are not illustrated here.

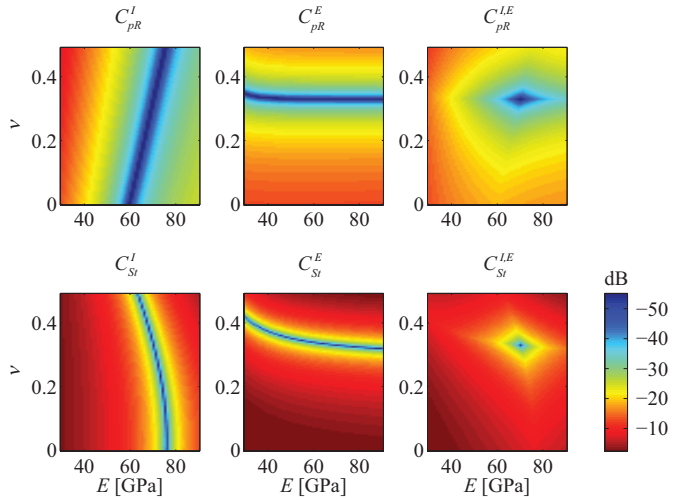

Figure 6.3: Separate cost functions for impedances I_β and ellipticities E_β ($\beta = \{pR, St\}$), and the joint cost functions in which these attributes are combined for each of the wavemodes.

6.3 Medium characterization

From Figure 6.2 it can be observed that for each of the pR- and St-waves, the impedance I_β and ellipticity E_β have quite different behaviors in the (E, ν)-domain. Obviously, both wave attributes carry the information which is present in the corresponding waveforms of the specific interface wave in a different way. This is an important observation that can be utilized when the impedance and ellipticity are simultaneously exploited to estimate the solid parameters E and ν. In this section we show a way to accomplish this.

We assume that the impedance and ellipticity of a single interface wavemode (pR or St) can be extracted from a multi-component measurement (u_1, u_3 and p_F; see Section 6.5). Then, taking advantage of the different behaviors in the (E, ν)-domain, we combine both quantities in a cost function according to (Ghose & Slob, 2006; van Dalen *et al.*, 2010a)

$$C_\beta^{I,E}(E,\nu) = \frac{|I_\beta(E,\nu) - I_{\beta,d}|}{2|I_{\beta,d}|} + \frac{|E_\beta(E,\nu) - E_{\beta,d}|}{2|E_{\beta,d}|}. \tag{6.19}$$

Here, $I_\beta(E,\nu)$ and $E_\beta(E,\nu)$ are model predictions of the impedance and ellipticity (see Figure 6.2), and $I_{\beta,d}$ and $E_{\beta,d}$ are the corresponding experimentally observed values (subscript "d" denotes "data"). The cost function is to be minimized to obtain estimates for E and ν. The two terms in the right-hand side of Eq. (6.19) are the cost functions related to the impedance and ellipticity separately (C_β^I and C_β^E), respectively (scaled by a factor 2).

In order to illustrate the behaviors of the cost functions in the (E, ν)-domain, we have performed a synthetic test for the water/aluminum configuration (Table 6.1). In this table also the theoretical values of the impedances and ellipticities computed

using Eqs. (6.16) and (6.17) are given. Taking these values as representative of the experimental observation $I_{\beta,d}$ and $E_{\beta,d}$, respectively, for both wavemodes we have computed the cost function (Eq. (6.19)) for varying values of E and ν. As the extraction of the phase of the impedance from a combined u_3,p_F-measurement can be difficult (see Section 6.5), we have only used the magnitudes of the impedances and ellipticities in the cost functions.

For each of the wavemodes the result is illustrated in Figure 6.3, where the separate cost functions and the joint cost function are shown. As the separate cost functions do not provide a unique minimum, it is clear that many combinations of E and ν can explain the observed impedance or ellipticity. However, each of the joint cost functions clearly shows a unique minimum, precisely at the values of E and ν of the aluminum (Table 6.1). Unique estimates of E and ν can thus be obtained when the impedance and ellipticity of one of the wavemodes are estimated together. The strength of this approach is that, by combining the wave attributes in the cost function, we simultaneously exploit the information in the waveforms of an interface wave as present in both the impedance and ellipticity.

In this numerical test, we have assumed that the values of the impedances and ellipticities can be extracted from a measurement with 100% accuracy. The effect of measurement inaccuracies on the estimated values of E and ν is discussed in Section 6.7.

6.4 Experiment-specific modeling

Obviously, the above estimation of E and ν involves the extraction of impedance and ellipticity of the interface wavemodes from a multi-component measurement (u_1, u_3 and p_F). Recently, an elegant way to detect the ellipticity using laser ultrasonics has been reported, showing promising results for the Rayleigh wave at the air/aluminum interface (Blum *et al.*, 2010). Similar results can be expected for the fluid/elastic-solid interface waves and therefore, in this chapter we restrict ourselves to the extraction of impedance from a simultaneous u_3,p_F-measurement.

In the experiment we have excited the waves at the fluid/elastic-solid interface using a pulsed laser source that is focused onto a narrow strip on the interface (see Figure 6.1b). It approximates an infinitely long line source and creates a thermal diffusion field and acoustic wavefronts that can be considered plane near the excitation site (Scruby & Drain, 1990; Desmet *et al.*, 1996, 1997). Depending on the energy density deposited by the laser pulse, the fields are either generated by the thermo–elastic expansion or by ablation forces (Scruby & Drain, 1990; Arias & Achenbach, 2003).

The displacement measurement has been performed using a laser Doppler vibrometer (LDV), where the LDV-beam crosses the (optically transparent) fluid and is focused at the interface. The pressure measurement has been carried out using a needle hydrophone placed very close to the surface under a small angle with the surface, and just next to the focal point of the LDV-beam (see Figure 6.1b). Details about the sample, instrumentation and acquisition in the experiment are given in Section 6.5.

To investigate the feasibility of the extraction of the interface-wave impedances from a combined (u_3, p_F)-measurement, we now first give the expressions for the acoustic response as excited by the laser source using elastic wave theory (Figure 6.1a; the specific source and the various wavemodes are explained below). We also model the effect of the interference of the LDV-beam and the acoustic waves present in the fluid (see Figure 6.1a). It is well-known that the optical refractive index of the fluid changes due to pressure variations induced by the acoustic waves (Allard *et al.*, 2004). Once the LDV-beam and the acoustic waves interfere, the laser light is perturbed. The integrated effect of all perturbations along the LDV-beam gives an (undesired) additional contribution to the surface displacement measurement.

6.4.1 Acoustic response

As we are only interested in the wave motion, we neglect the optical penetration and the thermal diffusion effects induced by the laser source. In this simplified model, laser excitation in the thermoelastic regime can be modeled by a shear traction dipole loading at the surface (Arias & Achenbach, 2003). Excitation in the ablation regime can be modeled by a vertical force (Scruby & Drain, 1990). Since we are dealing with excitation in the ablation regime, we use a line force $F(x_1, t) = S(t)\delta(x_1)$ (see Eq. (6.4)) to model the two-dimensional acoustic response (see Figure 6.1a). Here, $\delta(...)$ is the Dirac delta function and $S(t)$ is the time signature of the source representing the energy deposition, which we approximate by the four-point optimum Blackman window function. This is a pulse constituted by the sum of four different cosines functions multiplied with a box function (de Hoop & van der Hijden, 1983), and its shape is very similar to the Gaussian function that is often employed (Scruby & Drain, 1990).

The two-dimensional acoustic response, which is the solution of Eqs. (6.1)-(6.5), can be derived using the Cagniard-de Hoop method (de Hoop & van der Hijden, 1983; Chapman & Orcutt, 1985). The result is given in Appendix A. The exact Green's functions are known analytically in the time domain and the physical response in u_3 and p_F is found according to (see Eq. (6.31))

$$u_3(\mathbf{x}, t) = S(t) * G_{u_3}(\mathbf{x}, t), \tag{6.20}$$

$$p_F(\mathbf{x}, t) = \partial_t S(t) * G_{p_F}(\mathbf{x}, t), \tag{6.21}$$

when $0 < t < \infty$. Here, the asterisk denotes convolution over time, G_{u_3} and G_{p_F} are the Green's functions of the vertical particle displacement in the solid and of the fluid pressure, respectively (Eqs. (6.32) and (6.33), and (6.41)).

The response is schematically illustrated in Figure 6.1a. It consists of body waves, interface waves and lateral waves. The body waves are indicated by the solid lines: the compressional (P), shear (S) and fluid compressional (F) waves. The interface waves are indicated by short wavelets: the pseudo-Rayleigh (pR) wave and the Stoneley (St) wave. Lateral waves, i.e., either head waves (SP, FP and FS), or the FpR-wavefront radiated by the pR-wave, are indicated by dotted lines and addressed by double mode symbols (see caption Figure 6.1a).

6.4.2 Effect of optical refractive-index changes integrated along laser beam

Now, we derive a theoretical prediction of the effect of pressure-induced refractive-index changes in the fluid on the LDV-measurement. We show how the additional contribution in the measurement is related to the acoustic pressure in the fluid for arbitrary orientation γ of the LDV-beam (see Figure 6.1a).

The location of the LDV-beam is determined by the local coordinate ζ along the center of the beam (see Figure 6.1a). We denote the (unperturbed) refractive index of the fluid as $n_{F,0}$. Using the photoelastic effect, we can relate a local change (along the LDV-beam) in refractive index Δn_F to a change in local pressure p_F as (Scruby & Drain, 1990)

$$\Delta n_F(\zeta, t) = \frac{\partial n_F}{\partial p_F} p_F(\zeta, t). \tag{6.22}$$

Now, the locally perturbed wavenumber of the laser light can be written as

$$k_F(\zeta, t) = k_{F,0} \left(1 + \frac{1}{n_{F,0}} \frac{\partial n_F}{\partial p_F} p_F(\zeta, t) \right). \tag{6.23}$$

Here, $k_{F,0} = n_{F,0}\Omega/v$ is the unperturbed wavenumber, where Ω denotes the angular frequency of the light and v the light wave speed in vacuum. The resulting phase acquired by the optical signal is (Solodov *et al.*, 2009)

$$\theta = \Omega t - 2 \int_0^{L(t)} k_F(\zeta, t)\, d\zeta \tag{6.24}$$

$$= \Omega t - 2k_{F,0} \left(L_0 + u_{s,\gamma}(t) + u_{f,\gamma}(t) \right), \tag{6.25}$$

where

$$u_{f,\gamma}(t) = \frac{1}{n_{F,0}} \frac{\partial n_F}{\partial p_F} \int_0^{L(t)} p_F(\zeta, t)\, d\zeta, \tag{6.26}$$

and the length of the LDV-beam is given as $L(t) = L_0 + u_{s,\gamma}(t)$, where L_0 is the unperturbed length in the fluid and $u_{s,\gamma}(t)$ is the length variation due to the surface displacement (subscript s) at the focal point; $u_{f,\gamma}(t)$ is discussed below. In Eq. (6.25) it is taken into account that the beam picks up all changes twice.

In the unperturbed situation, the acquired (reference) phase of the optical signal is

$$\theta_{ref} = \Omega t - 2k_{F,0} L_0. \tag{6.27}$$

Subtraction of the phase related to the perturbed situation and the reference phase now yields

$$\theta - \theta_{ref} = -2k_{F,0} \left(u_{s,\gamma}(t) + u_{f,\gamma}(t) \right). \tag{6.28}$$

From this equation the total LDV-detected signal,

$$u_\gamma(t) = u_{s,\gamma}(t) + u_{f,\gamma}(t), \tag{6.29}$$

can be readily computed. It consists of two parts: the surface displacement $u_{s,\gamma}(t)$ in the direction γ, which is the desired contribution, and the integral over the refractive-index changes along the LDV-beam $u_{f,\gamma}(t)$ (Eq. (6.26)), which can be interpreted as the additional (virtual) displacement that is measured by the LDV in the fluid (the subscript f refers to the fluid). We address u_γ as the "apparent LDV-detected displacement".

For the line force excitation at the interface, which is representative of the laser excitation (see Section 6.4.1), the acoustic pressure field in the fluid is known (Eq. (6.21)). By substitution of this into Eq. (6.26) we obtain the following expression for the additional displacement

$$u_{f,\gamma}(t) = \frac{1}{n_{F,0}} \frac{\partial n_F}{\partial p_F} \left(\int_0^{L_0} G_{p_F}(\zeta, t)\, d\zeta \right) * \partial_t S(t). \tag{6.30}$$

Due to the use of the Cagniard-de Hoop scheme for the acoustic response, the integrand is known analytically (see Eqs. (6.41)-(6.45)). Hence, the integral can be readily evaluated. We note that the upper bound is taken as L_0 because the (linear) pressure field p_F is only defined for the unperturbed geometry of the system. We use Eq. (6.30) later to quantify the additional contribution to the apparent displacement waveforms, the effect on the extracted impedance (Section 6.6) and the angle dependence of the additional contribution (Section 6.7).

6.5 Experimental results and impedance extraction

In Section 6.4 we have briefly introduced the experimental set-up that we have used to perform a simultaneous (u_3, p_F)-measurement (see also Figure 6.1b). Here, we give the details about the sample, instrumentation and acquisition, and we show the results that we have obtained accordingly.

The specific configuration that we have used is aluminum in water (see Table 6.1 for properties). The aluminum sample with thickness of 50 mm has been put into an optically transparent water tank made of glass. The water layer thickness is also 50 mm. The excitation laser pulses (produced with a repetition rate of 10 Hz), generated with a broad band Nd:YAG laser, have a duration of 8 ns. A cylindrical lens has been used to focus the beam to a strip of approximately 20 μm wide and 15 mm long.

The laser Doppler vibrometer (PolyTec®) that we have used for the displacement measurement contains a high-frequency displacement decoder DD-300 having 50 kHz-20 MHz bandwidth. The smoothness and reflectivity of the aluminum sample are sufficiently high to ensure good quality of the LDV-signal. The pressure

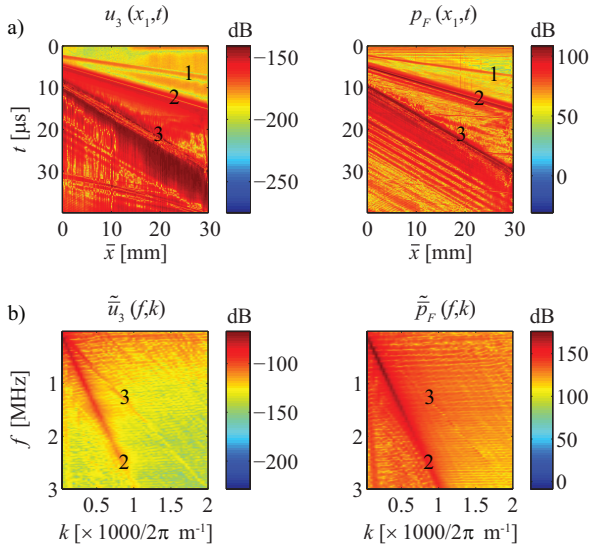

Figure 6.4: a) Observed spatiotemporal evolution of normal particle displacement u_3 (dB re. 1 m) and fluid pressure p_F (dB re. 1 Pa) using a laser Doppler vibrometer and a needle hydrophone, respectively, for a scanning source over a distance of $\bar{x} = x_1 - x_0 = 30$ mm (the smallest source-receiver distance $x_0 = 13$ mm). The P-wave is indicated by (1), the pR-wave by (2) and the interfering F- and St-wave arrivals by (3). b) Corresponding frequency-wavenumber domain spectra $|\tilde{\tilde{u}}_3(f,k)|$ and $|\tilde{\tilde{p}}_F(f,k)|$. The dominating joint F- and St-wave spectra have been eliminated as much as possible by tapering the time-domain signals to clearly identify the pR-wave spectra. The P-wave spectra are too weak to be distinguished.

measurement has been carried out using a needle hydrophone HNP-0400 with a preamplifier AH-2010 (Onda®), calibrated over 250 kHz-20 MHz.

During the experiment we have moved the excitation beam over a distance of 30 mm in x_1-direction with steps of $\Delta x_1 = 200$ μm using a scanning stage, keeping the position of the receivers fixed. The smallest source-receiver distance is 13 mm. For every location of the source, we have averaged the signals 256 times to improve the signal/noise ratio.

In Figure 6.4a the experimentally observed u_3 and p_F are shown. We have applied a low-pass filter at 3.5 MHz to all data to eliminate high-frequency noise. The p_F-data have been deconvolved by the frequency-dependent sensitivity of the needle hydrophone/amplifier combination. The u_3-data have been divided by the refractive index of water, $n_{F,0} = 1.333$ (Scruby & Drain, 1990), because the laser Doppler vibrometer is calibrated for measurements in air. In Figure 6.4a we clearly observe the P-wave arrival (appr. 6160 ms^{-1}), the pR-wave arrival (appr. 2960 ms^{-1}) and an interference of the F- and St-wave arrivals (appr. 1500 ms^{-1}); the latter arrivals cannot be distinguished from each other due to the small difference in propagation velocity (see Table 6.1). The observed propagation velocities closely match the predicted values (see Table 6.1). In addition, some (undesired) reflections from the sides and the sample's back can be distinguished (weak curved arrivals).

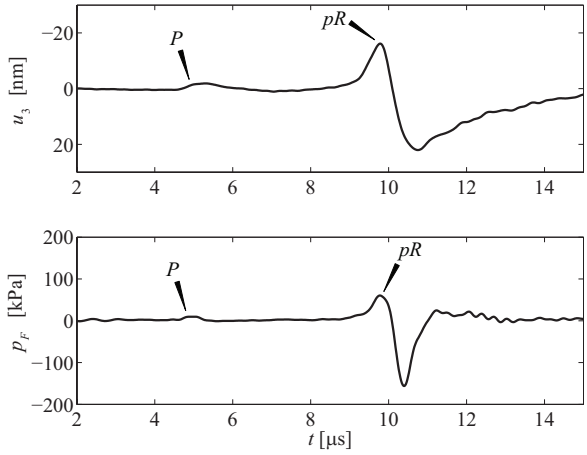

Figure 6.5: Observed normal particle displacement u_3 and fluid pressure p_F using a laser Doppler vibrometer and a needle hydrophone, respectively, for source-receiver distance of 28 mm. Only the time window of the P- and pR-waves is shown. The data have been filtered using a low-pass filter at $f = 3.5$ MHz.

In Figure 6.5 we show the typical waveforms of the P- and pR-wave in u_3 and p_F (in this case $x_1 = 28$ mm). We have time-windowed the response around the P- and pR-waves because the St-wave cannot be distinguished from the less interesting F-wave; therefore, we only focus on the extraction of the pR-wave impedance.

We have computed the (f, k)-domain spectra of u_3 and p_F using a standard two-dimensional Fourier transform algorithm (cf. Eq. (6.6)). Before applying the transforms, the data have been tapered in time to eliminate the interfering F- and St-waves and all subsequent arrivals, using a quarter period of a cosine squared (50 kHz) as taper function. The resulting spectra $\tilde{\tilde{u}}_3(f, k)$ and $\tilde{\tilde{p}}_F(f, k)$ are shown in Figure 6.4b. The combined F, St-spectra have not completely been filtered, and the P-wave is too weak to be identified. The pR-spectra can be clearly distinguished and it is confirmed that the wave propagates without dispersion. The frequency content of the pR-wave in $\tilde{\tilde{u}}_3$ is more narrow than that in $\tilde{\tilde{p}}_F$. This is reasonable since the fluid pressure is proportional to the divergence of the displacement, which involves multiplication by ω in the (k, ω, x_3)-domain; the more narrow frequency content in u_3 can also be observed from the waveforms in Figure 6.5.

Now, the impedance $I(f, k)$ can be computed from the measured response by division of the two spectra and by $\mathrm{i}\omega$. Its magnitude is shown in Figure 6.6. This figure shows the advantage of using a scan of measurements as the pR-wave impedance can be easily identified in the (f, k)-domain. In principle, however, a single source-receiver combination would suffice to extract the impedance in the $(\mathbf{x}, f)$-domain. The impedance $|I(f, k)|$ is relatively constant over all (f, k)-combinations that belong to the pR-wave, particularly between 0.25-1.5 MHz. However, it can be verified that it deviates from the magnitude of the theoretical plane-wave impedance, $|I_{pR}| = 1.731 \cdot 10^6$ kgm^{-2}s^{-1} (see Eq. (6.16) and Table 6.1). The reason is that, apart from measurement inaccuracies, in the displacement measurement also

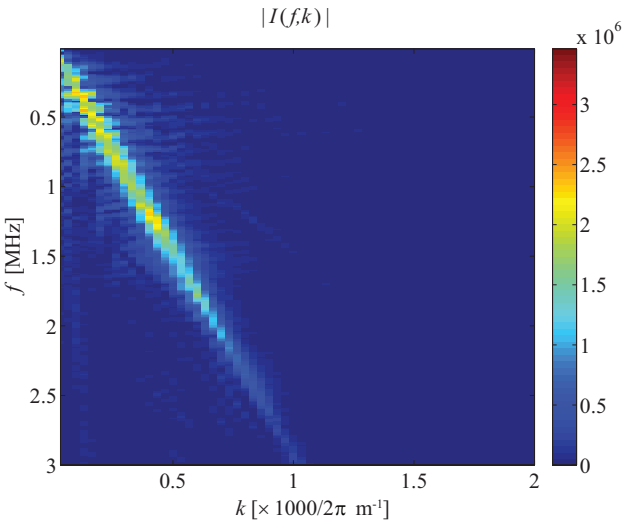

Figure 6.6: Magnitude of extracted impedance $I(f,k)$ as obtained by division of (the experimentally observed) $\tilde{\tilde{p}}_F(f,k)$ and $\tilde{\tilde{u}}_3(f,k)$ (see Figure 6.4b), and by $\mathrm{i}\omega$.

the effect of refractive-index changes along the LDV-beam is included, resulting in a modified measurement (see Eq. (6.29)). In the next section we quantify this effect.

The phase of the pR-wave impedance cannot be successfully retrieved from $\angle I(f,k)$ due to the small but unknown difference between the locations of the two detection spots, i.e., the focal point of the LDV-beam and the tip of the needle hydrophone (it can be verified that the waveforms in p_F in Figures 6.4a and 6.5 arrive slightly later than in u_3). This results in an additional unknown phase difference.

In conclusion, we can say that the extraction of the pR-wave impedance from a simultaneous (u_3, p_F)-measurement at the fluid/elastic-solid interface is feasible. Obviously, the extraction of the St-wave impedance is also feasible when this wave can be detected as a separate arrival, i.e., for configurations where its velocity is sufficiently different from the F-wave velocity or far away from the generation region, where the F-wave has vanished in the interface response.

6.6 Experimental observations versus model predictions

In this section we compare the experimentally observed waveforms using the laser Doppler vibrometer and the needle hydrophone with modeled equivalents. We quantify the effect of the pressure-induced refractive-index changes integrated along the LDV-beam on the predicted waveforms, and illustrate the influence on the impedance extracted from the (u_3, p_F)-measurement.

In Figure 6.5 we have shown the typical P- and pR-waveforms observed in u_3 and p_F. Now, the corresponding modeled waveforms obtained using the acoustic

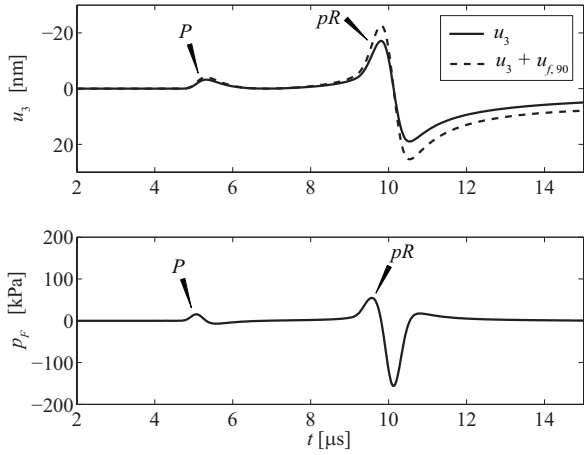

Figure 6.7: Modeled normal particle displacement u_3 and fluid pressure p_F for source-receiver distance of 28 mm excited by a line force with $S_{max} = 2.176 \cdot 10^{-3}$ Nm^{-1} and center frequency $f_0 = 1$ MHz. A prediction of the apparent LDV-detected displacement for $\gamma = 90°$, which includes the effect of refractive-index changes in the trespassed fluid, is also shown (see Eq. (6.29): u_3 is equivalent to $u_{s,90}$).

response at the interface only (Eqs. (6.20) and (6.21)) are shown in Figure 6.7 (the additional contribution of $u_{f,90}$ is referred to below). For the involved fitting parameters we have chosen $S_{max} = 2.176 \cdot 10^{-3}$ Nm^{-1} (force magnitude) and $f_0 = 1$ MHz (center frequency of the Blackman pulse; Section 6.4.1), where we have taken the pR-waveform in p_F as reference (cf. Figures 6.5 and 6.7). For these choices, the experimentally observed waveforms are very similar to those predicted theoretically. The measured P-wave in p_F is a bit weaker compared to the predicted result, and in u_3 the observed pR-wave magnitude is slightly larger, especially in the tail of the waveform. However, generally the magnitudes are consistent in the two components u_3 and p_F simultaneously, as well as the magnitudes of the P- and pR-waves relative to each other in the separate components. In both cases, this is independent of the fitting parameter values. The ripples that are present around 2 μs and immediately after the pR-wave in Figure 6.5 have no modeled equivalents. We consider them as noise. Further, by isolating different contributions in the acoustic response (Eqs. (6.20) and (6.21)) (van Dalen *et al.*, 2011), it can be shown that there is a weakly-excited S-wave present at the onset of the (modeled) pR-waveforms.

It can be verified that the smallest wavelength present in the observed responses (Figures 6.4a-6.5) is much larger than the width of the focal strip of the excitation laser beam. This validates the line source assumption in the model for the acoustic response which we have used to compute the theoretical waveforms.

Now, we address the effect of pressure-induced refractive-index changes on the apparent LDV-detected displacement (Eq. (6.29)). We have evaluated the integral over ζ in Eq. (6.30) numerically using an adaptive 8-point Legendre-Gauss algorithm (Abramowitz & Stegun, 1972; Davis & Rabinowitz, 1975) that is able to handle the integrable singularities present in the integrand (i.e., branch points; see Appendix

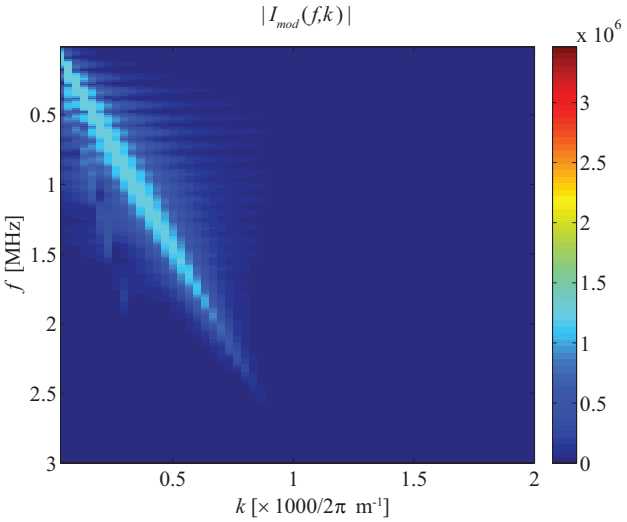

Figure 6.8: Predicted magnitude of modified impedance $I_{mod}(f,k)$ as obtained by division of the modeled $\tilde{\tilde{p}}_F(f,k)$ (Eq. (6.21)) and $\tilde{\tilde{u}}_{90}(f,k)$ (Eq. (6.29): including the effect of refractive-index changes), and by $\mathrm{i}\omega$.

A). Using $\partial n_F/\partial p_F = 1.444 \cdot 10^{-10}$ Pa^{-1} for water at 25°C (Scruby & Drain, 1990), a prediction of the additional contribution $u_{f,90}$ can be computed. The result is depicted in Figure 6.7 (for $\gamma = 90°$): the (modeled) additional contributions to the waveforms are in phase with and add up to the waveforms in the surface displacement so that the modeled total waveforms are (still) very similar to those observed experimentally (Figure 6.5). The influence of $u_{f,90}$ is significant, particularly for the pR-wave.

To quantify the implication of the modified displacement signal on the extracted pR-wave impedance, we have calculated the responses for a scanning source to mimic the experiment using Eqs. (6.21) and (6.29), by choosing the same force magnitude and center frequency as discussed above. A prediction of the magnitude of the modified impedance $I_{mod}(f,k) = \tilde{\tilde{p}}_F/(\mathrm{i}\omega\tilde{\tilde{u}}_{90})$ is shown in Figure 6.8. To extract the involved modified pR-wave impedance $|I_{pR,mod}|$ from $|I_{mod}(f,k)|$, we can take the average over all (f,k)-combinations pertaining to the pR-wave since the wave is non-dispersive. Taking 0.25-1.5 MHz, over which the value of $|I_{mod}(f,k)|$ is relatively constant, the result is $|I_{pR,mod}| = 0.74 \cdot |I_{pR}|$. Obviously, the extracted result is smaller than the (theoretical) plane-wave impedance of the pR-wave. This is consistent with the observation in Figure 6.7, where the (prediction of the) apparent LDV-detected displacement is larger than the surface displacement, resulting in larger spectral values in the denominator of $I_{mod}(f,k)$.

Comparing the (modeled) modified impedance (Figure 6.8) with the impedance as obtained from the measurement (Figure 6.6), and taking their averaged values over the mentioned frequency range, we find that the pR-wave impedance extracted from the measured data $|I_{pR,d}| = 1.51 \cdot |I_{pR,mod}|$ (where the subscript d refers to

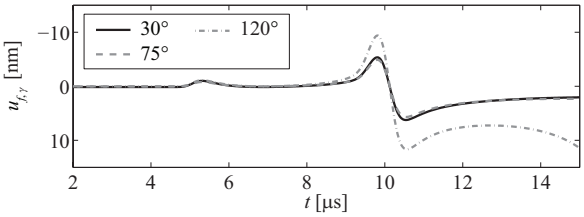

Figure 6.9: Prediction of additional contribution to LDV-detected displacements due to pressure-induced refraction index changes integrated along the laser beam for different orientation angles γ.

data; cf. Eq. (6.19)). This difference between the experiment and the model is quite significant and is, naturally, related to the larger pR-wave magnitude in the predicted apparent LDV-detected displacement compared to that in the experimentally observed displacement (cf. Figures 6.7 and 6.5). Based on the measurement inaccuracies in the equipment, the estimated uncertainty in the measurement is roughly $\pm 35\%$, which is smaller than the actual difference. We believe that the larger deviation can be due to some calibration error, particularly because the experimentally observed waveforms are almost identical to the modeled equivalents. Another possible cause is a misalignment of the two detection spots (focal point of LDV and tip of needle hydrophone) so that the two measurements are performed at different points on the wavefront. Once the amplitude is not exactly constant over the wavefront (in x_2-direction; see Figure 6.1a), this introduces magnitude inconsistencies.

6.7 Discussion

The additional contribution to the apparent LDV-detected displacement does not only modify the extracted impedance, but also the ellipticity once this would be extracted from a measurement. Hence, for different orientations of the LDV-beam (different values of γ), we show the modeled additional contribution $u_{f,\gamma}$ to the apparent displacement in Figure 6.9. The magnitude of $u_{f,\gamma}$ varies a little over $0 < \gamma < 90°$, but the contribution to the pR-wave rises for $\gamma > 90°$ and becomes slightly broader. This is because γ approaches the angle under which the FpR-wavefront is radiated by the pR-wave (149.4°; cf. Figure 6.1a), which means that the LDV-beam and the FpR-wavefront coincide more and more, and the length over which the beam and the acoustic waves interfere increases. The additional contribution to the P-wave would also increase once γ approaches the angle of radiation of the FP-head wave (166.1°). Obviously, the effect on the ellipticity can be very significant when it is extracted from a measurement where a LDV-beam is used with $\gamma > 90°$ (Nishizawa *et al.*, 1998), or when light scattered in many directions (including $\gamma > 90°$) is collected (Blum *et al.*, 2010).

To quantify the effect of the involved measurement uncertainties on the estimated values of E and ν using impedance and ellipticity simultaneously in the joint cost function (Section 6.3), we can apply perturbations to the extracted values $|I_{\beta,d}|$ and

$|E_{\beta,d}|$. Assuming that the experimental equipment is recalibrated and/or properly aligned to ensure higher measurement accuracies, and that the effect of the refractive-index changes can be corrected for, we take perturbations of $\pm 5\%$ for both the extracted impedance and the ellipticity. We find that the estimated values of E and ν can deviate quite significantly from the true values for the pR-wave, i.e., 49% and 20% at most. Using the St-wave, however, much more stable estimates of E and ν are obtained: at most 4% deviation for E and 5% deviation for ν. This difference between the pR- and St-waves is due to the much stronger sensitivity of the St-wave impedance and ellipticity to E and ν compared to those of the pR-wave (see Figure 6.2), which results in a sharper (see Figure 6.3) and, obviously, in a more stable minimum in the joint cost function of the St-wave.

6.8 Conclusions

The impedance and ellipticity of an interface wave are attributes of the wave that interrelate the full waveforms as observed in the different components. The attributes are defined as the spectral ratios of the fluid pressure at the interface and the normal particle velocity, and of the tangential and normal particle displacements, respectively.

In this chapter we showed that, for each of the pseudo-Rayleigh (pR) and Stoneley (St) waves at the fluid/elastic-solid interface, the impedance and ellipticity have quite different functional dependencies on the Young's modulus and Poisson's ratio. By combining the wave attributes in a joint cost function, unique estimates of these parameters can be obtained. Measurement inaccuracies in the impedance and ellipticity can strongly influence the estimated values of Young's modulus and Poisson's ratio when using the pR-wave. Using the St-wave, however, very stable estimates were obtained. This illustrates the feasibility of medium characterization using the interface-wave impedance and ellipticity, particularly when exploited simultaneously.

Subsequently, we showed that the impedance of the ultrasonic pR-wave at the water/aluminum interface can be successfully extracted in the frequency-wavenumber domain. This was accomplished with laser excitation and a simultaneous normal particle displacement and fluid pressure measurement using a laser Doppler vibrometer (LDV) and a needle hydrophone, respectively. The St-wave impedance could not be extracted in the water/aluminum configuration due to strong interference with the fluid compressional wave. The extraction of ellipticity has recently been performed by others (Blum *et al.*, 2010).

The extracted impedance does not only include the fluid pressure and normal particle displacement at the interface (which would give the plane-wave impedance), but also an additional contribution to the displacement measurement due to the interference of the LDV-beam, which crosses the fluid, and the acoustic waves in the fluid. The acoustic waves perturb the laser light by modifying the optical refractive index due to pressure variations. By integrating the refractive-index changes along the LDV-beam using the modeled fluid pressure, we predicted that the effect decreases the extracted impedance by some 26% compared to the theoretical plane-wave impedance. The actual impedance extracted from the experiment is, however,

51% larger than this model prediction. As there is excellent agreement between the shape of the observed and predicted pR-waveforms in both the displacement and fluid pressure, we believe that this difference is due to a calibration error in the measurement equipment or due to a misalignment in the detection points of the LDV and the needle hydrophone.

6.9 Appendix A: Cagniard-de Hoop solution

Here, we give the analytical expressions of the Green's functions associated with the vertical particle displacement and fluid pressure in the fluid/elastic-solid configuration excited by a line force applied normal to the interface, i.e., $F(x_1,t) = S(t)\delta(x_1)$ (Eqs. (6.8) and (6.9)), where $S(t)$ is the time signature. The functions are obtained using the Cagniard-de Hoop method (de Hoop & van der Hijden, 1983). We have followed the derivation of Chapman & Orcutt (1985) because in there the same transforms are used as we apply (Eq. (6.6) with $k = \omega p$). As the Cagniard-de Hoop method is well-established we only give the outcomes. We assume that $c_S > c_F$ and take x_3 positive downward (see Figure 6.1a).

The response u_3 in the solid ($x_3 \geq 0$) due to the line force is found by convolution of the associated Green's functions $G_{u_3}(\mathbf{x},\tau)$ and the time signature of the force according to

$$u_3(\mathbf{x},t) = \int_0^t S(t-\tau) G_{u_3}(\mathbf{x},\tau)\, d\tau, \tag{6.31}$$

when $0 < t < \infty$ and where τ is an auxilary time variable. The expressions that constitute $G_{u_3}(\mathbf{x},\tau) = G_{u_{3,P}}(\mathbf{x},\tau) + G_{u_{3,S}}(\mathbf{x},\tau)$ read

$$G_{u_{3,P}} = \begin{cases} 0, & -\infty < \tau < T_P, \\ \frac{1}{\pi}\mathrm{Im}(q_P \tilde{A}_P \partial_\tau p)\Big|_{p=\xi_P}, & T_P < \tau < \infty, \end{cases} \tag{6.32}$$

$$G_{u_{3,S}} = \begin{cases} 0, & -\infty < \tau < T_{SP}, \\ \frac{1}{\pi}\mathrm{Im}(-p\tilde{A}_S)\partial_\tau p\Big|_{p=\xi_{SP}}, & T_{SP} < \tau < T_S, \\ \frac{1}{\pi}\mathrm{Im}(-p\tilde{A}_S \partial_\tau p)\Big|_{p=\xi_S}, & T_S < \tau < \infty, \end{cases} \tag{6.33}$$

where, using $R^2 = x_1^2 + x_3^2$,

$$\xi_P = \frac{x_1}{R^2}\tau + \mathrm{i}\frac{x_3}{R^2}(\tau^2 - T_P^2)^{\frac{1}{2}}. \tag{6.34}$$

$$\xi_{SP} = \frac{x_1}{R^2}\tau - \frac{x_3}{R^2}(T_S^2 - \tau^2)^{\frac{1}{2}}. \tag{6.35}$$

$$\xi_S = \frac{x_1}{R^2}\tau + \mathrm{i}\frac{x_3}{R^2}(\tau^2 - T_S^2)^{\frac{1}{2}}. \tag{6.36}$$

$$T_P = Rs_P, \tag{6.37}$$

$$T_{SP} = x_1 s_S + x_3(s_S^2 - s_P^2)^{\frac{1}{2}}, \tag{6.38}$$

$$T_S = Rs_S. \tag{6.39}$$

Here, ξ_P denotes the Cagniard path associated with the P-wave running into the complex slowness (p) plane; ξ_{SP} and ξ_S denote the Cagniard paths associated with the SP-head wave (see Figure 6.1a) and the S-wave, respectively, running along the real p-axis and running into the complex p-plane. T_P is the arrival time of the P-wave, T_{SP} that of SP-head wave, and T_S that of the S-wave. The SP-wave is only present if

$$\frac{x_1}{R} > \frac{s_P}{s_S}. \tag{6.40}$$

In Eqs. (6.32) and (6.33) $\tilde{A}_P$ and $\tilde{A}_S$ are the amplitude factors of the (p, x_3, ω)-domain solution in the solid; see Eqs. (6.7) and (6.8). The involved square roots (vertical slownesses) $q_\alpha = (s_\alpha^2 - p^2)^{\frac{1}{2}}$ are defined such that $\mathrm{Im}(q_\alpha) \leq 0$, $\alpha = \{P, F, S\}$, along the Cagniard paths. The amplitude factors are singular at the body-wave slownesses (branch points) s_α and at the Stoneley pole (s_{St}), which is located at the real p-axis and only crossed by the Cagniard paths $\xi_P(\tau > T_P)$ and $\xi_S(\tau > T_S)$ when $x_3 = 0$ (the St-wave arrives later than all other waves) (de Hoop & van der Hijden, 1983). The pseudo-Rayleigh pole lies on another Riemann sheet close to the $\xi_P(x_3 = 0)$- and $\xi_S(x_3 = 0)$-paths (see also Section 6.2) (van der Hijden, 1984).

The response in the fluid pressure ($x_3 \leq 0$) due to the line force is found by convolution of the associated Green's function $G_{p_F}(\mathbf{x}, \tau)$ and the time derivative of the force (de Hoop & van der Hijden, 1983). The expression of $G_{p_F}(\mathbf{x}, \tau)$ reads

$$G_{p_F} = \begin{cases} 0, & -\infty < \tau < T_{FP}, \\ \frac{1}{\pi}\mathrm{Im}\left(\tilde{A}_F\right)\partial_\tau p\Big|_{p=\xi_{FP}}, & T_{FP} < \tau < T_F, \\ \frac{1}{\pi}\mathrm{Im}\left(\tilde{A}_F \partial_\tau p\right)\Big|_{p=\xi_F}, & T_F < \tau < \infty, \end{cases} \tag{6.41}$$

where

$$\xi_{FP} = \frac{x_1}{R^2}\tau - \frac{|x_3|}{R^2}(T_F^2 - \tau^2)^{\frac{1}{2}}, \tag{6.42}$$

$$\xi_F = \frac{x_1}{R^2}\tau + \mathrm{i}\frac{|x_3|}{R^2}(\tau^2 - T_F^2)^{\frac{1}{2}}, \tag{6.43}$$

$$T_{FP} = x_1 s_P + |x_3|(s_F^2 - s_P^2)^{\frac{1}{2}}, \tag{6.44}$$

$$T_F = R s_F. \tag{6.45}$$

Here, ξ_{FP} and ξ_F denote the Cagniard paths associated with the FP-head wave and the F-body wave, respectively, running along the real p-axis and running into the complex p-plane. T_{FP} is the arrival time of the FP-head wave (see Figure 6.1a), and T_F that of the F-wave. The FP-wave is only present if

$$\frac{x_1}{R} > \frac{s_P}{s_F}. \tag{6.46}$$

In Eq. (6.41) $\tilde{A}_F$ is the amplitude factor of the (p, x_3, ω)-domain solution of in the fluid ($x_3 \leq 0$); see Eq. (6.9).

The expressions of the Green's functions are known analytically throughout the entire $(\mathbf{x}, t)$-domain; they are used in the main text of the chapter.

Chapter 7

Impedance and ellipticity of fluid/porous-medium interface waves: medium characterization and simultaneous displacement - pressure measurements

7.1 Introduction

In the previous chapter we have argued that the impedance and ellipticity of an interface wave capture information about the medium in the multi-component waveforms. For a water/aluminum configuration, we have shown that the impedance of the ultrasonic pseudo-Rayleigh (pR) wave can be extracted successfully from the measurement of the normal component of the particle velocity and the fluid pressure at the interface, using a laser Doppler vibrometer (LDV) and a needle hydrophone, respectively. The Stoneley (St) wave could not be detected as a separate wavemode due to strong interference with the fluid body wave having nearly the same velocity. Further, we have illustrated that the Young's modulus and the Poisson's ratio can be accurately determined when the impedance and ellipticity of these fluid/elastic-solid interface waves are used simultaneously by combining them in a cost function, particularly for the St-wave.

The counterparts of the pR- and St-waves at the fluid/porous-medium interface waves are the pseudo-Rayleigh (pR) and pseudo-Stoneley (pSt) waves, respectively, as discussed in detail in Chapters 4 and 5. Only a few authors have reported on the experimental detection of these waves at the interface between water and a water-saturated porous medium at ultrasonic frequencies. Mayes *et al.* (1986) have experimentally validated the existence of the interface waves using a periodically corrugated sample surface. They have detected the pR- and pSt-waves, and, in addition, the slower true interface wave which only exists for certain parameters

combinations at the open-pore interface (Feng & Johnson, 1983a). Allard *et al.* (2004) have observed the pSt-wave at a flat interface using laser excitation in the thermoelastic regime (see Section 6.4) and a laser Doppler vibrometer (LDV) for the detection; in their configuration the pR-wave is absent due to the shear-wave velocity being smaller than fluid-wave velocity. Other publications in this field involve measurements at air/porous-medium interfaces (Nagy, 1992; Adler & Nagy, 1994; Allard *et al.*, 2002, 2003). In all cases the waves have been detected using a single-component measurement only (e.g., particle displacement u_3 or fluid pressure p_F).

Concerning the medium characterization using the fluid/porous-medium interface waves, there is a focus on permeability estimation using the attenuation of pSt-waves along a borehole (e.g., Burns, 1990; Tang & Cheng, 1996). Obviously, to use the attenuation for parameter estimation, only a single-component measurement is required. To our knowledge, Tang & Cheng (2004) are the only ones who employ the full waveform of the pSt-wave to estimate permeability and make use of the travel time and the frequency content. However, they use the information present in a single component only (p_F).

Hence, the extension of the framework introduced in Chapter 6 to the fluid/porous-medium pR- and pSt-waves is challenging, both in view of the two–component (u_3, p_F) experimental detection and the extraction of the impedances, and in view of the estimation of medium parameters using three-component (u_1, u_3, p_F) full waveforms. Therefore, in this chapter we aim to investigate the feasibility of using the ultrasonic fluid/porous-medium interface waves for the estimation of medium parameters, by simultaneously exploiting the corresponding impedances and ellipticities.

First, we define the impedances and ellipticities, and show their behaviors as a function of Young's modulus and Poisson's ratio, being parameters related to the porous frame, and as a function of permeability and porosity, which are parameters that govern the attenuation mechanism associated with the relative fluid-solid motion. For comparison, we include the behaviors of the wave attenuations because they are commonly exploited in medium characterization (see above). Then, using the joint cost functions as introduced in Section 6.3, we show that unique estimates of the four parameters can be obtained by combining either the impedance and ellipticity or the impedance and attenuation of the interface wavemodes. Next, we investigate the feasibility of the extraction of the interface-wave impedances from a simultaneous particle displacement and fluid pressure measurement using the same experimental set-up as described in Section 6.4. In this case, we use water-saturated QF20, which is an artificial porous material (Johnson *et al.*, 1994). Finally, we compare the experimental results with the theoretical predictions using the computational model developed in Chapters 4 and 5.

7.2 Impedance and ellipticity

In this section we derive expressions for the impedance and ellipticity associated with the pR- and pSt-waves at the fluid/porous-medium interface. Similar to the derivation for the fluid/elastic-solid interface waves, we use the plane-wave domain

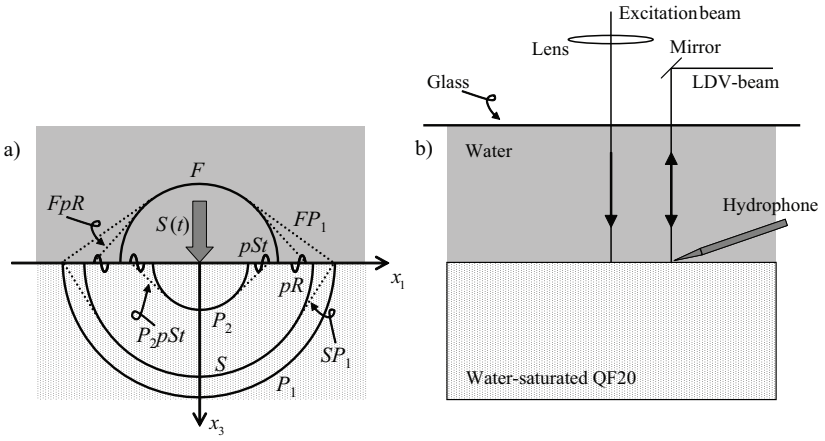

Figure 7.1: a) Fluid/porous-medium configuration, model for the acoustic response (laser modeled as normal line force with signature $S(t)$) and schematic response: fast (P_1) and slow (P_2) compressional waves, shear (S) wave, fluid (F) wave, pseudo-Rayleigh (pR) wave and pseudo-Stoneley (pSt) wave. The double-mode symbols (e.g., SP_1) indicate lateral waves: the first symbol denotes the wavemode of the specific arrival; the second denotes that from which it is radiated. Here, the F-wave velocity is assumed higher than the P_2-wave velocity. For clarity, we have omitted some arrivals: FS, P_2P_1, P_2S, P_2pR and P_2F. b) Schematic overview of the experimental set-up used for the simultaneous detection of waves at water/water-saturated QF20 interface.

solutions of the governing equations that correspond to interface waves (Section 6.2). We illustrate the behavior of the impedance and ellipticity of the pR- and pSt-waves as a function of Young's modulus and Poisson's ratio, and of permeability and porosity.

We consider the configuration displayed in Figure 7.1a, which is the same as discussed in Section 4.2: a fluid half-space on top of a fluid-saturated porous medium. We do not repeat the involved parameters, the governing equations and their solution but we just refer to Chapter 4. The only modification is that we consider wave propagation in only two dimensions here ((x_1, x_3)-plane): the field variables in the governing equations are functions of x_1 and x_3 only, and $\mathbf{u}(\mathbf{x}, t) = (u_1, u_3)^T$ (displacement of the solid), $\mathbf{U}(\mathbf{x}, t) = (U_1, U_3)^T$ (displacement of the fluid). Further, all derivatives in the x_2-direction vanish, which implies that $p_r = p_1$ and $p_2 = 0$ in the (p_r, ω, x_3)-domain solutions, and that the SH-mode cannot exist (Section 4.3 and Appendix A of Chapter 4).

The source that has been included in Figure 7.1a is assumed to be a line source (Dirac distribution in the x_1-direction) in view of the experiment-specific modeling (Section 7.4). However, for the current derivation of impedance and ellipticity this is not strictly required (cf. Section 6.2).

The wave slownesses of the pR- and pSt-waves are zeroes of the poroelastic Stoneley dispersion equation $\Delta_{St}(p_1, \omega) = 0$ (see Eq. (4.35)). As shown in Chapter 5, the zero related to the pSt-wave ($p_1 = s_{pSt}$) is complex-valued, with $\mathrm{Re}(s_{pSt}) > s_F$ and $\mathrm{Im}(s_{pSt}) < 0$, and lies either on the $\mathrm{sgn}(\mathrm{Im}(q_{P1}, q_{P2}, q_F, q_S)) = (- + --)$

Riemann sheet or on the $(----)$ sheet, depending on frequency. The zero related to the pR-wave ($p_1 = s_{pR}$) is also complex-valued, with $\mathrm{Re}(s_{pR}) > \mathrm{Re}(s_S)$ and $\mathrm{Im}(s_{pR}) < 0$, and lies either on the $(-++-)$ sheet or on the $(--+-)$ sheet, and depends on frequency as well; the wave exists only when $\mathrm{Re}(s_S) < s_F$. The velocity and attenuation of the interface waves are fully characterized by these slownesses, i.e., by their real and imaginary parts. At the interface, their far-field waveforms are fully captured by the residue contributions of the corresponding poles once the response (Eqs. (5.13) and (5.14)) is transformed to the $(\mathbf{x}, t)$-domain (see Chapter 5: method I).

Using the definitions of the impedances and the ellipticities of the interface wavemodes as given in Section 6.2, we find ($\beta = \{pR, pSt\}$)

$$I_\beta = \frac{\tilde{p}_F}{\mathrm{i}\omega\tilde{u}_3}\bigg|_{p=s_\beta,x_3=0} = -\frac{\rho_F}{s_S^2}\times \frac{(s_S^2-2p^2)(q_{P1}\phi_{P1}s_{P2}^2H_{P2} - q_{P2}\phi_{P2}s_{P1}^2H_{P1}) + 2p^2\Delta_2\phi_S}{\phi^2\rho_F\hat{\rho}_{22}^{-1}q_{P1}q_{P2}\Delta_1 + q_F\Delta_2}\bigg|_{p=s_\beta}, \quad (7.1)$$

$$E_\beta = \frac{\tilde{u}_1}{\tilde{u}_3}\bigg|_{p=s_\beta,x_3=0} = \frac{p}{s_S^2}\,\frac{(s_S^2-2p^2)\Delta_4 - 2q_S\Delta_5}{\Delta_5 - 2Gp^2(q_{P1}-q_{P2})}\bigg|_{p=s_\beta}, \quad (7.2)$$

where $\Delta_4 = s_{P2}^2K_{P2} - s_{P1}^2K_{P1}$ and $\Delta_5 = q_{P1}s_{P2}^2K_{P2} - q_{P2}s_{P1}^2K_{P1}$. I_β and E_β can be addressed as the far-field or plane-wave impedances and ellipticities, respectively (de Hoop, 1995). The impedance relates the fluid phase to the solid phase and it is therefore a "coupling impedance" (see Section 3.3). In the remainder of this chapter we simply refer to it as the (plane-wave) impedance.

Now, we illustrate the behavior of the impedances and ellipticities as a function of the Young's modulus E and Poisson's ratio ν of the solid frame (Figure 7.2), which are purely elastic parameters (Achenbach, 1973), and as a function of the permeability k_0 and porosity ϕ (Figures 7.3 and 7.4) being parameters of the porous frame that govern the attenuation mechanism (see Eq. (2.64)); we note that ϕ also influences the elastic and inertial mechanisms. We choose the values of the other (non-varying) material parameters in agreement with those of a water/water-saturated QF20 configuration (Johnson *et al.*, 1994); see Table 7.1. The properties of the water filling the upper half-space are $K_F = K_f$ and $\rho_F = \rho_f$.

The existence of the wavemodes has been verified for all parameter combinations shown in the Figures 7.2-7.4 using the Principle of the Argument (Fuchs *et al.*, 1964; van Dalen *et al.*, 2010b). We only show the magnitudes of the impedances and ellipticities as their phases hardly vary: $\angle I_{pR} \cong 3$, $\angle E_{pR} \cong -1.3$, $\angle I_{pSt} \cong -1.5$, $\angle E_{pSt} \cong -1.6$. These values show that the particle motions of the pR- and pSt-waves at the interface are retrograde elliptical (with the principal axes of the ellipse slightly rotated; cf. Section 6.2), and that the fluid pressure and the normal component of the particle velocity are approximately out-of-phase for the pR-wave and have approximately $\pi/2$ phase difference for the pSt-wave. This is comparable to the pR- and St-waves at the fluid/elastic-solid interface (see Section 6.2). Apart from the magnitudes of the impedances and ellipticities, we incorporate the attenuations in Figures 7.2-7.4. This enables us to compare the behaviors of the impedances and

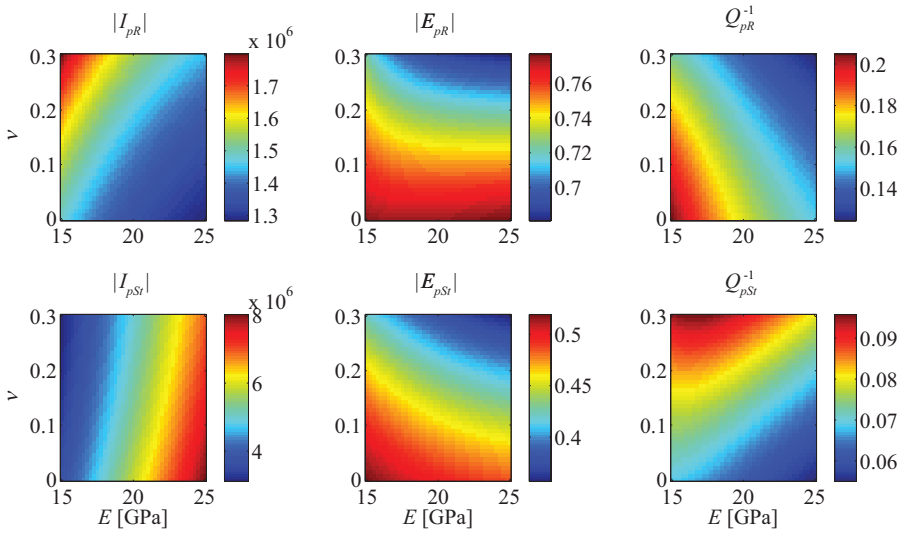

Figure 7.2: Magnitudes of impedances [kgm^{-2}s^{-1}], ellipticities [-] and attenuations [-] of the pR- and pSt-waves in the (E, ν)-domain for $f = 820$ Hz.

ellipticities with that of the attenuation of the pSt-wave, which is known to have particularly strong k_0-sensitivity (Rosenbaum, 1974; Winkler *et al.*, 1989; Burns, 1990). Here, we express the attenuations by the inverse quality factors, $Q_\beta^{-1} = 2 \cdot |\mathrm{Im}(s_\beta)/\mathrm{Re}(s_\beta)|$.

The ranges of E and ν in Figure 7.2 are restricted by two constraints. The first constraint is the physical requirement for the relation between porosity and the solid and grain bulk moduli (Eq. (2.24)),

$$\phi \leq 1 - \frac{K_b}{K_s} = 1 - \frac{1}{3(1-2\nu)} \frac{E}{K_s}. \tag{7.3}$$

This constraint is not fulfilled for all values of ν once values of $E > 25$ GPa would be incorporated (which can be verified by substituting the values of ϕ ands K_s from Table 7.1). The second constraint is that the pSt-wave does not exist for all values of ν when $E < 15$ GPa. Therefore, only the domain $15 \leq E \leq 25$ GPa is considered for the pSt-wave. For reasons of comparison, we depict the behavior of the pR-wave over the same ranges.

In Figure 7.2 it can be observed that $|I_{pR}|$, Q_{pR}^{-1}, $|I_{pSt}|$ and Q_{pSt}^{-1} are most sensitive to the parameters, i.e., their magnitudes vary significantly in the (E, ν)-domain. We only show the (E, ν)-domain behaviors for the frequency $f = 820$ Hz, which is approximately equal to the rollover frequency f_c. It can be verified that the behaviors are almost identical for all other frequencies. The patterns are similar and the specific values differ only slightly, which implies that the dependencies of the attributes on E and ν are hardly affected by the attenuation mechanism. Remarkably, the behavior in the (E, ν)-domain is independent of the behavior in the f-domain. This is because

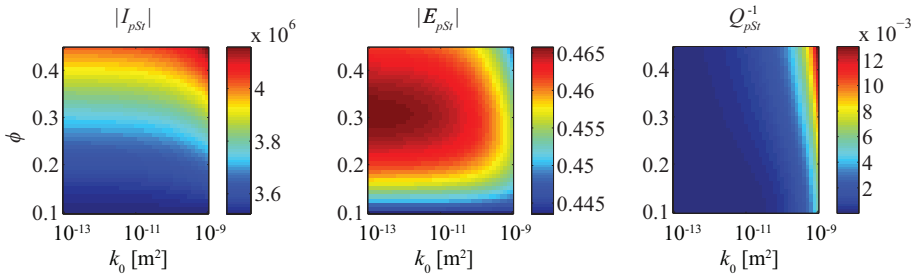

Figure 7.3: Magnitudes of impedance [kgm^{-2}s^{-1}], ellipticity [-] and attenuation [-] of the pSt-wave in the (k_0, ϕ)-domain at $f = 1$ Hz $\ll f_c$ for all (k_0, ϕ).

the Young's modulus and Poisson's ratio are solely related to the solid frame. Their influence on the relative fluid-solid motion is independent of frequency.

We have computed the behaviors of the impedances, ellipticities and attenuations as a function of permeability ($10^{-13} \leq k_0 \leq 10^{-9}$ m^2) and porosity ($0.1 \leq \phi \leq 0.445$) for three very different frequencies, i.e., $f = 1$ Hz $\ll f_c$ for all (k_0, ϕ)-combinations, $f = 5000$ Hz $\cong f_c$ for $k_0 \cong 5 \cdot 10^{-12}$ m^2 and $\phi = 0.3$, and $f = 2$ MHz $\gg f_c$ for all (k_0, ϕ)-combinations. Now, there is significant frequency-dependence: the behavior in the (k_0, ϕ)-domain is not independent of the behavior in the f-domain. This can be understood because variations in k_0 and ϕ imply variations of f/f_c (cf. Eq. (2.77)). It can be verified that a change in f/f_c works out differently in the behavior in the special cases of $f/f_c \ll 1$, $f/f_c \cong 1$ and $f/f_c \gg 1$. Further, recalling that an interface wavemode consists of a combination of body wavemodes (Achenbach, 1973), we can argue that especially the implicitly present highly f/f_c-dependent P_2-mode is responsible for the differences (see, e.g., Eq. (3.38)).

We illustrate the behaviors in the (k_0, ϕ)-domain only in those situations where the wavemodes have a relatively strong k_0-sensitivity: we show the attributes of the pSt-wave for $f \ll f_c$ (Figure 7.3) and those of both the pR- and pSt-waves for $f \cong f_c$ (Figure 7.4). In these situations the wavemodes are influenced by the attenuation mechanism. For $f \gg f_c$ the wavemodes are dominated by inertia effects and the k_0-sensitivity is weak.

From Figures 7.3 and 7.4 it can be observed that the sensitivity of Q^{-1}_{pSt} is very strong in both the k_0- and ϕ-directions. The strong k_0-dependence confirms findings in the literature and is because Q^{-1}_{pSt} is governed by the radiated P_2-mode to a large extent (P_2pSt-front; see Figure 7.1a). The impedances $|I_{pR}|$ and $|I_{pSt}|$ also have a relatively strong k_0-sensitivity for $f \cong f_c$ (Figure 7.4). They are also influenced by the relative fluid-solid motion, which can be understood as the impedances capture the resistance of the fluid phase to a motion of the solid phase (see Section 3.3). In the other situations of $f \ll f_c$ and $f \gg f_c$ the impedances are dominated by the inertial and elastic mechanisms. For each of the wavemodes the ellipticity has only weak k_0-sensitivity because it interrelates the waveforms in two solid displacement components only.

Further, the fact that a variation of k_0 or ϕ implies a variation of f/f_c can be

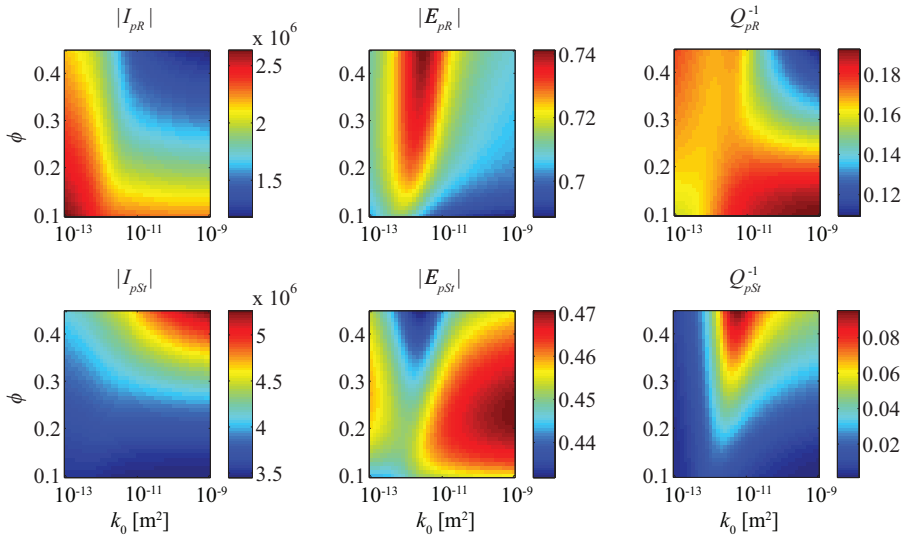

Figure 7.4: Magnitudes of impedances [kgm^{-2}s^{-1}], ellipticities [-] and attenuations [-] of the pR- and pSt-waves in the (k_0, ϕ)-domain at $f = 5000$ Hz $\cong f_c$ for $k_0 \cong 5 \cdot 10^{-12}$ m^2 and $\phi = 0.3$.

clearly observed in the Figure 7.4 ($f \cong f_c$): the transition behavior around $f/f_c = 1$ takes place when $k_0 \cong 5 \cdot 10^{-12}$ m^2.

7.3 Porous-medium characterization

In the previous section we have discussed the behaviors of the impedances, ellipticities and attenuations in the (E, ν)- and (k_0, ϕ)-domains. Their combinations can be used to uniquely estimate the medium parameters (cf. Section 6.3). In this section we show the combinations of the impedance and ellipticity, and of the impedance and attenuation, for each of the wavemodes. These are the most promising combinations: the most sensitive to parameter variations and the most different behaviors in the parameter domains of the combined attributes with respect to each other.

Like in Section 6.3, we assume that the impedances and ellipticities of the wavemodes can be extracted from a three-component measurement (see also Section 7.5); for the attenuations only a single-component measurement is required. We combine the attributes in a joint cost function similar to Ghose & Slob (2006)

$$C_\beta^{I,E}(E,\nu) = \left(\frac{\sum_f |I_\beta(E,\nu,f) - I_{\beta,d}(f)|^\gamma}{2\sum_f |I_{\beta,d}|^\gamma} + \frac{\sum_f |E_\beta(E,\nu,f) - E_{\beta,d}(f)|^\gamma}{2\sum_f |E_{\beta,d}|^\gamma} \right)^{\frac{1}{\gamma}}. \quad (7.4)$$

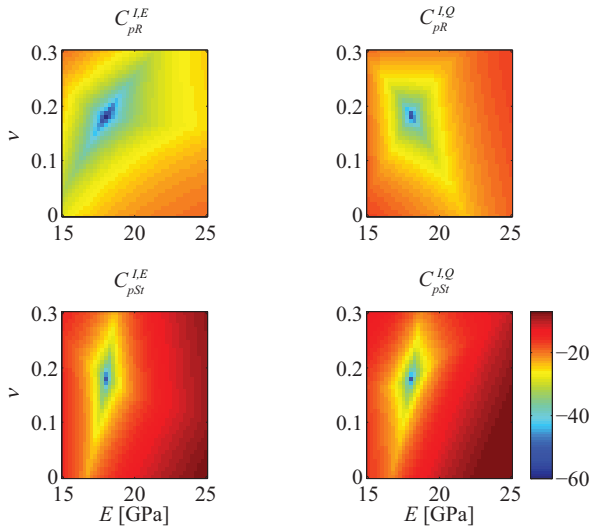

Figure 7.5: Joint cost functions in the (E, ν)-domain of impedance and ellipticity, and of impedance and attenuation, for each of the interface wavemodes at $f = 820$ Hz.

Here, $I_\beta(E, \nu, f)$ and $E_\beta(E, \nu, f)$ are model predictions of the impedance and ellipticity (see Figure 7.2), and $I_{\beta,d}$ and $E_{\beta,d}$ are the corresponding experimentally observed values (subscript "d" denotes "data"). The cost function involves summation over frequency f, which we incorporate in the case that the behavior of the cost function is expected to benefit from the frequency-dependence (see below). We use $\gamma = 2$, but in case of noisy data with a zero mean $\gamma = 1$ is preferred. The cost function can also combine the impedance and attenuation ($C_\beta^{I,Q}$) rather than the impedance and ellipticity ($C_\beta^{I,E}$). Then, Q_β^{-1} denotes the model prediction and $Q_{\beta,d}^{-1}$ the attenuation as extracted from the measurement. Further, in the case of the estimation of k_0 and ϕ, obviously these parameters appear in the argument instead of E and ν.

In order to illustrate the behavior of the cost function in the (E, ν)- and (k_0, ϕ)-domains, we have performed a synthetic test for the water/water-saturated QF20 configuration (the non-varying material parameters are given in Table 7.1). The corresponding theoretical impedance and ellipticity of the pR- and pSt-waves are computed using Eqs. (7.1) and (7.2), respectively. Taking those as representative of the experimental observation $I_{\beta,d}$ and $E_{\beta,d}$, respectively, we have computed the cost function (Eq. (7.4)) for varying values of E and ν, and for varying values k_0 and ϕ. In both cases we incorporate only one frequency component. For the estimation of k_0 and ϕ we take $f = 100$ kHz, which is at the lower end of the detected frequency range in our experiment (Section 7.5). We do not incorporate higher frequencies as they have weaker k_0-dependence and, thus, would reduce the k_0-sensitivity of the cost functions. For the estimation of E and ν we use $f = 820$ Hz, corresponding with the (frequency-independent) results in Figure 7.2, because the pSt-wave does

Table 7.1: Material parameters as used for water-saturated QF20 porous material. We have measured the magnitudes of ρ_s, ϕ and k_0 ourselves; the other values are taken from (Johnson *et al.*, 1994). The values of E and ν have been calculated from those of K_b and G.

Solid (frame) density ρ_s [kgm^{-3}]	2628
Fluid density ρ_f [kgm^{-3}]	1000
Tortuosity α_∞	1.89
Porosity ϕ	0.397
Permeability k_0 [μm^2]	40.8
Dynamic fluid viscosity η [Pa·s]	0.001
Pore shape factor M	1.75
Shear modulus G [GPa]	7.63
Bulk modulus K_b [GPa]	9.47
Grain bulk modulus K_s [GPa]	36.6
Fluid bulk modulus K_f [GPa]	2.22
Young's modulus E [GPa]	18.04
Poisson's ratio ν	0.182

not always exist in the chosen (E, ν)-domain for $f = 100$ kHz.

The behavior of the cost functions in both domains is illustrated in Figures 7.5 and 7.6, respectively. For each of the wavemodes, both the cost functions $C_\beta^{I,E}$ and $C_\beta^{I,Q}$ give unique minima in the (E, ν)-domain, exactly at the E- and ν-values of the QF20 (Table 7.1). This results from the different behaviors of the attributes in this domain (see Section 7.2), which can be clearly recognized from the shape of the valley in the joint cost functions. By simultaneously exploiting the attributes, unique estimates of E and ν can thus be obtained, similar to the findings in Section 6.3.

In the (k_0, ϕ)-domain, however, the joint cost functions as shown in Figure 7.6 do not have clear unique minima. The k_0-sensitivities are very weak. This is because the behavior of the combined attributes is not sufficiently different from each other and all of them have a weak k_0-sensitivity when $f \gg f_c$ (see Section 7.2). Consequently, in this case the combination of different attributes does not improve the behavior of the cost functions and only accurate estimates of ϕ can be obtained.

When, however, frequencies around $f \cong f_c$ are taken for the estimation of k_0 and ϕ, the cost functions do benefit from the combination of individual attributes. Taking three very distinct frequencies, $f = 82$, 820 and 8200 Hz, the cost functions as shown in Figure 7.7 all have clear unique minima, precisely at the k_0- and ϕ-values of the QF20 (Table 7.1). Remarkably, the combination of the impedance and ellipticity gives a unique minimum for each of the wavemodes, even though the ellipticities have relatively weak k_0-sensitivities (Figures 7.3 and 7.4). Obviously, the cost functions benefit from the frequency-dependence of the constituents (see Section 7.2). Generally speaking, the combination of wave attributes is advantageous for the estimation of medium parameters whenever the behaviors of the individual ones differ enough from each other. Incorporating frequency-dependence can be crucial in this respect.

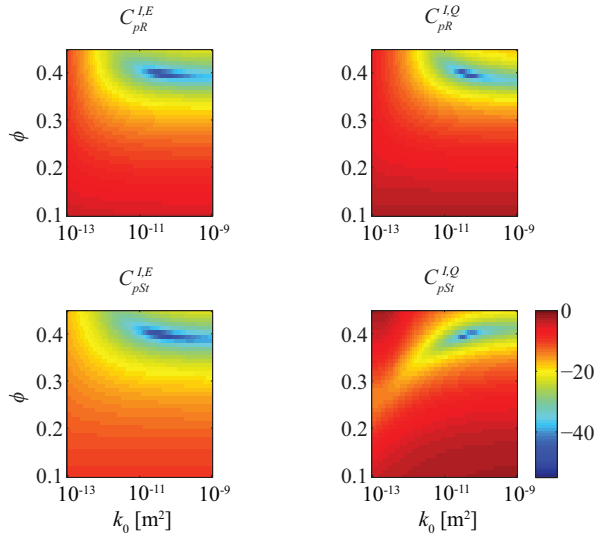

Figure 7.6: Joint cost functions in the (k_0, ϕ)-domain of impedance and ellipticity, and of impedance and attenuation, for each of the interface wavemodes at $f = 100$ kHz.

In the above numerical tests, we have assumed that the values of the impedances and ellipticities can be extracted from a measurement with 100% accuracy. To check the influence of measurement inaccuracies on the estimated values of E and ν, we have applied perturbations to $I_{\beta,d}$, $E_{\beta,d}$ and $Q^{-1}_{\beta,d}$ of $\pm 5\%$. It appears that the pSt-wave yields the most stable result: at most 4% deviation in the E-value and 34% in the ν-value when impedance and ellipticity are combined, and at most 5% deviation in the E-value and 27% in the ν-value when impedance and attenaution are combined. This is similar to the fluid/elastic-solid interface waves, where the St-wave yields the most stable result when perturbations are applied to the experimentally extracted attributes (Section 6.7). In both configurations, the estimated E- and ν-values obtained using the pR-wave are rather unstable.

To check the influence of measurement inaccuracies on the estimated values of k_0 and ϕ we have applied random perturbations between $\pm 10\%$ to each of the frequency components, separately to their real and imaginary parts. Overall, again the pSt-wave appears to yield the most stable estimates of the parameter values. In the case that we take the frequencies around $f \cong f_c$ (Figure 7.7), we find at most 16% deviation in k_0 and 3% deviation in ϕ for $C^{I,Q}_{pSt}$, which is very accurate. Using $C^{I,E}_{pSt}$, we find 38% deviation in k_0 and 12% deviation in ϕ, which is still quite good because one is usually interested in the order of magnitude of the permeability. Obviously, $C^{I,Q}_{pSt}$ yields the most stable result, which can be expected as the minimum of this cost function is the sharpest (Figure 7.7).

For the sake of completeness, we have checked the behavior of the cost function that combines I_{pSt} and Q^{-1}_{pSt} for the situation that $f \ll f_c$, which might be promising due to the different behaviors in the (k_0, ϕ)-domain (cf. Figure 7.3). It appears that

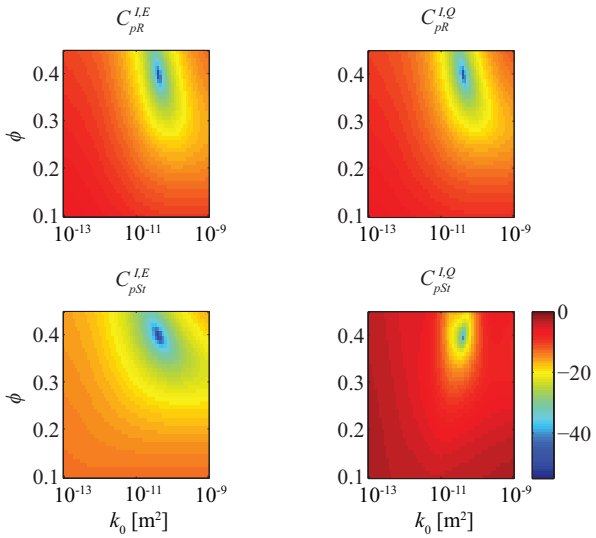

Figure 7.7: Joint cost functions in the (k_0, ϕ)-domain of impedance and ellipticity, and of impedance and attenuation, for each of the interface wavemodes incorporating frequencies around $f = f_c$, i.e., $f = 82,\ 820$ and 8200 Hz.

this combination is not successful: the separate cost function of the Q_{pSt}^{-1} gives the best results. Even though it has no unique minimum, it yields the most stable estimates of k_0 and ϕ because Q_{pSt}^{-1} has much stronger sensitivity to the parameters than I_{pSt}. This confirms the results in the literature that only employ the pSt-wave attenuation for the estimation of k_0 for $f \ll f_c$ (Burns, 1990; Tang & Cheng, 1996). In this case, a single-component measurement is sufficient for the parameter estimation.

7.4 Experiment-specific modeling

For the above estimation of medium parameters, obviously, the extraction of impedance and ellipticity of the interface wavemodes from a three-component measurement is required. Similar to the measurements in Chapter 6, here we restrict ourselves to the extraction of impedance from a simultaneous (u_3, p_F)-measurement because an elegant way to extract the ellipticity from a laser ultrasonic measurement has recently been reported (Blum *et al.*, 2010). We do not discuss the extraction of the frequency-dependent attenuation of the interface wavemodes, which can be done relatively straightforward from a single-component measurement (cf. Section 4.5.1).

In the experiment we have used the same set-up to excite and detect the waves as described in Section 6.4 (see also Figure 7.1b): a pulsed laser to excite the waves, a laser Doppler vibrometer (LDV) for the detection of the normal particle displacement and a needle hydrophone for the pressure measurement. Details about the sample and acquisition are given in Section 7.5.

For the comparison of the detected waveforms and the extracted impe–dance with the theoretical predictions according to the poroelastic wave theory, we first discuss a model for the acoustic response as excited by the laser source (Figure 7.1a). Similar as in Section 6.4, we are only interested in the wave motion and, therefore, we neglect the optical penetration and the thermal diffusion effects induced by the laser source. Since we are dealing with excitation in the ablation regime, we use a line force $F(x_1,t) = S(t)\delta(x_1)$ to model the two-dimensional acoustic response (see Figure 7.1a). Here, $\delta(...)$ is the Dirac delta function and $S(t)$ is the time signature of the source representing the energy deposition. The particular form of $S(t)$ is discussed is Section 7.6.

The two-dimensional acoustic response can be obtained by a modification of the three-dimensional response as derived in Chapter 4 (van Dalen *et al.*, 2010b). In Eq. (4.20) the factor $\frac{1}{2}\omega p_r H_0^{(2)}(\omega p_r r)$ in the integrand is replaced by $\exp(-\mathrm{i}\omega p_1 x_1)$. Further, the horizontal derivative operator ∂_h (now $h = 1$ only) in the argument of the Green's functions resulting from $-\mathrm{i}\omega p_1$ in the (p_r, ω, x_3)-domain is not required: the $-\mathrm{i}\omega p_1$ can be retained in the (p_1, ω, x_3)-domain integrand because the integration goes over p_1. Subsequently, we use the method I of integration (see Section 5.3) to perform the inverse spatial Fourier transform because the individual contributions (the loop integrals along the branch cuts and the poles) are related to separate wavemodes in the case that the wavemodes do not interfere; see Section 5.4.3.

The response is schematically illustrated in Figure 7.1a and explained in detail in Sections 4.5.1 and 5.5.

In this chapter we do not calculate the additional contribution in the LDV-measurement due to the pressure-induced refractive-index changes along the LDV-beam (see Section 6.4) because it is not required in the comparison of the experimental and modeled results (see Section 7.6). It is sufficient to keep in mind that the effect perturbs the measurement, giving larger magnitudes of the apparent LDV-detected displacement compared to the desired surface displacement (see Section 6.6).

7.5 Experimental results

Here, we give the results obtained using the simultaneous (u_3, p_F)-measurement illustrated in Figure 7.1b. The specific configuration is a water-saturated QF20 sample in water (see Table 7.1). The sample with thickness of 50 mm has been installed in an optically transparent water tank made of glass. The water layer thickness is also 50 mm. To ensure good quality of the LDV-signal, we have glued a small piece of retroreflective tape (PolyTec®) on the sample at the detection point.

During the experiment we have moved the excitation laser beam over a distance of 34.2 mm in the x_1-direction with steps of $\Delta x_1 = 200$ μm using a scanning stage, keeping the position of the receivers fixed. The smallest source-receiver distance is 23 mm. For every location of the source, we have averaged the signals 256 times to improve the signal/noise ratio.

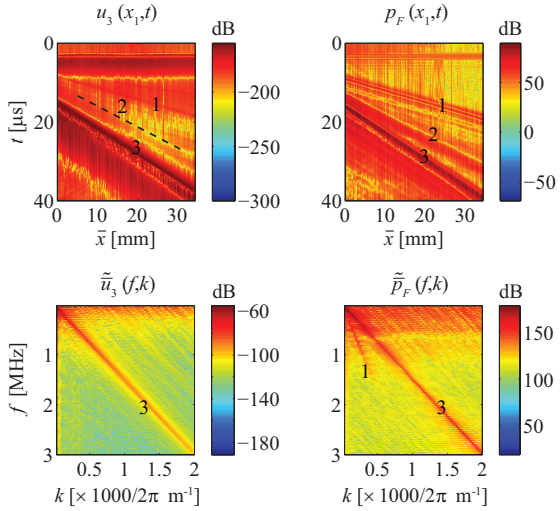

Figure 7.8: Observed spatiotemporal evolution of normal particle displacement u_3 (dB re. 1 m) and fluid pressure p_F (dB re. 1 Pa) using a laser Doppler vibrometer and a needle hydrophone, respectively, for a scanning source over a distance of $\bar{x} = x_1 - x_0 = 34.2$ mm (the smallest source-receiver distance $x_0 = 23$ mm). The P-wave is indicated by (1), the pR-wave by (2) and the interfering F- and St-wave arrivals by (3). The corresponding frequency-wavenumber domain spectra $|\tilde{\tilde{u}}_3(f,k)|$ and $|\tilde{\tilde{p}}_F(f,k)|$ are also shown. The pR-wave spectra are too weak to be identified. The P_1-wave can only be distinguished in $|\tilde{\tilde{p}}_F(f,k)|$.

In Figure 7.8 the experimentally observed u_3 and p_F are shown. We have applied a low-pass filter at 3 MHz to eliminate high-frequency noise. The p_F-data have been deconvolved by the frequency-dependent sensitivity of the needle hydrophone/amplifier set. The u_3-data have been divided by the refractive index of water $n_{F,0} = 1.333$ (Scruby & Drain, 1990) because the laser Doppler vibrometer is calibrated for measurements in air.

In $u_3(x_1,t)$ and $p_F(x_1,t)$ we can observe the P_1-wave arrival (appr. 3344 ms^{-1}), and an interference of the F- and pSt-wave arrivals (appr. 1500 ms^{-1}). Also the pR-wave is present in both the components, but quite weakly in u_3 (appr. 1872 ms^{-1}, indicated with the dashed line). These propagation velocities match the predicted values as shown in Figure 7.9 quite closely; the deviation is the largest for the P_1-wave (predicted as 3465 ms^{-1} for $f \to \infty$).

In Figure 7.10 we show the typical waveforms of the observed arrivals in u_3 and p_F (in this case $x_1 = 53$ mm). We have vertically clipped the response to clearly show the P_1- and pR-waveforms because the pSt-wave cannot be distinguished from the F-wave. The P_1-wave is clearly a separate arrival. However, the tail of the pR-wave, which has a relatively low-frequency waveform, seems to interfere with the combined F, pSt-waveform. Further, there is a very low-frequency oscillation present in u_3 starting at $t \cong 0$ ms, which cannot be filtered due to the low frequencies present in the pR-wave.

We have computed the (f,k)-domain spectra $\tilde{\tilde{u}}_3(f,k)$ and $\tilde{\tilde{p}}_F(f,k)$ using a stan–

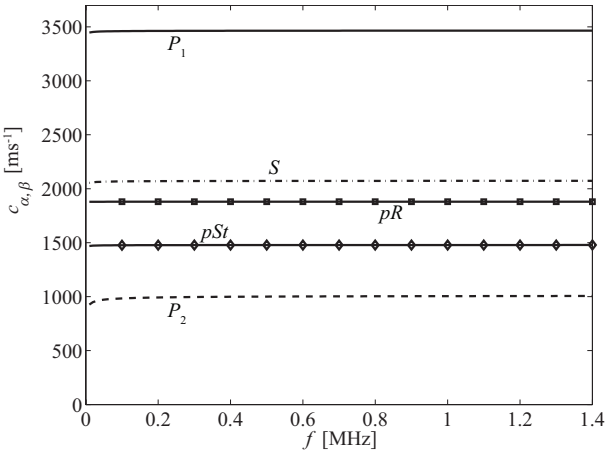

Figure 7.9: Theoretical predictions of the propagation velocities $c_{\alpha,\beta} = 1/\mathrm{Re}(s_{\alpha,\beta})$ of the body wavemodes ($\alpha = \{P_1, P_2, S\}$) and interface wavemodes ($\beta = \{pR, pSt\}$) as a function of frequency. The F-wave velocity is not shown as it almost coincides with the pSt-wave velocity: $c_F = 1489$ ms^{-1}.

dard two-dimensional Fourier transform algorithm (cf. Eqs. (2.1) and (2.3)). The spectra are shown in Figure 7.8 (lower part). In $\tilde{\tilde{u}}_3(f,k)$ only the combined F, St-spectrum can be distinguished. In $\tilde{\tilde{p}}_F(f,k)$ also the P_1-wave spectrum can be observed. The pR-wave spectra, however, cannot be observed in both components due to the weak magnitude of the pR-wave and because the spectra lie rather close to the joint F, St-spectra. Hence, we are not able to extract the pR- and pSt-wave impedances.

7.6 Experimental observations versus model predictions

In Figure 7.10 we have shown the (typical) experimentally observed waveforms. Now, we compare those with modeled equivalents as shown in Figure 7.11. To make the P_1-waveforms correspond in magnitude, frequency content and shape, as time signature of the source $S(t)$ we have taken the normalized time-derivative of the four-point optimum Blackman window function (de Hoop & van der Hijden, 1983). Remarkably, taking this time derivative is not required in the model for the fluid/elastic-solid configuration (Sections 6.4 and 6.6), where the experimentally observed P-waveform looks different particularly in p_F (cf. Figures 6.5 and 7.10); in Figure 7.10 the exact shape of the waveform in u_3 is difficult to observe due to the noise. The reason for the different source signature might be the very powerful excitation that we have applied to generate the pR-wave, for which the normal point force does not correctly describe the interaction of the excitation laser and the porous sample.

For the involved fitting parameters we have chosen $S_{max} = 7.996 \cdot 10^{-4}$ Nm^{-1}

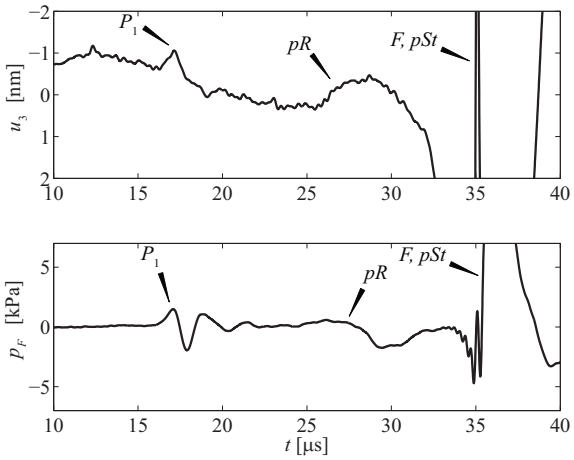

Figure 7.10: Observed normal particle displacement u_3 and fluid pressure p_F for source-receiver distance of 53 mm. The different wavemodes are indicated. The data have been filtered using a low-pass filter at $f = 3$ MHz.

and $f_0 = 350$ kHz (magnitude and the center frequency of the Blackman window function, respectively). For these choices, the modeled P_1-waveforms are pretty similar to the experimentally observed ones in u_3 and p_F (note the range difference between the u_3-axes in Figures 7.10 and 7.11). The arrival time difference is due to the different P_1-wave velocities between model and experiment (see Section 7.5). The modeled pR-waveforms are clearly different from the experimental ones: the frequency content is higher, and the shapes and the magnitudes are different. The reason for this seems to be that, due to the low-frequency content of the pR-wave and the corresponding relatively large wavelength, it behaves as a guided wavemode due to the finite depth of the water layer and the sample (Achenbach, 1973). Apparently, the excited frequencies are too small for the current experimental set-up, even though the excitation spectrum (laser) is very broad. Further, as the residue contribution of the pR-pole (see Sections 7.2 and 7.4), which we have incorporated in Figure 7.11, does not entirely coincide with the full-response waveform, there must be an interfering S-wave present in the modeled response at the onset of the pR-wave (in p_F, it is the FS-head wave generated by the S-wave; see Figure 7.1a, and Sections 4.5.1 and 5.5). It is not clear whether the S-wave is also present in the experimentally observed response. At least, in Figure 7.8 no arrival with the shear-wave velocity can be distinguished. Concerning the joint F, pSt-waveform, it can be seen that its magnitude is considerably underestimated in the u_3, and the waveforms look different in both the components. These differences might also be caused by the oversimplification of the modeled source.

The above deviations in the pR-waveforms cannot be caused by the refractive-index changes as their influence is expected to give an additive contribution in the displacement measurement only (which is in phase with the surface displacement; see Section 6.6).

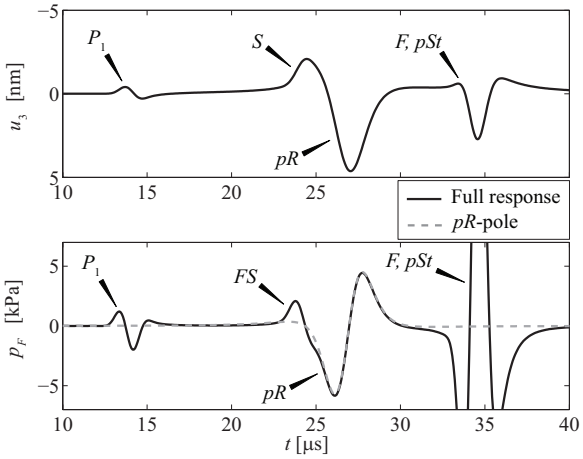

Figure 7.11: Modeled normal particle displacement u_3 and fluid pressure p_F for source-receiver distance of 53 mm excited by a line force with $S_{max} = 7.996 \cdot 10^{-4}$ Nm^{-1} and center frequency $f_0 = 350$ kHz. The dashed line indicates the pR-waveform in p_F as predicted by the corresponding pole residue.

In Section 7.5 we have argued that the extraction of the pR- and pSt-wave impedances from the measurements is not possible. It can, however, be verified that in principle the extraction of the pR-wave impedance is feasible when the layer thicknesses are sufficiently large. We have calculated the responses for a scanning source to mimic the experiment, using the same force magnitude and frequency content as described above. We have not included the perturbing effect of the refractive-index changes (cf. Section 6.6) because we are only interested in the feasibility of extracting the pR-wave impedance from any (u_3, p_F)-measurement (in which not necessarily a LDV is used). As the pR-waveform is much better separated from the combined F, pSt-waveform in the modeled response (cf. Figure 7.11; except for the very low frequencies), the pR-wave spectra can be distinguished in the (f, k)-domain and its impedance can be computed from the ratio of $\tilde{\bar{p}}_F(f, k)$ and $\tilde{\bar{u}}_3(f, k)$, divided by iω. The pR-wave impedance extracted from these modeled spectra closely matches the frequency-dependent plane-wave impedance I_{pR} (Eq. (7.1)). This might seem to be obvious, but it shows that the interfering S-wave hardly influences the extracted impedance, which is probably due to its weak presence. In principle, however, larger offsets should be taken for the extraction of the pR-wave impedance such that the S- and pR-waves are separated.

7.7 Conclusions

The impedance and ellipticity of an interface wave are attributes that interrelate the full waveforms in the different components. In this chapter we found that the impedances and ellipticities of the pseudo-Rayleigh (pR) and pseudo-Stoneley (pSt) waves at the fluid/porous-medium interface can be simultaneously used to uniquely

estimate Young's modulus (E) and Poisson's ratio (ν) of the porous solid, like those of the fluid/elastic-solid interface waves (see Section 6.3). The pSt-wave gives the most stable estimates against measurement uncertainties. For reasons of comparison, we showed that the combinations of the impedances and attenuations of the wavemodes give similar results.

For the permeability (k_0) and porosity (ϕ), which are parameters that govern the attenuation mechanism, we showed that the attributes can have different functional dependencies (like in the (E, ν)-domain), and are, in addition, frequency-dependent. The attenuation of the pSt-wave has a strong k_0-sensitivity in the low-frequency regime $f \ll f_c$ and for $f \cong f_c$ (f_c denotes Biot's rollover frequency; see Section 2.5.1), which is due to the radiation of the slow compressional (P_2) mode that governs the pSt-wave attenuation to a large extent. The pR- and pSt-wave impedances also have relatively strong k_0-sensitivity for $f \cong f_c$ as they interrelate the fluid to the solid phases and, thus, can sense the relative fluid-solid motion. The ellipticities have weak k_0-sensitivity as they only interrelate the solid displacement components.

Once the impedance and attenuation of the pSt-wave are combined in a cost function, unique and very stable estimates of k_0 and ϕ are obtained when we incorporate frequencies around $f \cong f_c$. In that case, also the combination of the pSt-wave impedance and ellipticity, that of the pR-wave impedance and ellipticity, and that of the pR-wave impedance and attenuation all give a unique minimum in the corresponding cost function, even though not all of the individual attributes have a strong sensitivity. This is due to their frequency-dependence. The corresponding minima are, however, less stable than that obtained from the pSt-wave impedance and attenuation. In the situation that $f \ll f_c$, the best results are obtained using the pSt-wave attenuation only. Even though the cost function has no unique minimum, it yields the most stable estimates of k_0 and ϕ because the pSt-wave attenuation has much stronger sensitivity to the parameters than any other attribute. This confirms the results in the literature that only employ the pSt-wave attenuation for the estimation of k_0 for $f \ll f_c$ (Burns, 1990; Tang & Cheng, 1996). In this case, a single-component measurement is sufficient for the parameter estimation.

Using the experimental set-up as introduced in Chapter 6, we showed that the impedance of the ultrasonic pR- and pSt-waves at the water/water-saturated QF20 (artificial porous material) interface cannot be successfully extracted. The pSt-wave interferes with the fluid compressional wave. The pR-wave is too weak and is influenced by the dimensions of the water layer and the sample: it behaves as a guided wavemode due to its low-frequency content. Using the computational model as developed in Chapter 4, however, it was shown that the extraction of the pR-wave impedance from a simultaneous particle displacement and fluid pressure measurement is in principle feasible once the layer thicknesses are sufficiently large.

Chapter 8

In-situ permeability from integrated poroelastic reflection coefficients[i]

Abstract

A reliable estimate of the in-situ permeability of a porous layer in the subsurface is extremely difficult to obtain. We have observed that at the field seismic frequency band the poroelastic behavior for different seismic wavemodes can differ in such a way that their combination gives unique estimates of in-situ permeability and porosity simultaneously. This is utilized in the integration of angle- and frequency-dependent poroelastic reflection coefficients in a cost function. Realistic numerical simulations show that the estimated values of permeability and porosity are robust against uncertainties in the employed poroelastic mechanism and in the data. Potential applications of this approach exist in hydrocarbon exploration, hydrogeology, and geotechnical engineering.

8.1 Introduction

Reliable information of the distribution of the Darcy permeability (k_0) in a porous layer in the subsurface is critically important in many disciplines, e.g., hydrocarbon exploration, hydrogeology and geotechnical engineering. Permeability can be highly variable, both vertically and horizontally. In general, in-situ k_0 can hardly be assessed directly (e.g., Ratnam *et al.*, 2005). The indirect methods are based on empirical relations involving other measured parameters and have large uncertainties. For instance, with the Kozeny-Karman equation and an independent measurement of the porosity (ϕ), only an approximate estimate of k_0 can be obtained.

[i]This chapter has been published as a journal paper in *Geophysical Research Letters* **37**, L12303 (van Dalen *et al.*, 2010a). Note that minor changes have been introduced to make the text consistent with the other chapters of this thesis.

There have been attempts to estimate in-situ k_0 from the attenuation of tube waves using poroelastic wave theory (e.g., Burns, 1990). More recently, seismic body waves have been used for k_0-estimation employing poroelasticity (De Barros & Dietrich, 2008; Lin *et al.*, 2009). Poroelasticity predicts a motion of the pore fluid relative to the skeleton as waves propagate through the porous medium. However, at field seismic frequencies (10-100 Hz in soft soil, as a conservative range) the relative fluid flow becomes negligible if the porous material is homogeneous or well cemented. The effects of local relative fluid flow become quite substantial if there are heterogeneities like gas inclusions. Goloshubin *et al.* (2008) have estimated k_0 from frequency-dependent fluid flow and scattering mechanisms.

Strong k_0-dependence can be observed in the mesoscopic-flow mechanisms that can explain the dispersion and attenuation at field seismic frequencies (Pride *et al.*, 2003). Accounting for mesoscopic-flow mechanisms opens the way for exploiting the frequency-dependent seismic reflectivity (Chapman *et al.*, 2006). The use of seismic reflection data seems particularly advantageous to study the spatial variations of k_0. A major difficulty, however, arises as many combinations of k_0 and ϕ can explain the observed frequency-dependent velocity and attenuation data, and no unique estimate can be reached.

Here we present the result of an integration of angle- and frequency-dependent poroelastic reflection coefficients of different seismic wavemodes at the interface of two fluid-saturated porous layers containing minute quantities of gas. Because the wavemodes behave differently in the (k_0, ϕ)-domain, their integration in a cost function leads to a unique and reliable estimate for in-situ k_0 and ϕ simultaneously. We first consider a realistic flow mechanism for the field seismic frequencies. Then we illustrate the results through tests on synthetic data, and finally discuss the scope of this approach.

8.2 Mesoscopic-flow mechanism

For homogeneous porous materials (e.g., glass beads), the wave velocities predicted by Biot's theory are quite accurate (Berryman, 1980). However, for fluid-saturated natural rocks or sediments, Biot's macroscopic (wavelength scale) flow mechanism cannot simultaneously explain the observed dispersion and attenuation. Recent studies have shown that the major cause of intrinsic attenuation in porous media can be wave-induced local fluid flow due to the presence of mesoscopic (sub-wavelength scale) heterogeneities causing fluid-pressure gradients. Inhomogeneities in the frame structure (e.g., pockets of weakly cemented grains) can be described by the double-porosity theory (Pride *et al.*, 2004). Inhomogeneities in the fluid (e.g., gas pockets larger than the grain size) can be modeled using an effective plane-wave modulus (White, 1975) or an effective fluid bulk modulus (Smeulders & van Dongen, 1997). A model for random distributions of inhomogeneities has been proposed by Müller & Gurevich (2005).

In order to investigate the seismic reflection coefficients at the boundary between two porous layers, we consider an unconsolidated near-surface situation made of two layers of water-saturated loose sands containing minute quantities of gas (bubbles).

Table 8.1: Realistic material parameters differing between the two layers.

	ρ_s [kgm^{-3}]	ϕ	k_0 [μm^2]	α_∞	G [MPa]	K_b [MPa]
layer 1	2500	0.4	8	1.75	42.75	79.75
layer 2	2550	0.3548	5.5	1.91	64.80	108.00

We use the mechanism of Smeulders & van Dongen (1997) and Vogelaar (2009), which uses the Rayleigh-Plesset equation for the gas-bubble behavior and is known to provide realistic results (e.g., Wijngaarden, 1972; Bedford & Stern, 1983). Both sand layers (1: upper layer, 2: lower target layer) have identical grain bulk modulus $K_s = 36.5$ GPa, fluid bulk modulus $K_f = 2.22$ GPa, fluid viscosity $\eta = 0.001$ Pa·s, fluid density $\rho_f = 1000$ kgm^{-3}, gas bubble radius $r_g = 5$ mm, gas fraction $s_g = 0.001$, and gas bulk modulus $K_g = 142$ kPa (air). The two layers differ in shear modulus G, bulk modulus K_b, porosity ϕ, matrix density ρ_s, tortuosity α_∞, and permeability k_0 (see Table 8.1).

Using the mesoscopic-flow mechanism, seismic wave velocities and attenuations can be computed for both layers. We illustrate in Figure 8.1 the results for layer 2 as a function of frequency (f). The presence of gas does not affect the shear (S) wave propagation. The fast compressional (P_1) wave is, however, strongly affected by the gas inclusion and shows significant dispersion. The frequency regime where the velocity c_{P1} sharply changes highly depends on r_g. For smaller bubbles, as encountered in pressurized marine sediments (Anderson & Hampton, 1980), the dispersive regime shifts towards higher frequencies (Figure 8.1). At low frequencies, the P_1-wave attenuation (expressed by the inverse quality factor Q_{P1}^{-1}) shows the typical behavior of sandy sediments (Buchanan, 2006). Values of Q_{P1}^{-1} exceeding 0.1 are reported in shallow loose sand layers (Malagnini, 1996). Therefore, our considered mechanism offers a realistic description of the seismic dispersion observed in the field.

In the low-frequency limit c_{P1} only depends on stiffnesses, densities, ϕ and s_g, and it senses k_0 only at the onset of the dispersive regime. While ϕ-information is present in both c_{P1} and Q_{P1}^{-1}, the k_0-information is mainly implicit in the frequency-dependent attenuation, as $Q_{P1}^{-1} \propto f/k_0$ (Pride *et al.*, 2004).

8.3 Permeability from integrated reflection coefficients

In this section we present the results of integration of different wavemodes to estimate k_0 and ϕ. We use the angle- and frequency-dependent reflection coefficients (e.g., Dutta & Odé, 1983) at the open-pore interface of the two water-saturated gassy sand layers. We incorporate the mesoscopic-flow mechanism as discussed above. Regarding reflection coefficients, Johnson *et al.* (1994) have shown that the coefficients

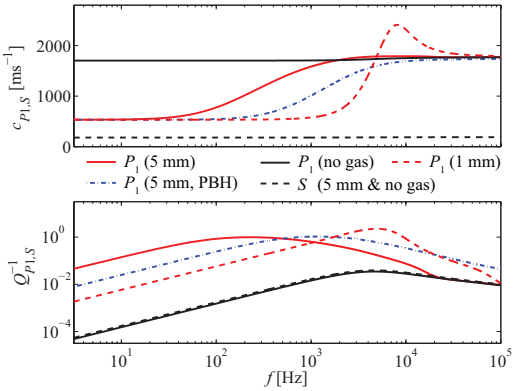

Figure 8.1: Wave velocities $c_{P1,S}$ and attenuations $Q^{-1}_{P1,S}$ in layer 2 for gassy and non-gassy situations (Smeulders & van Dongen, 1997; Vogelaar, 2009); values of the bubble radius r_g are given in brackets. PBH represents the patchy saturation model of Pride *et al.* (2004), which is used in Section 8.4.

at a fluid/porous-medium interface agree quite well with the experimental results.

In practice, both 3-component seismic (particle velocity) data and the pore-fluid pressure data need to be acquired for different seismic wavemodes (P_1P_1, P_1SV, SVP_1, $SVSV$, $SHSH$) at a given location. A reflection event present in these multiple datasets should correspond to a given interface and reflection point, e.g., common midpoint. The data need to be preprocessed to minimize all surface-related effects and various noise, and then decomposed into P_1, SV and SH waves. This is not a trivial task for the land data, but recent developments are promising. During all processing, amplitudes should be preserved. The feasibility of such processing has been reported earlier (e.g., Schalkwijk *et al.*, 2003; Ghose & Goudswaard, 2004; Holvik & Amundsen, 2005).

We assume that all properties of layer 1 are known, and that k_0 and ϕ are the only unknown properties for layer 2. We calculate the reflection coefficients of various wavemodes (R_{P1P1}, R_{P1SV}, R_{SVP1}, R_{SVSV} and R_{SHSH}) for varying values of k_0 and ϕ in the target layer (model space: $0.1 \leq k_0 \leq 100$ μm^2; $0.02 \leq \phi \leq 0.7$). In Figure 8.2 we illustrate the behavior of R_{P1P1}, R_{P1SV}, and R_{SVSV} in the parameter (k_0, ϕ)-domain. R_{SVP1} behaves identical to R_{P1SV} (apart from a normalization factor), and R_{SHSH} similar to R_{SVSV}. The presence of gas and the resulting high k_0-sensitivity can only be observed for the reflection coefficients associated with the P_1 wave, which is due to the influence of gas on c_{P1} and Q^{-1}_{P1} only (see Figure 8.1). Remarkably, the orientation of the contours in the (k_0, ϕ)-domain is very different, particularly for R_{P1P1} and R_{P1SV}. This is due to the difference in local (at reflection point) physical behavior of these two wavemodes.

Next, we take advantage of this difference and integrate two different wavemodes by combining their reflection coefficients in a cost function similar to Ghose & Slob

(2006):

$$C_{\alpha\chi,\kappa\varsigma}(k_0,\phi) = \left(\frac{\sum_{p,f} |\Delta_{\alpha\chi}|^\gamma}{2\left(\sum_{p,f} |\Delta_{\alpha\chi}|^\gamma\right)_{\max}} + \frac{\sum_{p,f} |\Delta_{\kappa\varsigma}|^\gamma}{2\left(\sum_{p,f} |\Delta_{\kappa\varsigma}|^\gamma\right)_{\max}} \right)^{\frac{1}{\gamma}}, \tag{8.1}$$

where $\Delta_{\alpha\chi} = \Delta_{\alpha\chi}(k_0,\phi) = R_{\alpha\chi}(p,f,k_0,\phi) - \bar{R}_{\alpha\chi}(p,f)$ is the difference between model prediction $R_{\alpha\chi}$, with χ denoting the incident wave and α the reflected, and the reflection coefficient $\bar{R}_{\alpha\chi}$ representing field observation, generated using the true values of k_0 and ϕ (Table 8.1). Similarly, $\Delta_{\kappa\varsigma}$ represents a different wavemode. The cost function involves summation over both the ray parameter p and the frequency f. Normalization using the maximum value of each of the terms $\Delta_{\alpha\chi}$ and $\Delta_{\kappa\varsigma}$ in the (k_0,ϕ)-domain, respectively, takes care of the magnitude differences. We use $\gamma = 2$, but in case of noisy data with a zero mean $\gamma = 1$ is preferred. The cost function $C_{\alpha\chi,\kappa\varsigma}$ is to be minimized to obtain estimates for k_0 and ϕ in the target layer.

For this numerical test, we adhere to the constraints of near-surface seismic field data in soft soil, viz. the low frequency content and the difficulty in measuring the P_1-wave dispersion in the field. Therefore, those values are taken only at two discrete frequencies: for P_1 40 and 100 Hz; for S 10 and 50 Hz. R_{P1SV} and R_{SVP1} have only frequencies that are common to both P_1 and S, hence 40 and 50 Hz. The number of p values is 48 and the corresponding station spacing is 0.75 m. We use only those p values that are related to propagating waves in layer 1.

In Figure 8.3 we show the separate cost functions C_{P1P1} and C_{P1SV} (individual terms in equation 8.1) and the integrated cost function $C_{P1P1,P1SV}$. While the separate cost functions do not provide sharp minima, the integrated cost function clearly shows a very sharp minimum (precisely at the correct k_0 and ϕ for layer 2, see Table 8.1). A unique solution for k_0 and ϕ can thus be obtained in the field seismic frequency band. The integration of C_{P1P1} and C_{P1SV} offers a good convexity because their individual local minima alignments are nearly orthogonal to each other in the (k_0,ϕ)-domain. This is due to the underlying physics, as shown in Figure 8.2: R_{P1P1} has a strong k_0-sensitivity as it is highly affected by the presence of mesoscopic heterogeneities (gas bubbles), while R_{P1SV} is more sensitive to ϕ. R_{P1SV} and R_{SVP1} are most suitable for integration with R_{P1P1}. The other reflection coefficients can only be used for ϕ-estimation.

The strength of this approach lies in exploiting the physical difference in the poroelastic behavior of the different seismic wavemodes reflected at an interface. Any mechanism of poroelasticity that reliably captures this difference at seismic frequencies will successfully allow such integration. Because the poroelastic reflection coefficients incorporate the effects of both frequency-dependent velocity and attenuation, and angle-dependence provides further constraint, such integration of reflection coefficients is promising. It has been so far impossible to obtain estimates of k_0 and ϕ that individually and simultaneously satisfy the field observations. The present approach provides a solution to this problem.

For pre-critical angles the reflection coefficients have non-zero imaginary parts due to attenuation. Since k_0 affects mainly the attenuation at the field seismic frequency band, one can intuit that the imaginary part of the reflection coefficient

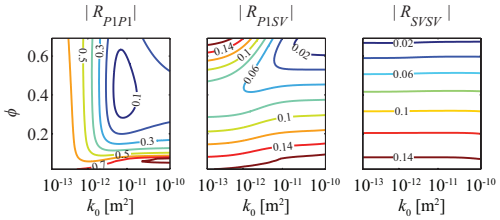

Figure 8.2: Behavior in the (k_0, ϕ)-domain of $|R_{P1P1}|$, $|R_{P1SV}|$ and $|R_{SVSV}|$ for $f = 50$ Hz, $p = 1.1 \cdot 10^{-3}$ m^{-1}.

would have the strongest k_0-sensitivity. In Figure 8.3 the results for both real and imaginary parts of the reflection coefficients are also illustrated. Because the pre-critical angles are used together with the post-critical ones, the k_0-sensitivity of the imaginary part decreases. The total reflection coefficient, in this case, offers the best result for integration, as it combines the effect of both real and imaginary parts.

8.4 Discussion

Because all mesoscopic-flow mechanisms exhibit strong k_0-dependence (Pride *et al.*, 2003), reliable estimation of in-situ k_0 is feasible. To verify the effect of inaccuracy

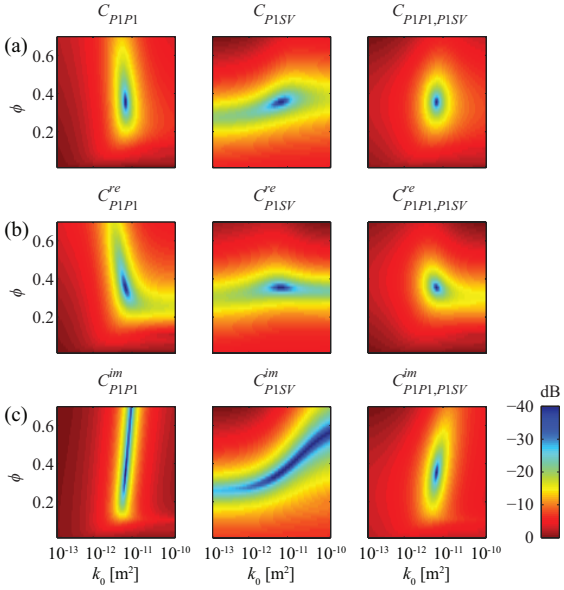

Figure 8.3: Separate (C_{P1P1} and C_{P1SV}) and integrated ($C_{P1P1,P1SV}$) cost functions in the (k_0, ϕ)-domain for (a) total, (b) real part, and (c) imaginary part of reflection coefficients.

in the observed $\bar{R}_{P1P1}(p,f)$ and $\bar{R}_{P1SV}(p,f)$, we have applied to each data point a random perturbation between $\pm 50\%$ (real and imaginary parts seperately). We find that the estimated values of k_0 and ϕ have less than 1% and 5% inaccuracy, respectiveley, indicating the robustness of the method. In order to evaluate the effect of mechanism uncertainty on the estimated values of k_0 and ϕ, we have tested two very different mechanisms. We have synthesized $\bar{R}_{P1P1}(p,f)$ and $\bar{R}_{P1SV}(p,f)$ using the patchy saturation mechanism of Pride *et al.* (2004), which also considers mesoscopic gas inclusions in the pore fluid, but employs a simple branching function to connect the low- and high-frequency limits of the frequency-dependent mesoscopic flow. On the other hand, for model predictions, we have, as before, used the mechanism of Smeulders & van Dongen (1997) and Vogelaar (2009). The dispersive regime and the frequency corresponding to the maximum attenuation are quite different between these two mechanisms (see Figure 8.1). Next, we have minimized the integrated cost function $C_{P1P1,P1SV}$. We find that the effect of mechanism uncertainty on the estimated values is small. The value of ϕ can be retrieved very accurately ($< 1\%$ inaccuracy). For k_0, the error in the retrieved value is less than 25%, which is acceptable for in-situ k_0. When the frequency restrictions in the field data are slightly relaxed, for instance 300 Hz for the maximum P_1-wave frequency and 150 Hz for the maximum P_1SV-wave frequency, then the inaccuracy in the k_0 estimate becomes less than 15%.

In this chapter we have considered only two layers. However, the methodology can be adapted to a stack of layers by progressively going downwards. Further, the approach can incorporate more unknown parameters in the lower layer; r_g and s_g can also be considered unknown. Alternatively, a priori estimates of r_g and s_g can be obtained from the low-frequency limit of c_{P1} and the corresponding slope of Q_{P1}^{-1} (e.g., Pride *et al.*, 2003). Starting with initial values of k_0 and ϕ, r_g and s_g can be estimated in an iterative manner.

A reflection coefficient relates to local plane-wave amplitudes and phases. Hence, it contains information about the local k_0 and it should, therefore, be possible to capture the lateral variation of k_0 in an otherwise homogeneous layer. The influence of k_0-fluctuation within a layer (e.g., Müller *et al.*, 2005) can be incorporated in the model reflection coefficients and in decomposition algorithms.

Although the proposed integration of reflection coefficients is powerful, the convexity of the integrated cost function (Figure 8.2) can also be sensitive to model parameters other than k_0 and ϕ. For instance, different combinations of bubble radius (r_g) and gas fraction (s_g) will require different maximum frequency in the data. For $r_g = 1$ mm and $s_g = 0.001$, which is typical for marine sediments (Anderson & Hampton, 1980), we find the best k_0-sensitivity for C_{P1P1} when the maximum P_1-wave frequency is 400 Hz; this is realistic for marine data. Therefore, one needs to consider a priori if and which reflection coefficients should be integrated, and if the frequency content allows such integration successfully. This can be accomplished through numerical tests. In the case that the mesoscopic gas inclusions are absent ($s_g = 0$), the integration is not successful due to the weak k_0-sensitivity of all reflection coefficients in the seismic frequency range. In this situation reliable k_0-estimation is very difficult.

8.5 Conclusions

We presented a concept for the estimation of in-situ permeability (k_0) together with porosity (ϕ) of a fluid-saturated porous layer containing minute gas inclusions. We found that reliable and unique estimates can be obtained by minimization of a cost function which integrates local angle- and frequency-dependent poroelastic reflection coefficients. Obtaining simultaneously permeability and porosity estimates from near-surface field seismic data using poroelasticity has so far not been possible. The approach presented here promises a solution to this problem. It takes advantage of the physical difference in the poroelastic behavior of the different seismic wavemodes reflected at the boundary between two porous layers. One needs a poroelastic mechanism that explains data at the field seismic frequencies; we incorporated a flow mechanism that accounts for mesoscopic inhomogeneity. The validity of the integration approach, however, is not dependent on a specific mechanism. Tests on realistic synthetic data illustrated that the approach is robust against uncertainties in the employed mesoscopic-flow mechanism and in the data.

Chapter 9

Conclusions

In the Introduction (Chapter 1) we formulated that in this thesis, we investigate the feasibility of exploiting full-waveform information present in multi-component acoustic observations for the estimation of poroelastic parameters, particularly for the permeability.

With regard to the poroelastic theory and its general solution we conclude (Chapters 2 and 3)

1. The body wavemodes computed using the Green's tensors of Biot's equations have different waveforms for different excitation frequencies. The coupling between the fluid- and solid-phase waveforms is also frequency-dependent, particularly for the slow compressional wave. For each of the wavemodes this coupling is described by the "coupling impedance", which can be addressed as a "multi-component full-waveform attribute".

With regard to the mathematical representation of the pseudo interface wavemodes we conclude (Chapters 4 and 5):

2. The relation of the pseudo-Rayleigh (pR) and pseudo-Stoneley (pSt) waves with the corresponding poles in the complex slowness plane is not unambiguous, depending on the choice of branch cuts. When vertical branch cuts are chosen for the evaluation of the inverse Fourier integral (which we denoted as method I), the Riemann sheets of the pR- and pSt-poles are such that the radiation condition is obeyed. Then, in the far field a separate pseudo interface wave is entirely captured by the corresponding pole residue because the loop integral along a branch cut only contributes to a separate body wave.

3. Contradictory to the conventional explanation about the origin of pseudo interface waves, poles related to the pR- and pSt-waves can also lie on the "principal" Riemann sheet. In this case, also the loop integrals along the hyperbolic branch cuts (which we denoted as method II) necessarily contribute to the pR-wave because the pR-pole is different from that in method I. They do not contribute to the pSt-wave when the pSt-pole lies on the principal Riemann sheet because the pole is identical to that in method I. However, when the

pSt-pole has migrated to another sheet, which occurs at some high frequency, the pSt-wave is fully captured by the loop integrals.

4. In general, the full waveform and the velocity and attenuation of a separate pseudo interface wave can be computed from the pole location in method I, but should be extracted from the full response in method II.

With regard to the medium characterization using fluid/elastic-solid interface waves, we conclude (Chapter 6):

5. The impedance and ellipticity have different functional dependencies on the Young's modulus and Poisson's ratio, for both the pR- and Stoneley (St) waves. Hence, by combining the multi-component full-waveform attributes in a cost function, unique estimates of these parameters can be obtained. The estimates are stable against measurement uncertainties, particularly for the St-wave.

6. Using a laser Doppler vibrometer (LDV) to measure the normal particle displacement and a needle hydrophone for the fluid pressure, we successfully extracted the laser-excited pR-wave impedance at the water/aluminum interface. The St-wave impedance can be extracted only when 1) its propagation velocity differs sufficiently from the fluid compressional-wave velocity, or 2) the St-wave is detected very far from the source where the fluid compressional wave has decayed.

7. Any LDV-measurement is perturbed by refractive-index changes along the LDV-beam once acoustic waves interfere with the beam. Using a model that accounts for these perturbations, we predicted an impedance decrease of 26% with respect to the plane-wave impedance of the pR-wave for the water/aluminum configuration. Although this deviation is different for the experimentally extracted pR-wave impedance, there is excellent agreement between the observed and predicted pR-waveforms in both the particle displacement and fluid pressure.

Then, regarding the medium characterization using the fluid/porous-medium interface waves, we conclude (Chapter 7):

8. The pR- and pSt-waves can also be used for the estimation of Young's modulus and Poisson's ratio. The results are very similar to those using the fluid/elastic-solid interface waves (cf. point 5): the pSt-wave yields the most stable estimates.

9. For each of the interface waves, both the combination of impedance and ellipticity, and that of impedance and attenuation, yield unique estimates of permeability and porosity when frequencies around Biot's rollover frequency are incorporated. The combination of the pSt-wave impedance and attenuation gives the most stable result because these attributes are most sensitive to permeability: the (coupling) impedance relates both the fluid and solid motions and the attenuation is controlled by the radiated slow compressional

mode. The ellipticity is less sensitive as it only relates the solid displacement components.

10. The extraction of the interface-wave impedance at the water/water-saturated QF20 (artificial porous material) interface is not feasible using the same set-up as described under point 6. The frequency content of the pR-wave is too low, which makes it behave as a guided wavemode, and the pSt-wave interferes with the fluid compressional wave.

Finally, regarding the characterization of a porous layer from a reflected wavefield, we conclude (Chapter 8):

11. At field seismic frequencies unique and stable estimates of permeability and porosity can be obtained from the combination of angle- and frequency-dependent poroelastic reflection coefficients of different wavemodes in a cost function, provided that a mesoscopic-flow mechanism is incorporated for realistic attenuation behavior.

Bibliography

Abramowitz, M., & Stegun, I.A. 1972. *Handbook of Mathematical Functions*. New York: Dover.

Achenbach, J.D. 1973. *Wave Propagation in Elastic Solids*. Amsterdam: North–Holland Publishing Company.

Adler, L., & Nagy, P.B. 1994. Measurements of acoustic surface waves on fluid–filled porous rocks. *J. Geophys. Res.*, **99**(B9), 17863–17869.

Aki, K., & Richards, P.G. 1980. *Quantitative Seismology*. New York: Freeman and Company.

Albers, B. 2006. Monochromatic surface waves at the interface between poroelastic and fluid half–spaces. *Proc. R. Soc. A*, **462**, 701–723.

Allard, J.F. 1993. *Propagation of Sound in Porous Media: Modelling of Sound Absorbing Materials*. Elsevier Applied Science.

Allard, J.F., Jansens, G., Vermeir, G., & Lauriks, W. 2002. Frame–borne surface waves in air–saturated porous media. *J. Acoust. Soc. Am.*, **111**(2), 690–696.

Allard, J.F., Henry, M., Glorieux, C., Petillon, S., & Lauriks, W. 2003. Laser–induced surface modes at an air–porous medium interface. *J. Appl. Phys.*, **93**(2), 1298–1304.

Allard, J.F., Henry, M., Glorieux, C., Lauriks, W., & Petillon, S. 2004. Laser–induced surface modes at water–elastic and poroelastic interfaces. *J. Appl. Phys.*, **95**(2), 528–535.

Anderson, L.A., & Hampton, L.D. 1980. Acoustics of gas–bearing sediments. I. Background. *J. Acoust. Soc. Am.*, **67**(6), 1865–1889.

Arias, I., & Achenbach, J.D. 2003. Thermoelastic generation of ultrasound by line–focused laser irradiation. *Int. J. Solids Struct.*, **40**, 6917–6935.

Attenborough, K., Hayek, S.I., & Lawther, J.M. 1980. Propagation of sound above a porous half–space. *J. Acoust. Soc. Am.*, **68**(5), 1493–1501.

Bachrach, R. 2006. Joint estimation of porosity and saturation using stochastic rock–physics modeling. *Geophysics*, **71**(5), O53–O63.

Bedford, A., & Stern, M. 1983. A model for wave propagation in gassy sediments. *J. Acoust. Soc. Am.*, **73**(2), 409–417.

Berryman, J.G. 1980. Confirmation of Biot's theory. *Appl. Phys. Lett.*, **37**(4), 382–384.

Berryman, J.G. 1981. Elastic wave propagation in fluid–saturated porous media. *J. Acoust. Soc. Am.*, **69**, 416–424.

Biot, M.A. 1955. Theory of elasticity and consolidation for a porous anisotropic solid. *J. Appl. Phys.*, **26**, 182–185.

Biot, M.A. 1956a. Theory of propagation of elastic waves in a fluid–saturated porous solid. I. Low–frequency range. *J. Acoust. Soc. Am.*, **28**, 168–178.

Biot, M.A. 1956b. Theory of propagation of elastic waves in a fluid–saturated porous solid. II. Higher frequency range. *J. Acoust. Soc. Am.*, **28**, 179–191.

Biot, M.A., & Willis, D.G. 1957. The elastic coefficients of the theory of consolidation. *J. Appl. Mech.*, **24**, 594–601.

Blum, T.E., van Wijk, K., Pouet, B., & Wartelle, A. 2010. Multicomponent wavefield characterization with a novel scanning laser interferometer. *Rev. Sci. Instr.*, **81**, 1–4.

Bonnet, G. 1987. Basic singular solutions for a poroelastic medium in the dynamic range. *J. Acoust. Soc. Am.*, **82**(5), 1758–1762.

Borcherdt, R. 2009. *Viscoelastic Waves in Layered Media*. Cambridge University Press.

Bracewell, R.N. 1986. *The Fourier Transform and Its Applications*. New York: McGraw–Hill.

Brekhovskikh, L.M. 1960. *Waves in Layered Media*. New York: Academic Press.

Brown, R.J.S., & Korringa, J. 1975. On the dependence of the elastic properties of a porous rock on the compressibility of the pore fluid. *Geophysics*, **40**, 608–616.

Buchanan, J.L. 2006. A comparison of broadband models for sand sediments. *J. Acoust. Soc. Am.*, **120**(6), 3584–3598.

Burns, D.R. 1990. *Acoustic waveform logs and the in–situ measurement of permeability – a review, in: Geophysical Applications for Geotechnical Investigations, Paillet, F.L., & Saunders, W.T. (eds.)*. Philadelphia: ASTM.

Burridge, R., & Keller, J.B. 1981. Poroelasticity equations derived from microstructure. *J. Acoust. Soc. Am.*, **70**, 1140–1146.

Burridge, R., & Vargas, C.A. 1979. The fundamental solution in dynamic poroelasticity. *Geophys. J. R. Astron. Soc.*, **58**, 61–90.

Carcione, J.M. 2007. *Wave Fields in Real Media: Wave Propagation in Anisotropic, Anelastic and Porous Media*. Elsevier.

Carcione, J.M., Morency, C., & Santos, J.E. 2010a. Computational poroelasticity – A review. *Geophysics*, **75**(5), 75A229–75A243.

Carcione, J.M., Gei, D., & Treitel, S. 2010b. The velocity of energy through a dissipative medium. *Geophysics*, **75**(2), T37–T47.

Chapman, C.H., & Orcutt, J.A. 1985. The computation of body wave synthetic seismograms in laterally homogeneous media. *Rev. Geophys.*, **23**, 105–163.

Chapman, M., Liu, E., & Li, X.-Y. 2006. The influence of fluid–sensitive dispersion and attenuation on AVO analysis. *Geophys. J. Int.*, **167**, 89–105.

Chotiros, N.P. 2002. An inversion for Biot parameters in water–saturated sand. *J. Acoust. Soc. Am.*, **112**(5), 1853–1868.

Cowin, S.C. 1999. Bone poroelasticity. *J. Biomech.*, **32**, 217–238.

Davis, A.T., & Rabinowitz, P. 1975. *Methods of Numerical Integration*. New York: Academic Press.

Davis, J.L. 1988. *Wave Propagation in Solids and Fluids*. Springer Verlag.

De Barros, L., & Dietrich, M. 2008. Perturbation of the seismic reflectivity of a fluid–saturated depth–dependent poroelastic medium. *J. Acoust. Soc. Am.*, **123**(3), 1409–1420.

De Barros, L., Dietrich, M., & Valette, B. 2010. Full waveform inversion of seismic waves reflected in a stratified porous medium. *Geophys. J. Int.*, **182**, 1543–1556.

de Hoop, A.T. 1995. *Handbook of Radiation and Scattering of Waves*. London: Academic Press.

de Hoop, A.T., & van der Hijden, J.H.M.T. 1983. Generation of acoustic waves by an impulsive line source in a fluid–solid configuration with a plane boundary. *J. Acoust. Soc. Am.*, **74**, 333–342.

Degrande, G., de Roeck, G., van den Broeck, P., & Smeulders, D. 1998. Wave propagation in layered dry, saturated and unsaturated poroelastic media. *Int. J. Solids Struct.*, **35**, 4753–4778.

Denneman, A.I.M., Drijkoningen, G.G., Smeulders, D.M.J., & Wapenaar, K. 2002. Reflection and transmission of waves at a fluid/porous–medium interface. *Geophysics*, **67**(1), 282–291.

Deresiewicz, H. 1962. The effect of boundaries on wave propagation in a liquid–filled porous solid: IV. Surface waves in a half–space. *Bull. Seismol. Soc. Am.*, **52**, 627–638.

Deresiewicz, H., & Skalak, R. 1963. On uniqueness in dynamic poroelasticity. *Bull. Seismol. Soc. Am.*, **53**, 783–788.

Desmet, C., Gusev, V., Lauriks, W., Glorieux, C., & Thoen, J. 1996. Laser–induced thermoelastic excitation of Scholte waves. *Appl. Phys. Lett.*, **21**, 2939–2941.

Desmet, C., Gusev, V., Lauriks, W., Glorieux, C., & Thoen, J. 1997. All–optical excitation and detection of leaky Rayleigh waves. *Opt. Lett.*, **22**(2), 69–71.

Drijkoningen, G.G., Rademakers, F., Slob, E.C., & Fokkema, J.T. 2006. A new elastic model for ground coupling of geophones with spikes. *Geophysics*, **71**, Q9–Q17.

Dutta, N.C., & Odé, H. 1983. Seismic reflections from a gas–water contact. *Geophysics*, **48**(2), 148–162.

Edelman, I., & Wilmanski, K. 2002. Asymptotic analysis of surface waves at vacuum/porous medium and liquid/porous medium interfaces. *Continuum Mech. Thermodyn.*, **14**, 25–44.

Ewing, W.M., Jardetzky, W.S., & Press, F. 1957. *Elastic Waves in Layered media.* New York: McGraw–Hill.

Feng, S., & Johnson, D.L. 1983a. High–frequency acoustic properties of a fluid/porous solid interface. I. New surface mode. *J. Acoust. Soc. Am.*, **74**(3), 906–914.

Feng, S., & Johnson, D.L. 1983b. High–frequency acoustic properties of a fluid/porous solid interface. II. The 2D reflection Green's function. *J. Acoust. Soc. Am.*, **74**(3), 915–924.

Ferreira, A.M.G., & Woodhouse, J.H. 2007. Observations of long period Rayleigh wave ellipticity. *Geophys. J. Int.*, **169**, 161–169.

Fuchs, B.A., Shabat, B.V., & Berry, J. 1964. *Functions of a Complex Variable and Some of Their Applications.* Oxford: Pergamon Press.

Gassmann, F. 1951. Elastic waves through a packing of spheres. *Geophysics*, **16**, 673–685.

Geertsema, T., & Smit, D.C. 1961. Some aspects of elastic wave propagation in fluid–saturated porous solids. *Geophysics*, **26**, 169–181.

Ghose, R., & Goudswaard, J. 2004. Integrating S–wave seismic reflection data and cone–penetration–test data using a multiangle multiscale approach. *Geophysics*, **69**(2), 440–459.

Ghose, R., & Slob, E.C. 2006. Quantitative integration of seismic and GPR reflections to derive unique estimates of water saturation and porosity in soil. *Geophys. Res. Lett.*, **33**, L05404.

Gilbert, F., & Laster, S.J. 1962. Excitation and propagation of pulses on an interface. *Bull. Seismol. Soc. Am.*, **52**, 299–319.

Glorieux, C., Van de Rostyne, K., Nelson, K., Gao, W., Lauriks, W., & Thoen, J. 2001. On the character of acoustic waves at the interface between hard and soft solids and liquids. *J. Acoust. Soc. Am.*, **110**(3), 1299–1306.

Goloshubin, G., Silin, D., Vingalov, V., Takkand, G., & Latfullin, M. 2008. Reservoir permeability from seismic attribute analysis. *The Leading Edge*, **27**(3), 376–381.

Gradshteyn, I.S., & Ryzhik, I.M. 1980. *Table of Integrals, Series and Products.* London: Academic Press.

Graff, K.F. 1975. *Stress Waves in Solids.* Oxford University Press.

Gubaidullin, A.A., Kuchugurina, O.Y., Smeulders, D.M.J., & Wisse, C.J. 2004. Frequency–dependent acoustic properties of a fluid/porous solid interface. *J. Acoust. Soc. Am.*, **116**(3), 1474–1480.

Gurevich, B. 1996. On: "Wave Propagation in heterogeneous, porous media: A velocity–stress, finite difference method," by Dai, N., Vafidis, A., & Kanasewich, E.R. (Geophysics **60**, pp. 327–340). *Geophysics*, **61**, 1230–1231.

Gurevich, B., & Schoenberg, M. 1999. Interface conditions for Biot's equations of poroelasticity. *J. Acoust. Soc. Am.*, **105**, 2585–2589.

Han, Q., Qian, M., & Wang, H. 2006. Investigation of liquid/solid interface waves with laser excitation and photoelastic effect detection. *J. Appl. Phys.*, **100**, 093101.

Harris, J.G. 2001. *Linear Elastic Waves.* Cambridge University Press.

Harris, J.G., & Achenbach, J.D. 2002. Comment on 'On the complex conjugate roots of the Rayleigh equation: The leaky surface wave'. *J. Acoust. Soc. Am.*, **112**(5), 1747–1748.

Holvik, E., & Amundsen, L. 2005. Elimination of the overburden response from multicomponent source and receiver seismic data, with source designature and decomposition into PP–, PS–, SP–, and SS–wave responses. *Geophysics*, **70**(2), S43–S59.

Jeffreys, H., & Jeffreys, B.S. 1946. *Methods of Mathematical Physics.* Cambridge University Press.

Jocker, J., Smeulders, D., Drijkoningen, G., van der Lee, C., & Kalfsbeek, A. 2004. Matrix propagator method for layered porous media: Analytical expressions and stability criteria. *Geophysics*, **69**(4), 1071–1081.

Johnson, D.L., Koplik, J., & Dashen, R. 1987. Theory of dynamic permeability and tortuosity in fluid–saturated porous–media. *J. Fluid Mech.*, **176**, 379–402.

Johnson, D.L., Plona, T.J., & Kojima, H. 1994. Probing porous media with first and second sound. II. Acoustic properties of water–saturated porous media. *J. Appl. Phys.*, **76**(1), 115–125.

Kelder, O. 1998. *Frequency–dependent Wave Propagation in Water–saturated Porous Media.* Delft: Delft University of Technology (Ph.D. thesis).

Lin, L. Peterson, M.L., Greenberg, A.R., & McCool, B.A. 2009. In situ measurement of permeability. *J. Acoust. Soc. Am.*, **125**(4), EL123–EL128.

Love, A.E.H. 1944. *A Treatise on the Mathematical Theory of Elasticity.* New York: Dover.

Lu, J.F., & Hanyga, A. 2005. Fundamental solution for a layered porous half space subject to a vertical point force or a point fluid source. *Comput. Mech*, **35**, 376–391.

Malagnini, L. 1996. Velocity and attenuation structure of very shallow soils: evidence for a frequency–dependent Q. *Bull. Seismol. Soc. Am.*, **86**(5), 1471–1486.

Malischewsky, P.G., & Scherbaum, F. 2004. Love's formula and H/V–ratio (ellipticity) of Rayleigh waves. *Wave Motion*, **40**, 57–67.

Manolis, G.D., & Beskos, D.E. 1989. Integral formulation and fundamental solutions of dynamic poroelasticity and thermoelasticity. *Acta Mechanica*, **76**, 89–104.

Markov, M.G. 2009. Low–frequency Stoneley wave propagation at the interface of two porous half–spaces. *Geophys. J. Int.*, **177**, 603–608.

Mattei, C., & Adler, L. 2000. Leaky wave detection at air–solid interfaces by laser interferometry. *Ultrasonics*, **38**(2), 570–571.

Mayes, M.J., Nagy, P.B., Adler, L., Bonner, B.P., & Streit, R. 1986. Excitation of surface waves of different modes at fluid–porous solid interface. *J. Acoust. Soc. Am.*, **79**, 249–252.

Müller, T.M., & Gurevich, B. 2005. A first–order statistical smoothing approximation for the coherent wave field in random porous media. *J. Acoust. Soc. Am.*, **117**(4), 1796–1805.

Müller, T.M., Lambert, G., & Gurevich, B. 2005. Dynamic permeability of porous rocks and its seismic signatures. *Geophysics*, **72**(5), E149–E158.

Müller, T.M., Gurevich, B., & Lebedev, M. 2010. Seismic wave attenuation and dispersion resulting from wave–induced flow in porous rocks – A review. *Geophysics*, **75**(5), 75A147–75A164.

Munirova, L.M., & Yanovskaya, T.B. 2001. Spectral ratio of the horizontal and vertical Rayleigh wave components and its application to some problems of seismology. *Izvestiya, Phys. Solid Earth*, **37**, 709–716 (translated from *Fizika Zemli*, **9**, 10–18 (2001)).

Nagy, P.B. 1992. Observation of a new surface mode on a fluid–saturated permeable solid. *Appl. Phys. Lett.*, **60**(22), 2735–2737.

Nishizawa, O., Satoh, T., & Lei, X. 1998. Detection of shear wave in ultrasonic range by using a laser Doppler vibrometer. *Rev. Sci. Instr.*, **69**(6), 2572–2573.

Norris, A.N. 1985. Radiation from a point source and scattering theory in a fluid–saturated porous solid. *J. Acoust. Soc. Am.*, **77**(6), 2012–2023.

Philippacopoulos, A.J. 1998. Spectral Green's dyadic for point sources in poroelastic media. *J. Fluid Mech.*, **124**, 24–31.

Phinney, R.A. 1961. Propagation of leaking interface waves. *Bull. Seismol. Soc. Am.*, **51**(4), 527–555.

Pierce, A.D. 2007. *Basic linear acoustics, in: Springer Handbook of Acoustics, Rossing, T.D. (ed.).* New York: Springer.

Plona, T.J. 1980. Observation of a second bulk compressional wave in a porous medium at ultrasonic frequencies. *Appl. Phys. Lett.*, **36**, 259–261.

Pride, S. 1994. Governing equations for the coupled electromagnetics and acoustics of porous media. **21**, 15678–15696.

Pride, S.R., & Berryman, J.G. 2003. Linear dynamics of double–porosity dual–permeability materials. I. Governing equations and acoustic attenuation. *Phys. Rev. E*, **68**, 036603.

Pride, S.R., Harris, J.M., Johnson, D.L., Mateeva, A., Nihei, K.T., Nowack, R.L., Rector, J.W., Spetzler, H., Wu, R., Yamomoto, T., Berryman, J.G., & Fehler, M. 2003. Permeability dependence of seismic amplitudes. *The Leading Edge*, **22**(6), 518–525.

Pride, S.R., Berryman, J.G., & Harris, J.M. 2004. Seismic attenuation due to wave–induced flow. *J. Geophys. Res.*, **109**, B01201.

Prudnikov, A.P., Brychkov, Yu.A., & Marichev, O.I. 1992. *Integrals and Series, Vol. 5: Inverse Laplace Transforms.* New York: Gordon and Breach.

Ratnam, S., Soga, K., & Whittle, R.W. 2005. A field permeability measurement technique using a conventional self–boring pressuremeter. *Géotechnique*, **55**(7), 527–537.

Ricker, N. 1953. Wavelet contraction, wavelet expansion, and the control of seismic resolution. *Geophysics*, **18**(4), 769–792.

Rix, G.J. 2005. *Near–surface site characterization using surface waves, in: Surface Waves in Geomechanics: Direct and Inverse Modelling for Soils and Rocks, Lai, C.G., & and Wilmanski, K. (eds.).* Udine: CISM.

Roever, W.L., Vining, T.F., & Strick, E. 1959. Propagation of elastic wave motion from an impulsive source along a fluid/solid interface. *Philos. Trans. R. Soc. London, Ser. A*, **251**(1000), 455–523.

Rosenbaum, J.H. 1974. Synthetic microseismograms: logging in porous formations. *Geophysics*, **39**(1), 14–32.

Sahay, P.N. 2001. Dynamic Green's functions for homogeneous and isotropic porous media. *Geophys. J. Int.*, **147**, 622–629.

Sayers, C.M., & Dahlin, A. 1993. Propagation of ultrasound through hydrating cement pastes at early times. *Advn. Cem. Bas. Mat.*, **1**(1), 12–21.

Schalkwijk, K.M., Wapenaar, C.P.A., & Verschuur, D.J. 2003. Adaptive decomposition of multicomponent ocean–bottom seismic data into downgoing and upgoing P– and S–waves. *Geophysics*, **68**(3), 1091–1102.

Schanz, M. 2009. Poroelastodynamics: Linear models, analytical solutions, and numerical methods. *Appl. Mech. Rev.*, **62**, 1–15.

Scholte, J.G. 1947. The range of existence of Rayleigh and Stoneley waves. *Mon. Not. Roy. Astr. Soc.: Geoph. Suppl.*, **5**, 120–126.

Scruby, C.B., & Drain, L.E. 1990. *Laser Ultrasonics: Techniques and Applications*. New York: Adam Hilger.

Sebaa, N., Fellah, Z.E.A., Fellah, M., Ogam, E., Mitri, F.G., Depollier, C., & Lauriks, W. 2008. Application of the biot Model to ultrasound in bone: Inverse problem. *IEEE Trans. Ultrason., Ferroelect., Freq. Contr.*, **55**(7), 1516–1523.

Smeulders, D.M.J. 1992. *On Wave Propagation in Saturated and Partially Saturated Porous Media*. Eindhoven: Eindhoven University of Technology (Ph.D. thesis).

Smeulders, D.M.J., & van Dongen, M.E.H. 1997. Wave propagation in porous media containing a dilute gas–liquid mixture: theory and experiments. *J. Fluid Mech.*, **343**, 351–373.

Smeulders, D.M.J., Eggels, R.L.G.M., & van Dongen, M.E.H. 1992. Dynamic permeability: reformulation of theory and new experimental and numerical data. *J. Fluid Mech.*, **245**, 211–227.

Solodov, I., Döring, D., & Busse, G. 2009. Air–coupled laser vibrometry: analysis and applications. *Appl. Optics*, **48**(7), C33–C37.

Stein, S., & Wysession, W. 2003. *An Introduction to Seismology, Earthquakes, and Earth Structure*. Blackwell.

Stoll, R.D. 1974. *Acoustic waves in saturated sediments, in: Physics of Sound in Marine Sediments, Hampton, L.D. (ed.)*. Plenum.

Straughan, B. 2008. *Stability and Wave Motion in Porous Media*. Springer.

Tang, X, & Cheng, C.H. 1996. Fast inversion of formation permeability from Stoneley wave logs using a simplified Biot–Rosenbaum model. *Geophysics*, **61**, 639–645.

Tang, X.M., & Cheng, A. 2004. *Quantitative Borehole Acoustic Methods.* Elsevier.

Tsang, L. 1978. Time–harmonic solution of the elastic head wave problem incorporating the influence of Rayleigh poles. *J. Acoust. Soc. Am.*, **63**(5), 1302–1309.

van Dalen, K.N., Drijkoningen, G.G., & Smeulders, D.M.J. 2008. *Characterization of subsurface parameters with combined fluid–pressure and particle–velocity measurements, in: Rome 2008 Leveraging Technology (Proc. 70th EAGE Conference).* Houten: EAGE.

van Dalen, K.N., Ghose, R., Drijkoningen, G.G., & Smeulders, D.M.J. 2010a. In–situ permeability from integrated poroelastic reflection coefficients. *Geophys. Res. Lett.*, **37**, L12303.

van Dalen, K.N., Drijkoningen, G.G., & Smeulders, D.M.J. 2010b. On wavemodes at the interface of a fluid and a fluid–saturated poroelastic solid. *J. Acoust. Soc. Am.*, **127**(4), 2240–2251.

van Dalen, K.N., Drijkoningen, G.G., & Smeulders, D.M.J. 2011. Pseudo interface waves observed at the fluid/porous–medium interface. A comparison of two methods. *J. Acoust. Soc. Am.*, **129**, (in press).

van der Hijden, J.H.M.T. 1984. Quantitative analysis of the pseudo–Rayleigh phenomenon. *J. Acoust. Soc. Am.*, **75**(4), 1041–1047.

van der Waerden, B.L. 1952. On the method of saddle points. *Appl. Sci. Res.*, **B2**, 33–45.

Verruijt, A. 1982. *The theory of consolidation, in: Proceedings of NATO Advanced Study Institute on Mechanics of Fluids in Porous Media, Bear, J. & Corapcioglu, M.Y. (eds.).* Dordrecht: Martinus Nijhoff Publishers.

Viktorov, I.A. 1967. *Rayleigh and Lamb waves: Physical Theory and Applications.* New York: Plenum Press.

Vogelaar, B.B.S.A. 2009. *Fluid Effect on Wave Propagation in Heterogeneous Porous Media.* Delft: Delft University of Technology (Ph.D. thesis).

Wapenaar, C.P.A., & Berkhout, A.J. 1989. *Elastic Wave Field Extrapolation.* Amsterdam: Elsevier.

White, J.E. 1975. Computed seismic speeds and attenuation in rocks with partial gas saturation. *J. Fluid Mech.*, **40**(2), 224–232.

Wiebe, Th., & Antes, H. 1991. A time domain integral formulation of dynamic poroelasticity. *Acta Mechanica*, **90**, 125–137.

Wijngaarden, L. 1972. One–dimensional flow of liquids containing small gas bubbles. *Annu. Rev. Fluid Mech.*, **4**, 369–396.

Winkler, K.W., Liu, H.L., & Johnson, D.L. 1989. Permeability and borehole Stoneley waves: Comparison between experiment and theory. *Geophysics*, **54**, 66–75.

Wisse, C.J. 1999. *On Frequency Dependence of Acoustic Waves in Porous Cylinders.* Delft: Delft University of Technology (Ph.D. thesis).

Summary

Multi-component acoustic characterization of porous media

In the area of characterization of porous media, up to now limited use is made of information captured in full acoustic waveforms. In addition, the information that can be obtained from multiple measurements is usually not employed to its full extent. However, when for example both the particle motion and the fluid pressure induced by a wavefield are detected, it can be expected that this information is sensitive to the poroelastic parameters as it combines the waveforms observed in both the solid and fluid phases. Therefore, in this thesis we investigate the feasibility of exploiting full-waveform information present in multi-component observations for the estimation of poroelastic parameters, particularly for the permeability. This parameter is very important for geotechnical and reservoir engineers, but is very difficult to determine accurately.

We focus on using the pseudo interface waves at the interface between a fluid and a fluid-saturated porous medium. Two methods are introduced for the evaluation of the inverse Fourier integral to compute the full waveforms excited by a point force: vertical branch cuts (I) and hyperbolic branch cuts (II) in the complex slowness plane. We find that the relation of the pseudo-Rayleigh (pR) and pseudo-Stoneley (pSt) waves with the corresponding pR- and pSt-poles in the slowness plane is not unambiguous, depending on the choice of branch cuts. In method I, the Riemann sheets of the pR- and pSt-poles are such that the radiation condition is obeyed. Then, in the far field a separate pseudo interface wave is entirely captured by the corresponding pole residue because the loop integral along a branch cut only contributes to a separate body wave. Opposite to the conventional explanation, poles related to the pR- and pSt-waves can also lie on the "principal" Riemann sheet, which is the sheet of integration in method II. In this case, also the loop integrals can contribute to the pseudo interface waves, i.e., necessarily to the pR-wave because the pR-pole is different from that in method I and for high frequencies also to the pSt-wave. In general, the full waveform and the velocity and attenuation of a separate pseudo interface wave can be computed from the pole (location) in method I, but should be extracted from the full response (which includes all contributions)

in method II.

Next, we investigate how the multi-component acoustic full-waveform information can be exploited and what parameters can be estimated. We start with the pR- and Stoneley (St) waves at the fluid/elastic-solid interface and use their impedances and ellipticities, which are attributes that interrelate the full waveforms as observed in different components. We find that unique estimates of the Young's modulus and Poisson's ratio can be obtained when the "multi-component full-waveform attributes" are exploited simultaneously by combining them in a so-called cost function, for both the pR- and St-waves. The uniqueness is a result of the different functional dependencies of the impedance and ellipticity on the medium parameters. The estimates are stable against measurement uncertainties, particularly for the St-wave. In a laboratory validation experiment, we have successfully extracted the laser-excited pR-wave impedance at the water/aluminum interface using a laser Doppler vibrometer (LDV) to measure the normal particle displacement and a needle hydrophone for the fluid pressure. The St-wave impedance can be extracted only when its propagation velocity differs sufficiently from the fluid wave velocity or very far from the source. Any LDV-measurement is perturbed by refractive-index changes along the LDV-beam once acoustic waves interfere with the beam. Using a model that accounts for these perturbations, we predict an impedance decrease of 26% with respect to the plane-wave impedance of the pR-wave for the water/aluminum configuration. Although this deviation is different for the experimentally extracted pR-wave impedance, there is excellent agreement between the observed and predicted pR-waveforms in both the particle displacement and fluid pressure.

The pR- and pSt-waves at the fluid/porous-medium interface can also be used for the estimation of the Young's modulus and Poisson's ratio. The results are very similar to those using the fluid/elastic-solid interface waves: the pSt-wave yields the most stable estimates. In addition, both the combination of impedance and ellipticity, and that of impedance and attenuation, yield unique estimates of permeability and porosity when frequencies around Biot's rollover frequency are used, for both the pR- and pSt-waves. The combination of the pSt-wave impedance and attenuation gives the best results because these attributes are most sensitivity to permeability: the impedance relates both the fluid and solid motions, and the attenuation is controlled by the radiated slow compressional mode. The ellipticity is less sensitive as it only relates the solid (horizontal and vertical) displacement components. Further, we find that the experimental extraction of the interface-wave impedances at the water/water-saturated QF20 (artificial porous material) interface is not feasible with our set-up. The frequency content of the pR-wave is too low, which makes it behave as a guided wavemode, and the pSt-wave interferes with the fluid wave.

Finally, in a synthetic application to the seismic frequency band we show that unique and stable estimates of permeability and porosity of a porous layer can be obtained from a wavefield by combining angle- and frequency-dependent poroelastic reflection coefficients of different wavemodes in a cost function. To correctly describe the seismic attenuation, we have incorporated a mesoscopic-flow mechanism, which causes the permeability sensitivity of the wavefield. The use of reflection coefficients implies that multi-component full-waveform information is employed.

Samenvatting

Multi-componenten akoestische karakterisering van poreuze media

Tot op heden wordt er op het gebied van de karakterisering van poreuze media slechts beperkt gebruikt gemaakt van de informatie die in volledige akoestische golfvormen ligt besloten. Daarnaast is het zo dat de informatie die kan worden verkregen uit meerdere metingen gewoonlijk niet volledig wordt benut. Wanneer echter bijvoorbeeld zowel de deeltjesbeweging als de vloeistofdruk, die zijn geïnduceerd door een golfveld, worden gemeten, kan worden verwacht dat deze informatie gevoelig is voor de poroelastische parameters omdat het de golfvormen gemeten in zowel het skelet als in de porievloeistof combineert. Om die reden onderzoeken we in dit proefschrift de haalbaarheid van de exploitatie van informatie die ligt besloten in volledige golfvormen en aanwezig in multi-componenten observaties, voor het schatten van poroelastische parameters, in het bijzonder van de permeabiliteit. Deze parameter is erg belangrijk voor geotechnische and reservoiringenieurs, maar is erg moeilijk nauwkeurig te bepalen.

We richten ons op het gebruik van pseudo-oppervlaktegolven ter plaatse van het grensvlak tussen een vloeistof en een vloeistofverzadigd poreus medium. Er worden twee methoden geïntroduceerd voor het evalueren van de inverse Fourier integraal die wordt gebruikt om de volledige golfvormen geëxciteerd door een puntlast, te berekenen: verticale vertakkingslijnen (I) en hyperbolische vertakkingslijnen (II) in het complexe inverse-snelheidsdomein. We vinden dat de relatie tussen de pseudo-Rayleighgolf (pR) en de pseudo-Stoneleygolf (pSt), en de corresponderende pR- en pSt-polen in het inverse-snelheidsdomein niet ondubbelzinnig is, afhankelijk van de keuze van de vertakkingslijnen. In methode I zijn de Riemannvlakken van de pR- en pSt-polen zodanig dat aan de stralingsconditie wordt voldaan. Een gescheiden pseudo-oppervlaktegolf (niet met andere golven interfererend) wordt dan in het verre veld volledig beschreven door het corresponderende poolresidu omdat de lusintegraal langs een vertakkingslijn alleen bijdraagt aan een gescheiden bulkgolf. In tegenstelling tot de conventionele opvatting kunnen polen die zijn gerelateerd aan de pR- en pSt-golven ook liggen op het hoofd-Riemannvlak; dat is het integratieoppervlak in methode II. In dat geval kunnen ook de lusintegralen bijdragen aan de pseudo-

oppervlaktegolven: noodzakelijkerwijze aan de pR-golf omdat de pR-pool een andere is dan in methode I en voor hoge frequenties ook aan de pSt-golf. In het algemeen kunnen de volledige golfvorm, de snelheid en de demping van een gescheiden pseudo-oppervlaktegolf in methode I worden berekend uit (de locatie van) de pool, maar deze moeten in methode II worden bepaald uit de volledige responsie (die bestaat uit de som van alle bijdragen).

Vervolgens onderzoeken we hoe de informatie in volledige akoestische golfvormen met behulp van multi-componenten metingen kan worden geëxploiteerd en welke parameters er kunnen worden geschat. We beginnen met de pR- en Stoneleygolven (St) ter plaatse van het grensvlak tussen een vloeistof en een elastisch medium en gebruiken hun impedanties en ellipticiteiten. Dat zijn attributen die de volledige golfvormen zoals geobserveerd in verschillende componenten aan elkaar relateren. We vinden dat unieke schattingen van de Young's modulus en de Poisson constante kunnen worden gevonden wanneer de "attributen van de volledige multi-componenten golfvorm" gelijktijdig worden geëxploiteerd door hen te combineren in een zogenaamde kostfunctie, voor zowel de pR- als de St-golf. De uniciteit is een gevolg van de verschillende afhankelijkheden van de impedantie en de ellipticiteit als functie van de mediumparameters. De schattingen zijn stabiel ten aanzien van meetonnauwkeurigheden, in het bijzonder voor de St-golf. In een validatie-experiment in het laboratorium hebben we de impedantie van de lasergeëxciteerde pR-golf ter plaatse van het grensvlak tussen water en aluminium succesvol bepaald met behulp van een laser Doppler vibrometer (LDV) voor de meting van de normale deeltjesverplaatsing en een naaldhydrofoon voor de vloeistofdruk. De impedantie van de St-golf kan alleen worden bepaald wanneer de voortplantingssnelheid voldoende verschilt van de snelheid van de vloeistofgolf, of heel ver verwijderd van de bron. Nu is het zo dat een LDV-meting wordt verstoord door variaties in de refractie-index langs de LDV-bundel wanneer akoestische golven met de bundel interfereren. Gebruikmakend van een model waarin deze verstoringen in beschouwing worden genomen, voorspellen we een impedantieafname van 26% ten opzichte van de vlakkegolfimpedantie van de pR-golf voor de water/aluminium configuratie. Hoewel deze afwijking verschilt voor de experimenteel bepaalde impedantie van de pR-golf, is er een uitstekende overeenkomst tussen de geobserveerde en voorspelde pR-golfvormen in zowel de deeltjesverplaatsing als de vloeistofdruk.

De pR- en pSt-golven ter plaatse van het grensvlak tussen een vloeistof en een poreus medium kunnen ook gebruikt worden voor het schatten van de Young's modulus en Poisson's ratio. De resultaten vertonen sterkte overeenkomsten met die van de golven ter plaatse van het grensvlak tussen een vloeistof en een elastisch medium: de pSt-golf levert de meest stabiele schattingen. Daarnaast kunnen unieke schattingen van permeabiliteit en porositeit worden verkregen met behulp van de combinatie van impedantie en ellipticiteit en met behulp van impedantie en demping wanneer frequenties rond Biot's transitiefrequentie gebruikt worden, zowel voor de pR- als de pSt-golf. De combinatie van de impedantie en de demping van de pSt-golf geeft de beste resultaten omdat deze attributen het meest gevoelig zijn voor permeabiliteit: de impedantie relateert de vloeistof- en skeletbewegingen, en de demping is afhankelijk van de uitgestraalde langzame compressiemode. De ellipticiteit is minder gevoe-

lig omdat het alleen de skeletverplaatsingscomponenten (horizontaal en verticaal) aan elkaar relateert. Verder vinden we dat de experimentele bepaling van oppervlaktegolfimpedanties ter plaatse van het grensvlak tussen water en waterverzadigd QF20 (kunstmatig poreus materiaal) niet haalbaar is met onze meetopstelling. De frequentie-inhoud van de pR-golf is te laag, waardoor deze zich gedraagt als een geleide golfmode, en de pSt-golf interfereert met de vloeistofgolf.

Tenslotte laten we in een synthetische toepassing voor de seismische frequentieband zien dat unieke en stabiele schattingen van permeabiliteit en porositeit kunnen worden verkregen uit een golfveld door middel van het combineren van hoek- en frequentieafhankelijke poroelastische reflectiecoefficienten van verschillende golfmodes in een kostfunctie. Om de seismische demping correct te beschrijven, hebben we een mesoscopisch stromingsmechanisme in het model opgenomen dat de gevoeligheid van het golfveld voor permeabiliteit veroorzaakt. Het gebruik van reflectiecoefficienten impliceert dat informatie uit volledige golfvormen zoals aanwezig in multi-componenten observaties wordt gebruikt.

Acknowledgments

According to the title page, I am supposed to be the only author of this thesis. However, like for many other dissertations, this is not really true. It is an open secret that usually many people contribute to a thesis, and in this chapter there is space to acknowledge these people. Let me first address those who contributed directly.

First of all, I would like to mention my promotors: Guy Drijkoningen, David Smeulders and Kees Wapenaar. I am very grateful to all efforts that you have put in helping me, particularly in taking the time to answer questions, reading the numerous draft versions of the papers and chapters, and asking critical questions about the fuzzy parts. Thank you very much for giving me the opportunity to "do this Ph.D.", to learn, to make errors, to develop, to elaborate my ideas and to publish. Further, I would like to express my gratitude to Christ Glorieux, Bart Sarens and Bert Verstraeten, my Belgian colleagues at KU-Leuven. You have given me the opportunity to perform experiments in your "labo" and you have even assisted me during many trials. We have managed to get experimental results that nicely connect to the theoretical part of my thesis. It was a great experience for me to see waveforms displayed on the oscilloscope during the final experiment that were so similar to the ones I had predicted using a computational model (cf. Figures 6.5 and 6.7). Concerning the laboratory work, I would also like to thank Karel Heller, who received the honorable nickname "Karel1" when I entered the laboratory more and more. In my opinion that nickname is not only justified due to my confusing presence in the laboratory (we share the same name; I was therefore called "Karel2"), but particularly because your presence in there was a necessary condition for me to do the experimental part of my Ph.D. successfully. Thanks a lot for all your help. I am also grateful to prof. Rixen and Muammer Ozbek from the Engineering Mechanics group (Faculty 3mE, TU-Delft). Thank you for the use of the equipment and your assistance.

In addition, I would like to thank my colleagues from the Applied Geophyscis and Petrophysics section. Evert Slob, thanks for your willingness to answer my questions whenever I dropped by. Ranajit Ghose, thanks for the fruitful collaboration on the estimation of permeability using "your method" and "my theory". I would also like to thank the (former) Ph.D. students and Postdocs: Ali, Alimzhan, Araz, Bobby, Bouko, Carlos, Christiaan, Daria, Dennis, Deyan, Elmer, Huajun, Martijn, Marwan, Mattia, Menne, Mohsen, Niels, Nihed, Jan, Joost, Jürg, Panos, Patrick, Petar, Ralph, Rik, Tristan and all others who I have forgotten to include. Some of you,

especially my neighbors in the office, have contributed quite a lot to this thesis with your knowledge about Matlab, Latex and Illustrator. Others have contributed in different ways: in asking critical questions, discussing things or just in proclaiming the daily coffee break around 16:00. I hope that, in turn, my presence in the office and my contribution to several discussions was constructive for you and your work.

I would also like to acknowledge the members of the Ph.D. defense committee: thank you for all your efforts.

Finally, I would like to thank all people who have contributed in a more indirect way. First of all my wife Jannine. I owe you a lot of thanks: you were the necessary stable factor during my Ph.D., always willing to listen to me when I was explaining the achievements, difficulties and challenges. In the end you were even able to explain how the topics of the different chapters of this thesis connect to each other. Coming home after a tough day of trying to find erroneous minus signs in a Matlab code, was like reaching an oasis. In that sense, you have provided the necessary variety of life. Thanks a lot for your love, patience and your willingness to live together with a perfectionist like me, and for taking care of our daughter during the daytime. I would also like to thank my parents and parents-in-law for their interest in my research and their support in several ways that definitely contributed to the successful finishing of my thesis, including the propositions. Further, I would like to express my gratitude to the people from the Missie Oost working group, particularly to Teus Donk. It is great to share the same mission and our missionary work is a welcome change for my daily work. All other friends: thanks for your support!

Above all, I am thankful to God for blessing me during the last four years in many different ways. Thinking about my life, I realize that the knowledge as presented in this thesis is very limited. It is limited in its scope: it focuses only on a pretty much specialized topic in the broad area of Geophysics, which, in turn, constitutes only a single research area next to many others. It is also limited by the nature of the knowledge: it is (applied) scientific knowledge. Only part of the reality can be meaningfully studied using this type of knowledge. It cannot be used to answer the big questions of life, e.g., about its meaning or our origin. Yet, in my opinion and experience, it does reveal something of God's creativity. While studying wave phenomena I am sometimes surprised by the beauty that is hidden in them. For instance, throw a stone into the water and look at the wonderful propagating patterns that occur (cf. the cover of this book). However, this revelation of God is rather incomplete. Who and how he really is, remains a question. That can only be discovered in Jesus Christ, in whom God has revealed himself full of grace and truth (John 1:14). Knowing God through Jesus Christ is the biggest blessing that exists. It is necessary and sufficient for everlasting peace and true happiness, even though we are only able to know God partly: like if we try to image the surrounding with a mirror (1 Corinthians 13:12), we can only see part of it due to our limited aperture. Therefore, I am looking forward to the day of full revelation. In the mean time I hope to live as a witness of God, and to serve him and the people around me. I believe that also my work of the last four years has contributed to that in some way.

Karel van Dalen

Curriculum Vitae

Personal information

Name	Karel Nicolaas van Dalen (Karel)
Place of birth	Papendrecht, The Netherlands
Date of birth	19 September 1981
Civil state	Married

Education and work

2010 -	Postdoctoral researcher Applied Geophysics and Petrophysics and lecturer for 3rd years course "Fields and Waves" (TU-Delft)
2009 - 2010	Several research visits Laboratory of Acoustics and Thermal Physics (Katholieke Universiteit Leuven, dr. Glorieux)
2008	Supervision of IDEA-league M.Sc. thesis student (A. Mahdad)
2006 - 2010	Ph.D. studies Applied Geophysics and Petrophysics (TU-Delft; prof. Wapenaar, prof. Smeulders, dr. Drijkoningen), defence March 2011
2005	Internship at IV-Groep (engineering firm - vibration problems)
2004 - 2006	M.Sc. studies Civil Engineering (TU-Delft), specialization Structural Mechanics (prof. Vrouwenvelder, dr. Metrikine), cum laude
2003 - 2005	Student-assistent for 2nd years course "Dynamics of Systems" (prof. Blaauwendraad, prof. Vrouwenvelder)
2000 - 2004	B.Sc. studies Civil Engineering (TU-Delft), cum laude
1999 - 2000	First-year studies Architecture (TU-Delft)
1999	VWO-diploma, Guido de Brès, Rotterdam

Journal papers

(1) van Dalen, K.N., Drijkoningen, G.G., Smeulders, D.M.J., Heller, H.K.J., Glorieux, C., Sarens, B., & Verstraeten, B. 2011. Impedance and ellipticity of fluid/ elastic–solid interface waves: medium characterization and simultaneous displacement – pressure measurements. *Journal of the Acoustical Society of America*, submitted. (Chapter 6 of this thesis)

(2) van Dalen, K.N., Drijkoningen, G.G., & Smeulders, D.M.J. 2011. Pseudo interface waves observed at the fluid/porous–medium interface. A comparison of two methods and physical interpretation. *Journal of the Acoustical Society of America*, **129**, (in press). (Chapter 5 of this thesis)

(3) van Dalen, K.N., Ghose, R., Drijkoningen, G.G., & Smeulders, D.M.J. 2010. In–situ permeability from integrated poroelastic reflection coefficients. *Geophysical Research Letters*, **37**, L12303. (Chapter 8 of this thesis)

(4) van Dalen, K.N., Drijkoningen, G.G., & Smeulders, D.M.J. 2010. On wave-modes at the interface of a fluid and a fluid–saturated poroelastic solid. *Journal of the Acoustical Society of America*, **127** (5), 2240–2251. (Chapter 4 of this thesis)

(5) van Dalen, K.N., & Metrikine, A.V. 2008. Transition radiation of elastic waves at the interface of two elastic half–planes. *Journal of Sound and Vibration*, **310** (3), 702–717.

Conference papers (peer reviewed)

(1) van Dalen, K.N., & Ghose, R. 2010. *In-situ permeability from physics-based integration of poroelastic reflection coefficients, in: Barcelona 2010 A New Spring for Geoscience (Proc. 72th EAGE Conference)*. Houten: EAGE.

(2) van Dalen, K.N., Mahdad, A., Drijkoningen, G.G., & Smeulders, D.M.J. 2009. *Wave modes at the interface of a fluid and a fluid-saturated poroelastic solid, in: Proceedings of the Fourth Biot Conference on Poromechanics, Ling, H.I., Smyth, A., & Betti, R. (eds.)*. New York: Destech.

(3) van Dalen, K.N., Drijkoningen, G.G., & Smeulders, D.M.J. 2008. *Characterization of subsurface parameters with combined fluid-pressure and particle-velocity measurements, in: Rome 2008 Leveraging Technology (Proc. 70th EAGE Conference)*. Houten: EAGE.